

THE ANGULAR DISTRIBUTIONS AND ENERGY SPECTRA  
OF PHOTONEUTRONS FROM HEAVY ELEMENTS

by

GORDON SINCLAIR MUTCHLER  
S.B., Massachusetts Institute of Technology

SUBMITTED IN PARTIAL FULFILLMENT  
OF THE REQUIREMENTS FOR THE  
DEGREE OF DOCTOR OF  
PHILOSOPHY

at the

MASSACHUSETTS INSTITUTE OF  
TECHNOLOGY

February, 1966

Signature of Author . . . . .

Department of Physics, October 4, 1966

Certified by . . . . .

Thesis Supervisor

Accepted by . . . . .

Chairman, Departmental Committee on Graduate Studies

5941  
4722

## ABSTRACT

### The Angular Distributions and Energy Spectra of Photoneutrons from Heavy Elements

by Gordon S. Mutchler

Submitted to the Department of Physics on October 4, 1965 in partial fulfillment of the requirement for the degree of Doctor of Philosophy.

The energy spectra of photoneutrons from Bi, Pb<sup>208</sup>, Pb<sup>207</sup>, Pb<sup>206</sup>, Tl, Hg, Au, W, Ta, Er, Ho, Sm, Pr, La, I, Sn, and In were measured at 24°, 76° and 156° relative to the photon beam from the MIT Linear Accelerator. Bremsstrahlung spectra were used with endpoints of 15, 14 and 13 MeV. The neutron energies were determined using a time-of-flight spectrometer with 10 meter flight paths and 8 ns resolution. Subtracting the 14 MeV (or 13 MeV) data (properly normalized) from the 15 MeV (or 14 MeV) data yields neutron spectra generated by an equivalent photon spectrum peaked at 14 MeV (or 13 MeV) with a FWHM of 2 MeV.

The angular distributions of the photoneutron spectra from these three bremsstrahlung spectra were analyzed in the form  $W(\theta) = a_0 + a_1 P_1(\cos\theta) + a_2 P_2(\cos\theta)$ .  $a_1$  was found to be approximately constant with energy for each target, and to range from -0.07 to +0.05 with statistical errors of  $\pm 0.02$  and estimated systematic errors of  $\pm 0.09$ . Therefore  $a_1$  was assumed to be zero for all targets, and the angular distributions are presented in the form  $W(\theta) = a_0 + a_2 P_2(\cos\theta)$ . The anisotropy ( $a_2/a_0$ ) was found to increase with neutron energy. The low energy photoneutrons (< 3 MeV) are isotropic ( $a_2/a_0 = 0$ ) and the anisotropy is maximum at or near the neutron endpoint. This maximum value of the anisotropy shows marked shell effects. It is a maximum ( $-a_2/a_0 = 0.6$  to  $0.7$ ) near the closed shell nuclei Pb<sup>208</sup> and Pr, and it has a minimum ( $-a_2/a_0 = 0.15$  to  $0.3$ ) between these two closed shells, in the region of the deformed nuclei.

The neutron difference spectra are characterized by an isotropic evaporation component which dominates at low neutron energies, and an anisotropic resonance direct component which dominates at high neutron energies. The transition from one component to the other is quite abrupt, typically taking place in an energy interval of about one to two MeV.

It was found to be possible to fit the neutron difference spectra with the theoretical curve  $dN/dE_n = \text{const } E_n \sigma_C \omega(U) + kS(E_n)$ , where  $\omega(U)$  is the level density of the residual nucleus at an excitation energy  $U$ ,  $\sigma_C$  is the inverse capture cross section, and  $S(E_n)$  is the energy spectrum of the direct component. The data was analyzed using three approximations for the level density,  $\exp(2\sqrt{a_3/2U})/(U+t)^{3/2}$ ,  $[\exp(2\sqrt{a_2U})/(U+t)^2]$ , and  $\exp(-E_n/T)$ , where  $t$  is given by the equation  $U = a_m t^2 - t$ .  $S(E_n)$  was calculated using Wilkinson's model of the giant resonance. In the above equations,  $a_m$  (or  $T$ ), and  $k$  were the only adjustable parameters.

The values of  $a_2$  generally follow the predictions of Newton,  $a_2 = K(j_z + 1)A^{2/3}$ .  $K$  was found to be 0.067. The fraction of directly emitted neutrons, defined as the integral of the direct spectrum divided by the integral of the total spectrum, was found to be about 14%, and approximately constant with  $A$ , the mass number.

Thesis Supervisor: William Bertozzi, Associate Professor of Physics

## TABLE OF CONTENTS

Chapter I Introduction . . . . .	12
A. Purpose of the Experiment . . . . .	12
B. Description of the Giant Resonance and Corresponding Nuclear Models . . . . .	15
C. Energy Spectra of Emitted Nucleons . . . . .	22
D. Angular Distributions . . . . .	24
Chapter II Apparatus . . . . .	29
A. General Description . . . . .	29
B. Neutron Detectors . . . . .	32
C. Beam Monitoring . . . . .	33
a) Analyzing Magnet . . . . .	33
b) Charge Integrator . . . . .	33
D. Time-of Flight Spectrometer . . . . .	35
a) General Description . . . . .	35
b) Detector Circuitry . . . . .	35
c) Time-to-Height Convertor . . . . .	37
d) Calibration . . . . .	39
Chapter III Experiment . . . . .	42
A. Experimental Procedure . . . . .	42
B. Background and Shielding . . . . .	44
C. Uranium Ratios . . . . .	48
D. Geometry Effects . . . . .	53
E. Detector Response . . . . .	54
Chapter IV Treatment of Data . . . . .	64
A. Preliminary Treatment . . . . .	64
a) Coincidence Correction . . . . .	64
b) Background Subtraction . . . . .	69
c) Time-to-Energy Spectrum . . . . .	69
d) Correction for Neutron Detector Efficiency, Target Scattering and Collimator Shadowing . . . . .	72
B. Angular Distribution . . . . .	73
C. Difference Spectrum . . . . .	79
D. Level Density and Direct Component . . . . .	84
a) Separation into Components . . . . .	84
1) Method I . . . . .	89
2) Method II . . . . .	91
b) Least Squares Fit . . . . .	91
E. Direct Spectrum . . . . .	93

Chapter V Discussion of the Data . . . . .	97
A. Bismuth and Lead 208 . . . . .	97
a) Experimental Data . . . . .	97
b) Direct Spectrum . . . . .	97
c) Evaporation Component . . . . .	111
d) Neutron Energy Spectra . . . . .	118
e) Angular Distributions . . . . .	118
B. Lead 207 . . . . .	123
a) Experimental Data . . . . .	123
b) Direct Spectrum . . . . .	123
c) Evaporation Spectrum . . . . .	129
d) Angular Distributions . . . . .	129
C. Lead 206 and Thallium . . . . .	133
a) Experimental Data . . . . .	133
b) Direct Spectrum . . . . .	133
c) Evaporation Spectrum . . . . .	138
d) Angular Distributions . . . . .	145
D. Mercury and Gold . . . . .	145
a) Experimental Data . . . . .	145
b) Direct Spectrum . . . . .	145
c) Evaporation Spectrum . . . . .	158
d) Angular Distributions . . . . .	158
E. Deformed Nuclei: Tungsten, Tantalum, Erbium, Holmium and Samarium . . . . .	165
a) Experimental Data . . . . .	165
b) Direct Spectrum . . . . .	165
c) Evaporation Spectrum . . . . .	181
d) Angular Distributions . . . . .	189
F. Praseodymium and Lanthanum . . . . .	189
a) Experimental Data . . . . .	189
b) Direct Spectrum . . . . .	197
c) Evaporation Spectrum . . . . .	201
d) Angular Distributions . . . . .	201
G. Iodine . . . . .	206
a) Experimental Data . . . . .	206
b) Direct Spectrum . . . . .	208
c) Evaporation Spectrum . . . . .	208
d) Angular Distributions . . . . .	208
H. Tin and Indium . . . . .	212
a) Experimental Data . . . . .	212
b) Direct Spectrum . . . . .	212
c) Evaporation Spectrum . . . . .	225
d) Angular Distributions . . . . .	225
I. Level Density Parameter . . . . .	228
J. Direct Fraction . . . . .	245



K. Angular Distribution . . . . .	255
L. Summary . . . . .	261
Appendix I Scattering Calculations . . . . .	270
Appendix II Electronics . . . . .	281
A. Photomultiplier Circuitry and Tubes . . . . .	281
B. Photomultiplier Gate Generator . . . . .	283
C. Tunnel Diode Pulse Shaper . . . . .	283
D. Triple Coincidence . . . . .	286
E. Linear Gate . . . . .	288
F. Time-to-Height Convertor (THC) . . . . .	290
G. Charge Integrator . . . . .	292
Appendix III Uranium Reference Spectra . . . . .	294
A. Asymmetry . . . . .	294
B. Anisotropy . . . . .	296
C. Above 5 MeV . . . . .	296
Appendix IV Detector Efficiency Calculation . . . . .	298
Bibliography . . . . .	302
Acknowledgement . . . . .	307
Biographical Note . . . . .	308

## List of Figures

Fig. 1	MIT Linear Accelerator Facility . . . . .	30
Fig. 2	Target Orientation . . . . .	31
Fig. 3	Time-of-Flight Spectrometer Block Diagram . . . . .	34
Fig. 4	Neutron Detector Circuitry Block Diagram . . . . .	36
Fig. 5	Time-to-Height Convertor Block Diagram . . . . .	38
Fig. 6	Target Room . . . . .	46
Fig. 7	Detector Response . . . . .	58
Fig. 8	14.0 MeV Experimental Bremsstrahlung Spectrum . . . . .	62
Fig. 9	Photoneutron Time Spectra . . . . .	71
Fig. 10	Photon Energy Spectra . . . . .	81
Fig. 11	Photon Difference Spectra Multiplied by the Photon Absorption Cross Section . . . . .	83
Fig. 12	Photoneutron Spectra from a 14 MeV Photon Difference Spectrum . . . . .	85
Fig. 13	Neutron Energy Spectra - Bismuth (15 and 14 MeV Data)	98
Fig. 14	Neutron Energy Spectra - Bismuth (14 and 13 MeV Data)	99
Fig. 15	Neutron Energy Spectra - Lead 208 (15 and 14 MeV Data)	100
Fig. 16	Neutron Energy Spectra - Lead 208 (14 and 13 MeV Data)	101
Fig. 17	Lead 208 - Direct Spectrum (14 MeV Difference Photon Spectrum) . . . . .	104
Fig. 18	Bismuth - Direct Spectrum (14 MeV Difference Photon Spectrum) . . . . .	105
Fig. 19	Lead 208 - Direct Spectrum (13 MeV Difference Photon Spectrum) . . . . .	106
Fig. 20	Bismuth - Direct Spectrum (13 MeV Difference Photon Spectrum) . . . . .	107
Fig. 21	Neutron Evaporation Spectrum - Bismuth (14 MeV Difference Photon Spectrum) . . . . .	112
Fig. 22	Neutron Evaporation Spectrum - Bismuth (13 MeV Difference Photon Spectrum) . . . . .	113
Fig. 23	Neutron Evaporation Spectrum - Lead 208 (14 MeV Difference Photon Spectrum) . . . . .	114
Fig. 24	Neutron Evaporation Spectrum - Lead 208 (13 MeV Difference Photon Spectrum) . . . . .	115
Fig. 25	Neutron Evaporation Spectrum - Lead 208 Isotropic Component . . . . .	116
Fig. 26	Photoneutron Angular Distributions - Bismuth . . . . .	119
Fig. 27	Photoneutron Angular Distributions - Lead 208 . . . . .	120
Fig. 28	Neutron Energy Spectra - Lead 207 (15 and 14 MeV Data)	124
Fig. 29	Neutron Energy Spectra - Lead 207 (14 and 13 MeV Data)	125
Fig. 30	Lead 207 - Direct Spectrum (14 MeV Difference Photon Spectrum) . . . . .	127
Fig. 31	Lead 207 - Direct Spectrum (13 MeV Difference Photon Spectrum) . . . . .	128

Fig. 32	Neutron Evaporation Spectrum - Lead 207 (14 MeV Difference Photon Spectrum) . . . . .	130
Fig. 33	Neutron Evaporation Spectrum - Lead 207 (13 MeV Difference Photon Spectrum) . . . . .	131
Fig. 34	Photoneutron Angular Distributions - Lead 207 . . . . .	132
Fig. 35	Neutron Energy Spectra - Lead 206 (15 and 14 MeV Data)	134
Fig. 36	Neutron Energy Spectra - Lead 206 (14 and 13 MeV Data)	135
Fig. 37	Neutron Energy Spectra - Thallium (15 and 13 MeV Data)	136
Fig. 38	Lead 206 - Direct Spectrum (14 MeV Difference Photon Spectrum) . . . . .	139
Fig. 39	Lead 206 - Direct Spectrum (13 MeV Difference Photon Spectrum) . . . . .	140
Fig. 40	Thallium - Direct Spectrum (13.5 MeV Difference Photon Spectrum) . . . . .	141
Fig. 41	Neutron Evaporation Spectrum - Lead 206 (14 MeV Difference Photon Spectrum) . . . . .	142
Fig. 42	Neutron Evaporation Spectrum - Lead 206 (13 MeV Difference Photon Spectrum) . . . . .	143
Fig. 43	Neutron Evaporation Spectrum - Thallium (13.5 MeV Difference Photon Spectrum) . . . . .	144
Fig. 44	Photoneutron Angular Distributions - Lead 206 . . . . .	146
Fig. 45	Photoneutron Angular Distributions - Thallium . . . . .	147
Fig. 46	Neutron Energy Spectra - Mercury (15 and 14 MeV Data)	148
Fig. 47	Neutron Energy Spectra - Mercury (14 and 13 MeV Data)	149
Fig. 48	Neutron Energy Spectra - Gold (15 and 14 MeV Data)	150
Fig. 49	Neutron Energy Spectra - Gold (14 and 13 MeV Data)	151
Fig. 50	Mercury - Direct Spectrum (14 MeV Difference Photon Spectrum) . . . . .	154
Fig. 51	Mercury - Direct Spectrum (13 MeV Difference Photon Spectrum) . . . . .	155
Fig. 52	Gold - Direct Spectrum (14 MeV Difference Photon Spectrum) . . . . .	156
Fig. 53	Gold - Direct Spectrum (13 MeV Difference Photon Spectrum) . . . . .	157
Fig. 54	Neutron Evaporation Spectrum - Mercury (14 MeV Difference Photon Spectrum) . . . . .	159
Fig. 55	Neutron Evaporation Spectrum - Mercury (13 MeV Difference Photon Spectrum) . . . . .	160
Fig. 56	Neutron Evaporation Spectrum - Gold (14 MeV Difference Photon Spectrum) . . . . .	161
Fig. 57	Neutron Evaporation Spectrum - Gold (13 MeV Difference Photon Spectrum) . . . . .	162
Fig. 58	Photoneutron Angular Distributions - Mercury . . . . .	163
Fig. 59	Photoneutron Angular Distributions - Gold . . . . .	164
Fig. 60	Neutron Energy Spectra - Tungsten (15 and 14 MeV Data)	166
Fig. 61	Neutron Energy Spectra - Tantalum (15 and 14 MeV Data)	167
Fig. 62	Neutron Energy Spectra - Tantalum (14 and 13 MeV Data)	168

Fig. 63	Neutron Energy Spectra - Erbium (15 and 14 MeV Data)	169
Fig. 64	Neutron Energy Spectra - Holmium (15 and 14 MeV Data)	170
Fig. 65	Neutron Energy Spectra - Samarium (15 and 14 MeV Data)	171
Fig. 66	Tungsten - Direct Spectrum (14 MeV Difference Photon Spectrum) . . . . .	175
Fig. 67	Tantalum - Direct Spectrum (14 MeV Difference Photon Spectrum) . . . . .	176
Fig. 68	Tantalum - Direct Spectrum (13 MeV Difference Photon Spectrum) . . . . .	177
Fig. 69	Erbium - Direct Spectrum (14 MeV Difference Photon Spectrum) . . . . .	178
Fig. 70	Holmium - Direct Spectrum (14 MeV Difference Photon Spectrum) . . . . .	179
Fig. 71	Samarium - Direct Spectrum (14 MeV Difference Photon Spectrum) . . . . .	180
Fig. 72	Neutron Evaporation Spectrum - Tungsten (14 MeV Difference Spectrum). . . . .	182
Fig. 73	Neutron Evaporation Spectrum - Tantalum (14 MeV Difference Spectrum). . . . .	183
Fig. 74	Neutron Evaporation Spectrum - Tantalum (13 MeV Difference Spectrum). . . . .	184
Fig. 75	Neutron Evaporation Spectrum - Erbium (14 MeV Difference Photon Spectrum) . . . . .	185
Fig. 76	Neutron Evaporation Spectrum - Holmium (14 MeV Difference Photon Spectrum) . . . . .	186
Fig. 77	Neutron Evaporation Spectrum - Samarium (14 MeV Difference Photon Spectrum) . . . . .	187
Fig. 78	Photoneutron Angular Distributions - Tungsten . . . . .	190
Fig. 79	Photoneutron Angular Distributions - Tantalum . . . . .	191
Fig. 80	Photoneutron Angular Distributions - Erbium . . . . .	192
Fig. 81	Photoneutron Angular Distributions - Holmium . . . . .	193
Fig. 82	Photoneutron Angular Distributions - Samarium . . . . .	194
Fig. 83	Neutron Energy Spectra - Praseodymium (15 and 14 MeV Data) . . . . .	195
Fig. 84	Neutron Energy Spectra - Lanthanum (15 and 14 MeV Data)	196
Fig. 85	Praseodymium - Direct Spectrum (14 MeV Difference Photon Spectrum) . . . . .	199
Fig. 86	Lanthanum - Direct Spectrum (14 MeV Difference Photon Spectrum) . . . . .	200
Fig. 87	Neutron Evaporation Spectrum - Praseodymium (14 MeV Difference Photon Spectrum). . . . .	202
Fig. 88	Neutron Evaporation Spectrum - Lanthanum (14 MeV Difference Photon Spectrum) . . . . .	203
Fig. 89	Photoneutron Angular Distributions - Praseodymium	204
Fig. 90	Photoneutron Angular Distributions - Lanthanum . . . . .	205
Fig. 91	Neutron Energy Spectra - Iodine (15 and 14 MeV Data)	207

Fig. 92	Iodine - Direct Spectrum (14 MeV Difference Photon Spectrum) . . . . .	209
Fig. 93	Neutron Evaporation Spectrum - Iodine (14 MeV Difference Photon Spectrum) . . . . .	210
Fig. 94	Photoneutron Angular Distributions - Iodine . . . . .	211
Fig. 95	Neutron Energy Spectra - Tin (15 and 14 MeV Data)	213
Fig. 96	Tin - Direct Spectrum (14 MeV Difference Photon Spectrum) . . . . .	219
Fig. 97	Photoneutron Angular Distributions - Tin . . . . .	221
Fig. 98	Neutron Evaporation Spectrum - Tin (14 MeV Difference Photon Spectrum) . . . . .	222
Fig. 99	Neutron Energy Spectrum - Indium (15 and 14 MeV Data)	223
Fig. 100	Indium - Direct Spectrum (14 MeV Difference Photon Spectrum) . . . . .	224
Fig. 101	Neutron Evaporation Spectrum - Indium (14 MeV Difference Photon Spectrum) . . . . .	226
Fig. 102	Photoneutron Angular Distributions - Indium . . . . .	227
Fig. 103	Fermi Gas Level Density Coefficient vs Atomic Mass . . . . .	244
Fig. 104	Fraction of Direct Neutrons . . . . .	248
Fig. 105	Photoneutron Angular Distributions from 15 MeV Bremsstrahlung Spectra vs Atomic Mass . . . . .	256
Fig. 106	Angular Distribution of Fast Neutrons . . . . .	260
Fig. 107	Scattering in the Uranium Cylinder . . . . .	278
Fig. 108	7046 Voltage String and Anode Current Limiter . . . . .	282
Fig. 109	Photomultiplier Gate Generator . . . . .	284
Fig. 110	Tunnel Diode Pulse Shaper . . . . .	285
Fig. 111	Triple Coincidence Circuit . . . . .	287
Fig. 112	Linear Gate . . . . .	289
Fig. 113	Time-to-Height Convertor Circuitry . . . . .	291
Fig. 114	Beam Integrator . . . . .	293

List of Tables

I	Targets . . . . .	43
II	Pb <sup>206</sup> Photoneutron Energy Spectra and Background from a 15 MeV Bremsstrahlung Spectrum . . . . .	49
III	Uranium Photoneutron Spectra Ratios . . . . .	51
IV	Thickness of Shielding in Flight Paths (In Inches) . . . . .	52
V	Geometrical Factor . . . . .	52
VI	Thick Target Bremsstrahlung Spectrum and Neutron Target Scattering Corrections . . . . .	57
VII	Detector Response . . . . .	61
VIII A	Comparison of Measured and Calculated Correction for Coincidences Between Two Counters . . . . .	68
VIII B	Comparison of Spectral Shape Before and After Self-coincidence Correction (Spectrum Corrected for Coincidences Between Two Counters . . . . .	68
IX	Examples of Background Normalization Statistics . . . . .	70
X	Ratio of Photoneutron Spectrum at 24 <sup>o</sup> to Spectrum at 156 <sup>o</sup> . . . . .	75
XI	Corrected Ratio of Photoneutron Spectrum at 24 <sup>o</sup> to Spectrum at 156 <sup>o</sup> (Summed from 3.0 MeV to E <sub>n max</sub> ) . . . . .	77
XII	Optical Model Capture Cross Sections for Representative Elements as a Function of Neutron Energy . . . . .	88
XIII	Possible Dipole Transitions for Closed Shell at N = 126 . . . . .	102
XIV	Pb <sup>207</sup> Energy Levels . . . . .	102
XV	Bi <sup>208</sup> Energy Levels . . . . .	109
XVI	Angular Distribution of Photoneutrons from the 2f <sup>5/2</sup> Level of Bi . . . . .	122
XVII	Excited States of Pb <sup>206</sup> . . . . .	126
XVIII	Excited States of Pb <sup>205</sup> . . . . .	137
XIX	Ground State Configuration for Deformed Nuclei . . . . .	173
XX	Isotopic Abundances and Thresholds for the Deformed Nuclei . . . . .	173
XXI	Possible Dipole Transitions for a Closed Shell at N = 82 . . . . .	198
XXII	Energy Levels for a Nucleus with N = 82 . . . . .	198
XXIII	Angular Distribution of Photoneutrons from La . . . . .	206
XXIV	Isotopic Abundance and Neutron Thresholds for the Tin Isotopes . . . . .	215
XXV	Energy Levels of Sn <sup>116</sup> , Sn <sup>117</sup> , Sn <sup>118</sup> , Sn <sup>119</sup> . . . . .	215
XXVI	Configuration of Levels of Sn <sup>116</sup> , Sn <sup>117</sup> , Sn <sup>118</sup> , Sn <sup>119</sup> , Sn <sup>120</sup> . . . . .	216
XXVII	Parentage Coefficients for Sn <sup>116</sup> , Sn <sup>117</sup> , Sn <sup>118</sup> , Sn <sup>119</sup> . . . . .	217
XXVIII	Pairing Energy and Maximum Excitation Energy for the Residual Nuclei . . . . .	232
XXIX	Level Density Parameters: Uncorrected for Direct Spectrum . . . . .	234

XXX	Level Density Parameters: Direct Spectrum Derived from Method I . . . . .	235
XXXI	Level Density Parameters: Direct Spectrum Derived from Method II . . . . .	236
XXXII	Level Density Parameters: Comparison with Thermal Neutron Capture Experiments . . . . .	238
XXXIII	Level Density Parameters: Comparison With (n, n') Experiments . . . . .	239
XXXIV	Nuclear Temperatures for Pb and Bi from ( $\gamma$ , n) Experiments . . . . .	242
XXXV	Nuclear Level Density Parameters from Livermore Data	242
XXXVI	Fraction of Direct Neutrons: Experimental Values . . . . .	247
XXXVII	Fraction of Direct Neutrons: Calculated Values . . . . .	249
XXXVIII	Fraction of Direct Neutrons: Comparison of Theory and Experiment . . . . .	252
XXXIX	Angular Distribution of Direct Component . . . . .	259
XL	Angular Distribution of Fast Photoneutrons . . . . .	262
XLI	Scattering Corrections . . . . .	275
XLII	Scattering Correction Due to Plastic Coating on the Target	280
XLIII	Counter Efficiency . . . . .	301

## Chapter I

### Introduction

#### A. Purpose of the Experiment

Photonuclear reactions have long been considered an important tool for studying the nucleus. Unlike reactions initiated by nucleons, where neither the structure of the nucleus, nor the nuclear interaction with the incident particles is known, photonuclear reactions have the advantage that the electromagnetic field properties are well known. It has not been possible to take full advantage of this avenue of research because of a number of practical difficulties in performing photonuclear experiments. Specifically, these are a relatively small yield and the problems of analyzing the results, due to the continuous bremsstrahlung spectrum. The ideal experiment would consist of shining a variable-energy monochromatic photon beam of known intensity on a monoisotopic target, and measuring the energy spectrum, angular distribution and polarization of all reaction products along with the relevant cross sections. The nearest this ideal has been approached is in the series of experiments by W. John et al (1), on deuterium and beryllium using 2.75 MeV gamma rays from  $\text{Na}^{24}$ . This method is necessarily limited to these two targets. Other experiments (2) using monochromatic gamma ray beams from nuclear reactions are hampered by low yields. Moreover the photon spectra in such reactions generally consist of more than one line. Most research on photonuclear reactions has been done with the bremsstrahlung spectra from electron machines.

The early experiments were performed using betatrons and synchrotrons. Photon absorption cross sections were measured by irradiating targets and measuring the activity induced in a sample as a function of the incident bremsstrahlung endpoint energy. Various methods (3) have been devised which permit the calculation of the photon absorption cross section from the yield curves thus measured. All of these methods are very sensitive to small errors in the measurement of the yield, to inaccuracies and lack of knowledge of the shape



of the photon spectrum, and to the uncertainties in the correction for neutron multiplicity above the  $(\gamma, 2n)$  threshold. Another disadvantage of this procedure is the fact that  $(\gamma, p)$  reactions almost always lead to either stable or very long-lived isotopes. Thus only the  $\sigma(\gamma, n) + 2\sigma(\gamma, 2n) + \sigma(\gamma, np)$  etc cross section is measured. One could measure both the angular distributions and energy spectra of photoneutrons with nuclear emulsions. \* Until recently, this has been the most widely used method. However, emulsion scanning is very laborious. A program of study of a broad range of targets would require a prohibitive amount of time, if good statistical accuracy were desired. Another commonly used method of determining the angular distribution of fast photoneutrons is the use of threshold detectors. \* The photoneutrons are detected by the radioactivity induced in the threshold detector by the  $(n, p)$  or  $(n, \alpha)$  reaction. The disadvantages of this system are the low  $(n, p)$  and  $(n, \alpha)$  cross sections, the experimental uncertainty in the values of these cross sections, and the meagre spectral knowledge obtained for the photoneutrons. Such detectors clearly only measure the integral of the neutron flux times the  $(n, p)$  or  $(n, \alpha)$  cross section from the threshold to the neutron endpoint.

The situation is a little better in the case of fast protons, deuterons, alphas, fission fragments, etc. The energy spectrum and angular distributions of energetic charged particles can be determined by measuring the energy loss in a scintillator or emulsion. \*\* With the introduction of high resolution solid state detectors, it has become possible to measure the energy spectra of charged particles with great accuracy. However as  $Z$  increases, charged particle emission is suppressed by the coulomb barrier. Therefore below about 20 MeV photon energy, in the region of heavy elements one can generally only study the neutron spectra.

Introduction of high-current linear accelerators has led to the feasibility

---

\* References to many such experiments will be found in Tables XXXIX and XL of Chapter V of this thesis.

\*\* The  $(\gamma, p)$ ,  $(\gamma, \alpha)$ , etc, experiments are too numerous to list individually here. A listing of these experiments can be found in a comprehensive bibliography of photonuclear reactions by M. E. Toms (4).

ity of two new techniques: photon monochromatization, and photoneutron time-of-flight spectrometry. Photon beams with a relatively narrow spectral interval are formed from the in-flight annihilation of positrons. However the conversion from electron to positron beams have typical efficiencies of  $10^{-5}$ , and the radiator must be a thin, low-Z foil to preserve the narrow photon spectrum. Thus at the present stage of development, very weak gamma beams are produced. For the most part, the experiments are limited to total cross section measurements without spectral information of the emitted particle (5, 6, 7). On the other hand, time-of-flight techniques used with high-current linacs allow a measurement of the photoneutron energy spectrum and angular distribution with relatively high counting rates.

A system combining a photon monochromator and a neutron time-of-flight spectrometer has been developed for use in conjunction with the Illinois betatron (8). The electron beam is passed through a thin radiator, and the energy of the scattered electrons is determined with a magnet analyzer. Electrons radiating photons of the desired energy can then be selected. The energy of the photoneutrons in coincidence with the selected electrons is measured by their flight time over a 1.5 meter flight path. In principle this is a close approach to the ideal experiment discussed above. In practice the requirement of only one photon per resolving time of the electronics results in very low counting rates. Typical experiments require on the order of 100 hours of beam time to accumulate about 10,000 counts. Thus it would be very time consuming to study a broad range of targets.

A photoneutron time-of-flight spectrometer was developed by Bertozzi, et al (9) for use with the MIT linear accelerator and used to investigate the possibilities of measuring photoneutron spectra. This work was reported in ref 10. The equipment was later expanded to include angular distribution measurements, and the machine current was increased by an order of magnitude (11). More recently the experimental groups at Harwell (12), Rensalaer Polytechnic Institute (13), in the USSR(14) and others are also using time-of-flight spectrometers in conjunction with high-current linacs. At present these groups only measure photoneutron spectra at one fixed angle, usually

90°. In view of the counting rate limitations imposed on the emulsion and monochromator experiments, and limitation of the single angle of other time-of-flight facilities, the MIT facility is, for the present, uniquely suited to the measurement of the angular distributions of photoneutron energy spectra.

It was therefore decided to make a systematic survey of the angular distributions of the energy spectra of photoneutrons from the giant resonance of elements heavier than tin. The high counting rates available with this equipment makes it possible to perform measurements at several maximum bremsstrahlung energies to assist in removing the ambiguities introduced by the continuous photon spectrum. The bremsstrahlung endpoints were chosen to approximately straddle the giant resonance. Elements lighter than tin were not included because of machine energy limitations.

#### B. Description of the Giant Resonance and Corresponding Nuclear Models

In this section and the following ones, the experimental data collected from photodisintegration experiments and the nuclear models developed to explain these results will be briefly discussed. The references cited are not intended to be exhaustive. Rather, they are merely intended to give examples illustrating the more pronounced features of the photonuclear reactions. A comprehensive bibliography of photonuclear reactions has been compiled by M. E. Toms (4). There are several extensive articles reviewing nuclear photodisintegration: Wilkinson (15), Levinger (16), Shevchenko (17), and Fuller and Hayward (18). The reader is referred to these reviews for a more detailed discussion of the experimental results and nuclear models.

Previous experiments have shown that the absorption of photons by nuclei leads to several possible reactions. These are the elastic and inelastic scattering of photons, single and multiple particle emission (where energetically feasible), and, in the case of the very heavy elements, fission. Because of the coulomb barrier, neutron emission is the predominant particle reaction for elements with  $Z > 20$ . Photon emission rapidly becomes negligible above the photoneutron threshold. The striking feature of the absorption cross section [ $\sigma(E_\gamma) = \sigma(\gamma, n) + \sigma(\gamma, p) + \sigma(\gamma, 2n) + \sigma(\gamma, np) + \sigma(\gamma, \gamma) + \sigma(\gamma, \gamma')$  etc] is the strong

resonant behavior common to all elements in the periodic table (19). This is commonly called the "giant resonance" for photon absorption. It is also seen in the inverse reactions,  $(p, \gamma)$ ,  $(n, \gamma)$ , etc (20). This thesis examined the  $(\gamma, n)$  spectra produced by photons in this resonance region for several elements with  $A > 100$ .

Throughout the greater part of the periodic table, the photon absorption peaks at  $E_m \approx 80A^{-1/3}$  MeV (21). At lower mass numbers  $E_m$  falls below this line and is roughly constant at 20 to 23 MeV below  $A \approx 40$ . For the nuclei of interest in this thesis,  $E_m$  varies from 16 MeV for Sn to 13.5 MeV for Pb. The width of the giant resonance at half maximum is roughly 5 to 7 MeV throughout the periodic table (22). Near the region of closed shells, the width decreases to 4 MeV. In the region of nuclei with large deformations, such as Ho, the photon absorption cross section splits into two resonances: one at about  $12\frac{1}{2}$  MeV, the other at about 16 MeV. The lower resonance is very narrow (about 2 MeV); the higher resonance is about 4 MeV wide (6, 18).

Soon after the giant resonance had been observed experimentally, it was found to be due to electric dipole absorption. This was indicated by the following:

(1) At the energy of the giant resonance the wavelength of the incident photon is greater than the radius of most nuclei. Thus it is expected that the dipole term will be dominant.

(2) The cross section integrated over the region of the giant resonance is almost entirely exhausted by the electric dipole sum rule.

(3) The angular distributions of the emitted protons and neutrons are symmetric about  $90^\circ$ . With the inclusion of a considerable admixture of electric quadrupole or magnetic dipole transitions, the angular distributions would be asymmetric.

Provided that the interaction between the nucleons does not involve exchange forces or velocity-dependent forces, the integral cross sections of the dipole gamma absorption will not depend on the structure of the ground state or the model used (23). Thus

$$\int \sigma_{E_1}(\gamma) dE_\gamma = \frac{2\pi^2 e^2 \hbar}{mc} \frac{NZ}{A} = 0.06 \frac{NZ}{A} \text{ MeV-barns} \quad (1)$$

If exchange forces are taken into account, the integral absorption cross section has the form

$$\int \sigma_{E_1}(\gamma) dE_\gamma = 0.06 \frac{NZ}{A} (1 + \Delta) \quad (2)$$

where  $\Delta$  depends on the type of interaction between nucleons. Bethe and Levinger (23) have shown that  $\Delta \approx 0.4$  for an equal mixture of exchange and ordinary forces. Experimentally, the photon absorption cross section integrated up to 25 MeV for the heavy elements is about 1.3 measured in units of  $0.06 \frac{NZ}{A}$  MeV-barns (18). This indicates that the dipole strength is indeed exhausted and in fact requires  $\Delta > 0$ . However the data is not accurate enough to draw unambiguous conclusions regarding the mixture of forces required to produce  $\Delta > 0$ .

It should be pointed out that above 20 MeV in the heavy elements, the photoproton angular distribution (24), and to some extent the photoneutron angular distribution (25) show a definite forward peaking. This requires the interference of a positive parity transition with the electric dipole absorption, and has been interpreted as indicating electric quadrupole absorption (26). Theoretical estimates indicate the possible existence of a quadrupole resonance at about 10 MeV higher than the giant dipole resonance (17). At the energy of this experiment ( $< 15$  MeV) the quadrupole transitions may be completely neglected.

Historically, two apparently different models have been proposed to account for the features of the dipole absorption resonance. The first is the collective or hydrodynamic model, in which the nucleus is treated as a fluid with the protons and neutrons vibrating against one another. The second is the independent particle model (IPM), in which the nucleons make transitions between two shells of some shell model description of the nucleus. Several forms of the collective model were proposed by Goldhaber and Teller (27). Steinwedel and Jensen (28) showed that their second hypothesis (in which the total nuclear density remains constant and the relative proton-neutron densities change when the collective mode is excited) predicts  $E_m = 82A^{-1/3}$  MeV. This model was later extended to the deformed nuclei by Danos (29) and others, where it made another striking prediction borne out by experiment. The model predicts that the giant resonance should split into two peaks; one due to oscillations along the axis of symmetry with energy  $\hbar\omega_z$ , and one perpendicular to the axis of symmetry with energy  $\hbar\omega_\perp$ . If the nucleus is prolate (as the rare earth nuclei are),  $\hbar\omega_z < \hbar\omega_\perp$ . This splitting of the giant resonance has been observed in many deformed nuclei (7).

Fuller et al (21) has shown, with the use of polarized holmium targets, that the lower peak is associated with oscillations perpendicular to the symmetry axis and the upper peak is associated with oscillations along the symmetry axis as predicted. However the collective model makes no attempt to explain the photoproton and photoneutron yields, and their angular and energy distributions.

The independent particle model attempts to explain the giant resonance by invoking nucleon transitions from one shell model orbit to the next upon absorbing photons. In the case of the harmonic oscillator all such transitions have an energy  $\hbar\omega$ , and the absorption is a delta function for this energy (about 8 MeV). In a more realistic potential, a great many shell model E1 transitions are in general possible at many energies. Wilkinson (30) has shown, from direct computations using a square well, that the possible transitions do tend to cluster in energy about the energy of separation from the next major oscillator shell. This comes about because (a) levels of a given sequence such as 1s, 1p, 1d, . . . , or 2s, 2p, 2d, . . . , still follow each other at approximately equal intervals near the top of the Fermi surface; and (b) the matrix elements are much larger for the transitions that were allowed for the harmonic oscillator (one oscillator quantum transitions) than for those which were forbidden (multiple quantum transitions).

He further finds that the important transitions which make up the giant resonance correspond to absorption by closed shells. Absorption by nucleons in unfilled shells is spread over a large energy (about  $\hbar\omega$ ). In addition, all of the nucleons (except the valence nucleons) become involved in the breaking up of a closed shell so that this absorption accounts for a major part of the integrated cross section, and exhausts the sum rule. This surprising result is explained by the fact that the downward transitions (stimulated emission) are counted negatively (31). Thus the low lying states, A, which are inhibited from making upward transitions,  $A \rightarrow B$ , because the higher states, B, are filled, make a contribution to the integrated cross section by preventing negative downward transitions,  $B \rightarrow A$ , from the higher states. In this way one can think of the contribution from a lower shell being passed upwards from shell to shell until it comes to the Fermi surface.

Wilkinson's model has several difficulties. He predicts the A dependence of  $E_m$ , but the energy difference between oscillator shells is only 7 to 8 MeV, in the medium to heavy elements, whereas  $E_m$  is 13 to 16 MeV. Since particle binding energies are typically about 7 MeV, many of the single particle states excited in Wilkinson's model occupy the region of negative energies. As a result nucleon emission would be suppressed and the calculated yields less than the experimental ones. He corrects the value of  $E_m$  by introducing an effective nucleon mass  $M^* \approx \frac{M}{2}$  to account for the many-body character of the system. This increases  $E_m$  to the proper value, and much better agreement with experimental yields is obtained. Wilkinson's model of the giant resonance neglected the interaction between the particle excited by the photon and the resulting hole in the closed shell. Since the particle and hole are strongly correlated they exert a large effect on one another. In the spirit of the single particle shell model, all pair interactions between nucleons are approximated by a self-consistent central potential. However it is well known that in addition to this central potential, there is also needed a so-called residual interaction between pairs of nucleons (or holes) which does not lend itself to a reduction to a central potential (17). Considering only closed shell nuclei, the Hamiltonian can be written as

$$H = \sum_i H_i + \frac{1}{2} \sum_{ij} W_{ij} \quad (3)$$

where  $H_i$  is the Hamiltonian of the independent particle or hole, and  $W_{ij}$  the residual effective particle-hole interaction. The true wave function of the nucleus can be represented by

$$\psi = \sum_n c_n \phi_n \quad (4)$$

where the  $\phi_n$  are the single particle functions of a central potential used as a basis for the expansion. In an actual calculation, the mixing of states is taken into account only within the limits of one major shell. Therefore the basis functions,  $\phi_n$ , are truncated to include only those  $\phi_n$  making up the two major shells involved in the dipole transitions. That is, the hole state is a linear combination of the  $\phi_n$  of one major shell, and the particle state is a linear combination of the  $\phi_n$  of the next higher major shell. From the equation

$$H\psi = E\psi \quad (5)$$

and equations 3 and 4, one finds the matrix

$$|(E_f - E_i) \delta_{ii'} \delta_{ff'} + \frac{1}{2} \langle \phi_i^* \phi_f^* | W_{ij} | \phi_i, \phi_{f'} \rangle |$$

which is diagonalized to find the dipole state energies. In the above,  $E_i$  and  $E_f$  are the energies of the unperturbed single particle states, and  $\langle \phi_i^* \phi_f^* | W_{ij} | \phi_i, \phi_{f'} \rangle$  are the off-diagonal elements;  $i$  denotes the hole states and  $j$  the particle states.  $E_f - E_i$  would be the energy derived from the Wilkinson model for a given potential without the assumption,  $M^* = \frac{M}{2}$ , of an effective mass. Another approximation commonly used in these calculations is the use of the energy levels of  $A - 1$  and  $A + 1$  nuclei to determine the values of  $E_i$  and  $E_j$ . These levels are found by pickup and stripping reactions (32). This takes into account the nucleon interactions in the  $A + 1$  or  $A - 1$  nuclei.

The physical features of the result of this diagonalization were first pointed out by Brown and Bolsteri (33). They showed that if one made a number of special assumptions (rejecting weak transitions, taking all single particle transition energies to be  $E_0$ , and equating all the radial integrals), one obtains a high-lying collective dipole state which absorbs all of the dipole sum. That is, a "schematic" particle-hole interaction introduces sufficient coherence in the single particle model to elevate a few of the many dipole states to the correct energy region and concentrate the bulk of the dipole strength in these few states. Detailed calculations have been undertaken by many authors on  $C^{12}$  (34),  $O^{16}$  (35),  $Ca^{40}$  (36),  $Pb^{208}$  (37), and other elements. These calculations do indeed predict a few states containing most of the dipole strength at the appropriate energies. In the case of light nuclei, agreement was good not only for the position of the dipole resonance and its integral value, but also for the characteristics of the nucleon spectra (36). Poorer agreement is found in the medium to heavy nuclei, where only the position of the giant resonance is correctly predicted (38). This may be explained by the increasing importance in the heavy nuclei of more complicated configurations such as two-particle-two-hole states.

The above discussion concerns closed shells only. Calculations involving unfilled shells are quite difficult and are not generally available. As



Wilkinson (30) has pointed out, the transitions due to valence neutrons are much weaker than those from the core. The primary effect of an unfilled shell therefore is to widen the giant resonance. Thus he correctly predicts a minimum in the width of the giant resonance at closed-shell nuclei.

As the number of nucleons in a shell decreases (from the filled shell) a region is reached where the nucleus becomes deformed. The collective model correctly predicted a splitting of the giant resonance in this case. Wilkinson has attempted to investigate deformed nuclei using the IPM (39). Using the nuclear levels scheme of Nilsson (40), he calculated the energies of the parent type  $\ell \rightarrow \ell + 1$  and  $2\ell \rightarrow 2\ell + 1$ \* transitions in a deformed potential. He found that the giant resonance is still predicted but it is widened. If the deformation is large enough ( $\delta = 0.3$ ), the giant resonance splits into two peaks. In addition there was tendency for the transitions in the higher energy peak to come from the larger values of  $\Omega$ , the projection on the nuclear symmetry axis of the individual  $j$  of the nucleon in question, while the smaller  $\Omega$  values are found in the lower peak. Classically, high values of  $\Omega$  correspond to orbits lying in the plane of the minor axes of the ellipsoid, and low values of  $\Omega$  to nucleon motion in planes at right angles to this. This is in agreement with the predictions of the collective model. The more complicated particle-hole interaction calculations have been extended to deformed nuclei by Nilsson et al (41) for  $Mg^{24}$  and  $C^{12}$ . In dipole transitions  $\Delta\Omega = 0$  and  $\Delta\Omega = \pm 1$ .  $\Delta\Omega = 0$  corresponds to states excited by that component of the dipole moment operator  $d_{\parallel}$ , which is parallel to the symmetry axis, and  $\Delta\Omega = \pm 1$  corresponds to  $d_{\perp}$ , perpendicular to the symmetry axis. When they perform the rather involved calculation, Nilsson et al find that there are a few dipole states containing most of the dipole integrated cross sections, which are elevated in energy, as in the spherical case. Also the levels resolve into two groups, with the  $\Delta\Omega = 0$  transitions forming the low energy peak and  $\Delta\Omega = \pm 1$  transitions forming the high energy peak. Thus the IPM, with the inclusion of the residual

\* Throughout this thesis the notation  $n\ell$  refers to the harmonic oscillator notation.  $\ell$  is the orbital angular momentum and  $n$  is associated with the number of nodes of the radial function. Specifically,  $n$  is the number of nodes (including the origin) minus  $\ell$ .

particle-hole interaction, can describe all of the gross features observed in the giant resonance.

### C. Energy Spectra of Emitted Nucleons

In the resonant single particle model of Wilkinson, one particle absorbs the entire photon energy, and the resulting energy spectrum of emitted particles will be made up of several components. Some particles will emerge directly with no further interactions with the nucleus; these are called "resonant direct" particles. Others will emerge after suffering some inelastic collisions with nucleons; and still other particles will be emitted directly as knock-ons from internal collisions. Finally there will be some particles that are lost in a statistical mixing with the consequent formation of a compound nucleus. Unfortunately, one would expect all of these components to be important since for the energies used, the mean free path for these inelastic collisions is the same magnitude at the nuclear radius (42). Nevertheless, in order to make a comparison with experiment, the features of the particle spectrum will be discussed from the point of view of compound nucleus decay and the resonant direct process with no inelastic collisions.

The energy spectrum of nucleons emitted from a compound nucleus of excitation  $E_\gamma$  is given (43) by the equation

$$\frac{dN}{dE_n} \approx E_n \sigma_C(E_n) \omega(U) \quad (6)$$

where  $E_n$  is the energy of the emitted particle and  $\sigma_C(E_n)$  is the cross section for the formation of a compound nucleus by the absorption of a nucleon of energy  $E_n$  into the residual nucleus at an excitation energy  $U = E_\gamma - E_t - E_n$ .  $E_t$  is the threshold for the process, and  $\omega(U)$  is the density of levels in the residual nucleus at an excitation energy  $U$ . The dominant term in this expression for neutron emission is the parameter  $\omega(U)$ , which has the form (44)

$$\omega(U) \approx \left(\frac{1}{U}\right)^2 e^{2\sqrt{aU}} \quad (7)$$

For proton emission, the coulomb barrier is important at low energies, as it decreases  $\sigma_C(E_n)$  considerably.

The energy spectrum of the resonance direct neutrons depends largely on the assumptions made about the energy distributions of the hole states in the residual nucleus. Wilkinson spread these hole states over several MeV. Then the spectrum of particles impinging on the nuclear boundary from within the nucleus is roughly constant with energy, extending from zero energy to an energy given by  $E_\gamma - E_t$ . The probability for direct emission is proportional to the appropriate potential barrier penetration factors  $T_\ell(E_n)$ , for a nucleon of orbital angular momentum  $\ell$  and energy  $E_n$ , and the strength,  $f_\ell$ , of the transitions leading to neutrons with angular momentum  $\ell$  (39).

Authors who have dealt with the particle-hole interaction type calculations (36) generally use discrete hole states, corresponding to their basis wave functions. Then the neutron energy spectrum is concentrated at high energies. The direct spectrum is calculated (17) from the equation

$$\sigma_{\alpha i}(E) = \sigma(E) \frac{\Gamma_{\alpha i}}{\Gamma} \quad (8)$$

where  $\Gamma_\alpha$  is the partial width for particle,  $\alpha$ , emission to the state  $i$ , and  $\Gamma$  is the total width. The widths,  $\Gamma_{\alpha i}$ , are estimated (43) from

$$\Gamma_{\alpha i} = \sum_\ell 2k\gamma_\ell^2 T_\ell(k) \quad (9)$$

where  $k$  is the wave number of the outgoing nucleon,  $\gamma_\ell^2$  is the reduced width for the transition to a given level of the residual nucleus when a nucleon is emitted with orbital angular momentum  $\ell$ , and  $T_\ell$  is the barrier penetration coefficient.

$$\gamma_\ell^2 = \frac{3\hbar^2}{4MR} \sum |C_{j_1 j_2}^i|^2 \quad (10)$$

where  $C_{j_1 j_2}^i$  is the coefficient of the particle-hole states making up the dipole state. The sum is performed over all configurations making a contribution to the state of the residual nucleus in question. These calculations have proved successful only for nuclei with low  $A$  where more complicated configurations are not important (36). In the region of the heavy elements, the calculated resonant direct spectrum is appreciably shifted to higher energies than the experimental spectra (38).

## D. Angular Distributions

The angular distributions of the resonant direct neutrons is given by Courant (45) as

$$W(\Theta) = 1 + \frac{B}{A} \sin^2 \Theta \quad (11)$$

where  $\frac{B}{A} = \frac{1}{2} \frac{\ell+2}{\ell}$  for  $\ell \rightarrow \ell+1$  and  $\frac{B}{A} = \frac{1}{2} \frac{\ell-1}{\ell+1}$  for  $\ell \rightarrow \ell-1$

These equations make some definite predictions about the transitions involved. If  $\frac{B}{A} > 1.5$ , then the reaction involves some neutrons making  $\ell = 0 \rightarrow \ell = 1$  transitions. If  $\frac{B}{A} = 0$ , then the reaction is necessarily  $\ell = 1 \rightarrow \ell = 0$  transitions. Finally if  $\frac{B}{A} < 0.5$ ,  $\ell \rightarrow \ell-1$  transitions must be involved. However the above equations do not include the effects of the neutron spin. These are taken into account by Heiss (46). Then the angular distribution is still given by equation 11, but  $B/A$  depends on the total angular momentum,  $j$ , of the neutrons in the initial state as indicated by equations 12 and 13 (shown on the next page). In equations 12 and 13,  $K_{\ell+1}^{j+1}$  is defined to be the integral  $\int_0^\infty dr r^3 g_{\ell,j}(r) f_{\ell+1,j+1}(r)$ . The other radial integrals,  $K_{\ell+1}^j$ , etc, are similarly defined.  $g_{\ell,j}(r)$  and  $f_{\ell+1,j+1}(r)$ , etc, are the initial and final radial wave functions of a neutron with an orbital angular momentum  $\ell$  and total angular momentum  $j$  in the initial state, and orbital angular momentum  $\ell+1$  and total angular momentum  $j+1$  in the final state. (See ref 46 for details of these functions.)  $\delta_{++}$ ,  $\delta_{+0}$ , etc, are respectively the phase shifts of the final wave functions  $f_{\ell+1,j+1}$ ,  $f_{\ell-1,j}$ , etc. The matrix element  $K_{\ell+1}^{j+1}$  corresponds to  $\ell \rightarrow \ell-1$ ,  $j \rightarrow j$ , etc, neutron transitions, etc.

It is immediately apparent that the simple predictions of Courant's approximations are lost due to the interference terms between different final  $j$ 's. For example, the  $\ell = 0 \rightarrow \ell = 1$  transition now has

$$\frac{B}{A} = \frac{2 |K_{\ell+1}^{j+1}|^2 + 6 |K_{\ell+1}^{j+1} K_{\ell+1}^j| \cos(\delta_{++} + \delta_{0+})}{2 |K_{\ell+1}^{j+1}|^2 + 2 |K_{\ell+1}^j|^2 - 4 |K_{\ell+1}^{j+1} K_{\ell+1}^j| \cos(\delta_{++} + \delta_{0+})} \quad (14)$$

If the transition is pure  $s^{1/2} \rightarrow p^{3/2}$ ,  $\frac{B}{A} = 1$ ; if it is  $s^{1/2} \rightarrow p^{1/2}$ ,  $\frac{B}{A} = 0$ .

Only if the two  $j$  values have equal strength and the phase shifts add up to 0 or

When  $j = \ell + \frac{1}{2}$

$$A = \frac{1}{2\ell+3} \frac{(\ell+1)(\ell+2)}{2\ell+3} K_{\ell+1}^{j+1} K_{\ell+1}^{j-1} + \frac{2(2\ell+1)(2\ell+3) + 4\ell(\ell+2)}{3(2\ell+1)^2(2\ell+3)} K_{\ell+1}^j K_{\ell+1}^j + \frac{2\ell(2\ell+1)(2\ell+3) - \ell(\ell-1)\sqrt{4\ell^2-9}}{3(2\ell+1)^2} K_{\ell-1}^{j-1} K_{\ell-1}^{j-1} \quad (12a)$$

$$+ \frac{2\ell(\ell+2)}{2\ell+1} K_{\ell+1}^{j+1} K_{\ell-1}^{j-1} \cos(\delta_{++} - \delta_{--}) - \frac{2(\ell+2)}{(2\ell+1)(2\ell+3)} K_{\ell+1}^{j+1} K_{\ell+1}^j \cos(\delta_{++} - \delta_{+0}) + \frac{2\ell}{(2\ell+1)^2} K_{\ell+1}^j K_{\ell-1}^{j-1} \cos(\delta_{+0} - \delta_{--})$$

$$B = \frac{1}{2\ell+3} \frac{(\ell+2)(\ell+3)}{2(2\ell+3)} K_{\ell+1}^{j+1} K_{\ell+1}^{j-1} + \frac{\ell(\ell-1)\sqrt{4\ell^2-9}}{2(2\ell+1)^2} K_{\ell-1}^{j-1} K_{\ell-1}^{j-1} - \frac{2\ell(\ell+2)}{(2\ell+1)^2(2\ell+3)} K_{\ell+1}^j K_{\ell+1}^j - \frac{3\ell(\ell+2)}{2\ell+1} K_{\ell+1}^{j+1} K_{\ell-1}^{j-1} \cos(\delta_{++} - \delta_{--}) \quad (12b)$$

$$+ \frac{3(\ell+2)}{(2\ell+1)(2\ell+3)} K_{\ell+1}^{j+1} K_{\ell+1}^j \cos(\delta_{++} - \delta_{+0}) - \frac{3\ell}{(2\ell+1)^2} K_{\ell+1}^j K_{\ell-1}^{j-1} \cos(\delta_{+0} - \delta_{--})$$

When  $j = \ell - \frac{1}{2}$

$$A = \frac{\ell(\ell+1)}{(2\ell+1)^2} K_{\ell+1}^{j+1} K_{\ell+1}^{j-1} + \frac{2(2\ell+1)(2\ell-1)(2\ell+3) + 4(\ell^2-1)\sqrt{4\ell^2-9}}{3(2\ell+1)^2(2\ell-1)^2(2\ell+3)} K_{\ell-1}^j K_{\ell-1}^j + \frac{2(\ell-1)(2\ell-1)(2\ell+3) - (\ell-1)(\ell-2)\sqrt{4\ell^2-9}}{3(2\ell-1)^2(2\ell+3)} K_{\ell-1}^{j-1} K_{\ell-1}^{j-1} \quad (13a)$$

$$- \frac{2(\ell-1)\sqrt{4\ell^2-9}}{(2\ell+1)(2\ell+3)(2\ell-1)} K_{\ell-1}^j K_{\ell-1}^{j-1} \cos(\delta_{--} - \delta_{-0}) + \frac{2(\ell^2-1)}{(2\ell+1)(2\ell-1)} K_{\ell+1}^{j+1} K_{\ell-1}^{j-1} \cos(\delta_{++} - \delta_{--})$$

$$+ \frac{2(\ell+1)}{(2\ell+1)^2(2\ell-1)} K_{\ell+1}^{j+1} K_{\ell-1}^j \cos(\delta_{++} - \delta_{-0})$$

$$B = \frac{(\ell+1)(\ell+2)}{2(2\ell+1)^2} K_{\ell+1}^{j+1} K_{\ell+1}^{j-1} + \frac{(\ell-1)(\ell-2)\sqrt{4\ell^2-9}}{2(2\ell-1)^2(2\ell+3)} K_{\ell-1}^{j-1} K_{\ell-1}^{j-1} - \frac{2(\ell^2-1)\sqrt{4\ell^2-9}}{(2\ell+1)^2(2\ell+3)(2\ell-1)^2} K_{\ell-1}^j K_{\ell-1}^j + \frac{3(\ell-1)\sqrt{4\ell^2-9}}{(2\ell-1)^2(2\ell+1)(2\ell+3)} K_{\ell-1}^j K_{\ell-1}^{j-1} \quad (13b)$$

$$+ X \cos(\delta_{--} - \delta_{-0}) - \frac{3(\ell^2-1)}{(2\ell+1)(2\ell-1)} K_{\ell+1}^{j+1} K_{\ell+1}^{j-1} \cos(\delta_{++} - \delta_{--}) - \frac{3(\ell+1)}{(2\ell+1)^2(2\ell-1)} K_{\ell+1}^{j+1} K_{\ell-1}^j \cos(\delta_{++} - \delta_{-0})$$

$2\pi$  does  $B/A = \infty$ , as in the Courant formulas. As a result of this, it has become practically impossible to predict the angular distribution, unless the neutron wave function and phase shifts are calculated using a reasonably good model of the nucleus. \* This has been done by Heiss for several nondeformed nuclei. (Of course, for  $j \gg 1$ ,  $\frac{B}{A} \approx \frac{1}{2}$  for both spin orientations.)

If the photon interaction is purely dipole (or any pure multipole, for that matter) the neutron angular distribution is fore-aft symmetric and (for dipole) no more complex than  $\sin^2 \Theta$ . Inclusion of the next higher multipole, E2, involves another parity and thus the possibility of  $\cos \Theta$  terms. The angular distributions for photoneutrons including E2 terms is given by Eichler and Weidenmuller (26). Their equations are for spinless particles, and are therefore the same order of approximation as Courant's equations. The complete angular distribution with spin orbit coupling and all multipoles is given in terms of the Racah algebra coefficients by Fujii (47).

Eichler and Weidenmuller find that the angular distribution of resonant direct nucleons is given by

$$W(\Theta) = a + b \sin^2 \Theta + A \cos \Theta + B \sin^2 \Theta \cos \Theta \quad (15)$$

where  $a$  and  $b$  are proportional to  $e_1$ , the effective dipole charge, and  $A$  and  $B$  are proportional to  $2e_2 k_\gamma$ , the effective quadrupole charge.  $k_\gamma$  is the photon wave number. For protons

$$e_1 = \frac{eN}{A} \approx \frac{1}{2}e \quad e_2 \approx e \left( 1 - \frac{Z}{A} \right) \approx e \quad (16a)$$

and for neutrons

$$e_1 = \frac{eZ}{A} \approx \frac{1}{2}e \quad e_2 \approx \frac{eZ}{A} \approx \frac{e}{2A} \quad (16b)$$

where  $e$  is the electron charge,  $Z$  the number of protons in the nucleus,  $N$  the number of neutrons,  $A = N + Z$ , and  $|k_\gamma| = \frac{\omega}{c}$ .

\* Actually this is an overly pessimistic view of the problem. The relative transition strengths calculated by Wilkinson allow one to choose the dominant transition and to estimate the magnitude of the interference terms, although not the phase shifts. Thus it is generally possible to reduce the limits on the possible angular distributions.

According to Eichler and Weidenmuller, the  $\cos \Theta$  term can be comparable to the dipole terms at  $E_{\gamma} \approx 20$  MeV for protons, and a considerable fore-aft asymmetry might arise. This has been observed in many cases (24). On the other hand the effective quadrupole charge of the neutron is less than 1 per cent of the effective quadrupole charge of the proton, so that the fore-aft symmetry of photoneutrons is preserved. However fore-aft asymmetries have been observed for neutrons (25) for bremsstrahlung energies between 20 and 55 MeV.\* Recently an attempt has been made by Quirk et al (48) to relate the observed forward asymmetry in the fast photoneutron angular distributions to the corresponding forward-peaking photoproton angular distributions. It is suggested that some of the protons excited in the absorption process are not emitted, but undergo collisions with other nucleons. The angular distributions of the resulting knock-on neutrons will have the same qualitative appearance as the proton angular distribution producing it, that is, a peak in the forward direction. Using a Fermi gas model, they estimate the mean free path for a proton to collide with a neutron in nuclear matter, and they predict that this mechanism will increase with increasing mass number and proton energy. At  $A = 210$ , photoneutron asymmetry is not expected below about  $E_{\gamma} = 20$  MeV since the proton mean free path rapidly becomes larger than the nuclear radius with decreasing energy.

Whatever mechanism causes the forward peaking of the photoneutrons, it requires E2 photons. As has been mentioned earlier, the quadrupole giant resonance is expected to occur at a higher energy than the dipole giant resonance. In Pb, the quadrupole giant resonance has been estimated to occur at about 21 MeV, in good agreement with the results of proton and neutron angular distribution measurements. Since this experiment will be dealing with much lower photon energies ( $E_{\gamma} \leq 15$  MeV), the directly emitted neutrons are expected to be symmetric about  $90^{\circ}$ .

In a final word about angular distributions, the statistically emitted neutrons are well known to be symmetric about  $90^{\circ}$ . In addition the statis-

---

\*References to many photoneutron angular distribution measurements will be found in Tables XXXIX and XL of this thesis, Chapter V.

tical model implies that there will be a strong tendency toward isotropy.

According to Ericson (49) the angular distribution of evaporated neutrons is given by

$$W(\Theta) \propto 1 + \frac{4}{3} \frac{MR^2}{\tau} \frac{E_{\text{rot}}}{2T} \cos^2 \Theta \quad (17)$$

if the angular momentum of the emitted nucleon is totally uncorrelated to the angular momentum of the incoming particle, and is given by

$$W(\Theta) \propto 1, \quad \sin \Theta < \frac{j_f}{I} \quad (18a)$$

If the angular momentum of the emitted nucleon is completely aligned with that of the incoming particle,

$$W(\Theta) \propto \frac{2}{\pi} \arcsin \frac{j_f}{I \sin \Theta} \quad \sin \Theta > \frac{j_f}{I} \quad (18b)$$

In the above equations,  $T$  = nuclear temperature (about 1 MeV),  $M$  = nucleon mass,  $R$  = nuclear radius,  $\tau$  = rigid body moment of inertia ( $\frac{2}{5}MAR^2$ ),  $E_{\text{rot}}$  = energy of rotation  $\approx \hbar^2 I^2 / 2\tau$ ,  $I$  = angular momentum of the compound nucleus, and  $j_f$  = angular momentum of the residual nucleus. In the case of the giant resonance, the excitation energy is large enough to make a wide range of  $j_f$ 's available. Therefore the angular momentum of the emitted particle is not correlated to  $I$  and the angular distribution is given by equation 17. For Bi ( $I = \frac{9}{2} \pm 1$ )

$$W(\Theta) \approx 1 + 4 \times 10^{-4} \cos^2 \Theta \quad (19)$$

Therefore in addition to symmetry about  $90^\circ$ , the evaporated neutrons are expected to be isotropic.



## Chapter II

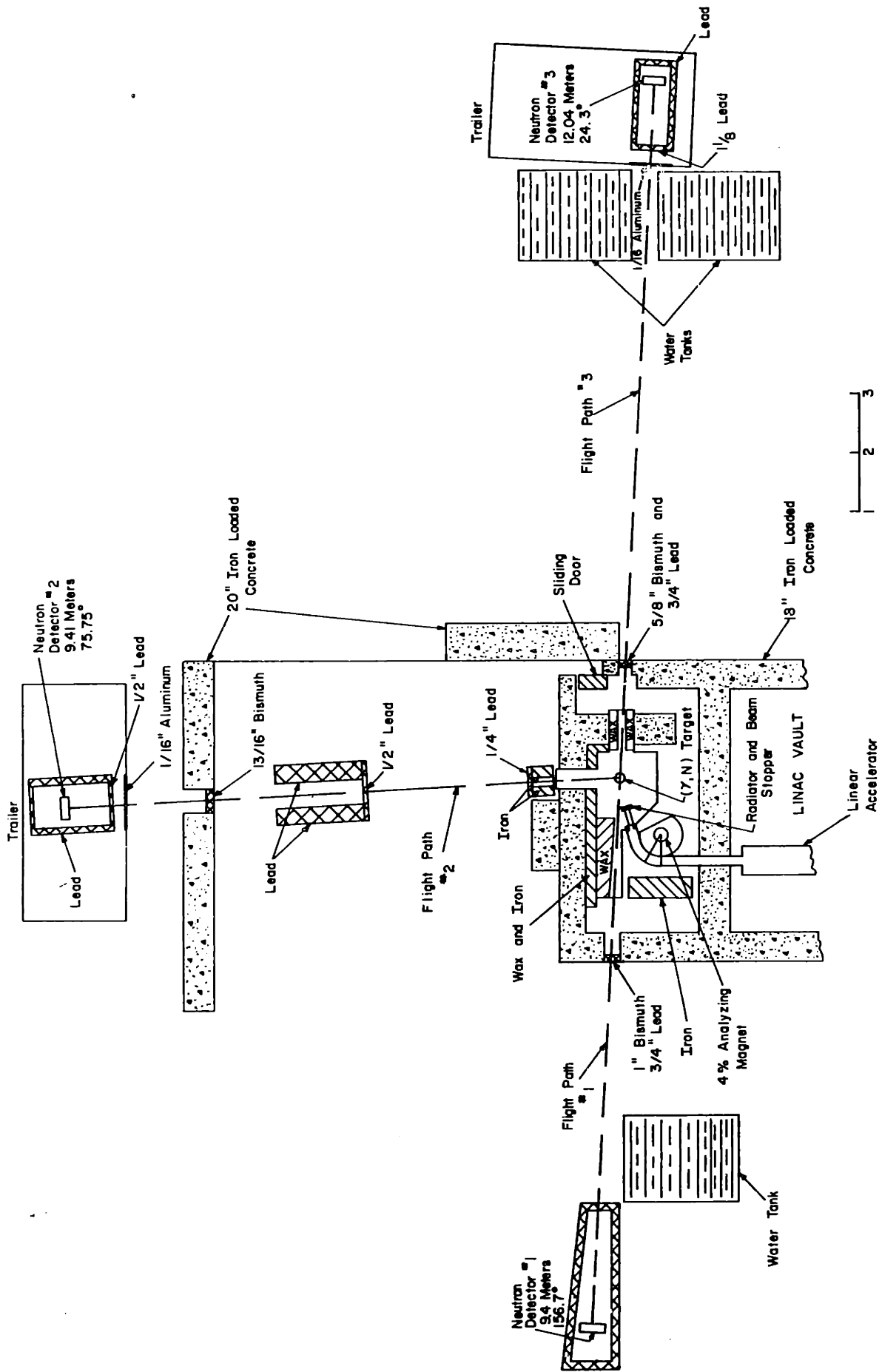
### Apparatus

#### A. General Description

A plan view of the MIT Linear Accelerator facility is shown in Fig. 1. Electron bursts with an 8 ns width and a repetition rate of 120 per sec are generated by pulsing a Peirce-type cylindrical beam electron gun located in the high voltage terminal of a 2.0 MeV Van de Graaf. The electron source is a 7.65 mm diameter Siemens Mk-81 capillary-type cathode with a peak emission of 5 amperes. The Van de Graaf injects about 750 ma at 1.5 MeV into the first section of the MIT 17 MeV Linac. Approximately 100 ma of this current is accelerated to within 10 per cent of the accelerator's maximum energy, which is variable from 2 to 17 MeV. This beam is momentum-analyzed to 4 per cent FWHM by a  $60^\circ$  bending magnet. A peak current of 40 ma reaches the bremsstrahlung radiator, a 10 mil tantalum foil backed by  $1\frac{1}{2}$ " of carbon. This carbon block stops the electron beam and the current collected by it is used to monitor the linac electron beam as described in section C. The photon beam emerges from the bremsstrahlung radiator in a cone with half angle equal to 150 MeV-degrees due to multiple electron scattering in the thick tantalum radiator and carbon block. That is, 60 per cent of the photon beam intensity is inside a cone making an angle  $\theta$  with the beam. The product of this angle  $\theta$  and the incident electron energy is 150 MeV-degrees. There is no collimation of this gamma ray beam.

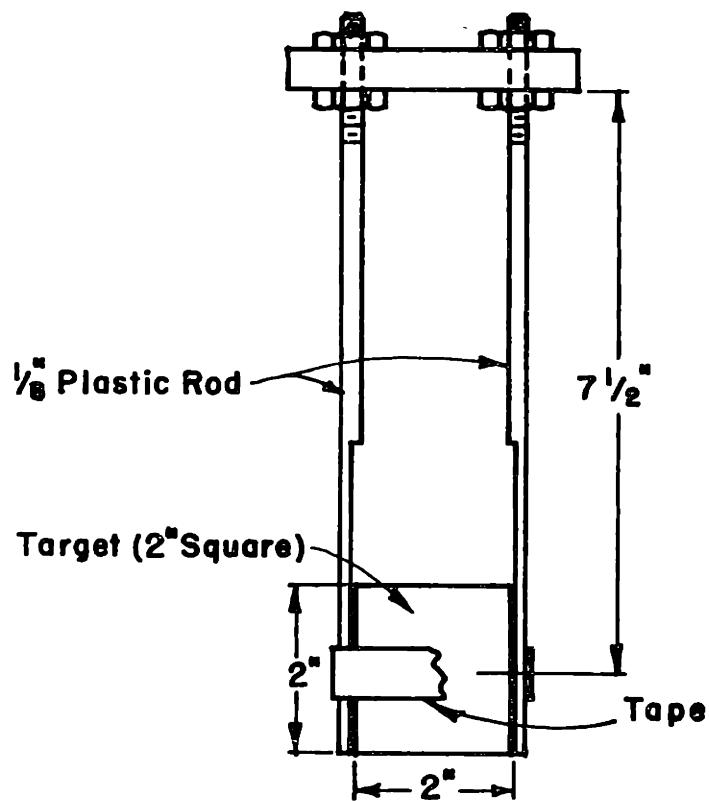
The ( $\gamma$ , n) target was suspended 33 cm from the bremsstrahlung target at the intersection of the bremsstrahlung beam and the three neutron flight paths. Cylindrical targets were suspended by a thread; flat targets were taped to  $\frac{1}{8}$ " plastic rods and oriented at  $40^\circ$  to the photon beam (Fig. 2).

The neutron energies are determined by measuring their flight times to the three neutron counters located at  $24\frac{3}{8}$ " to the beam at 12.0 meters,  $75\frac{3}{4}$ " to the beam at 9.4 meters, and  $155\frac{5}{8}$ " to the beam also at 9.4 meters. The counters are cylindrical liquid-scintillator proton-recoil detectors coaxial with the neutron beam.

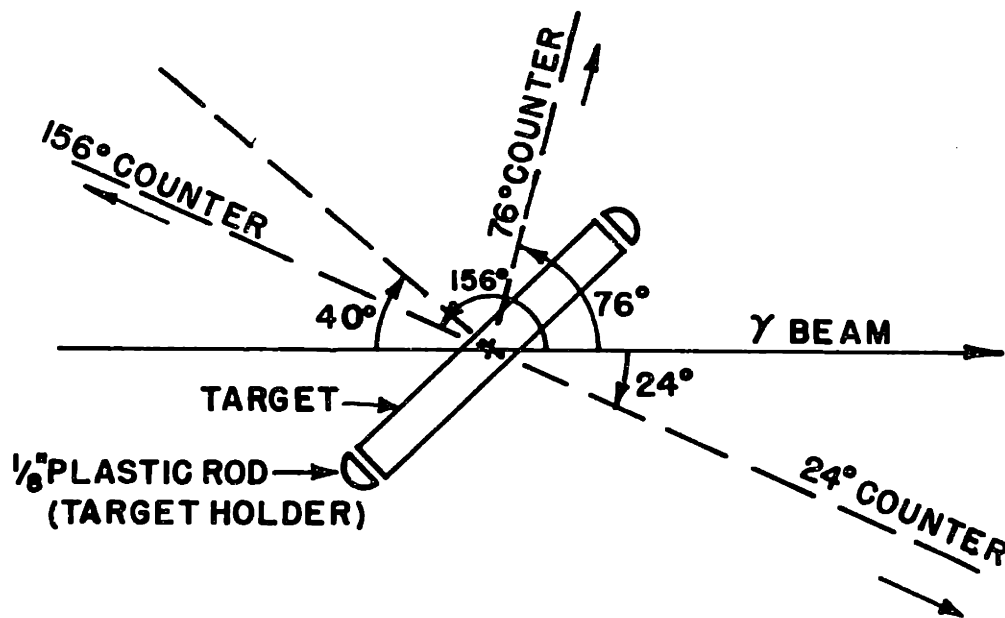


PLAN VIEW OF LINAC

Fig. 1



**TARGET HOLDER**



**TARGET ORIENTATION**

Fig. 2

## B. Neutron Detectors

The three proton-recoil neutron detectors are cylindrical brass containers 5" deep with an inside diameter of 14". Each is filled with 12 liters of toluene in which is dissolved 0.2 gm/l of P-Bis[2-(5-Phenyloxazolyl)]-Benzene (POPOP) and 4 gm/l of P-Terphenyl. The active volume is viewed by three 5" photomultiplier tubes (RCA 7046) mounted with their axes at  $5^\circ$  to the detector axis with their photocathodes immersed in the liquid. The walls of the brass container are coated with a suspension of magnesium oxide in sodium silicate to increase the reflectivity.

A block diagram of the detector circuitry is shown in Fig. 4. Pulses from the anode have a rise time of 6 ns, a width of 15 ns and vary in amplitude over three orders of magnitude. When the output of a photomultiplier exceeds  $\frac{1}{2}$  ma into a 120  $\Omega$  load, it triggers a 15 ns fast pulse shaper. Large pulses are limited to 10 ma by diodes. Such a large pulse may trigger the pulse shapers more than once, but as the timing is done on the first pulse, this does not affect the resolution.

An intense flux of scattered gamma rays arrives at the counter after each machine pulse. This large gamma flash paralyzes the photomultiplier circuitry and results in excessive tube noise for a few microseconds afterwards. Therefore the tubes are biased off by applying -100 V to the first focusing grid, G1, thus trapping photoelectrons in the cathode region. (Tube noise is apparently generated by the residual gases which are ionized by the heavy electron flow.) A +200 V gate pulse 1.2  $\mu$ sec long is applied to G1 about 0.10  $\mu$ sec after the beam pulse, to turn on the photomultiplier. Since the high resistivity of the photomultiplier would prevent the grid-to-cathode fields from building up rapidly, an open grid of fine platinum wire is placed against the face of the photomultiplier and grounded. This allows the grid-to-cathode fields to follow the 80 ns rise time of the gate pulse.

The neutron energy threshold, below which a neutron is essentially undetectable, is determined by the photomultiplier gain and the pulse shaper threshold. The +200 V gate pulse feeds through the tube base circuitry and

causes 0.1 to 0.2 ma pulses in the anode circuit. Hence the pulse shaper threshold was set at 0.5 ma to obtain the maximum sensitivity while discriminating against the gate pulse feed through. The tube gain was set so that 50 to 70 per cent of the photoelectrons from the cathode resulted in more than 0.5 ma anode current. Under these conditions the neutron threshold was about  $\frac{1}{4}$  MeV. (This discussion assumes the maximum gain that was normally used. The counter in the forward direction was run at much lower gains, as will be discussed later.)

### C. Beam Monitoring

#### a) Analyzing Magnet

The energy of the electrons reaching the bremsstrahlung target was kept to within  $\pm 2$  per cent of the average value by the magnet analyzing system. Carbon entrance slits at the end of the linear accelerator, having a  $\frac{3}{4}$ " aperture and a length of 6", define the position of the incoming beam. A magnetic field bends the beam in an arc with a radius of curvature of 12". The high energy component of the beam is focussed at the center of the exit slits which are made of brass slugs  $2\frac{3}{4}$ " long with a  $\frac{9}{16}$ " aperture. These exit slits are 74 cm from the ( $\gamma, n$ ) target. Nickel shot and wax are used to shield the ( $\gamma, n$ ) target from gamma rays and neutrons originating at the slits.

The analyzing magnet's field is monitored by the output of a coil rotating at 3600 rpm in the magnetic field. The coil's 60 cps AC output is compared to the output of an AC generator mounted on the same shaft to correct for variations in rpm. The energy scale of this monitor is calibrated by measuring the endpoint of the energy spectra of photoneutrons from deuterium. The mean electron energy reaching the bremsstrahlung target can be regulated to about 1 per cent using the "flip" coil meter.

#### b) Charge Integrator

The insulated carbon block backing the tantalum target is connected to a 0.05  $\mu$ fd low-leakage capacitor in an electrometer circuit (see Appendix II, section G). In this circuit, when the capacitor voltage reaches about 1 V

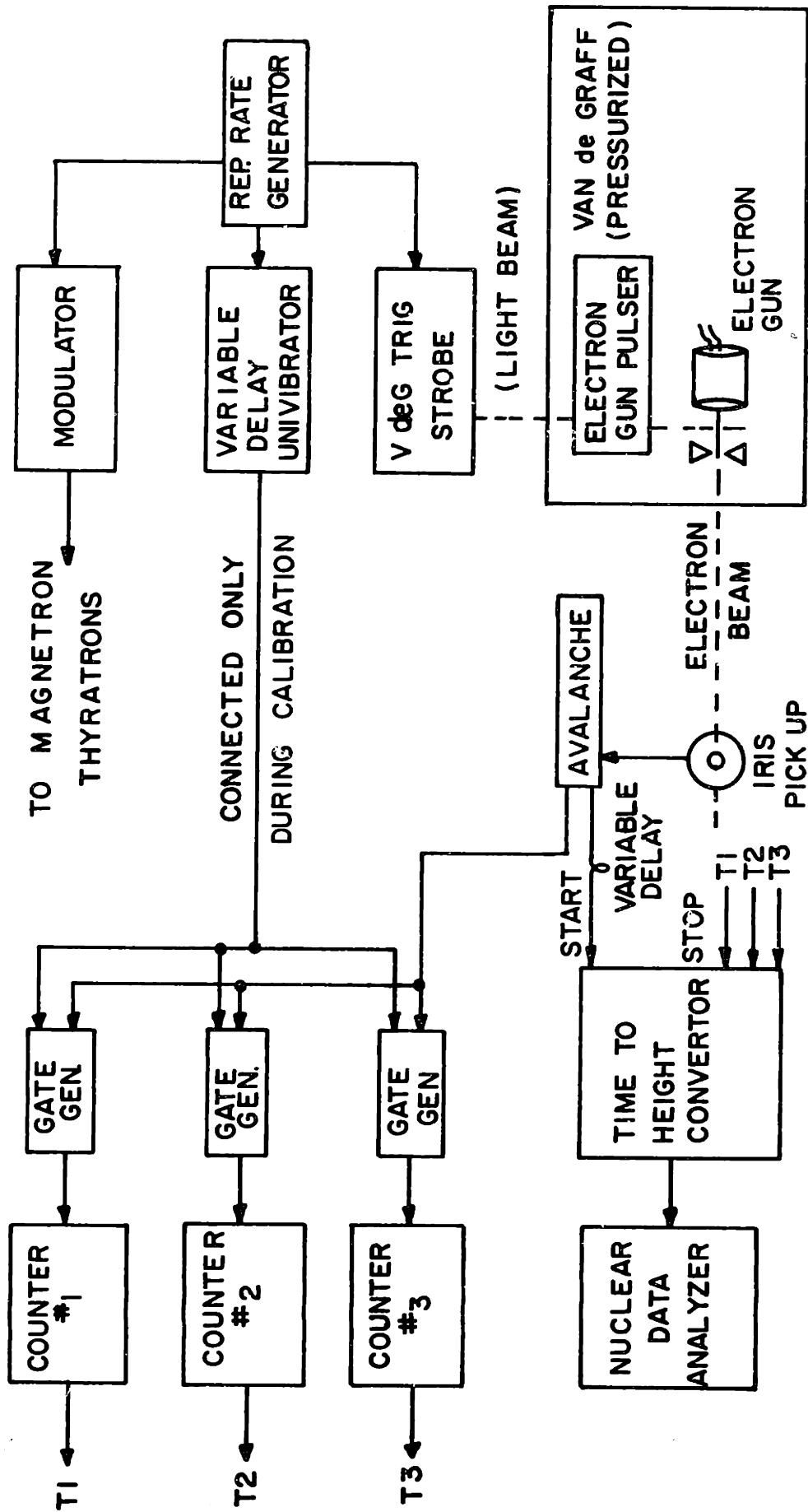


Fig. 3 Time of Flight System Block Diagram

(corresponding to about  $5 \times 10^{-8}$  coulomb of charge), the electrometer activates two relays, one of which shorts the capacitor to ground, while the other advances a mechanical register. In this manner the integrated charge delivered to the bremsstrahlung target during an experiment is measured.

#### D. Time-of-Flight Spectrometer

##### a) General Description

Fig. 3 is a block diagram of the flow of signals in the spectrometer. As an electron burst from the Van de Graaf passes through an iris, located in the drift space between the Van de Graaf and the first section of the linac, a timing signal  $T_0$  is generated. This pulse starts the time-to-pulse-height convertor (THC) and after a suitable delay, turns on the photomultipliers in the counters. The THC is stopped at time  $T$  by a pulse from the first counter that detects a neutron, and a pulse whose height is proportional to the time  $(T - T_0)$  is sent to a Nuclear Data 1024-channel analyzer. Routing pulses, triggered by the detection signals, direct the analogue pulse to one of four groups of 256 channels. The first three groups accumulate time spectra from the three counters. If more than one detector registers a neutron following a beam pulse, the event with the shortest flight time is entered in the fourth quadrant, which accumulates these coincidence spectra. In some cases counting rates as high as 15 counts per second were encountered, which corresponds to a loss of 10 per cent of the counts.

##### b) Detector Circuitry

The neutron detector circuitry is shown in block diagram form in Fig. 4. The output of each of the three photomultipliers triggers a 15 ns fast pulse shaper with a rise time of 2 ns. Each of the three pulse shapers has two 1 V outputs. One output from each pulse shaper feeds a triple coincidence circuit which opens a 30 ns wide linear gate. The other three outputs are added and go to the linear gate through 30 ns of delay. If a triple coincidence has occurred and the gate is open, the summed pulses pass through and are presented to the THC as the time  $T$  pulse. The leading edge of the summed pulse is formed by the leading

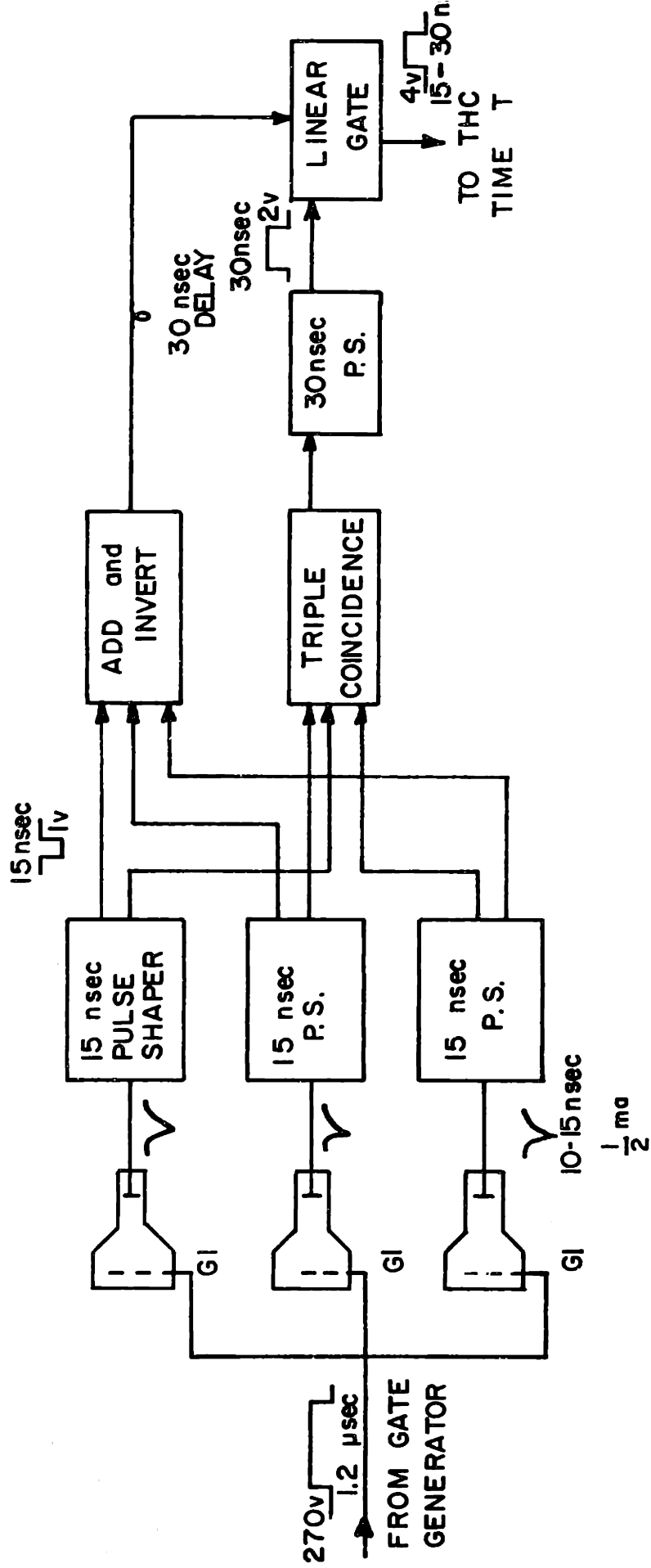


Fig. 4 Neutron Detector Circuitry Block Diagram



edge of the first pulse to reach the summing circuit, and hence the timing is done on the first photon to be detected by the photomultipliers. The leading edge of the summed pulse has a rise time of 2 ns and an amplitude of 2 to 3 V, depending on how the summed pulses overlap. If the gate is closed (less than three simultaneous pulses ) the feedthrough is less than 0.1 V.

### c) Time-to-Height Convertor

A portion of the electron beam from the Van de Graaf injector is collected on the iris in front of the first section of the linac and fed to an avalanche circuit. The iris pulse is 5 to 15 V with a 1 to 2 ns rise time. The avalanche circuit has a 1 V threshold and an output ( $T_0$ ) of 20 V, 3 ns wide. The fast rise time of the iris pulse and low avalanche threshold result in a  $T_0$  time jitter of less than 1 ns.

A block diagram of the THC is shown in Fig. 5. The  $T_0$  pulse causes a capacitor to be connected to a constant current source, and triggers a 2  $\mu$ sec univibrator. This opens a gate in each of the three time T lines and allows the pulses from the counters to pass. The first time T pulse to arrive at the THC disconnects the capacitor, and after a delay, opens a gate that samples the voltage on the capacitor. This voltage (0 to 3 V, 1.25  $\mu$ sec) is the analogue pulse sent to the multichannel analyzer through a 5  $\mu$ sec delay cable. If more than one counter transmits a pulse during the 2  $\mu$ sec that the THC gate is open, a coincidence circuit routes the analogue pulse to the fourth quadrant of the analyzer. Finally, the capacitor is discharged 8  $\mu$ sec later by the "restore dump" line.

The analogue pulse applied to the multichannel analyzer passes through a gate circuit in the analyzer. This gate is opened with a pulse generated by a univibrator triggered by any time T pulse that passes the time T gate (Fig. 5). Hence the analyzer is capable of analyzing an event only if a  $T_0$  pulse and a time T pulse have reached the THC. In addition all pulses and logic signals going to the analyzer are delayed 5  $\mu$ sec. This insures that spurious pulses (such as voltage surges on the power lines from the modulator) are not analyzed, since the analyzer is not operative until 5  $\mu$ sec after the machine pulse.

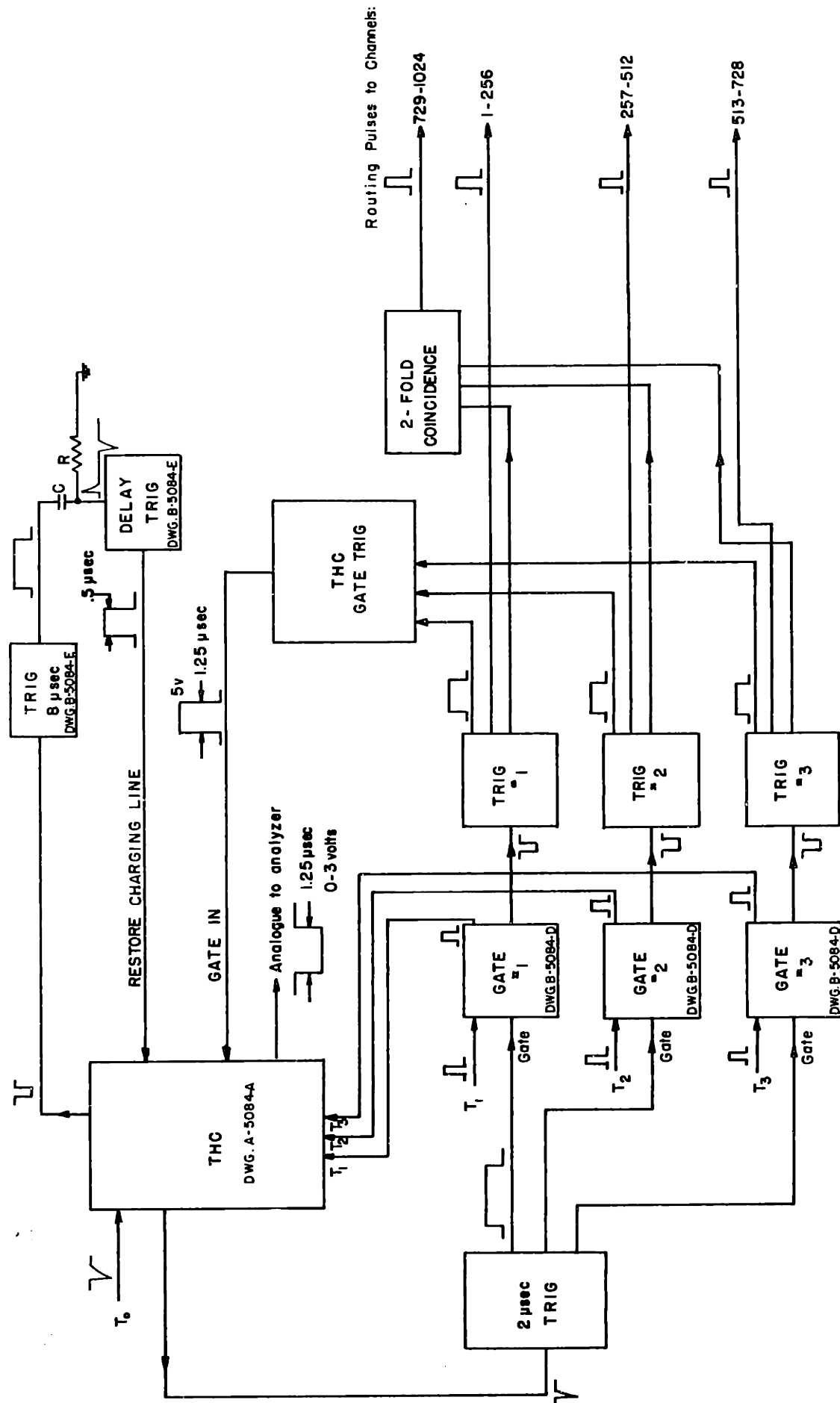


Fig. 5 Time-to-Height Converter Block Diagram

Resolution tests using the time spread of coincidence between detected pairs of positron-annihilation gamma rays indicate a timing resolution of less than 5 ns for the entire spectrometer system. These tests were made by placing two neutron counters face to face about 3 m apart. A  $\text{Na}^{22}$  source was placed midway between them. Pulses from one counter were used as a  $T_0$  signal to turn on the THC, and pulses from the other counter were delayed with 273 feet of RG-63 cable and used as a time T pulse to stop the THC. A time slope of 1 ns/channel was used, and the spike due to annihilation gamma rays was found to be about 4 to 5 channels FWHM. This is the time resolution with two counters. The resolution of a single counter could be as low as 3.5 ns.

#### d) Calibration

In this experiment the energy of a neutron is determined by measuring its flight time over a 9.4 or a 12 m flight path. In order to avoid the ambiguity introduced by the several electronic delay times due to photomultipliers, etc, one measures an interval of time which is the neutron arrival time relative to the arrival time of the gamma rays scattered by the  $(\gamma, n)$  target in the bremsstrahlung beam. The neutron flight time is then this interval plus 31.6 ns, which is the flight time of the scattered gamma rays (over 9.4 m).

The channel corresponding to the gamma ray flight time is determined by gating the photomultipliers on before the machine is pulsed. Then the time T pulse is delayed with a standard cable and a second group of channels are populated in the analyzer. The number of channels between the groups is used to determine the time slope of the THC in ns/channel. This can be measured to about  $\frac{1}{2}$  channel out of 100. The average value of the time slope was  $4.075 \pm 0.025$  ns/channel and it did not vary more than 0.5 per cent during the course of the experiment (about one month).

The differential linearity (the variation in  $\Delta t$ /channel over the range of channels used) was measured by turning on the THC and a counter with a pulser and measuring a time spectrum of a radioactive source. When 2500 counts per channel had been accumulated and the data corrected for counting losses (see section A of Chapter IV), the spectrum was a straight line between

30 ns and 1200 ns with a slope representing a fractional change in the counts per ns of  $-2 \times 10^{-5} \text{ ns}^{-1}$ . As will be pointed out in section A, the approximations used in correcting for the counting losses cause the curve to slope down at later times. Therefore the spectrum is horizontal to better than 2 per cent in 1000 ns. Since 70 per cent of the points lie within one standard deviation of the average value, the local variations in  $\Delta t/\text{channel}$  are less than  $2\frac{1}{2}$  per cent. This is more than adequate for the present experiments. Below 30 ns the spectrum increases sharply, reaching a peak at 0 ns. This is due to the fact that the time T pulses are from 15 to 30 ns wide. Therefore pulses occurring from -30 ns to 0 ns are still present when the time T gate is opened at 0 ns and hence increase the counting rate near 0 ns.

The width of the channel groups populated by the bremsstrahlung flash in a calibration check corresponds to the over-all time resolution of the time-of-flight spectrometer, including the width of the electron beam. This was about 8 ns FWHM (determined by increasing the time slope to 2 ns/channel), which corresponds to about 0.5 MeV FWHM energy resolution at 10 MeV neutron energy, and 0.025 MeV FWHM at 1 MeV neutron energy.

The time delays of the cables have been previously calibrated (9) by observing the frequencies of standing wave resonances established on the cables with one end short circuited. The sequence  $f, 2f, 3f, \dots, nf$ , with  $5 \leq n \leq 10$ , was measured for each cable, allowing a sufficiently precise measurement of  $f$  to determine the time delay of each cable to about  $\frac{1}{3}$  ns. Cables ranging in length from 75 to 275 feet were used. The delay was found to be 1.23 ns/ft for RG-63 cable.

The time-of-flight and energy of a neutron are given by

$$t = 4.075(C - C_0) + 31.6 + D \quad (20)$$

$$E_n = \frac{K}{t^2} \quad (21)$$

where 4.075 = time slope of spectrometer in ns/channel

C = channel in which the neutron count appears

$C_0$  = channel in which the gamma flash appears without the cable delay D

$31.6 =$  flight time of the gamma rays in ns

$D =$  delay\* of the cable placed in series with  $T_0$

$K =$  a constant proportional to the flight path length

In these equations, the time slope, 4.075 ns/channel, and the delay,  $D$ , were found using a value of 1.23 ns/ft delay for the RG-63 cable. The value of  $K$  and the flight time of the gamma rays depend on the flight path length. If one assumes that the neutrons interact approximately half way through the counter, one obtains  $K = 0.470 \pm 0.05$ , where the limits correspond to taking the flight path length to the face and to the back of the counter.

An independent check of the neutron energy scale had been made (50) by measuring the transmission through carbon ( $20 \text{ gm/cm}^3$ ) of the spectrum of neutrons from a beryllium target. In this measurement the familiar features of the  $C^{12}$  total neutron cross section are observed. These energies were consistent with a choice of  $K = 0.480 \pm 0.005$ , and  $1.23 \pm 0.01$  ns/ft for the delay cable. Since the exact length of the flight path is in doubt, and the origin of the gamma flash (and hence of the gamma ray flight path) is uncertain to one foot\*\*, the set of parameters derived from the carbon calibration was used in this experiment.

In addition the value of  $K$  for the  $24^\circ$  counter was determined by comparing peaks in the  $Pb^{208}$  photoneutron spectrum measured at  $24^\circ$  and  $76^\circ$ . These peaks were 1.88 MeV and 0.62 MeV as determined by the constants for the  $76^\circ$  counter. This corresponds to  $K = 0.787 \pm 0.015$  in the  $24^\circ$  counter.

---

\*The purpose of delaying the time  $T_0$  pulse with cable  $D$  is to suppress below channel zero some of the "empty" channels that represent times before the arrival of the first photoneutrons. When a time calibration is made, this cable must be removed in order for the gamma flash to appear on the analyzer. Therefore this delay must be included in the neutron flight time.

\*\*The gamma flash could originate at either the  $(\gamma, n)$  target or the bremsstrahlung target.

## Chapter III

### Experiment

#### A. Experimental Procedure

The neutron time spectra for the separated lead isotopes,  $\text{Pb}^{208}$ ,  $\text{Pb}^{207}$ , and  $\text{Pb}^{206}$ , and 14 other elements were measured at three angles:  $155.625^\circ \pm 0.125^\circ$ ;  $75.75^\circ \pm 0.125^\circ$ ; and  $24.375^\circ \pm 0.125^\circ$ . The targets used are listed in Table I, with their dimensions, masses, and geometrical factors (which will be explained in section D).

The data were taken using bremsstrahlung endpoints of 15 and 14 MeV with a time slope of 4.075 ns/channel. In addition the photoneutron spectra from the separated lead isotopes,  $\text{Pb}^{208}$ ,  $\text{Pb}^{207}$ , and  $\text{Pb}^{206}$ , and from Bi, Tl, Au, Hg, and Ta were measured using a bremsstrahlung endpoint of 13 MeV with 4.075 ns/channel time slope, and using a 15 MeV endpoint with a time slope of 2 ns/channel. In the latter case, the purpose was to obtain better statistics and energy resolution for the high energy neutrons. The low energy neutrons were suppressed during the runs made with a time slope of 2 ns/channel by making the time T gates only 0.5  $\mu\text{sec}$  wide instead of the 2.5  $\mu\text{sec}$  width that is used with a time slope of 4 ns/channel. This allowed the use of higher beam intensities without encountering severe counting losses due to coincidences between two counters.

The data were taken in cycles of approximately 6 hours. A cycle consisted of a time calibration, a deuterium run, a uranium run, several data runs with different targets, and finally a background measurement without a target.

The time calibration, as described in the previous section, was made by determining the analyzer channel corresponding to the flight time of the scattered gamma rays. Its position was found to shift by about two channels during the course of a day. This change was probably due to small changes in the THC or analyzer zero points. As this drift was slow and regular, the analyzer channel corresponding to the flight time of the scattered gamma rays was interpolated linearly between adjacent calibrations. It is felt that the channel

Table I

## Targets

Element	Mass in grams	Dimensions and Shape	Geometrical Factor*
Bi**	61.3	$1\frac{3}{16}$ " x $\frac{5}{8}$ " dia cyl	1.0
Pb <sup>208</sup>	99.8	4 cm dia, $\frac{1}{4}$ " thick disk	1.0
Pb <sup>207</sup>	94.4	4 cm dia, $\frac{7}{32}$ " thick disk	1.0
Pb <sup>206</sup>	95.6	4 cm dia, $\frac{7}{32}$ " thick disk	1.0
Tl	110	3 cyl, $1$ " x $\frac{1}{2}$ " dia	1.0
Hg	68.2	$1\frac{5}{8}$ " x $\frac{1}{2}$ " dia bottle	1.0
Au	104.2	2" dia, $\frac{1}{4}$ " thick disk	1.04
W	224	2" dia, $\frac{7}{32}$ " thick disk	1.06
Ta 1)	217.5	2" square, $\frac{3}{16}$ " thick	1.09
2)	192.1	2" dia, $\frac{7}{32}$ " thick disk	1.06
3)	85.75	$1\frac{1}{4}$ " square, $\frac{3}{16}$ " thick (hex)	1.00
Er	235	2" square, $\frac{3}{8}$ " thick	1.09
Ho <sub>2</sub> O <sub>3</sub>	150	$1\frac{3}{4}$ " x 2" dia bottle	1.00
Sm	196	2" square, $\frac{3}{8}$ " thick	1.09
Pr	177	2" square, $\frac{3}{8}$ " thick	1.09
La	116.5	2" dia, $\frac{3}{8}$ " thick disk	1.06
I	151.2	$1\frac{3}{4}$ " dia, $1\frac{1}{4}$ " deep bottle	1.00
Sn	113.2	5 rods, $1\frac{7}{8}$ " x $\frac{3}{8}$ " dia	1.06
In	121.8	$1\frac{5}{8}$ " dia, $\frac{7}{16}$ " thick disk	1.00
U	92	$1\frac{3}{8}$ " x $1\frac{1}{2}$ " dia cyl (hollow, $\frac{1}{16}$ " walls)	1.00
CD <sub>2</sub>	45	$1\frac{1}{4}$ " x $1\frac{1}{2}$ " aluminum can	---

\*for counters at 156° and 240°. All geometric factors for the 76° counter are 1.0 as discussed in section D.

\*\*except one run with 13 MeV bremsstrahlung endpoint, with following target:

Bi	205.6	2" dia, $\frac{3}{8}$ " thick disk	1.06
----	-------	------------------------------------	------

corresponding to  $t = 0$  ns was thus determined to better than one channel.

The deuterium target consisted of 2.76 moles of deuterated polyethylene in a thin-walled aluminum can. The deuterium runs were used to determine the endpoint, energy spectrum, and relative intensity of the bremsstrahlung beam. For this purpose, deuterium has the advantage of a one-to-one correspondence between neutron and photon energy. Also the photodisintegration cross section is well known experimentally and theoretically. A recent calculation of the deuterium photodisintegration by Partovi (51), which has been very successful in fitting the existing experimental data, has been used in this thesis.

The uranium runs were made with a 92 gram cylinder about  $\frac{1}{16}$  " thick. These runs were used to monitor differences in the counter efficiencies due to differences in geometry, detector threshold, and neutron absorption in the flight paths. Uranium was used because it has low  $(\gamma, n)$  and  $(\gamma, f)$  thresholds which results in a high counting rate even for low bremsstrahlung energies. The angular distribution of the emitted neutrons has been measured in this laboratory using a 14 MeV endpoint bremsstrahlung beam (see Appendix III). For this reason most of the uranium runs were made at 14 MeV, even if the cycle in progress involved a different energy.

## B. Background and Shielding

The positions of the counters and the shielding used in this experiment is shown in Fig. 1. The linear accelerator and the target room are enclosed by iron-loaded concrete walls 14" thick. The counters are enclosed in 3 to 5 inches of lead shielding made of 2'x3'x6" lead bricks covered with several thicknesses of  $\frac{1}{8}$  " lead sheet. This shields the counter from scattered gamma rays ("skyshine") and low energy cosmic ray secondaries. Water tanks 5 ft thick are placed as shown in the figure to shadow the counters from the intense sources of gamma rays and neutrons formed by the collimating slits at the end of the machine, the walls of the curved wave guide in the magnet, and the material in the path of the photon beam as it leaves the target room. The walls of the target room, and the extra iron and concrete blocks shown in the diagram are also an important part of the shielding from these intense gammas



and neutrons.

Figure 6 gives a more detailed view of the shielding placed in the target room. The neutron flight paths emerge through three holes about 8 inches in diameter. The hole for the  $^{76}\text{O}$  counter is offset from the machine axis and almost perpendicular to the gamma beam. As a result this counter has the best shielding from the bremsstrahlung target and does not view any portion of the target room in the direct path of the beam. The  $^{156}\text{O}$  flight path passes close to the bremsstrahlung target and the  $^{156}\text{O}$  counter views the wall of the target room struck by the gamma beam. Several 2-ft long concentric iron pipes have been inserted into the hole leading to this counter to reduce the area viewed to less than 3" diameter. In addition, as much iron and wax as possible was inserted between the bremsstrahlung target and the flight path. Since the  $^{24}\text{O}$  counter is in the forward direction, the face of the collimator intercepts an appreciable flux of photons. Therefore it is made of wax, to avoid generating photoneutrons near the flight path. Additional shielding of about 12" of carbon is placed between this collimator and the bremsstrahlung target.

With all of this shielding in place, the background level in the three counters was still unacceptable at the highest bremsstrahlung energies used. It was apparently due to one or more of the following causes:

- 1) Background counts produced by the gamma flash exciting a long-delay component in the scintillator.
- 2) Background from the cloud of positrons injected into the environment of the target sample by the bremsstrahlung flash. The positrons form ortho-positronium in air which decays with a mean life of about 150 ns.
- 3) Background due to gamma rays from the accelerator dark current. Since the r-f decay time in the accelerator cavities is about 1  $\mu\text{sec}$  after the beam pulse, it is possible to accelerate electrons emitted from cathode material sputtered onto the focussing grid, stray electrons in the linac from Van de Graaf internal arcing, or electrons produced by ionization of the residual gas by the original electron beam. These gamma rays are characterized by an envelope similar to the r-f envelope in the cavities.
- 4) Background arising from neutrons produced in materials other than



the ( $\gamma, n$ ) target and directly detected by proton recoils in the counters. This is ordinarily of little importance for bremsstrahlung energies less than about 13 MeV, but it can be important above this, especially beyond the ( $\gamma, n$ ) threshold of aluminum, since much of the material surrounding the target is aluminum.

In the  $156^\circ$  and  $76^\circ$  counters the background due to (2) and (3) are primarily low energy gammas, 0.51 MeV for positronium and less than 1 MeV for dark current gamma rays, Compton-scattered at large angles by the ( $\gamma, n$ ) target or the bremsstrahlung target. These gamma rays were greatly reduced by inserting lead and bismuth absorbers in the neutron flight paths. About 1" of lead plus 1" of bismuth was found to give the best signal-to-noise ratio. These photon filters also improve the background due to (1) in all counters.

This added shielding was sufficient to reduce the background in the  $156^\circ$  detector to the desired level (about 3 per cent of the photoneutron counts at 1 MeV from a typical target with a machine energy of 15 MeV). The  $156^\circ$  and  $76^\circ$  backgrounds have the same value below 13 MeV machine energy, but at 15 MeV a larger number of counts appear at late flight times at  $156^\circ$ . These are presumably low energy neutrons generated in the aluminum walls of the target box in the path of the gamma beam. Such neutrons would have to penetrate a substantial amount of shielding or be scattered several times to reach the  $76^\circ$  counter. However they can enter the  $156^\circ$  flight path either directly or by small angle scattering. The  $156^\circ$  collimator aperture could not be made smaller, so this background had to be accepted. (The portion of the target box viewed by the  $156^\circ$  counter was lined with wax which somewhat reduced the neutrons generated in the aluminum wall.) Below 2 MeV the background was from 3 to 4 times that at  $76^\circ$ , but was about the same at higher neutron energies.

The background at  $24^\circ$  was so large that 3" of lead and bismuth in the flight path still did not reduce it to a tolerable level. As this much lead represents a large neutron absorption, it was doubtful if the signal-to-noise ratio was actually being improved. It was found that lowering the gain of the phototubes greatly reduced the background. From this it was deduced that the gamma flash was depositing such a large amount of energy in the scintillator that the

single photons emitted in the tail of the long scintillator decay components were numerous enough to cause a triple coincidence within the resolving time of the detector circuits. Reducing the gain required more photons per coincidence and thus discriminated against these photons. However it also reduced the low energy neutron detection efficiency. It was found that the  $24^\circ$  counter could not be operated with a threshold lower than about 0.9 MeV at the higher machine energies. This still left a large amount of background with a time dependence that seemed to follow the r-f envelope. Since the counter is at  $24^\circ$ , the dark current gamma rays still have an appreciable fraction of their energy (2 to 4 MeV for 5 to 15 MeV gammas) after Compton scattering. In this energy region the attenuation of photons in lead is about 4 per cent per gram and, for 1 to 10 MeV neutrons, about 2 to 3 per cent per gram. Therefore placing extra lead in the flight paths does not improve the signal-to-noise ratio rapidly. 2" of lead and 1" of bismuth were used. In addition the flux of the Compton-scattered gammas is much larger at  $24^\circ$  than at, say,  $76^\circ$  (about 10 times larger). The background-to-photoneutron ratio at  $24^\circ$  was about 5 to 10 times that of the  $76^\circ$  counter at high neutron energies (2 to 8 MeV) and the  $24^\circ$  counter efficiency was very small below 1 MeV.

The background shapes as a function of flight time are shown later in Fig. 9 of Chapter IV (section A). Table II lists some typical photoneutron data after background subtraction and the corresponding backgrounds.

### C. Uranium Ratios

In order to calculate the angular distributions one must know the ratios of the detector response as a function of neutron energy. The photoneutron spectrum from uranium was used for this purpose. The uranium data taken with 14 MeV machine energy was corrected for counts lost due to THC dead time and coincidence losses, and the background was subtracted (see Chapter IV, sections a and b of part A). This data was then summed and converted to an energy spectrum with 0.4 MeV bins.

The ratios of neutron counts at angles  $156^\circ$  and  $76^\circ$  and at angles  $24^\circ$  and

Table II  
 $\text{Pb}^{206}$  Photoneutron Energy Spectra and Background from a  
 15 MeV Bremsstrahlung Spectrum

Neutron Energy (MeV)	$^{156}\text{O}$		$^{76}\text{O}$		$^{24}\text{O}$	
	Data	Bkg	Data	Bkg	Data	Bkg
0.6	5341	826	5058	438	66	42
1.0	9347	548	8333	228	464	97
1.4	9835	342	8654	135	1517	149
1.8	8184	208	7318	78	2104	194
2.2	5547	130	5287	57	1674	230
2.6	3726	85	3515	44	1086	225
3.0	2196	51	2300	36	703	197
3.4	1402	31	1609	30	546	171
3.8	1068	23	1212	26	390	146
4.2	772	20	1007	26	324	126
4.6	587	18	872	23	259	110
5.0	440	16	778	23	201	97
5.4	390	14	681	22	186	86
5.8	266	13	452	22	104	79
6.2	206	13	366	22	67	72
6.6	118	12	237	22	31	66
7.0	43	11	86	23	10	61
7.4	9	10	16	26	14	56

$156^\circ$  were calculated and are listed in Table III. These ratios for uranium are given by

$$R(\Theta_i/\Theta_j) = \frac{W_U(\Theta_i) g_i \eta_i \Delta\Omega_i}{W_U(\Theta_j) g_j \eta_j \Delta\Omega_j} \quad (22)$$

where  $W_U(\Theta_i)$  = the angular distribution of the uranium neutron spectrum at angle  $\Theta_i$

$\eta_i$  = efficiency of the detector at angle  $\Theta_i$

$g_i$  = neutron absorption in the lead and bismuth photon filter in the flight paths at angle  $\Theta_i$

$\Delta\Omega_i$  = solid angle subtended by the detector at angle  $\Theta_i$

All of these quantities, except possibly  $\Delta\Omega$ , are functions of neutron energy. The solid angles subtended by the  $156^\circ$  and  $76^\circ$  counters were identical. The thresholds of these two counters were set as close together as possible by equalizing the low end of the uranium photoneutron spectra. This resulted in nearly identical detector efficiencies, especially at neutron energies above 2 MeV, where small differences in the thresholds have a negligible effect on the efficiency. The neutron absorption in the photon filters was approximately 5 per cent less at  $156^\circ$  than at  $76^\circ$  due to the different amounts of lead and bismuth (see Table IV).

The solid angle subtended by the counter at  $24^\circ$  was 0.6 of the solid angle subtended by the  $156^\circ$  counter due to the longer flight path. This  $24^\circ$  counter has a much higher threshold (0.9 MeV vs 0.25 MeV) and hence a lower efficiency. In addition the neutron absorption is nearly twice as great as that at  $156^\circ$  due to the extra inch of lead in the flight path.

To illustrate the use of the uranium ratios  $R(\Theta_i/\Theta_j)$ , consider the data for element A. The ratio of the counts at angle  $\Theta_i$  to the counts at angle  $\Theta_j$  at a given neutron energy is given by

$$\frac{C(\Theta_i)}{C(\Theta_j)} = \frac{W_A(\Theta_i) g_i \eta_i \Delta\Omega_i}{W_A(\Theta_j) g_j \eta_j \Delta\Omega_j} \quad (23)$$

$W_A(\Theta_i)/W_A(\Theta_j)$  is the ratio desired. Thus

Table III

## Uranium Photoneutron Spectra Ratios

Neutron Energy (MeV)	$\frac{W_U(156^\circ)}{W_U(76^\circ)}$	Error	$R\left(\frac{156^\circ}{76^\circ}\right)$	Error	$R\left(\frac{240^\circ}{156^\circ}\right)$	Error
0.6	1.00	0.005	0.967	0.006	0.008	0.125
1.0	1.00	0.005	1.069	0.006	0.055	0.018
1.4	1.00	0.005	1.067	0.006	0.155	0.013
1.8	1.00	0.005	1.068	0.007	0.251	0.012
2.2	0.99	0.005	1.058	0.009	0.289	0.017
2.6	0.98	0.005	1.049	0.010	0.323	0.017
3.0	0.97	0.005	1.019	0.014	0.356	0.017
3.4	0.95	0.005	1.010	0.016	0.362	0.020
3.8	0.93	0.0075	1.000	0.017	0.389	0.023
4.2	0.915	0.01	0.980	0.019	0.429	0.023
4.6	0.910	0.015	0.960	0.021	0.434	0.028
5.0	0.900	0.020	0.940	0.023	0.440	0.034
5.4	0.890	0.025	0.930	0.028	0.430	0.035
5.8	0.885	0.0275	0.920	0.030	0.420	0.043
6.2	0.880	0.030	0.915	0.034	0.400	0.050
6.6	0.910	0.04	0.950	0.038	0.380	0.050
7.0	0.950	0.03	0.99	0.045	0.370	0.067
7.4	0.960	0.02	1.00	0.050	0.360	0.082
7.8	0.960	0.01	1.00	0.050	0.355	0.11
8.2	0.960	0.01	1.00	0.050	0.350	0.12

$\frac{W_U(\theta_i)}{W_U(\theta_j)}$  is the ratio of the angular distributions of the uranium photoneutron spectra at angle  $\theta_i$  to that at angle  $\theta_j$  from McConnell (52)

$R(\theta_i/\theta_j)$  is the ratio of the measured uranium photoneutron spectrum at angle  $\theta_i$  to that at angle  $\theta_j$  for a 14 MeV bremsstrahlung spectrum. These measured uranium spectra have been corrected for counting losses.

Table IV

Thickness of Shielding in Flight Paths (In Inches)

Angle of Counter	Bismuth	Lead
24°	$\frac{5}{8}$	$1\frac{7}{8}$
76°	$1\frac{3}{16}$	$1\frac{1}{4}$
156°	1	1

Table V

Geometrical Factor

Target	Number of Neutrons in the Interval 1.4 to 3.0 MeV			Ratios of Neutrons		Geometrical Factor
	156°	76°	24°	$\frac{156^\circ}{76^\circ}$ $N_1/N_2$	$\frac{24^\circ}{156^\circ}$ $N_3/N_1$	
Tantalum						
1 $\frac{1}{4}$ " dia	26,562	24,785	26,335	1.08 ± 0.008	0.99 ± 0.02	1.00
2" dia	15,343	15,155	14,777	1.01 ± 0.01	0.96 ± 0.02	1.06 ± 0.01
2" square	19,847	20,314	19,355	0.98 ± 0.01	0.98 ± 0.02	1.09 ± 0.01
Bismuth						
cylinder	71,823	72,482	56,943	0.991 ± 0.005	0.99 ± 0.01	1.00
disk	36,546	39,268	25,915	0.930 ± 0.007	1.006 ± 0.015	1.064 ± 0.009

Bismuth runs include scattering corrections.

All runs include corrections for detector efficiency and neutron absorption in the photon filters.



$$\frac{C(\Theta_i)}{C(\Theta_j)} / R(\Theta_i/\Theta_j) = \frac{W_A(\Theta_i)g_i\eta_i\Delta\Omega_i}{W_A(\Theta_j)g_j\eta_j\Delta\Omega_j} \times \frac{W_U(\Theta_j)g_j\eta_j\Delta\Omega_j}{W_U(\Theta_i)g_i\eta_i\Delta\Omega_i} = \frac{W_A(\Theta_i)}{W_A(\Theta_j)} \times \frac{W_U(\Theta_j)}{W_U(\Theta_i)} \quad (24)$$

or

$$\frac{W_A(\Theta_i)}{W_A(\Theta_j)} = \frac{C(\Theta_i)}{C(\Theta_j)} \times \frac{W_U(\Theta_i)}{W_U(\Theta_j)} / R(\Theta_i/\Theta_j) \quad (25)$$

Thus the uranium data allows one to remove the efficiency, absorption and solid angle factors, if the angular distribution,  $W_U(\Theta_i)$ , of photoneutrons from uranium is known. This has been measured at this laboratory by Dr. D. B. McConnell (see Appendix III) and is tabulated in Table III.

#### D. Geometry Effects

Because of the stringent shielding requirements of the  $24^\circ$  and  $156^\circ$  detectors as described in Chapter III, section B, the collimators of these counters were made to view as small an area as possible. Therefore a series of runs on different sized targets were made to determine if either of these counters were being shadowed, as a visual inspection suggested that they might be. The  $76^\circ$  counter, with its 8" diameter hole was assumed to view the entire target.

For this purpose three runs were made using tantalum targets with the following geometry: (a) 2"x2" square,  $\frac{3}{16}$ " thick, (b) 2" diameter disk,  $\frac{7}{32}$ " thick, and (c)  $1\frac{1}{4}$ " diameter disk,  $\frac{3}{16}$ " thick. Visual inspection showed that the  $1\frac{1}{4}$ " disk was small enough to be seen by the  $24^\circ$  and  $156^\circ$  counters. The total number of neutrons counted in this series of experiments, and the ratios  $N_1/N_2$  and  $N_3/N_1$ , from 1.4 to 3.0 MeV are given in Table V.

The last column of the table lists the geometrical factor. It is the factor required to normalize the ratio of  $N_1/N_2$  for each target to the ratio  $N_1/N_2$  for the smallest target. It represents the geometrical shadowing of these targets at  $156^\circ$ . As can be seen from the fourth column, the same factor is required for the  $24^\circ$  counter within the accuracy of the data. The geometric factor for each target is listed in Table I. Since the lead targets are only 1" in diameter, they have a factor of 1.0. All 2" square targets have a factor of 1.09 and all 2" diameter disks have a factor of 1.06 except gold. The gold target

consisted of loose chips in a 2" diameter plastic container. The chips did not fill the container to the top, and the shadowing was therefore reduced. Based on observations made with a transit, the geometrical factor for gold was estimated to be 1.05. The tin target was approximately  $1\frac{7}{8}$ " square. The geometrical factor for tin was estimated to be about 1.06.

An additional check was made using two different bismuth targets: a 2" diameter disk,  $\frac{3}{8}$ " thick, and a cylinder  $\frac{3}{16}$ " long and  $\frac{5}{8}$ " in diameter. The cylinder was small enough to have a factor of 1.0. After the effects of neutron scattering in the disk target had been taken into account, the geometric factor was 1.06 as expected. Neutron scattering must be taken into account because it distorts the angular distribution by different amounts in the two targets (see Appendix I). Neutron scattering could be neglected in the comparison of the three tantalum targets because they are the same thickness and were placed with the same orientation to the gamma beam.

#### E. Detector Response.

To derive the photoneutron energy spectra from the raw data, one must determine  $\eta(E_n)$ , the detector efficiency, and  $g(E_n)$ , the neutron attenuation due to the lead and bismuth photon filters in the neutron flight paths. Ideally the efficiency of the neutron detector should be determined experimentally. However the lack of a calibrated source of monoenergetic neutrons made this impossible. Instead, the detector response ( $g\eta$ ) was determined by two different indirect methods. The first method consists of estimating the detector response from the photoneutron spectrum of deuterium, measured at  $76^\circ$ . Because of the proton recoil, the neutron energy is approximately one-half the gamma ray energy. Thus a 15 MeV bremsstrahlung beam produces neutrons with a maximum energy of only about 6 MeV. Furthermore statistical accuracy of the deuterium data is such that the detector response cannot be determined to the desired accuracy above about 4 MeV neutron energy. Therefore this method is used to determine  $\eta(E_n)g(E_n)$  from 0.4 to 4.0 MeV. The second method consists of calculating the detector efficiency,  $\eta(E_n)$ , from the n-p and n-C scattering cross sections (Appendix IV). At low neutron energies, the photomul-

was taken from ref 55. The angular distribution of multiply-scattered electrons was taken from ref 56. In order to simplify the calculation, electrons multiply-scattered outside of the solid angle subtended by the ( $\gamma, n$ ) target at a given layer of the bremsstrahlung target were assumed to contribute no photons to the beam. Those inside this solid angle were assumed to contribute photons with a Schiff spectrum. The calculation should enable one to estimate the range of validity of the Schiff spectrum. Table VI lists the ratio, R, of the calculated thick target bremsstrahlung spectrum, to the Schiff thin target spectrum, normalized to unity at 3.5 MeV gamma ray energy. The results deviate from unity by less than 5 per cent below 9.0 MeV.

Also listed in the table is the result of a calculation estimating the neutron scattering in the deuterium target (see Appendix IV). The numbers listed are the ratios, C, of the "scattering-corrected" photoneutron spectrum to the measured spectrum. The values of C are listed for the neutron energies,  $E_n$ , corresponding to the gamma ray energies,  $E_\gamma$ , listed in the first column. The next column lists C/R normalized to 1.0 at  $E_n = 1.2$  MeV.

According to equation 26 and the definitions of R and C, the true detector response is given by

$$g(E_n)\eta(E_n) = g'(E_n)\eta'(E_n) \frac{C}{R} \quad (27)$$

Except near 3.0 MeV neutron energy, where the carbon scattering cross section has a large resonance, and hence the calculated neutron scattering in the  $CD_2$  target has some structure, C/R is  $1.0 \pm 0.02$  from 0.4 to 4.0 MeV neutron energy. Thus  $g\eta \approx g'\eta'$  from 0.4 to 4.0 MeV. At higher neutron energies, the calculated thick target bremsstrahlung spectrum diverges from the Schiff spectrum causing C/R to increase rapidly. The values of  $g'\eta'$  are shown graphically in Fig. 7.

The second method of estimating the detector efficiency is to calculate it from the n-p and n-C neutron cross section.\* This calculation is outlined in Appendix IV. Detection of a neutron occurs indirectly through the kinetic

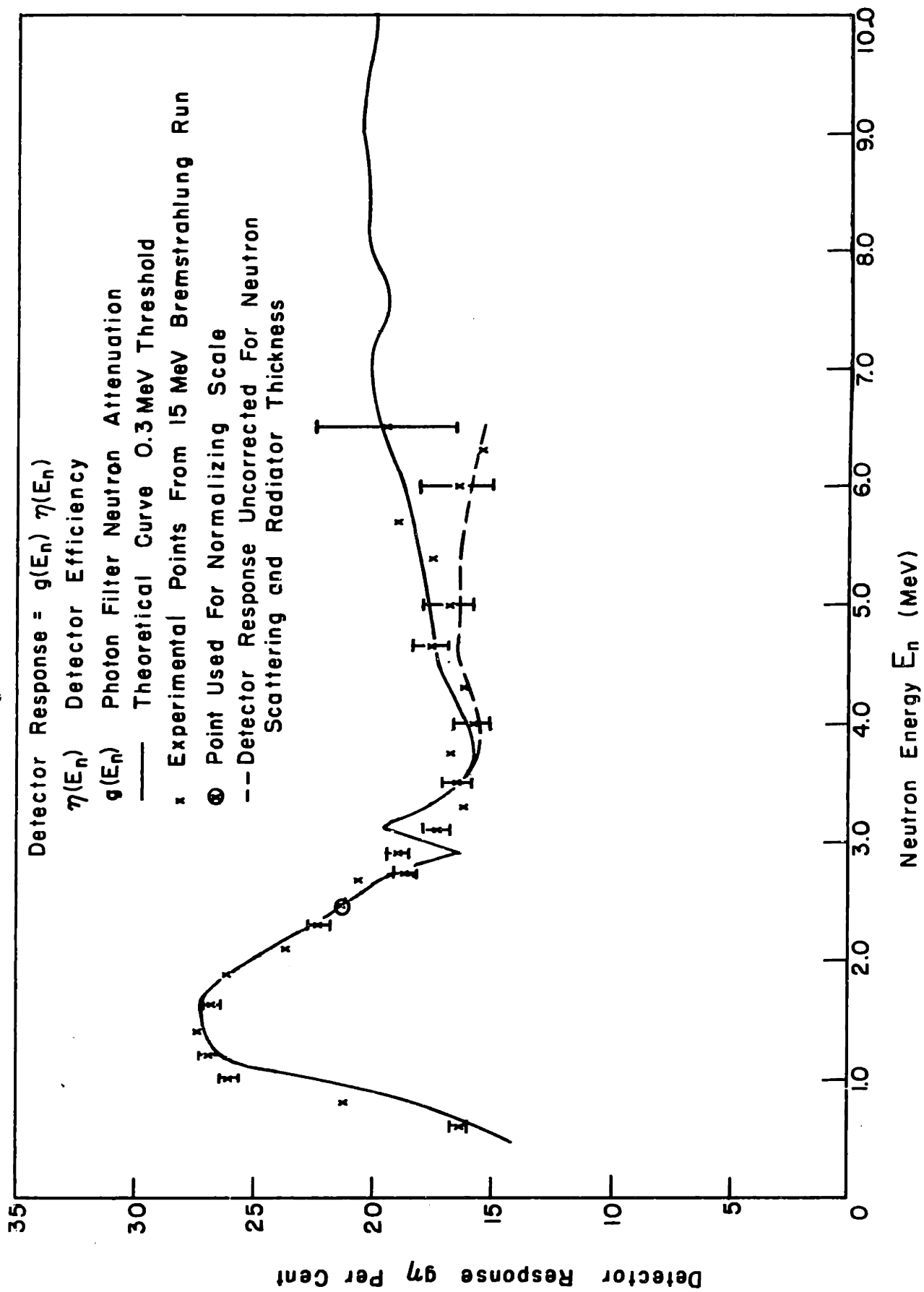
\*The n-C cross section is needed because the scintillator is toluene.

Table VI  
Thick Target Bremsstrahlung Spectrum and  
Neutron Target Scattering Corrections

$E_{\gamma}$	R	$E_n$	C	$\frac{C}{R}^*$
3.0	0.98	0.40	1.15	0.98
3.5	0.99	0.65	1.19	1.00
4.0	1.00	0.95	1.21	1.00
4.5	1.00	1.20	1.21	1.00
5.0	1.00	1.40	1.21	1.00
5.5	1.00	1.70	1.20	1.00
6.0	1.00	1.96	1.18	0.99
6.5	1.00	2.20	1.17	0.98
7.0	0.99	2.46	1.15	0.97
7.5	0.98	2.73	1.13	0.96
8.0	0.97	3.00	1.11	0.95
8.5	0.96	3.25	1.13	0.98
9.0	0.95	3.50	1.14	1.00
9.5	0.94	3.75	1.14	1.00
10.0	0.93	4.00	1.14	1.02
10.5	0.91	4.30	1.13	1.03
11.0	0.90	4.55	1.13	1.05
11.5	0.87	4.80	1.12	1.07
12.0	0.86	5.05	1.12	1.08
12.5	0.84	5.30	1.11	1.10
13.0	0.81	5.65	1.10	1.13
13.5	0.77	5.8	1.10	1.19
14.0	0.67	6.1	1.09	1.36
14.5	0.49	6.4	1.08	1.83
15.0	0.37	6.65	1.07	2.41

\* Normalized to 1.0 at  $E_n = 1.2$

Fig. 7



energy transferred to a proton in an elastic collision. The efficiency of the detector for a neutron of a given energy therefore depends primarily upon the n-p scattering cross section at that energy. However a given energy neutron yields a continuous energy spectrum of recoil protons. The fraction of detected recoils is proportional to  $(E_n - E_0)/E_n$ .  $E_0$  is the lowest energy neutron capable of producing a scintillation that the electronic circuitry can respond to, ie, the threshold. The threshold was estimated by linearly extrapolating the low energy end of the photoneutron spectra to zero counts. This gave a value of 0.3 MeV or less. The calculation of detector efficiency outlined in Appendix IV was made using the value of 0.3 MeV. The results are tabulated there in Table XLIII.

At neutron energies comparable to the threshold, the photomultiplier electron multiplication statistics, circuit drifts, and multiple scattering in the scintillator contribute to the uncertainty of  $E_0$ , and affect the validity of the calculated shape of  $\eta(E_n)$ . Above  $2\frac{1}{2}$  to 3 MeV, however, the efficiency shape is essentially determined by the n-p scattering cross section. Even when plural scattering effects are considered, the calculations show that the shape is quite insensitive to the precise value of the threshold used (see Appendix IV).

The detector response is found by multiplying the calculated values of  $\eta(E_n)$  by  $g(E_n)$ , the neutron absorption, calculated from the total neutron cross sections listed in ref 53. This product is the solid curve in Fig. 7. The broad minimum from 2.0 to 6.0 MeV neutron energy is due to the maximum in the lead and bismuth cross section in this region, and the sharp drop below 1.5 MeV is due to the non-zero threshold. The structure at 3.0 and 7.5 MeV is due to structure in the carbon scattering cross section. The structure at 3.0 MeV has not been observed in the deuterium photoneutron spectrum. It is possible that the assumptions made in the calculations (such as elastic scattering from carbon nuclei) have exaggerated the influence of this structure.

The results of the two methods of determining  $g\eta$  are shown in Fig. 7. The X's are the values of  $g\eta$  determined from the deuterium photoneutron spec-

trum using a Schiff thin target photon spectrum with a 15.0 MeV endpoint and  $C/R = 1.0$ , (ie,  $g'\eta'$ ). The solid curve is the calculated values of  $\eta(E_n)$  from Appendix IV multiplied by  $g(E_n)$  calculated using the total neutron cross section from ref 53. The values of  $g'\eta'$  were normalized to the solid curve at  $E_n = 2.4$  MeV ( the circled point in the figure). The vertical scale is the percent of incident neutrons detected. The two methods were normalized at this low energy because of the structure in the calculated curve around 3.0 MeV, and the large statistical scatter in the experimental points around 4.0 MeV. The dotted line is the solid curve multiplied by  $R/C$ . If the calculation of the thick target spectrum and the neutron scattering in the target were correct, the experimental detector response ( $g'\eta'$ ) would fit the dashed line rather than the solid curve. The statistical scatter is large, but it appears that the data favors the solid curve rather than the dashed curve. This is probably due to approximations made in the thick target calculations.

As was mentioned at the beginning of this section,  $g\eta$  was taken equal to  $g'\eta'$  from 0.4 to 4.0 MeV, and equal to the calculated values (solid curve in Fig. 7) from 4.0 to 10.0 MeV. The values of  $g\eta$  used in the data reduction are listed in the last column of Table VII. Neither method determines the absolute scale of  $g\eta$  accurately, only the shape. This is sufficient for the present experiment, which deals with neutron energy spectra, not absolute cross sections. Therefore the errors in  $g\eta$  listed in Table VII do not contain an estimate of the uncertainties of the absolute value of  $g\eta$ . They refer to the uncertainties in the shape only.

Once  $g\eta$  has been determined, equation 26 can be used to determine the experimental bremsstrahlung spectrum. The photon spectrum for a run with an endpoint of 14 MeV is shown in Fig. 8. The solid curve is a Schiff spectrum fitted to the data from 8.0 to 12.0 MeV. The fit is very good, especially from 10 to 13 MeV. Actually if the Schiff spectrum had been normalized in a lower energy region, say 4.0 to 10.0 MeV, the solid curve would apparently lie higher than the data near the high energy end, as one would expect from the thick target calculations. In any case, the thick target calculation seems to overestimate

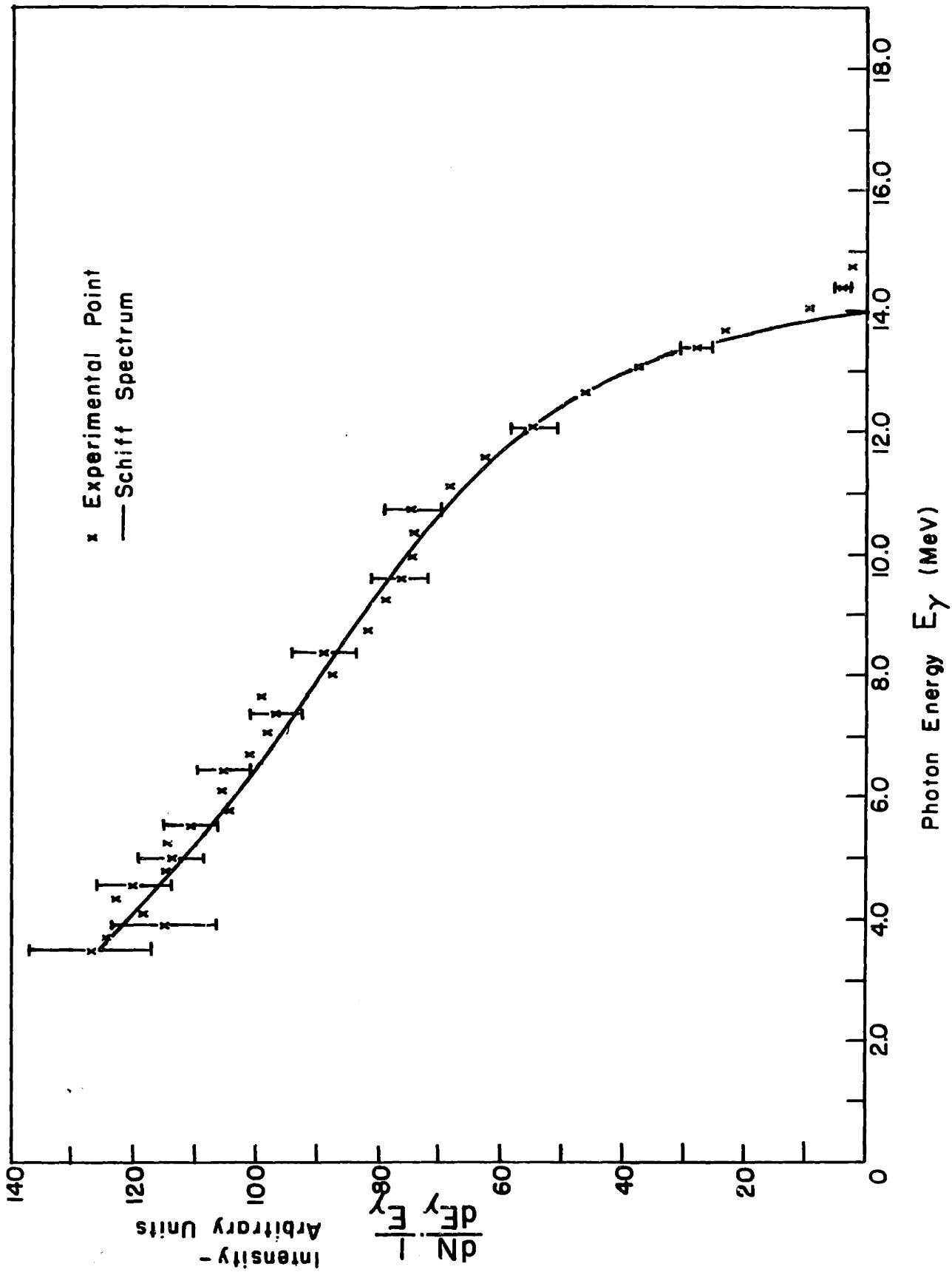
Table VII  
Detector Response

$E_n$	$g\eta$	$\Delta(g\eta)$
0.6	0.170	0.002
1.0	0.270	0.003
1.4	0.283	0.003
1.8	0.269	0.003
2.2	0.240	0.004
2.6	0.209	0.005
3.0	0.185	0.005
3.4	0.175	0.006
3.8	0.165	0.007
4.2	0.170	0.008
4.6	0.177	0.009*
5.0	0.180	0.009
5.4	0.184	0.009
5.8	0.198	0.01
6.2	0.198	0.01
6.6	0.203	0.01
7.0	0.206	0.01
7.4	0.200	0.01
7.8	0.200	0.01
8.2	0.205	0.01
8.6	0.208	0.01
9.0	0.209	0.01
9.4	0.207	0.01
9.8	0.204	0.01

\* Calculation assigned 5 per cent errors.



Fig. 8 14.0 MeV Experimental Bremsstrahlung Spectrum



the deviation from the Schiff spectrum. The experimental points are not zero above 14.0 MeV as the Schiff spectrum predicts. This is due to the 4 per cent spread in the electron beam energy. Throughout this thesis, the bremsstrahlung endpoint will be referred to in terms of the endpoint energy  $E_0$ , of a Schiff spectrum that is fitted to the data, rather than the endpoint of the experimental spectra. This is done because the tailing off at the tip fluctuates with the machine tuning, and hence the Schiff spectra endpoints characterize the photon spectra in a more fundamental manner.

## Chapter IV

### Treatment of Data

#### A. Preliminary Treatment

##### a) Coincidence Correction

The first step in the reduction of the data is the correction for counts lost due to coincidences. The counts recorded in the analyzer are less than the number of neutrons detected for two reasons. First, if a counter detected more than one neutron during a beam burst, only the first neutron will be recorded since the THC is inoperative for  $8 \mu\text{sec}$  after it receives the first pulse. There was no provision for determining the number of such events electronically. Second, if two counters detect an event during a beam burst, neither event is stored in the block of the analyzer corresponding to these counters. Instead, the first event in time is stored in the fourth quadrant of the analyzer, and the second event is not recorded. In the case of triple events (either single counts from three counters, two counts from one detector and one count from another, or three counts from one detector), the first pulse is stored in the fourth quadrant (or in the last case mentioned, in the quadrant corresponding to the proper counter), and the other two are lost. Events of higher multiplicity are so rare as to be unimportant.

If two counters each detect a neutron during the same beam burst, neither count is recorded in the analyzer blocks 1 to 3, regardless of the order or time of the two signals. Therefore the resulting distortion of the spectra is a uniform reduction in amplitude. That is, to correct for counting loss due to signals from more than one counter, one need only multiply the stored data by a constant, independent of the channel in which the data is stored. On the other hand, if two neutrons are detected by the same counter, the first count will be recorded and the second lost. Therefore one must apply a correction that increases with increasing channel number.

The two different types of counting losses affect one another only if there are at least three neutrons present, two from one counter and one from

another, and hence their interaction is a second order effect which will be neglected. One should calculate the loss due to two neutrons from one counter after correcting for the loss due to two neutrons from separate counters. This is due to the fact that the number of counts lost due to coincidences between two counters has been measured, while the number of counts lost due to self coincidences must be calculated. Therefore a more accurate correction for the losses due to self coincidences can be achieved if the other correction is performed first. Since the effect of the self coincidence losses on the two counter coincidence losses is of second order, the correction for two counter coincidence losses can be calculated to a high degree of accuracy, without having performed the self coincidence correction.

For each set of experimental data the following are known:

- $n_i$  = total number of recorded counts from the counter at angle  $\Theta_i$
- $N_c$  = total number of recorded coincidences between two counters
- $T$  = duration of the run, in seconds
- $\tau$  = inverse of the repetition rate ( $\frac{1}{\tau} = 120/\text{sec}$ )

The purpose of the calculation is to find the actual number of counts,  $N_i$ , from the counter at angle  $\Theta_i$ . For each counter

$$N_i = n_i + C_{ii} + C_{ij} + C_{ik} + (\text{higher orders}) \quad (28)$$

where  $C_{ii}$  = counts lost due to self coincidences in counter  $i$

$C_{ij}, C_{ik}$  = counts lost due to coincidence with counters  $j$  and  $k$  respectively.

Let  $\bar{N}_i = N_i - C_{ii}$ , then, neglecting higher orders

$$\bar{N}_i = n_i + C_{ij} + C_{ik} \quad (29)$$

and for low counting rates

$$C_{ij} \approx \frac{\tau}{T} (\bar{N}_i \bar{N}_j) \quad (30)$$

and

$$C_{ik} \approx \frac{\tau}{T} (\bar{N}_i \bar{N}_k) \quad (31)$$

In the above expressions  $T/\tau$  = number of beam bursts. Also the recorded coincidences,  $N_c$ , are given by

$$N_c = \frac{\tau}{T} (\bar{N}_1 \bar{N}_2 + \bar{N}_1 \bar{N}_3 + \bar{N}_2 \bar{N}_3) \quad (32)$$

which is half the number of neutrons lost from two-counter coincidences.

Equations 29, 30, 31, and 32 are combined to give

$$\bar{N}_1 = n_1 + N_c - \frac{\tau}{T} \bar{N}_2 \bar{N}_3 \quad (33a)$$

$$\bar{N}_2 = n_2 + N_c - \frac{\tau}{T} \bar{N}_1 \bar{N}_3 \quad (33b)$$

$$\bar{N}_3 = n_3 + N_c - \frac{\tau}{T} \bar{N}_1 \bar{N}_2 \quad (33c)$$

where  $n_1$ ,  $n_2$ ,  $n_3$ ,  $N_c$ ,  $\tau$ , and  $T$  are known quantities. These equations yield three fifth order equations in  $\bar{N}_1$ ,  $\bar{N}_2$ , and  $\bar{N}_3$ .

However, the above equations are derived on the assumption that the counting rate was maintained at a constant value for precisely  $T$  seconds. This implies that all beam pulses were identical and there were  $T/\tau$  pulses. The MIT linac does not have such stability. The beam can fluctuate widely from pulse to pulse. Over periods of an hour, the machine requires tuning, which results in the loss of an unknown number of pulses. Therefore in the analysis of the data, the measured value of  $T$  was used as a first approximation in equations 33a, b, and c, which are then solved for  $\bar{N}_1$ ,  $\bar{N}_2$ , and  $\bar{N}_3$ . These values are then used to calculate a value of  $N_c$ , called  $N'_c$ , from equation 32. This is checked against the measured value of  $N_c$ , and  $T$  is varied in small steps until  $N'_c = N_c \pm 0.5$  per cent. In this manner an effective value of  $T$ , called  $\bar{T}$ , is found, which is always smaller than the measured  $T$ . The corresponding values of  $\bar{N}_1$  are used to correct for losses due to two counter coincidences. The data in each channel is multiplied by the constant  $\bar{N}_1/n_1$ .

To calculate the correction for self coincidences, consider the channel  $x$ , with a real counting rate of  $m(x)$ . The number of counts recorded per unit time in channel  $x$  will be

$$m'(x) = m(x) P(x) \quad (34)$$

where  $P(x)$  is the probability that there were no counts in channels 1 to  $x-1$  during that unit time. The probability that there was no count in channel  $y$  during a unit time is given by the zero<sup>th</sup> Poisson distribution

$$P_0(y) = \frac{m(y)^0}{0!} e^{-m(y)} = e^{-m(y)} \quad (35)$$

and hence the probability that there were no counts in channels 1 to  $x-1$  is

$$P(x) = \prod_{y=1}^{x-1} P_o(y) = \prod_{y=1}^{x-1} e^{-m(y)} = e^{-\left(\sum_{y=1}^{x-1} m(y)\right)} \quad (36)$$

where  $m(x) = N_i(x) \frac{\tau}{T}$  = number of counts per beam burst in channel x.

Therefore

$$N_i(x) = \bar{N}_i(x) e^{-\left(\sum_{y=1}^{x-1} N_i(y) \frac{\tau}{T}\right)} \quad (37)$$

The self coincidence rate is low enough to approximate this equation by

$$N_i(x) = \bar{N}_i(x) e^{-\left(\sum_{y=1}^{x-1} \bar{N}_i(y) \frac{\tau}{T}\right)} \quad (38)$$

using the value of  $\bar{T}$  found above.

To check these calculations, radioactive sources were placed near each of the three counters such that the counting rates were in the same ratios as those encountered in an experiment (3:3:1). The rates were similar to the higher rates encountered in these experiments (about 25 counts/sec total). Each counter was allowed to accumulate data for 20 minutes with the other two disconnected from the THC, to determine  $\bar{N}_i$ . Data was then accumulated for  $16\frac{1}{2}$  hours with the three counters connected to the THC.

The accumulated data was treated as described above and the results are listed in Table VIII. In Table VIII A,  $\bar{N}_{i \text{ meas}}$  is the counts from counter  $\Theta_i$  measured with the other counters disconnected to eliminate coincidence losses due to two counters;  $n_i$  is the number of recorded counts from counter  $\Theta_i$  with the three counters operative.  $\bar{N}_{i \text{ calc}}$  is the number of counts from counter  $\Theta_i$  corrected for losses due to two counter coincidences. This measured value of T was 30,620 sec; the calculated value of T, called  $\bar{T}$ , was 29,700 sec (a difference of 3 per cent). The last two columns list the ratio of  $n_i$  and  $\bar{N}_{i \text{ calc}}$  to  $\bar{N}_{i \text{ meas}}$ . As can be seen from these last two columns, this correction is good to within the accuracy of the check.

In Table VIII B, A is the sum of the data in counter  $\Theta_i$  from 140 to 220 ns, after the two counter coincidence correction has been applied to the data, and B is the sum from 880 to 960 ns under the same conditions. A' and B' are the sums of the data from counter  $\Theta_i$  from 140 to 220 ns and 880 to 960 ns respectively, after the self coincidence correction has been applied to the data.

Table VIII A  
Comparison of Measured and Calculated Correction  
for Coincidences Between Two Counters

Counter Angle $\Theta_i$	$\bar{N}_{i \text{ meas}}$	$n_i$	$\bar{N}_{i \text{ calc}}$	$\frac{n_i}{\bar{N}_{i \text{ meas}}}$	$\frac{\bar{N}_{i \text{ calc}}}{\bar{N}_{i \text{ meas}}}$
156°	374,000 $\pm 1\frac{1}{4}$	326,920	373,147	0.874	0.998
76°	365,800 $\pm 1\frac{1}{4}$	316,409	362,374	0.865	0.991
24°	91,360 $\pm 2\frac{1}{2}$	72,091	90,441	0.789	0.990

Table VIII B  
Comparison of Spectral Shape Before and After  
Self-coincidence Correction (Spectrum Corrected  
for Coincidences Between Two Counters)

Counter Angle $\Theta_i$	A	B	$\frac{B}{A}$	A'	B'	$\frac{B'}{A'}$
	140-220 ns	880-960 ns		140-220 ns	880-960 ns	
156°	21,498	19,906	0.926	24,969	24,498	0.981 $\pm 0.01$
76°	20,474	18,990	0.928	23,869	23,392	0.980 $\pm 0.01$
24°	4,069	3,990	0.981	5,125	5,079	0.991 $\pm 0.02$

A comparison of the ratios  $B/A$  and  $B'/A'$  (which would be unity in the absence of a self coincidence counting loss), shows that the correction leaves a slope representing a fractional change in the counts per nanosecond of about  $-2 \times 10^{-5} \text{ (ns)}^{-1}$ , which is probably due to the substitution of  $\bar{N}_i$  for  $N_i$  in equation 37.

#### b) Background Subtraction

As was explained in Chapter III, section B, the background shape remains constant, but the magnitude varies with the tuning of the accelerator. Therefore it was necessary to normalize the background magnitude for each set of data. A standard shape was determined for each counter for a given set of running conditions and energies. Then the background was normalized to the data in the region between the neutron endpoint and the earliest channels containing background data. The normalization was performed separately for each counter, and the background was subtracted. Table IX lists three examples,  $\text{Pb}^{206}$ , Er, and  $\text{Pb}^{207}$ , with various bremsstrahlung endpoints. The sum of counts in the normalization channels is listed for each counter. Also shown is the statistical accuracy of this sum. In general the level of the background is determined to 10 per cent.

Figure 9 shows a typical time spectrum with the amount of background and the region over which the normalization took place. To see what a 10 per cent error in the magnitude of the background means, refer back to Table II where the number of counts and the amount of background for each 0.4 MeV bin is given. The background is only a few per cent of the  $76^{\circ}$  and  $156^{\circ}$  data except near the neutron endpoints. At  $24^{\circ}$ , the background is 10 per cent to 100 per cent of the data, and presents a much more serious error in the data.

#### c) Time-to-Energy Spectrum

The data now consists of time spectra  $\frac{\Delta^2 N(\Theta_i, t)}{\Delta t \Delta \Theta_i}$  taken in 256 channels. The time spectra are converted to energy spectra by summing the time spectra over those channels (or fractions of channels) corresponding to the desired energy bin.



Table IX  
Examples of Background Normalization Statistics

Target	Brem. Endpoint Energy	Counter Angle $\Theta_i$	Number of Counts in Normalization Channels	Statistics of Counts (per cent)
Pb <sup>206</sup>	15 MeV	156°	63	12
		76°	260	6
		24°	280	6
Er	14 MeV	156°	170	8
		76°	306	6
		24°	260	6
Pb <sup>207</sup>	13 MeV	156°	88	11
		76°	150	8
		24°	115	10

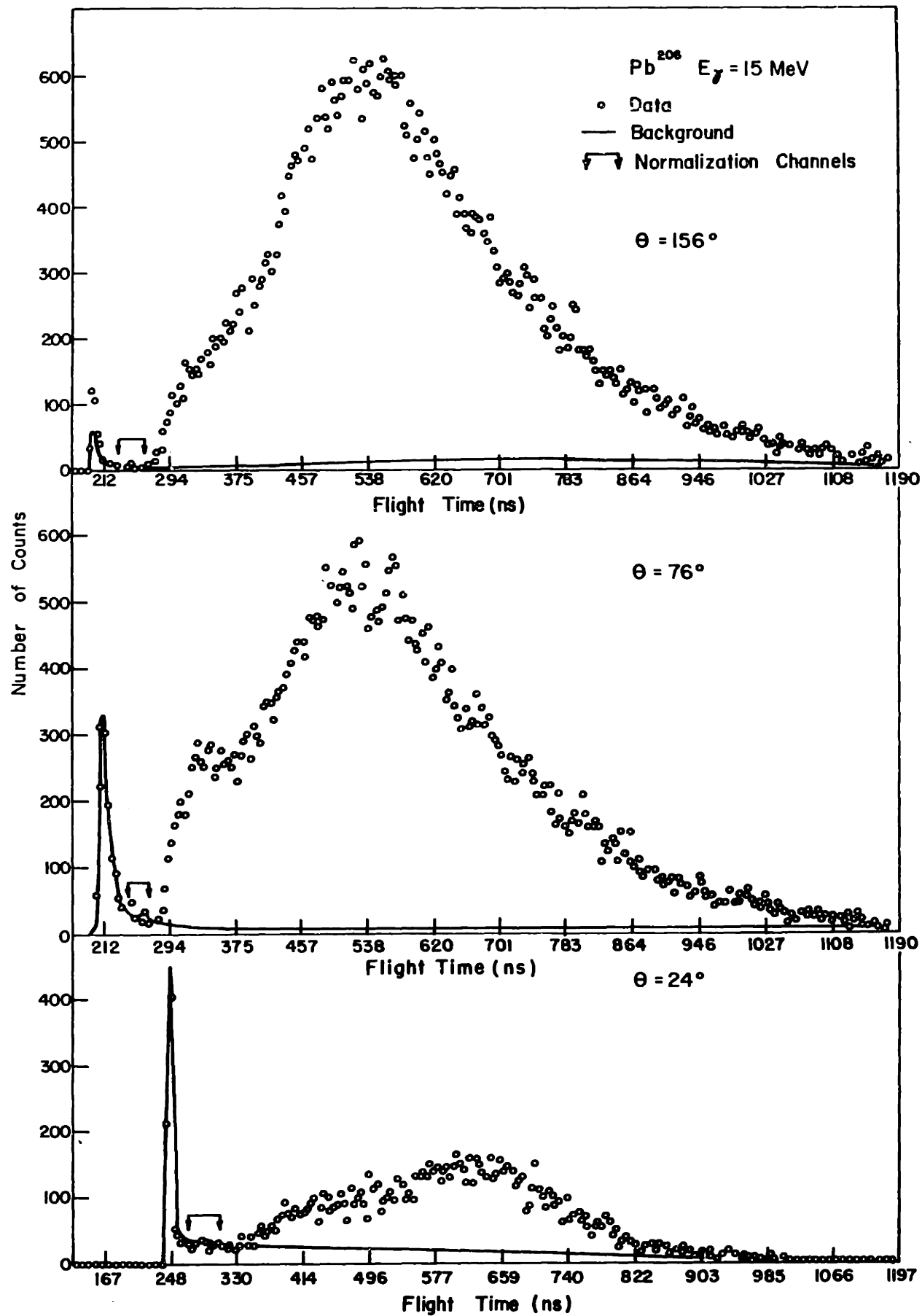


Fig. 9 Photoneutron Time Spectra

$$\frac{\Delta^2 N(\Theta_i)}{\Delta E_n \Delta \Omega} = \sum_{t_1}^{t_2} \frac{\Delta^2 N(\Theta_i)}{\Delta t \Delta \Omega} / \Delta E_n \quad (39)$$

$\Delta E_n = E_2 - E_1 = 0.4$  MeV, where  $t_1$  corresponds to energy  $E_1$  and  $t_2$  corresponds to  $E_2$ . In the following discussions the delta notation will be replaced by  $\frac{d^2 N(\Theta_i)}{dE_n d\Omega}$ . In all calculations involving neutron spectra, equations using this latter quantity will be evaluated at  $E_n = \frac{1}{2}(E_2 - E_1)$ , using the value of  $\frac{\Delta^2 N(\Theta_i)}{\Delta E_n \Delta \Omega}$  for  $\frac{d^2 N(\Theta_i)}{dE_n d\Omega}$ .

d) Correction for Neutron Detector Efficiency, Target Scattering and Collimator Shadowing

If  $\frac{d^2 N(\Theta_i)}{dE_n d\Omega}$  is the neutron spectrum incident on the counter at  $\Theta_i$  in the absence of all distortions, and  $\frac{d^2 N'(\Theta_i)}{dE_n d\Omega}$  is the measured neutron spectrum corrected for coincidence losses and background, then

$$\frac{d^2 N(156^\circ)}{dE_n d\Omega} = \frac{d^2 N'(156^\circ)}{dE_n d\Omega} \frac{S(156^\circ, E_n) f}{R(156^\circ/76^\circ) g(E_n) \eta(E_n)} \frac{W_U(156^\circ)}{W_U(76^\circ)} \quad (40a)$$

$$\frac{d^2 N(76^\circ)}{dE_n d\Omega} = \frac{d^2 N'(76^\circ)}{dE_n d\Omega} \frac{S(76^\circ, E_n)}{g(E_n) \eta(E_n)} \quad (40b)$$

$$\frac{d^2 N(24^\circ)}{dE_n d\Omega} = \frac{d^2 N'(24^\circ)}{dE_n d\Omega} \frac{S(24^\circ, E_n) f}{R(24^\circ/156^\circ) W_U(156^\circ)} \frac{\Delta \Omega_{156^\circ}}{\Delta \Omega_{24^\circ}} \quad (40c)$$

where  $S(\Theta_i, E_n)$  = the fraction of neutrons transmitted through the target at angle  $\Theta_i$  and energy  $E_n$ , plus the fraction of neutrons scattered into angle  $\Theta_i$  at energy  $E_n$ . (Table XLI, Appendix I)

$f$  = the inverse geometrical shadowing factor for the detectors at  $156^\circ$  and  $24^\circ$ .  $f$  is unity for the detector at  $76^\circ$ . (Table I, Chapter III)

$R(\Theta_i/\Theta_j)$  = ratio of uranium spectra at angle  $\Theta_i$  to that at angle  $\Theta_j$ . (Table III, Chapter III)

$g(E_n) \eta(E_n)$  = the detector response of the  $76^\circ$  counter. (Table IV, Chapter III)

$$\frac{W_U(\Theta_i)}{W_U(\Theta_j)} = \text{ratio of uranium angular distribution at angle } \Theta_i \text{ to that at angle } \Theta_j. \text{ (Note that } \frac{W_U(24^\circ)}{W_U(156^\circ)} = 1.0 \text{) (Table III, Chapter III)}$$

$$\frac{\Delta\Omega_{24^\circ}}{\Delta\Omega_{156^\circ}} = 0.6, \text{ the ratio of the solid angle subtended by the } 24^\circ \text{ counter to that subtended by the } 156^\circ \text{ counter. } \Delta\Omega_{156^\circ} = \Delta\Omega_{76^\circ}.$$

The factors  $f$ ,  $R(\Theta_i/\Theta_j)$ ,  $W_U(\Theta_i)/W_U(\Theta_j)$ , and  $g(E_n)\eta(E_n)$  are discussed and tabulated respectively in sections C, D, and E of Chapter III. The factor  $S(\Theta_i, E_n)$  is tabulated and discussed in Appendix I.

The neutron energy spectrum  $\frac{d^2N(\Theta_i)}{dE_n d\Omega}$  is modified by neutron scattering in the  $(\gamma, n)$  target, by shadowing by the collimators, by neutron absorption in the photon filters placed in the flight paths, and by the efficiency of the neutron detector. The factor  $S(\Theta_i, E_n)$  corrects the measured neutron spectrum for the effects of target scattering. The factor  $f$  corrects for collimator shadowing. The factor  $g(E_n)$  corrects for neutron absorption in the photon filters and  $\eta(E_n)$  for the detector efficiency. Finally the data from the  $24^\circ$  counter is corrected for the difference in solid angle.

The photon filter absorption  $g(E_n)$  and detector efficiency  $\eta(E_n)$  were determined for the  $76^\circ$  counter only. These quantities were measured relative to counter  $76^\circ$  for the counters at  $156^\circ$  and  $24^\circ$ , with the use of uranium neutron spectra as described in Chapter III. Thus in equation 40a,

$$\frac{1}{g_{156^\circ}(E_n)\eta_{156^\circ}(E_n)} = \frac{W_U(156^\circ)}{W_U(76^\circ)} \frac{1}{R(156^\circ/76^\circ)g(E_n)\eta(E_n)} \quad (41a)$$

and in equation 40c,

$$\frac{1}{g_{24^\circ}(E_n)\eta_{24^\circ}(E_n)} = \frac{W_U(24^\circ)}{W_U(156^\circ)} \frac{1}{R(24^\circ/156^\circ)} \quad (41b)$$

In this last equation, only neutron spectra of  $24^\circ$  relative to  $156^\circ$  are determined. The absolute neutron spectra for the  $24^\circ$  data has not been calculated because this quantity is not used (see section B of this Chapter). Of course they could easily be calculated.

## B. Angular Distribution

The angular distributions are presented in the form

$$W(\Theta) = a_0 + a_1 P_1 + a_2 P_2 \quad (42)$$

where the P's are the Legendre polynomials. Remembering that the data was taken at angles  $\Theta_1 = 156^\circ \approx \pi - \Theta_3$ ,  $\Theta_2 = 76^\circ$ ,  $\Theta_3 = 24^\circ$ ,  $a_1$  and  $a_2$  are given by

$$\frac{a_1}{a_0} = \frac{(1 - R_1)R_2[(3\cos^2\Theta_2 - 1) - (3\cos^2\Theta_1 - 1)]}{(3\cos\Theta_3 - 1)[2\cos\Theta_3 + R_2\cos\Theta_2(1 - R_1)] - (3\cos^2\Theta_2 - 1)(1 + R_1)R_2\cos\Theta_3} \quad (43a)$$

$$\frac{a_2}{a_0} = \frac{2[2\cos\Theta_3 + R_2\cos\Theta_2(1 - R_1) - R_2\cos\Theta_3(1 + R_1)]}{(3\cos^2\Theta_3 - 1)[2\cos\Theta_3 + R_2\cos\Theta_2(1 - R_1)] - (3\cos^2\Theta_2 - 1)(1 + R_1)R_2\cos\Theta_3} \quad (43b)$$

where  $R_1 = \frac{dN(24^\circ)/dE_n}{dN(156^\circ)/dE_n}$  and  $R_2 = \frac{dN(156^\circ)/dE_n}{dN(76^\circ)/dE_n}$

As can be seen from Table II, the background at  $24^\circ$  is very large and the counting rate is about one-third of the rates at  $156^\circ$  and  $76^\circ$ . As a result, the data at  $24^\circ$  are subject to large statistical uncertainties. To improve the statistical accuracy of the ratio,  $R_1$  was calculated for two energy bins: 1.4 to 3.8 MeV and 3.8 MeV to the neutron energy endpoint, instead of the 0.4 MeV bins used for  $R_2$ . (The sum is started at 1.4 MeV because of the low counter efficiency below this energy.)  $R_1$  for the various targets fell between 0.93 and 1.05 in the low energy bin with an average statistical error of 0.02, and between 0.92 and 1.14 with an average statistical error of 0.08 in the high energy bin. (The errors of course varied from run to run. See Table X.) The results are listed in Table X for data from 15 MeV bremsstrahlung runs. The errors quoted are statistical errors only, and do not include an estimate for systematic uncertainties.

Since low energy neutrons are predominantly statistically emitted, and therefore fore-aft symmetric, one would expect  $R_1$  to equal 1.0 for the low energy bin at least. However the experimental values of  $R_1$  differ from unity by more than the statistical errors for many targets. Therefore the effect of the following systematic errors on  $R_1$  were investigated.

- (1) Variations in the counter threshold. Because the  $24^\circ$  counter threshold is much higher than that of the other two counters, its efficiency is more sensitive to small changes of the threshold in the low energy bin. The counter efficiency is proportional to  $(E_n - E_0)/E_n$  (see section

Table X  
Ratio of Photoneutron Spectrum at  $24^{\circ}$  to Spectrum at  $156^{\circ}$

Element	$R_1$ summed from 1.4 to 3.0 MeV	$\Delta R_1$	$R_1$ summed from 3.0 MeV to $E_{n \max}$	$\Delta R_1$
Bi	1.046	0.023	1.069	0.084
Pb <sup>208</sup> *	1.017	0.018	1.045	0.075
)	1.011	0.017	1.092	0.08
Pb <sup>207</sup>	0.988	0.018	0.931	0.074
Pb <sup>206</sup> *	0.992	0.017	0.994	0.063
)	1.024	0.018	0.996	0.06
Tl	1.008	0.020	0.985	0.085
Hg	0.935	0.023	0.965	0.096
Au	0.944	0.025	1.005	0.090
W	0.944	0.018	1.141	0.064
Ta	1.022	0.024	1.075	0.092
Er	0.974	0.017	0.955	0.052
Ho	0.930	0.020	0.924	0.074
Sm	0.930	0.020	0.965	0.08
Pr	1.01	0.031	1.05	0.115
La	0.928	0.020	0.992	0.089
W	1.273	0.018	1.397	0.054
I	1.312	0.024	1.524	0.105
Sn	1.301	0.023	1.259	0.083
In	1.272	0.026	1.47	0.096

\* Two different measurements were made.

E of Chapter III) for neutron energies near the threshold  $E_0$  (0.9 MeV). However if the threshold shifts to  $E'_0$ ,  $R_1$  should be corrected by  $(E_n - E_0)/(E_n - E'_0)$ . First  $R'_1$  is assumed to be unity for the low energy bin, then the value of  $E'_0$  necessary to correct  $R_1$  to  $R'_1 = 1.0$  is calculated, and finally the above correction is applied to the  $24^\circ$  spectrum. The results are tabulated in Table XI, along with the values of  $E'_0$  for each target. The corrected value of  $R_1$  is listed for each target for the high energy bin. After the correction,  $R_1$  falls between 0.93 and 1.15 in the high energy bin with statistical errors of 0.08. It required at most a 6 per cent change in  $E_0$  to normalize the low energy bin to unity

(2) Background normalization. The magnitude of the background is known to about 10 per cent, which represents a sizable uncertainty in the data in the high energy bin. In addition, the background shape at  $24^\circ$  did not appear to be as constant as in the other two counters. The background was resubtracted to make  $R_1 = 1.0$  in the low energy bin. The results and the per cent change,  $\Delta B/B$ , in the background are listed in Table XI.  $R_1$  falls between 0.95 and 1.28 with statistical errors of 0.08. A change in the background of up to 28 per cent was required to normalize the low energy bin. A few cases required an unrealistic amount of background (ie, background was added, rather than subtracted).

(3) Counting losses due to simultaneous counts in two counters. From equation 33 it is apparent that the counting losses for the counter at angle  $\theta_i$  are equal to  $N_c - \frac{\tau}{T} N_j N_k$ . Since  $N_c$  is measured, errors introduced by the coincidence calculation will be primarily due to the term  $\frac{\tau}{T} N_j N_k$ . That is, the per cent error will be proportional to  $\Delta(\tau/T)(N_j N_k/N_i)$ . (Errors due to  $\Delta N_j$  and  $\Delta N_k$  will be smaller by the factor  $(\tau/T)$ .) Since the counting rate in the  $24^\circ$  counter was one-third that of the other two counters, its error can be as much as 10 times as great.\* Since the result of the coincidence correction is to multiply the entire spectrum by a constant, both energy bins will be equally affected. Therefore the low energy bin was normalized to unity and the high energy bin was corrected by the factor required to do this. The results are listed in Table XI along with C, the coincidence correction calculation from equation 33 and  $\Delta C/C$ , the per cent change in C required to normalize the low energy bin.  $R_1$  falls between 0.97 and 1.21 with an average statistical error of 0.08 in the high energy bin. The largest variation in C was 7 per cent.

Four sets of data have been excluded from the above discussion. These are I, Sn, In and a second W run. These runs were made at a time during which

$$\frac{\Delta_3}{\Delta_1} = \frac{\Delta \left( \frac{\tau}{T} \right) \frac{N_1 N_2}{N_3}}{\Delta \left( \frac{\tau}{T} \right) \frac{N_3 N_2}{N_1}} \approx \frac{N_1^2}{N_2^2} \approx 10, \text{ where } \Delta_3 \text{ and } \Delta_1 \text{ are the errors of the correction}$$

for counting losses in counters at  $24^\circ$  and  $156^\circ$  respectively, and  $N_1, N_2,$  and  $N_3$  are the total number of counts in the counters at  $156^\circ, 76^\circ$  and  $24^\circ$  respectively.

Table XI  
 Corrected Ratio of Photoneutron Spectrum at 24<sup>o</sup>  
 to Spectrum at 156<sup>o</sup>  
 (Summed from 3.0 MeV to E<sub>n max</sub>)

Element	$R'_1 = R \left( \frac{E_n - E_o}{E_n - E'_o} \right)$		R <sub>1</sub> After Background Renormalization		$R'_1 = \frac{R_1(3.0 - E_{n \max})}{R_1(1.4 - 3.0)}$		
	R' <sub>1</sub>	E' <sub>o</sub>	R' <sub>1</sub>	$\frac{\Delta B}{B}$	R' <sub>1</sub>	C	$\frac{\Delta C}{C}$
Bi	1.058	0.861	0.97	0.17	1.022	1.39	0.05
Pb <sup>208</sup>	1.090	0.890	1.07	0.09	1.080	1.40	0.01
"	1.042	0.885	1.01	0.06	1.028	1.40	0.02
Pb <sup>207</sup>	0.933	0.911	0.96	0.05	0.942	1.36	0.06
Pb <sup>206</sup>	0.996	0.907	1.01	0.02	1.002	1.46	0.01
"	0.990	0.879	0.95	0.12	0.973	1.45	0.02
Tl	0.983	0.893	0.97	0.03	0.977	1.40	0.01
Hg	0.978	0.951	1.11	0.21	1.032	1.27	0.06
Au	1.017	0.944	1.12	0.15	1.065	1.38	0.06
W	1.154	0.944	1.28	0.28	1.209	1.50	0.06
Ta	1.069	0.880	1.02	0.11	1.052	1.45	0.02
Er	0.960	0.918	1.02	0.10	0.984	0.03	1.53
Ho	0.938	0.956	1.08	0.18	0.994	1.56	0.07
Sm	0.978	0.956	1.14	0.22	1.038	1.53	0.07
Pr	1.047	0.891	1.02	0.02	1.040	1.36	0.01
La	1.009	0.958	1.17	0.16	1.069	1.34	0.07
W					1.097	1.65	0.27
I					1.162	1.27	0.31
Sn					0.968	1.14	0.30
In					1.156	1.17	0.27



the circuitry was later found to be defective. The pulse-routing circuitry misrouted coincidence pulses to the analyzer. As a result, the data was improperly corrected for counting losses ( $N_c$  was not known). Therefore these runs have been included only in the third case.

In conclusion,  $R_1$  differs from 1.0 by more than the statistical errors (about 0.02) in the low energy bin for many of the targets. However the low energy bin can be corrected to unity by small changes in the threshold (about 6 per cent), the coincidence correction (7 per cent), and larger changes in the background (20 per cent). Varying the threshold results in very little change in  $R_1$  in the high energy bin, varying the background has a sizable effect on  $R_1$  in the high energy bin, and changing the coincidence correction affects both bins equally. In general in the high energy bin,  $R_1 = 1.0 \pm 0.08$ , after the low energy bin has been corrected to unity.

Since the ratio  $R_1 = \frac{dN(24^0)}{dE_n} / \frac{dN(156^0)}{dE_n}$  is so sensitive to small changes in the threshold, background magnitude, and the coincidence correction calculation, it appears that the systematic errors in this data are larger than the statistical errors, especially in the low energy bin. Therefore  $R_1$  is assumed to be 1.0 at all energies for all the elements used, and this value is not inconsistent with the experimental measurements. The theoretical reasons for choosing this value of  $R_1$  are outlined in Chapter I, section D.

Using this assumption,  $a_1 = 0.0$ ,

$$-\frac{a_2}{a_0} = \frac{2(1 - R_2)}{(3\cos^2\Theta_3 - 1) - R_2(3\cos^2\Theta_2 - 1)} \quad \text{and } W(\Theta) = a_0 + a_2 P_2(\Theta) \quad (44)$$

The angular distributions are presented in this thesis in this form. They are plotted as  $-a_2/a_0$  vs  $E_n$  for each of the 17 targets used in this experiment. These graphs are in Chapter V. The error bars on the data points include an estimate of the systematic errors discussed below. Systematic errors due to background magnitude, changes in thresholds, and coincidence corrections are negligible for the  $156^0$  and  $76^0$  counters. The neutron scattering in the target,  $S(\Theta_1, E_n)$ , increases the ratio  $R_2$  by an appreciable amount (up to 8 per

cent). As is explained in Appendix I,  $S(\Theta_1, E_n)$  is estimated to about 20 per cent. The other two systematic changes in the ratio  $R_2$  -- the geometry correction,  $f$ , and the correction for differences in detector response -- are known with better accuracy. The geometry correction decreases  $R_2$  by 0 to 9 per cent  $\pm$  1 per cent, depending on the target shape. The detector response difference is an increase of about 5 per cent  $\pm$  1 per cent. The net result is a shift in  $R_2$  of up to 10 per cent  $\pm$  3 per cent depending on the target shape. Therefore the systematic uncertainties in  $R_2$  may be larger than the statistical errors at low neutron energies.

One more quantity will be needed:  $\frac{dN}{dE_n}$ , the integral of  $\frac{d^2N(\Theta)}{dE_n d\Omega}$  over the angle  $\Theta$ .

$$\frac{d^2N(\Theta)}{dE_n d\Omega} = \frac{dN}{dE_n} \sum_{n=0} a_n P_n(\cos \Theta) \quad (45)$$

Since the giant resonance is a dipole interaction, this sum is approximately given by

$$\frac{d^2N(\Theta_1)}{dE_n d\Omega} = \frac{dN}{dE_n} [1 + a_2 P_2(\cos \Theta_1)] \quad (46)$$

Solving for  $\frac{dN}{dE_n}$  one finds

$$\frac{dN}{dE_n} = \frac{1}{1 - P_2(\cos \Theta_1)} \left[ \frac{dN(\Theta_1)}{dE_n d\Omega} - \frac{P_2(\cos \Theta_1) d^2N(\Theta_2)}{P_2(\cos \Theta_2) dE_n d\Omega} \right] \quad (47)$$

where  $\Theta_1$  and  $\Theta_2$  could be any two angles;  $\Theta_1 = 156^\circ$  and  $\Theta_2 = 76^\circ$  have been used. Then

$$\frac{dN}{dE_n} = 0.63 \frac{d^2N(156^\circ)}{dE_n d\Omega} + 0.637 \frac{d^2N(76^\circ)}{dE_n d\Omega} \quad (48)$$

$156^\circ$  and  $76^\circ$  were used because the data at these angles is the most reliable. Also, since these counters are approximately  $90^\circ$  apart, these data are the most sensitive to  $P_2(\cos \Theta)$ .

### C. Difference Spectrum

In the interpretation of a photoneutron spectrum produced by a bremsstrahlung spectrum, serious ambiguities are introduced by the question of which photon was involved for a particular neutron. To alleviate this problem,

two sets of experiments have been performed at different maximum bremsstrahlung energies, 15 MeV and 14 MeV (three sets in the case of the elements near lead, with maximum energies of 15 MeV, 14 MeV, and 13 MeV). A neutron energy spectrum from somewhat monoenergetic photons can be obtained by means of a properly normalized subtraction. If  $\sigma(E_\gamma)$  is defined as the photon absorption cross section,  $\rho(E_\gamma)$  as the bremsstrahlung spectrum caused by electrons of energy  $E$ , and  $dN(E_n, E_\gamma)/dE_n$  as the neutron spectrum integrated over angles for a photon of energy  $E_\gamma$ , then the neutron spectrum caused by the bremsstrahlung spectrum of maximum energy  $E_1$  is given by the expression

$$\frac{dN(E_n, E_1)}{dE_n} = \int_0^{E_1} \frac{dN(E_n, E_\gamma)}{dE_n} \sigma(E_\gamma) \rho_{E_1}(E_\gamma) dE_\gamma \quad (49)$$

The difference of two such neutron spectra caused by the bremsstrahlung spectra  $\rho_{E_1}(E_\gamma)$  and  $\rho_{E_2}(E_\gamma)$  is given by

$$\frac{dN(E_n, \tilde{E}_\gamma)}{dE_n} = \int_0^{E_1} \frac{dN(E_n, E_\gamma)}{dE_n} \sigma(E_\gamma) [\rho_{E_1}(E_\gamma) - K\rho_{E_2}(E_\gamma)] dE_\gamma \quad (50)$$

where  $\tilde{E}_\gamma$  is the average energy of photon absorption due to the photon difference spectrum and  $K$  is an arbitrary normalization constant.  $K$  is adjusted so that  $\rho_{E_1}(E_\gamma) - K\rho_{E_2}(E_\gamma) = 0$  at the desired energy. Let

$$\rho_\Delta(E_\gamma) = \rho_{E_1}(E_\gamma) - K\rho_{E_2}(E_\gamma) \quad (51)$$

where  $\Delta$  represents the energy interval  $E_1 - E_2$ .

Figure 10 shows  $\rho_{E_1}(E_\gamma)$  and  $\rho_{E_2}(E_\gamma)$  where  $E_1 = 15.4$  MeV and  $E_2 = 14.4$  MeV. The dashed curve is the difference of the two photon spectra where  $K$  has been adjusted so that  $\rho_\Delta = 0$  at 11 MeV. At lower energies  $\rho_\Delta$  is negative, but since  $\sigma(E_\gamma)$  goes to zero below 10 MeV, this does not seriously affect the results. The photon spectrum was determined by measuring the photoneutron spectrum from deuterium at each electron energy used.

$$\rho(E_\gamma) \approx \frac{dN_{D_2}}{dE_n} \frac{1}{\sigma_D(E_\gamma) g(E_n) \eta(E_n)} \quad (52)$$

where  $\sigma_D(E_\gamma)$ , the deuterium photodisintegration cross section, is taken from

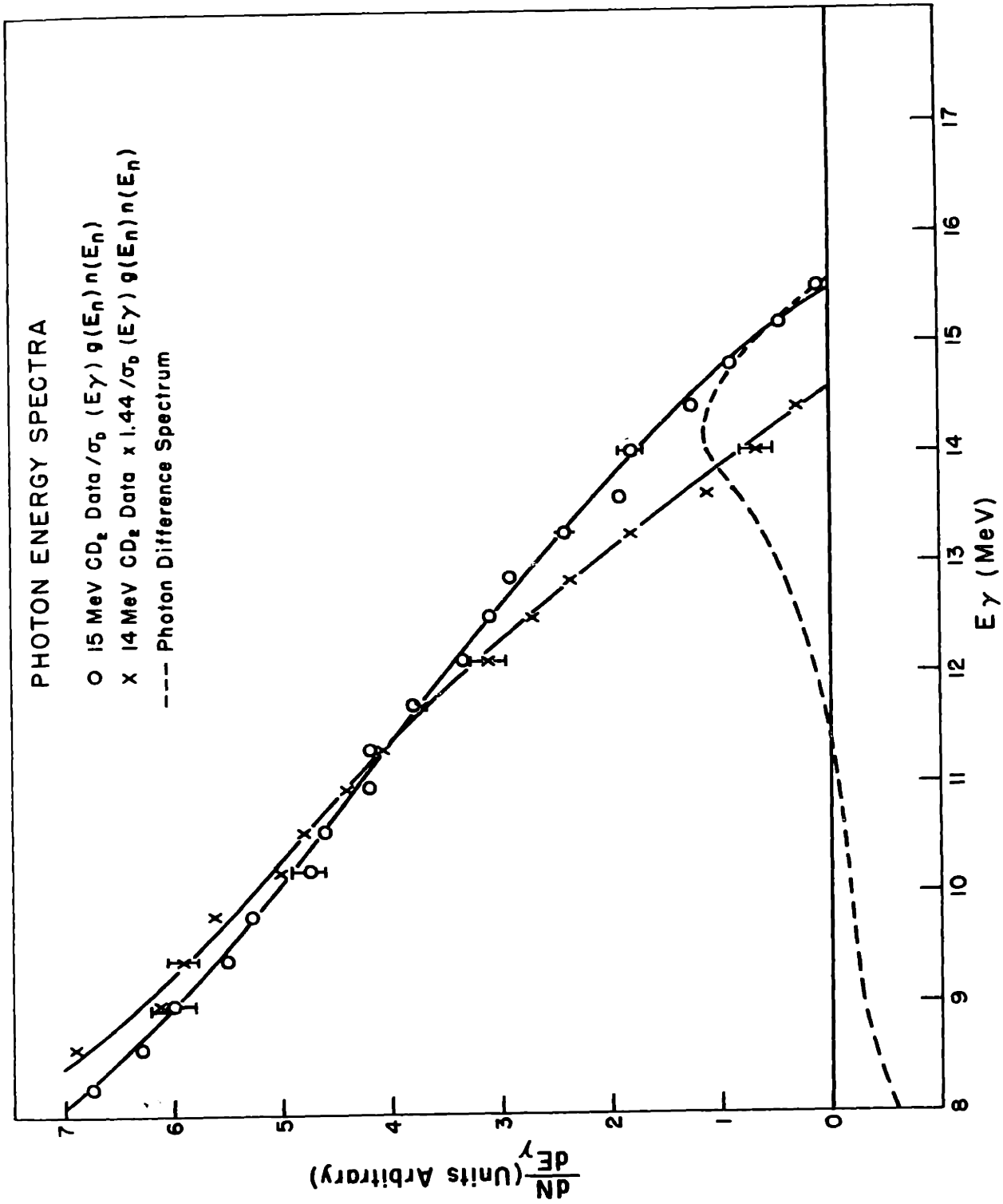


Fig. 10

calculations by Partovi (51), and  $g(E_n)\eta(E_n)$ , the detector response, was given in Chapter III, Table VII.

Figure 11 shows a plot of  $\sigma(E_\gamma)\rho_\Delta(E_\gamma)$  for a few representative cases. These absorption curves are all localized at  $\tilde{E}_\gamma \approx 14.0$  MeV with about 2 MeV FWHM and  $\tilde{E}_\gamma \approx 14.4$  MeV in the deformed region and near praseodymium. The absorption curves for the 14 to 13 MeV difference spectrum are localized at  $\tilde{E}_\gamma \approx 13.2$  MeV with about 2 MeV FWHM. The values of  $\sigma(E_\gamma)$  were obtained from refs 5, 6, 7, and 57. Thus the photon difference spectrum corresponds to a photon beam with about a 10 per cent energy spread, which is a great improvement over a bremsstrahlung spectrum, despite the larger statistical errors introduced by the subtraction.

When the two deuterium runs in Fig. 10 had been normalized to the same integrated charge (as measured by the current collected on the carbon beam stopper) and  $\rho_\Delta$  set equal to zero at 11 MeV, K was found to be 1.44. In the case of the 14.4 to 13 MeV difference spectrum, K equals 1.33 when  $\rho_\Delta$  was set equal to zero at 10 MeV. Therefore the neutron spectrum resulting from the photon difference spectrum is given by

$$\frac{dN(E_n, \tilde{E}_\gamma)}{dE_n} = \frac{dN(E_n, E_{15})}{dE_n} - K \frac{dN(E_n, E_{14})}{dE_n} \quad (53)$$

for a 15 and 14 MeV set of data, for example. In the above equation  $\frac{dN(E_n, E_{15})}{dE_n}$  and  $\frac{dN(E_n, E_{14})}{dE_n}$  have been normalized to the same integrated current, and  $K = 1.44$ .

It was noticed that neutron spectra from deuterium runs made at the same energy but on different days did not agree in magnitude to within statistics. The integral number of photoneutrons, normalized to a unit charge, varied from the average value by 6 per cent (rms) with a maximum deviation of 12 per cent. This is far outside the statistical fluctuation since a typical run contained about 20,000 counts (0.7 per cent). This fluctuation was apparently caused by small changes in the current measuring device (see section C of Chapter II) such as fluctuations in the electrometer gain, and variations of the leakage current. Since the fluctuations in the charge meter reading seemed

Photon Difference Spectra Multiplied by the  
Photon Absorption Cross Section.

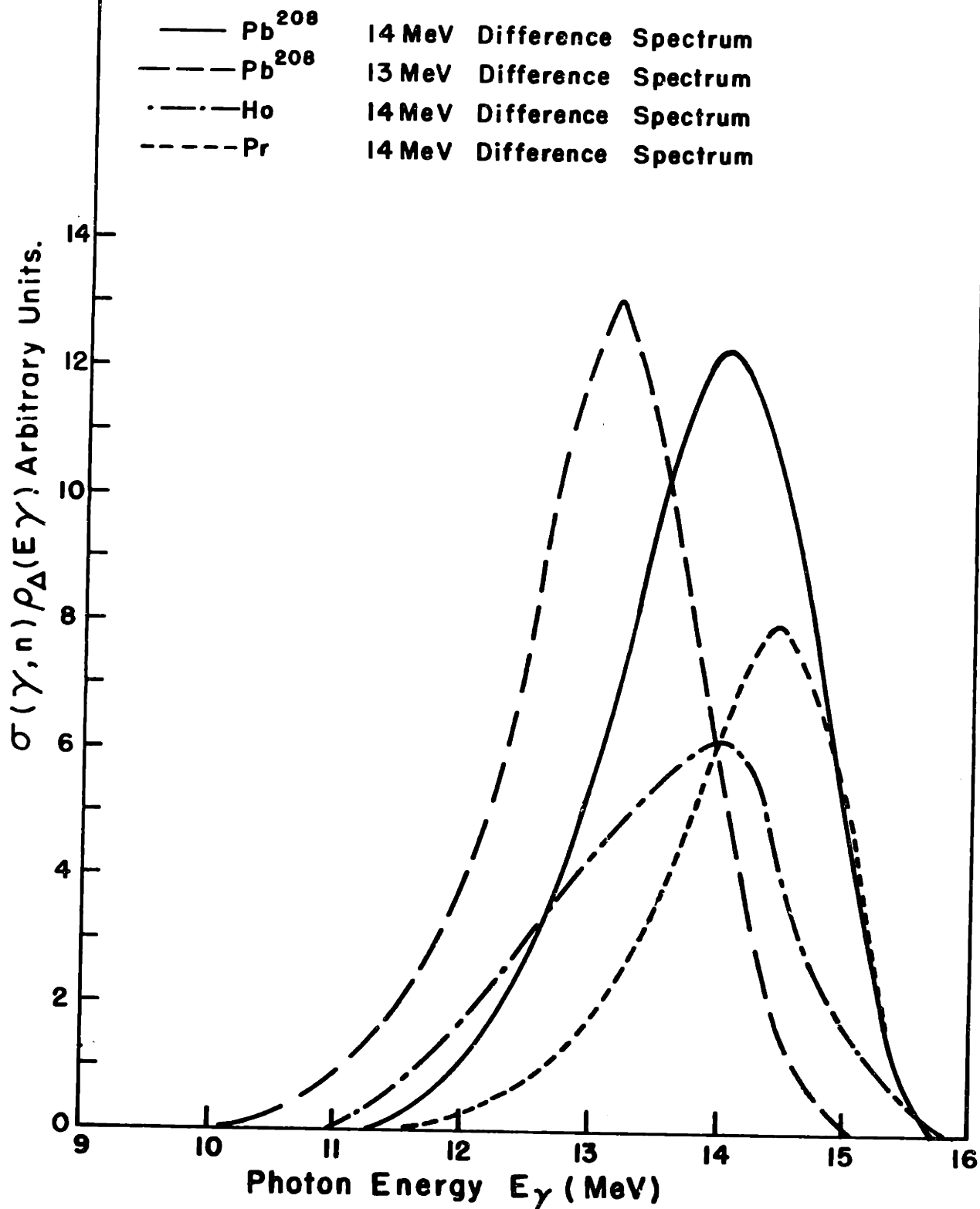


Fig. 11

to vary slowly, an attempt was made to normalize any given experimental run to an accuracy better than the 6 per cent normally found. First, all of the deuterium data for a given bremsstrahlung endpoint was averaged. Then the two deuterium runs closest in time, Before and after, to an experimental run with a particular target were selected. Their per cent deviation from the average value for all deuterium runs of the corresponding energy was calculated, and extrapolated linearly to the time that the run under discussion was made. In this manner a correction to the charge reading could be determined. As an example, two  $\text{Pb}^{208}$  runs made on different days differed in magnitude by 10 per cent using the uncorrected charge readings. After correction they differed by less than 1 per cent. However not all runs are immediately adjacent (within 2 to 4 hours) to deuterium runs (as the two runs in the example were). A series of short deuterium runs made over a period of 6 hours indicated that the normalization can shift appreciably in this short time. Therefore there will be an error in the normalization, which however should be less than 6 per cent.

After making these corrections, the neutron difference spectra,  $\frac{dN(E_n, \tilde{E}_\gamma)}{dE_n}$  were calculated for the 17 targets used, with  $\tilde{E}_\gamma = 14.0$  MeV, and with  $\tilde{E}_\gamma = 13.2$  MeV for the elements near lead. In addition the difference spectra were computed at each angle separately. From this data it is possible to calculate the angular distribution of the difference spectrum.

Figures 12a and 12b show a plot of  $\frac{dN(E_n, \tilde{E}_\gamma)}{dE_n}$  vs  $E_n$  for all of the elements with  $\tilde{E}_\gamma = 14.0$  MeV. Two neutron spectra (either 15 and 14 MeV or 14 and 13 MeV) and the difference spectrum are plotted individually in Chapter V. These are plots of  $\log \frac{dN}{dE_n} \cdot \frac{1}{E_n}$  vs  $E_n$ .

#### D. Level Density and Direct Component

##### a) Separation into Components

As outlined in the first chapter, the statistical model of the nucleus predicts that the neutron spectrum from a compound nucleus is given by

$$\frac{dN}{dE_n} = C E_n \sigma_C \omega(U) \quad (54)$$

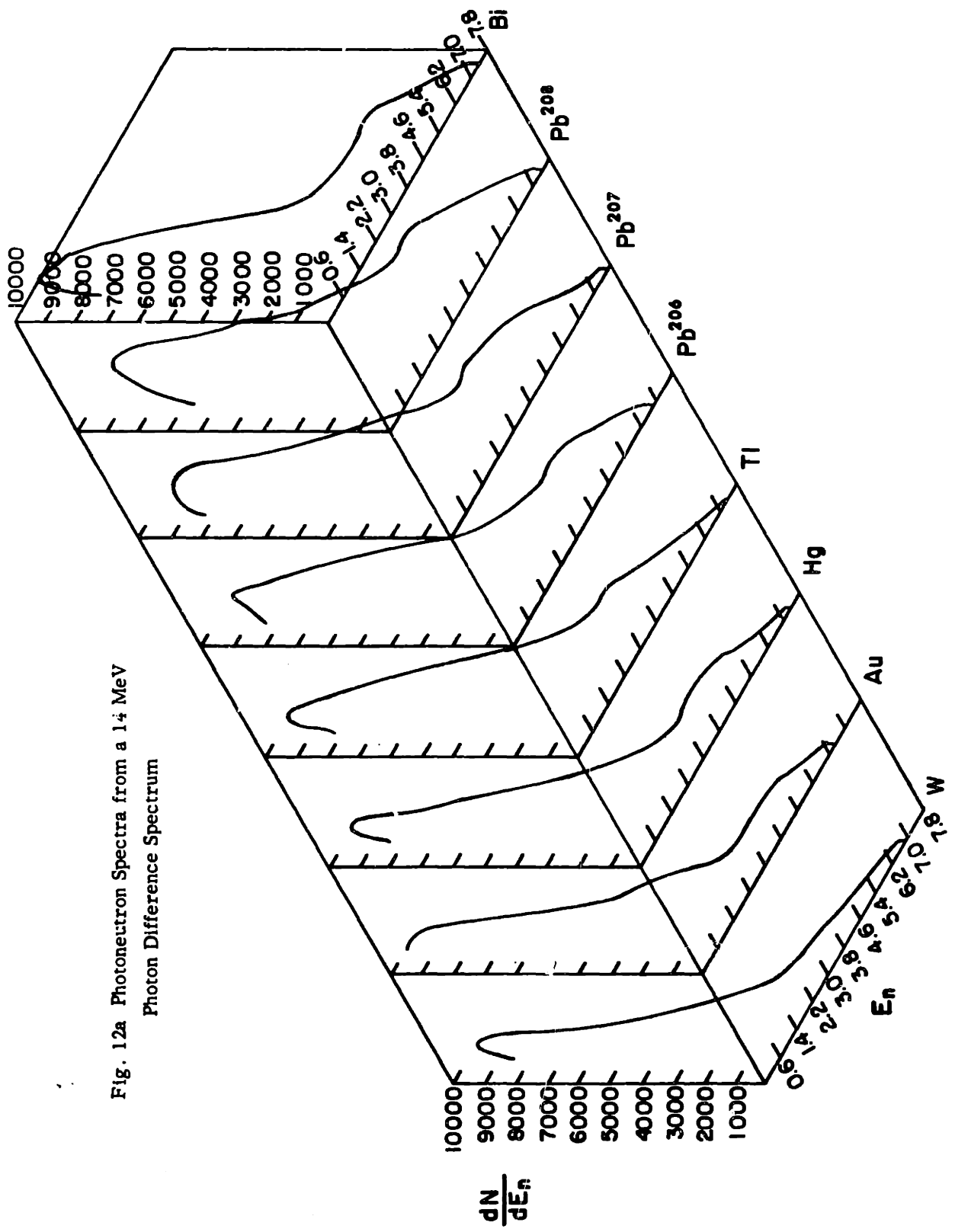


Fig. 12a Photon Neutron Spectra from a 14 MeV  
Photon Difference Spectrum



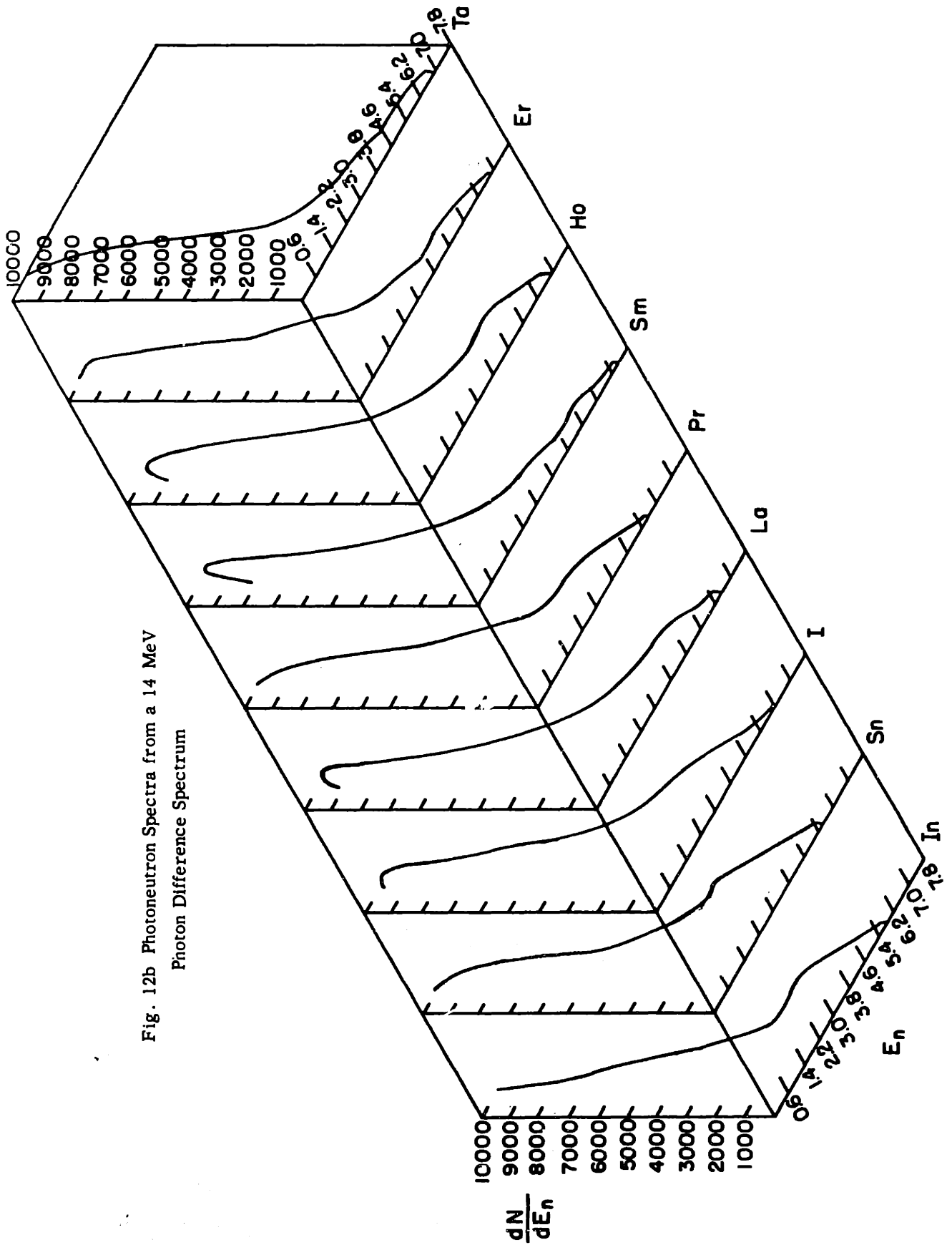


Fig. 12b Photon Neutron Spectra from a 14 MeV  
Photon Difference Spectrum

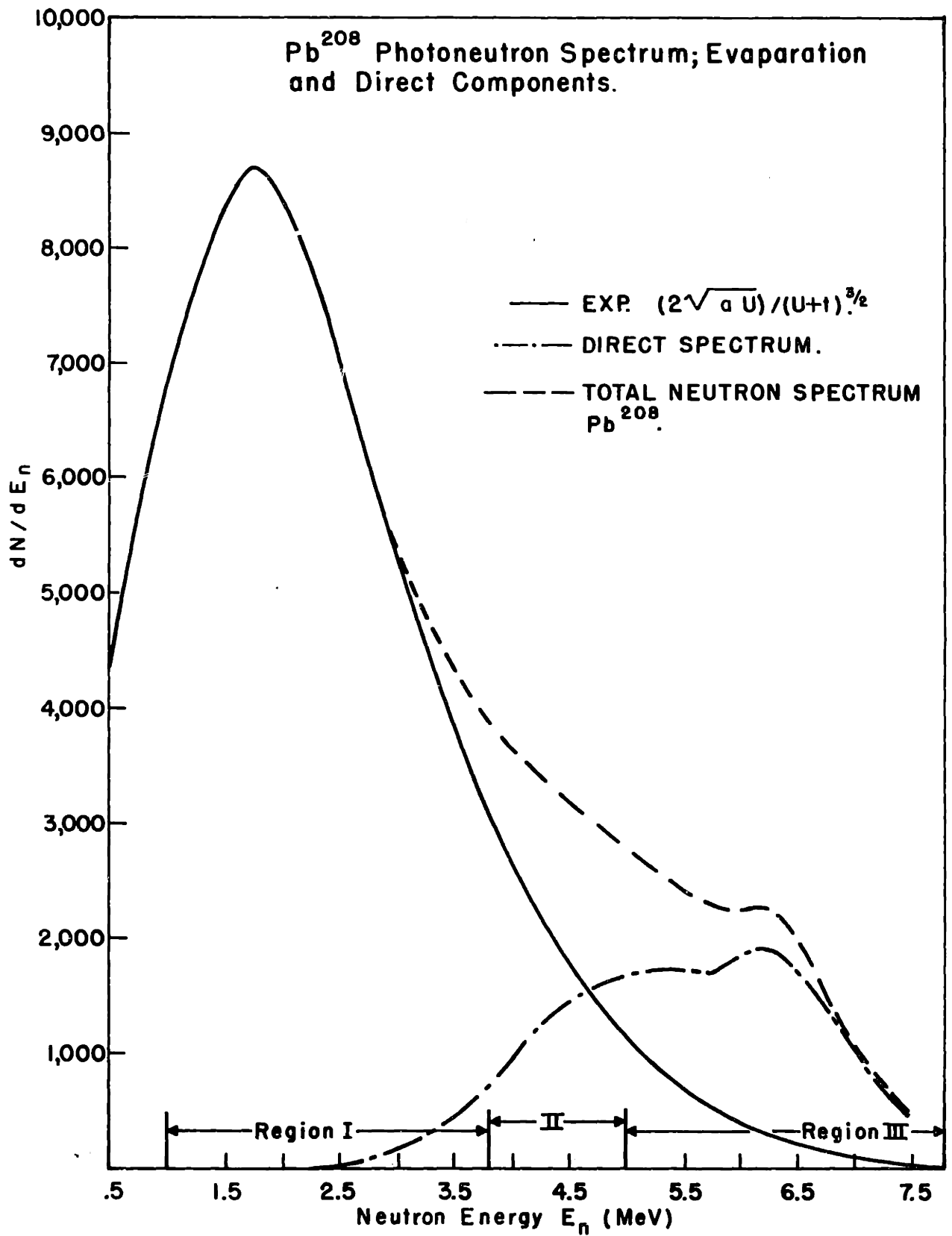


Fig. 12 c

where  $C =$  a constant

$\sigma_C =$  the inverse capture cross section

$\omega(U) =$  the density of levels in the residual nucleus at an excitation energy  $U$ , for

$$U = \tilde{E}_\gamma - E_{th} - \delta_p \quad (55)$$

where  $E_{th} =$  the neutron binding energy

$\delta_p =$  the pairing energy

and  $\tilde{E}_\gamma$  has been defined in the previous section. The pairing energy,  $\delta_p$ , is the energy required to break the last neutron and/or proton pair. This energy is subtracted from the residual nucleus excitation energy to account for the pairing effect seen in nuclear level densities (58). The values of  $\delta_p$  calculated by Nemirovsky and Adamchuk (59) were used.

The level density has been estimated by Lang and le Couteur (60), using the Fermi gas model, as

$$\omega(U) = \frac{e^{2\sqrt{aU}}}{(U+t)^m} \quad (56)$$

where  $a$  is the Fermi gas level density parameter,  $U = at^2 - t$ , and  $m$  depends on the assumptions used (60). In this thesis the data has been analyzed using both  $m = \frac{3}{2}$  and  $m = 2$ .

In equation 54 above,  $\sigma_C(E_n)$  represents the cross section for the formation of the compound nucleus from a neutron of energy  $E_n$  incident on the residual nucleus with an excitation energy of  $E^*$ . Such cross sections are not generally known, so they have been approximated by using the ground state cross sections calculated from the optical model. The values of  $\sigma_C$  calculated in refs 61 and 62 have been used. The values of  $\sigma_C$  for  $E_n = 0.6$  to 7.0 MeV for several representative elements are given in Table XII.

The neutron difference spectrum shown in Figs. 12a and 12b clearly cannot be fit with equation 54 over all neutron energies. At approximately 3 to 4 MeV these spectra exhibit a sharp break in slope, and show a larger number of high energy neutrons than equation 54 would predict. Furthermore, statistically evaporated neutrons are expected to be isotropic, while the angular distribution curves plotted in Figs. 105a and 105b (Chapter V) show that the

Table XII

Optical Model Capture Cross Sections for Representative  
Elements as a Function of Neutron Energy

$E_n$	116	127	140	152	165	168	170	181
0.6	1.92	2.17	3.39	3.52	2.96	2.74	2.64	2.29
1.0	1.87	2.42	3.34	3.18	2.65	2.47	2.40	2.21
1.4	1.92	2.52	2.96	2.74	2.34	2.25	2.21	2.22
1.8	1.98	2.46	2.62	2.41	2.19	2.16	2.16	2.35
2.2	2.02	2.36	2.37	2.23	2.14	2.16	2.19	2.49
2.6	2.06	2.26	2.22	2.15	2.15	2.21	2.25	2.55
3.0	2.10	2.17	2.14	2.12	2.18	2.26	2.31	2.53
3.4	2.10	2.09	2.10	2.10	2.24	2.30	2.34	2.47
3.8	2.06	2.03	2.08	2.11	2.28	2.31	2.33	2.39
4.2	2.00	2.00	2.06	2.13	2.28	2.30	2.30	2.32
4.6	1.94	1.97	2.05	2.17	2.26	2.26	2.26	2.27
5.0	1.89	1.95	2.05	2.20	2.22	2.21	2.20	2.23
5.4	1.85	1.93	2.07	2.20	2.16	2.16	2.16	2.22
5.8	1.81	1.92	2.09	2.17	2.12	2.12	2.13	2.22
6.2	1.78	1.91	2.10	2.11	2.09	2.10	2.11	2.22
6.6	1.76	1.92	2.09	2.06	2.06	2.09	2.10	2.23
7.0	1.75	1.93	2.05	2.00	2.05	2.08	2.10	2.25
$E_n$	184	197	200	204	206		208	209
0.6	2.25	2.62	2.81	3.11	3.27		1.75	1.39
1.0	2.23	2.71	2.90	3.15	3.27		1.94	1.55
1.4	2.32	2.99	3.16	3.31	3.36		2.27	1.92
1.8	2.52	3.11	3.18	3.23	3.23		2.53	2.33
2.2	2.65	3.01	3.02	3.03	3.03		2.59	2.45
2.6	2.66	2.83	2.83	2.83	2.82		2.52	2.36
3.0	2.59	2.66	2.66	2.65	2.65		2.41	2.23
3.4	2.49	2.53	2.53	2.53	2.52		2.31	2.13
3.8	2.40	2.43	2.44	2.45	2.45		2.21	2.07
4.2	2.33	2.38	2.39	2.41	2.41		2.11	1.99
4.6	2.28	2.36	2.37	2.39	2.40		2.03	1.89
5.0	2.25	2.35	2.37	2.39	2.40		1.97	1.78
5.4	2.25	2.35	2.37	2.40	2.42		1.94	1.70
5.8	2.25	2.37	2.39	2.43	2.44		1.95	1.67
6.2	2.25	2.39	2.42	2.44	2.45		1.98	1.70
6.6	2.27	2.41	2.43	2.44	2.43		2.00	1.76
7.0	2.29	2.41	2.41	2.40	2.39		2.00	1.82

The values for elements with  $A = 106$  to  $206$  are taken from ref 61. \*

The values for  $Pb^{208}$  and  $Bi^{209}$  were taken from ref 62.

\*Ref 61 only tabulates  $\sigma_C$  from 0.2 to 3.0 MeV. We would like to thank Dr. E. Auerbach for extending these calculations to 7.0 MeV.

neutrons are approximately isotropic at low neutron energies, then increase rapidly to a large anisotropy at high neutron energies. The midpoint of the anisotropy curve and the abrupt change in slope of the difference spectrum roughly correspond for each element.

Therefore, since the difference spectrum seems to be dominated by isotropic evaporation neutrons at low energies, and at high energies by an excess of neutrons (compared to the evaporation spectrum) with a strong angular distribution, the neutron spectrum has been separated into two components: a statistical component and a resonant direct component.\* Two different procedures have been used to effect this separation.

### (1) Method I

In the first method, at low energies (region I, Fig. 12c), the data is fitted with the formula

$$\frac{dN}{dE_n} \frac{1}{E_n \sigma_C} = \frac{C e^{2\sqrt{a_m U}}}{(U+t)^m} \quad (57)$$

using a least squares fit, with  $a_m$  as an adjustable parameter, and  $C$  as the normalization constant. The total number of "evaporation" neutrons at higher neutron energies (region III, Fig. 12c) can then be calculated from equation 57. These evaporation neutrons are subtracted from the experimental data in region III to give the total number of resonant direct neutrons in this region. If an energy spectrum,  $S(E_n)$ , is known for the direct neutrons, one can calculate the number of direct neutrons in region I. These are then subtracted from the data,

$$\frac{dN'}{dE_n} = \frac{dN}{dE_n} - k S(E_n) \quad (58)$$

to give a better approximation to an evaporation spectrum.

The data,  $\frac{dN'}{dE_n}$ , is again fitted with equation 57 and a second approximation to  $a_m$ , called  $a'_m$ , is found. The above procedure is iterated until  $a_m$  converges. The constant  $k$  is found by normalizing the integral of  $S(E_n)$  over region III, to the integral of  $\frac{dN}{dE_n}$  over the same region. The direct spectrum,

\*The term "resonant direct" is used here with the same meaning as used by Wilkinson (30).

$S(E_n)$ , is discussed in the next section. The curves in Fig. 12c are for  $Pb^{208}$ , and show the results when  $a_m$  has converged.

## (2) Method II.

In the second method of separating the neutron spectrum into two components, the angular distribution of the direct component is assumed to be a constant determined by the high energy region (III in Fig. 12c), and the statistical component is assumed to be isotropic. The angular distribution in the high energy region is found by summing the difference data in each counter over region III. The ratio of this sum for the  $156^0$  data to the  $76^0$  data is called  $r_2$ . This ratio for the low energy portion of the curve (region I) is found in a similar manner and is designated  $r_1$ , ( $r_1 \approx 1.0$ ).

Then, if  $x$  is the ratio at energy  $E_n$ ,

$$\frac{dN'}{dE_n} = \frac{dN}{dE_n} \left[ 1 - \frac{(0.363 r_1 + 0.637)[x(E_n) - r_2]}{[0.363 x(E_n) + 0.637](r_1 - r_2)} \right] \quad (59)$$

$\frac{dN'}{dE_n}$  is substituted for  $\frac{dN}{dE_n}$  in equation 57 and  $a_m$  is determined as before. Given  $a_m$ , the number of evaporation neutrons in region III is calculated and subtracted from  $\frac{dN'}{dE_n}$ . This changes the value of  $r_2$ , and hence  $\frac{dN'}{dE_n}$ . This procedure is iterated until  $r_2$  converges.

### b) Least Squares Fit

In this section the least squares fit will be explained in more detail. Equation 54 assumes that the compound nucleus has an excitation energy  $\bar{E}_\gamma$ . Actually the photon difference spectrum has a FWHM of about 2 MeV. Taking this width into account

$$\frac{dN}{dE_n} = C E_n \sigma_C(E_n) \frac{\int \omega(E_n, E_\gamma) \rho_\Delta(E_\gamma) dE_\gamma}{\int \rho_\Delta(E_\gamma) dE_\gamma} \quad (60)$$

where  $\rho_\Delta(E_\gamma)$  is the photon difference spectrum. To facilitate computer analysis, the integral is approximated by the sum

$$\frac{dN}{dE_n} = C E_n \sigma_C(E_n) \frac{\sum_{i=-4}^4 \omega(E_n, E_{\gamma i}) \rho_\Delta(E_{\gamma i})}{\sum_{i=-4}^4 \rho_\Delta(E_{\gamma i})} \quad (61)$$

where  $E_{\gamma i} = \tilde{E}_{\gamma} + i\Delta$ ,  $\Delta = 0.4$  MeV, the bin width. Nine bins were found to include more than 90 per cent of  $\rho_{\Delta}(E_{\gamma})$ . Substituting equation 56 for  $\omega(E_n, \tilde{E}_{\gamma})$ ,

$$\frac{dN}{dE_n} = CE_n \sigma_C(E_n) \sum_{i=-4}^4 \bar{\rho}_{\Delta}(\tilde{E}_{\gamma} + i\Delta) \frac{e^{2\sqrt{a_m U}}}{(U+t)^m} \quad (62)$$

where  $U = \tilde{E}_{\gamma} + i\Delta - E_n - E_{th} - \delta_p$ ,  $t = \frac{1}{2a_m} + \frac{1}{2a_m} \sqrt{1+4a_m U}$ , and

$$\bar{\rho}_{\Delta}(U) = \frac{\rho_{\Delta}(U)}{\int \rho_{\Delta}(U) dU}. \text{ Let } U_0 = \tilde{E}_{\gamma} - E_n - E_{th} - \delta_p, \text{ then } U = U_0 + i\Delta, \text{ and}$$

$$\frac{dN}{dE_n} = CE_n \sigma_C(E_n) \left[ \sum_{i=-4}^4 \bar{\rho}_{\Delta}(\tilde{E}_{\gamma} + i\Delta) \frac{e^{2(\sqrt{a_m U} - \sqrt{a_m U_0})}}{(U + \frac{1}{2a_m} + \frac{1}{2a_m} \sqrt{1+4a_m U})^m} \right] e^{2\sqrt{a_m U_0}} \quad (6)$$

$$\frac{dN}{dE_n} \frac{1}{E_n \sigma_C(E_n)} \left[ \sum_{i=-4}^4 \bar{\rho}_{\Delta}(\tilde{E}_{\gamma} + i\Delta) \frac{e^{2(\sqrt{a_m U} - \sqrt{a_m U_0})}}{(U + \frac{1}{2a_m} + \frac{1}{2a_m} \sqrt{1+4a_m U})^m} \right]^{-1} = Ce^{2\sqrt{a_m U_0}} \quad (6)$$

$$\log \left[ \frac{dN}{dE_n} \frac{1}{E_n \sigma_C(E_n)} \left[ \sum_{i=-4}^4 \bar{\rho}_{\Delta}(\tilde{E}_{\gamma} + i\Delta) \frac{e^{2(\sqrt{a_m U} - \sqrt{a_m U_0})}}{(U + \frac{1}{2a_m} + \frac{1}{2a_m} \sqrt{1+4a_m U})^m} \right]^{-1} \right] = 2\sqrt{a_m U_0} + \log C \quad (6)$$

The equation has now been reduced to the point where a least square fit can be performed. That is, the data is divided by  $E_n \sigma_C$  and the factor in brackets above, and the log is taken. This constitutes the input data to the equation

$$y_j = s x_j + c \quad (66)$$

$$\text{where } y_j = \log \left[ \frac{dN}{dE_n} \frac{1}{E_{nj} \sigma_C(E_{nj})} \left[ \sum_{i=-4}^4 \bar{\rho}_{\Delta}(\tilde{E}_{\gamma} + i\Delta) \frac{e^{2(\sqrt{a_m U} - \sqrt{a_m U_0})}}{(U + \frac{1}{2a_m} + \frac{1}{2a_m} \sqrt{1+4a_m U})^m} \right]^{-1} \right]$$

$$s = 2\sqrt{a_m}$$

$$x_j = \sqrt{E_{\gamma} - E_{nj}}$$

$$c = \text{scale factor} = \log C$$

$$j = \text{index labeling the values of } \frac{dN}{dE_n} \text{ at } E_{nj} = (0.4j + 0.2)$$

The parameter  $s$  is found from the equation (see ref 11)

$$s = \frac{k \sum (x_j y_j) - \sum x_j \sum y_j}{k \sum x_j^2 - (\sum x_j)^2} \quad (67)$$

and

$$c = \frac{\sum x_j^2 \sum y_j - \sum x_j \sum (x_j y_j)}{k \sum x_j^2 - (\sum x_j)^2} \quad (68)$$

where  $k =$  the number of values of  $x_j$ .

The parameters  $s$  and  $c$  are inserted into equation 63, to calculate the number of statistical neutrons in region III. Either one of the two methods for determining the direct spectrum outlined in section (a) is used to calculate  $\frac{dN'}{dE_n}$ , the neutron spectrum corrected for directly emitted neutrons.  $\frac{dN'}{dE_n}$  is substituted for  $\frac{dN}{dE_n}$  in equation 65 and a new set of parameters  $s'$  and  $c'$  are determined. The process is repeated until the new value of  $s$  agrees with the old value within 0.5 per cent.

### E. Direct Spectrum

In order to separate the neutron energy spectrum into two components, a knowledge of the shape of the energy spectrum,  $S(E_n)$ , of the directly emitted neutrons is required. In the absence of a detailed calculation,  $S(E_n)$  is estimated using the following model. First the assumption is made that the gamma absorption takes place through a single particle interaction, such as that described by Wilkinson (30). The excited neutron is either ejected immediately, a "direct resonance" emission, or damps into the compound nucleus, which subsequently decays by statistical emission. The two components of the neutron energy spectrum represent these two processes. Next it is assumed that each single particle transition is spread over the entire giant resonance, ie, that the giant resonance is uniform and featureless. Finally it is assumed that the excited nucleus, where the region of excitation is given by the product of the gamma spectrum  $\rho_\Delta$  and the photon absorption cross section,  $\sigma(\gamma, n)$ , decays directly to the levels (hole states) of the residual nucleus, if the neutron is directly emitted.

The probability for direct emission for a given single particle transition is given by Wilkinson\* (30) as

$$C = \frac{\Gamma_\alpha}{\Gamma_a + \Gamma_\alpha} \quad (69)$$

where  $\Gamma_\alpha =$  width for particle emission

\*Wilkinson uses  $C = \frac{\Gamma_\alpha}{\Gamma_a}$ . We have used  $C = \frac{\Gamma_\alpha}{\Gamma_T} = \frac{\Gamma_\alpha}{\Gamma_a + \Gamma_\alpha}$  as a better approximation



and  $\Gamma_a$  = width for particle absorption.

$\Gamma_a$  was estimated from the imaginary, or absorption, part of the optical potential,  $\Gamma_a = 2W$ . The particle emission width is estimated by Blatt and Weisskopf (43) for a square well of radius R and depth  $V_0$  as

$$\Gamma_a \approx \frac{\hbar^2 K T_\ell}{2MR} \quad (70)$$

where  $K = \sqrt{k^2 + K_0^2}$ , the nucleon wave number in the nucleus for which

$$k = \frac{1}{\hbar} \sqrt{2ME_n} = \text{wave number of the emitted nucleon}$$

$$K_0 = \frac{1}{\hbar} \sqrt{2MV_0} = \text{wave number of a nucleon in the square well } V_0$$

$T_\ell$  = transmission coefficient for an  $\ell$  wave particle

M = mass of the nucleon

$$R = R_0 A^{1/3}, \text{ for } R_0 = 1.25 \times 10^{-13} \text{ cm}$$

Then

$$C = \frac{\frac{\hbar T_\ell \sqrt{2M(E_n + V_0)}}{2MR_0 A^{1/3}}}{2W + \frac{\hbar T_\ell \sqrt{2M(E_n + V_0)}}{2MR_0 A^{1/3}}} \quad (71)$$

In the above equation the transmission coefficients used were those calculated by E. Auerbach and Moore (62) or Perey and Buck (61) using the optical model. (Actually the neutron transmission coefficient depends on the spin orientation and hence should be labelled  $T_j$ .) W was estimated by Lane and Wandel (63), to be

$$W = 2.5 + 0.4 E_n \text{ (MeV)} \quad (72)$$

The transmission coefficients for the closed shell nuclei, Bi and  $\text{Pb}^{208}$ , from ref 62 were calculated using smaller W's than were used for the general nuclei of ref 61. Therefore the W's used for Bi and  $\text{Pb}^{208}$  were reduced by factors of 1.85 and 1.27 respectively, to take this fact into account. \*

The energy distribution of the directly emitted neutrons for a given transition  $\ell \rightarrow \ell'$  is given by

\*These references used a surface adsorption term  $V_{\text{img}}(r) = W \exp[-(r-R)^2/b^2]$ ,  $W = 7.0$  MeV for general nuclei,  $W = 3.78$  MeV for Bi and  $W = 5.5$  MeV for  $\text{Pb}^{208}$ . Equation 72 gives the imaginary potential for a volume absorption term,  $V = (U + iW) \cdot V(r)$ .

$$S_{\ell}(E_n) = \rho_{\Delta}(E_{\gamma})\sigma(E_{\gamma}) \frac{\Gamma_{\alpha}(E_n)}{\Gamma_T} \quad (73)$$

where all quantities have been defined above.

If the residual nucleus levels are known, the direct spectrum can be calculated by summing over all transitions\* weighted by the relative transition strength,  $f_{\ell}$ .

$$S(E_n) = \sum_{\ell} S_{\ell}(E_n) f_{\ell} \quad (74)$$

where  $f_{\ell}$  is normalized to unity. The  $f_{\ell}$ 's are the product of the radial overlap integrals times a factor dependent on the  $\ell$  value, which accounts for the transfer of oscillator strength from lower shells (see ref 30). They are discussed in detail for each element in Chapter V.

When the level structure is quite complicated and the intrinsic levels cannot be singled out,  $S(E_n)$  is calculated assuming that the hole states are uniformly distributed over the region of excitation of the residual nucleus.

In this case

$$S_{\ell}(E_n) = D(E_n) \frac{\Gamma_{\alpha}(E_n)}{\Gamma_T} \quad (75)$$

where  $\int_0^{E_n \text{ max}} D(E_n) dE_n = \int_B^{E_{\gamma} \text{ max}} \rho_{\Delta}(E_{\gamma}) dE_{\gamma}$ ,  $E_{\gamma} = E_n + B$  for  $B =$  neutron binding energy, and  $E_n \text{ max}$  and  $E_{\gamma} \text{ max}$  are the maximum neutron and gamma ray energies respectively. Since  $\rho_{\Delta}(E_{\gamma})\sigma(E_{\gamma})$  is sharply peaked,

$$D(E_n) \approx \frac{1}{E_n \text{ max}} \int_{E_{\gamma}}^{E_{\gamma} \text{ max}} \rho_{\Delta}(E_{\gamma})\sigma(E_{\gamma}) dE_{\gamma} \quad (76)$$

That is,  $D(E_n)$  is a constant below the photon absorption peak, and rapidly fall to zero above it. (Equation 76 would be exact if  $\rho_{\Delta}(E_{\gamma}) = \delta(E_{\gamma} - E_{\gamma} \text{ max})$ .)  $D(E_n)$  takes into account the tailing off of  $S_{\ell}(E_n)$  due to the finite width of  $\rho_{\Delta}(E_{\gamma})$ . The resonance direct spectrum,  $S(E_n)$ , is given by  $\sum_{\ell} S_{\ell}(E_n) f_{\ell}$  as before.

A few comments about the assumptions are in order. It is obvious

\*Both neutron and proton transitions. Note however that  $T_{\ell} = 0$  for all  $\ell$  is the case for protons.

that the excited nucleon can be emitted after one or a few collisions and be neither a direct resonance, nor a statistically emitted nucleon. Although this picture is more realistic, it is far too complicated to include in this simplified model. This process will result in loss of energy, which will tend to increase the low energy portion of  $S(E_n)$  at the expense of the high energy portion, and to recouple the neutron angular momentum. The latter may be an important effect in the region of the distorted nuclei, where the bulk of the single particle strength is in high  $\ell$  transitions which have small  $T_\ell$ 's. Thus collisions resulting in lowered angular momentum would increase the escape probability. The assumption of a uniform distribution of residual levels is a very crude approximation, and it is adopted only in ignorance of the true distribution. However since the direct spectrum is dominated by  $T_\ell$  at low neutron energies, and by  $\rho_\Delta(E_n)$  at high neutron energies,  $S(E_n)$  will provide a fair fit, despite the crude assumptions. Finally single particle calculations of the giant resonance (30, 34, 35, 36, 37, and 41) predict discrete states, not a uniform smear. However each state will have an intrinsic width (estimated by Wilkinson to be about  $W$ ) and each state is a linear combination of individual particle-hole states. Therefore a given particle-hole state tends to spread out over the entire giant resonance.

Chapter V  
Discussion of the Data

A. Bismuth and Lead 208

a) Experimental Data

The photoneutron energy spectra  $\frac{dN}{dE_n} \frac{1}{E_n}$  for Bi and Pb<sup>208</sup> are plotted versus  $E_n$  in Figs. 13 to 16. Each graph contains two experimental photoneutron spectra and their difference. The two neutron spectra were generated by two bremsstrahlung spectra with endpoints of either 15 and 14 MeV or 14 and 13 MeV. The difference represents the photoneutron spectrum resulting from a photon spectrum peaked at 14 MeV or 13 MeV respectively, which is the difference of the corresponding bremsstrahlung spectra. The procedure for taking this difference was discussed in Chapter IV, section C. Error bars have been placed on a few representative points. In general the error bars are smaller than the symbols used to distinguish the three curves. The error bars include the statistical uncertainties and an estimate of the systematic errors in the corrections applied to the data. These corrections were discussed in Chapter IV. The solid curve represents the theoretical fit to the data. It is a graph of the equation

$$\frac{dN}{dE_n} \frac{1}{E_n} = C\sigma_C \frac{e^{2\sqrt{aU}}}{(U+t)^{3/2}} + \frac{K}{E_n} S(E_n) \quad (78)$$

The symbols used in the above equation have been defined in Chapter IV, section D. The first term is the evaporation component and the second term is the resonance direct component. This equation contains only two adjustable parameters,  $a$  and  $K$  (and an arbitrary scale factor  $C$ ).\*

b) Direct Spectrum

The resonance direct neutron energy spectra,  $S(E_n)$ , for Pb<sup>208</sup> and Bi were calculated from equation 74 in Chapter IV, section D, using discrete hole states in the residual nuclei. Table XIII lists the important single particle di-

\* The above description of the graphs applies to all of the targets, except thallium (which will be discussed in section C of this chapter).

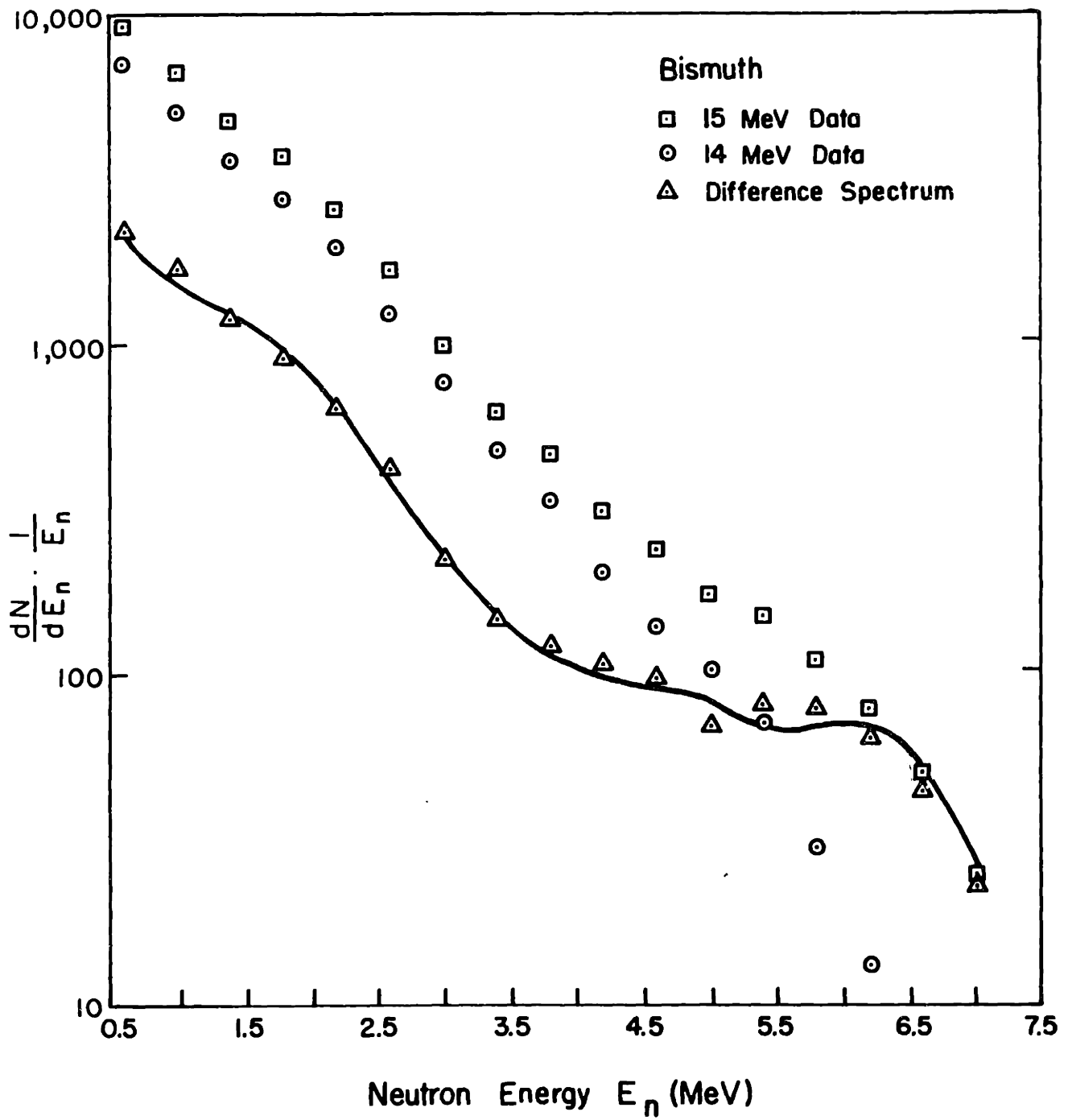


Fig. 13 Neutron Energy Spectra

# BISMUTH

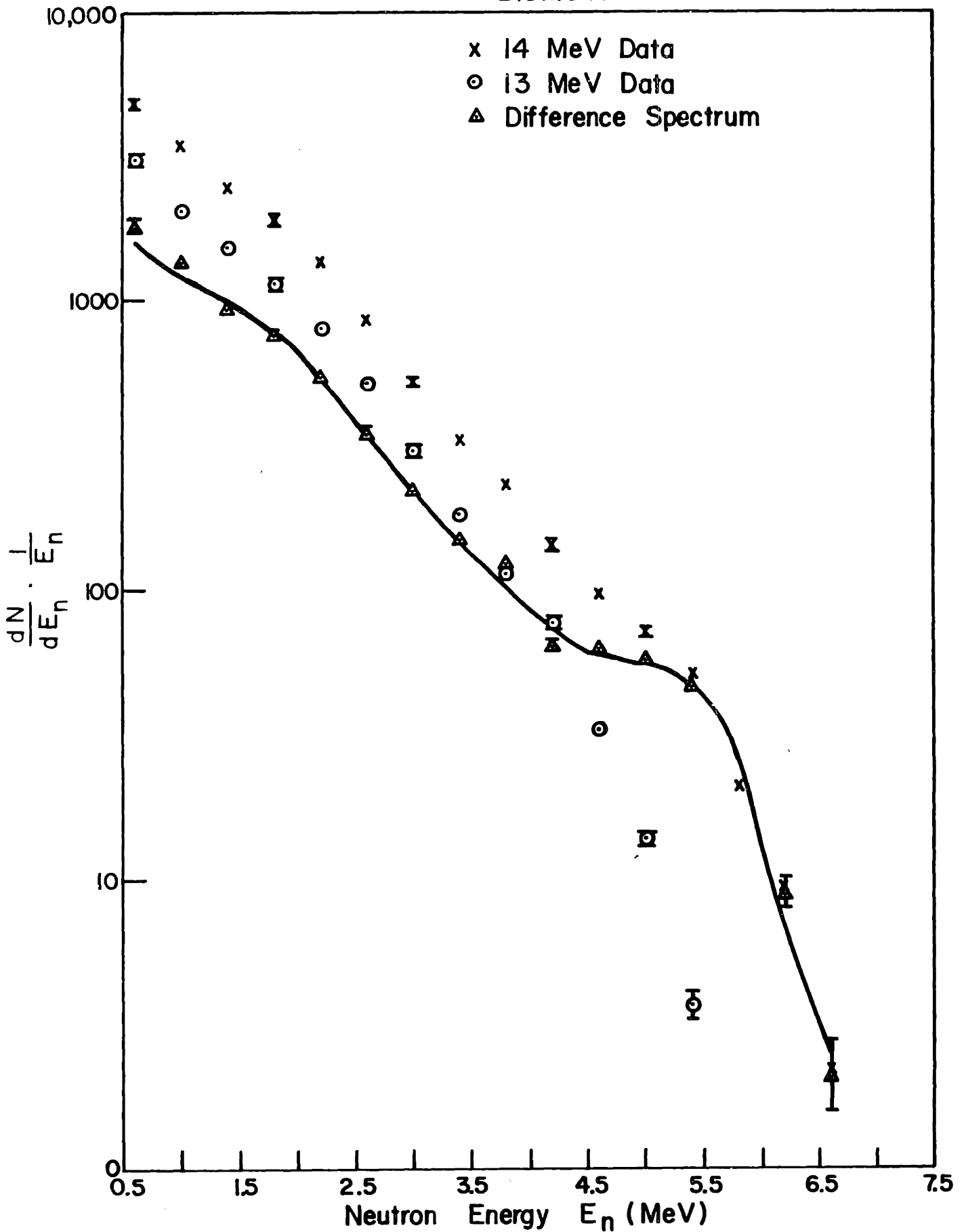


Fig. 14 Neutron Energy Spectra

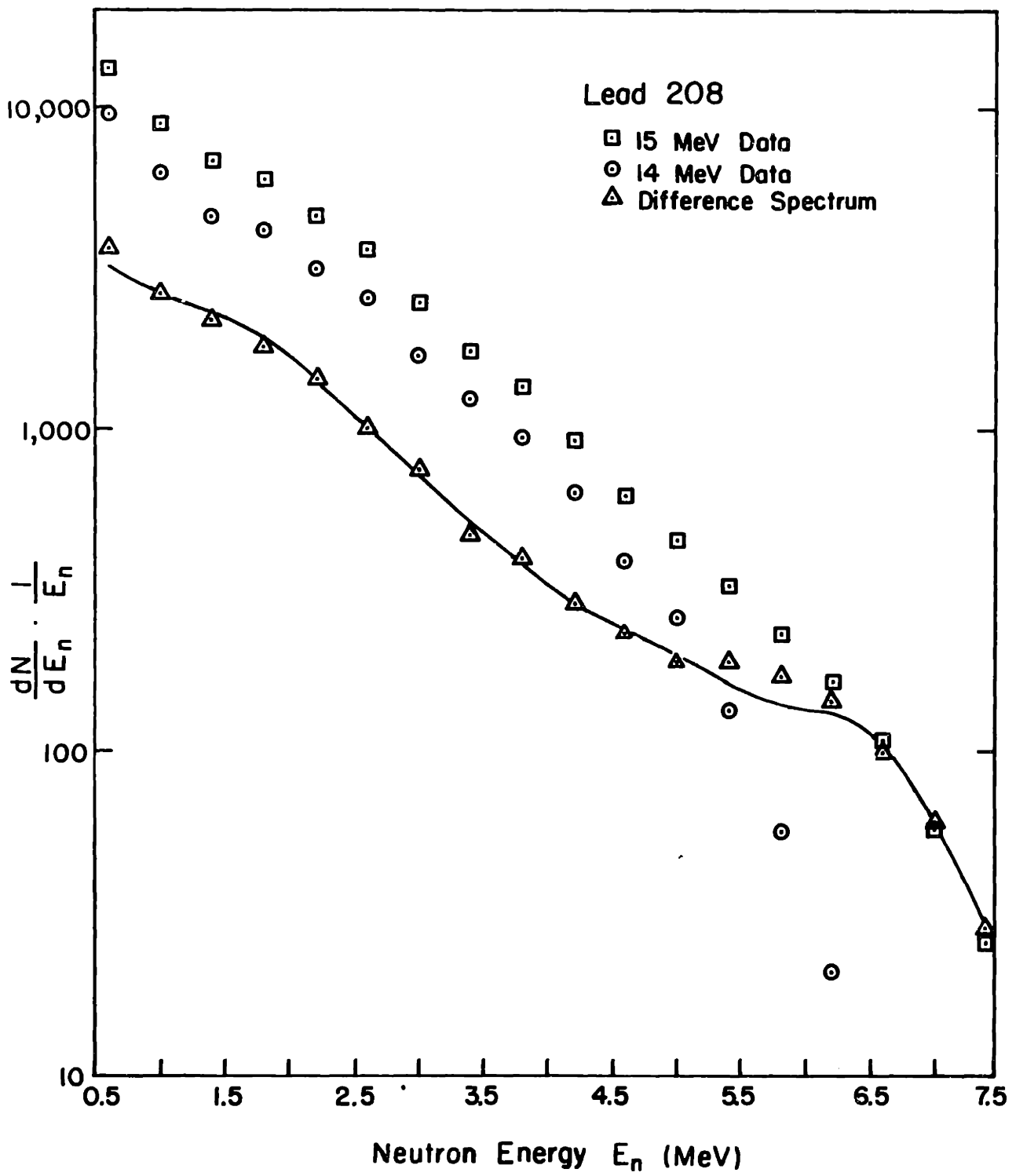


Fig. 15 Neutron Energy Spectra

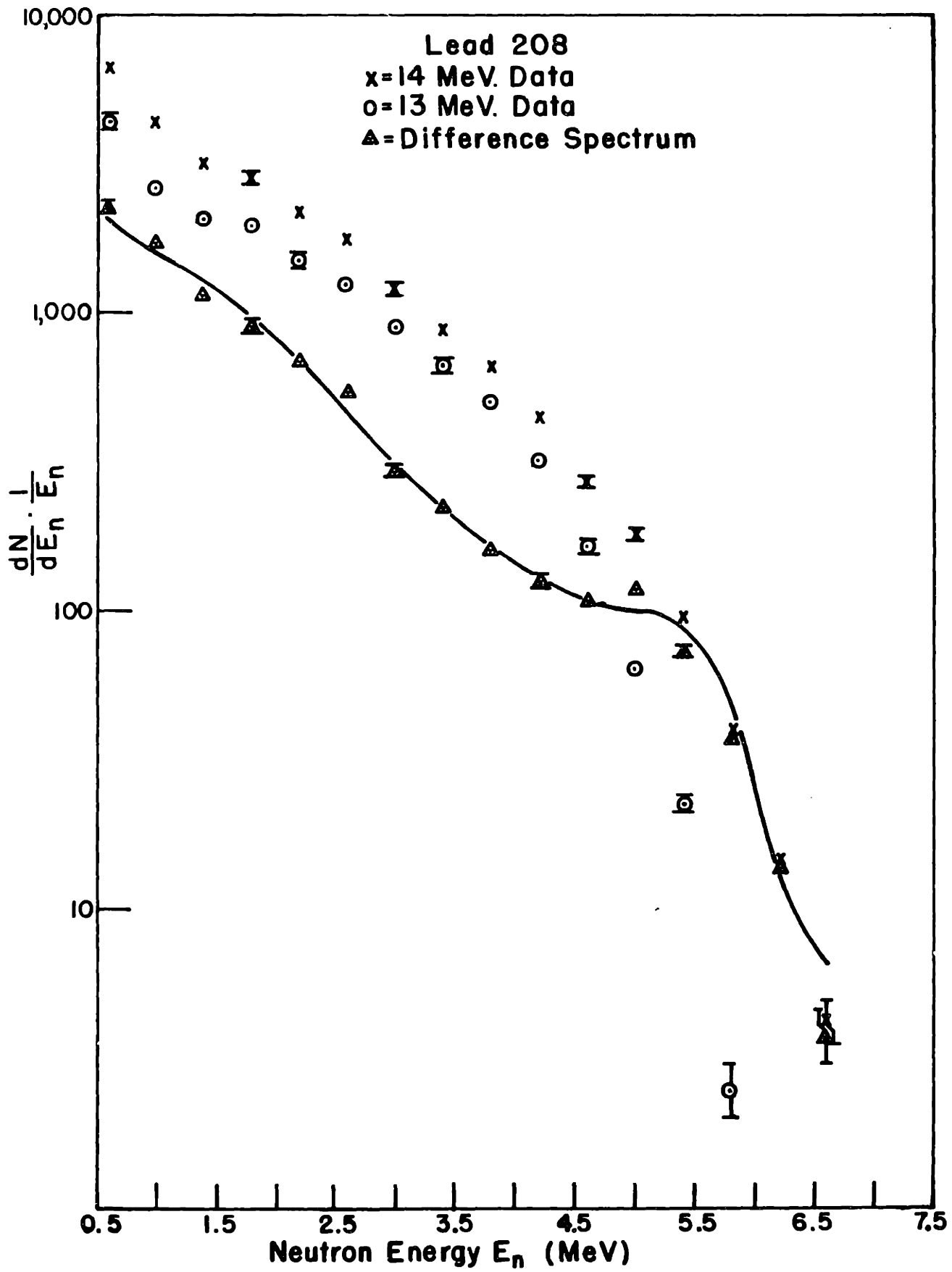


Fig. 16 Neutron Energy Spectra



Table XIII

Possible Dipole Transitions for Closed Shell at N = 126

Transitions	Transition Strength $f_l$		Angular Distribution*** $-a_2/a_0$
	Square Well*	Saxon-Wood**	
$3p^{1/2} \rightarrow 3d^{3/2}$	0.17	0.02	0.5
$3p^{3/2} \rightarrow 3d^{3/2}$	0.03	0.003	0.5
$3p^{3/2} \rightarrow 3d^{5/2}$	0.30	0.07	0.5
$2f^{5/2} \rightarrow 2g^{7/2}$	0.63	0.34	0.357
$2f^{7/2} \rightarrow 2g^{7/2}$	0.02	0.05	0.357
$2f^{7/2} \rightarrow 2g^{9/2}$	0.82	0.43	0.357
$1h^{9/2} \rightarrow 2g^{7/2}$	0.08	0.07	0.182
$1h^{9/2} \rightarrow 1i^{11/2}$	1.53	1.37	0.318
$1h^{11/2} \rightarrow 2g^{9/2}$	0.10	0.02	0.182
$1h^{11/2} \rightarrow 1i^{11/2}$	0.02	0.04	0.318
$1i^{13/2} \rightarrow 2h^{11/2}$	0.10	0.03	0.192
$1i^{13/2} \rightarrow 1j^{13/2}$	0.02	0.08	0.30
$1i^{13/2} \rightarrow 1j^{15/2}$	2.16	1.76	0.30

\*Wilkinson (30)                      \*\*Pal et al (65)                      \*\*\*Courant (45)

Table XIV

Pb<sup>207</sup> Energy Levels

Energy (MeV)*	Spin*	Shell Model States**
0.0	$\frac{1}{2}^-$	$p^{1/2}$
0.57	$\frac{5}{2}^-$	$f^{5/2}$
0.89	$\frac{3}{2}^-$	$p^{3/2}$
1.6	$\frac{13}{2}^+$	$i^{13/2}$
1.9	?	
2.34	$\frac{7}{2}^-$	$f^{7/2}$
2.74	$\frac{9}{2}^+$	
3.47	$\frac{9}{2}^-$	$h^{9/2}$

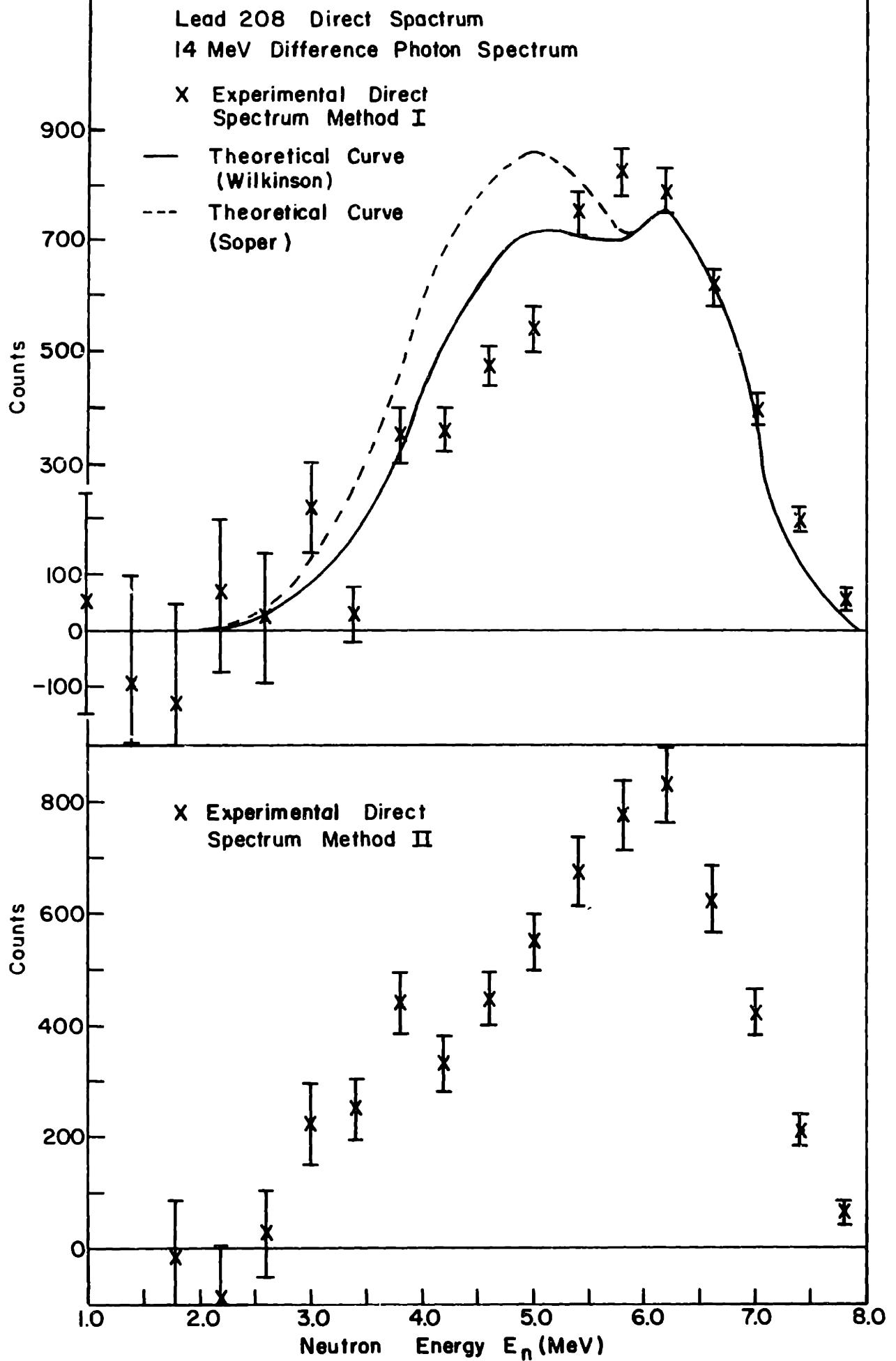
\*Nuclear Data Sheets (66)

\*\*Cohen et al (32)

pole transitions for  $\text{Pb}^{208}$ , based on the single particle level scheme taken from a calculation by Ross et al (64), for a diffuse nuclear potential. Other dipole transitions are excluded because either the shell to which the neutron should go is filled (this occurs for all transitions of the type  $n\ell \rightarrow n\ell - 1$ ), or else the transition strength is very small. The second column of the table lists the relative intensities,  $f_\ell$ , of the transitions, taken from Wilkinson (30). The  $f_\ell$ 's are the product of the square of the radial overlap integral for the electric dipole transition evaluated using a square well, times a factor dependent on the  $\ell$  value which accounts for the transfer of oscillator strength from lower shells. The third column of the table lists the relative intensities,  $f_\ell$ , of the transitions taken from a calculation by Pal, Soper and Stamp (65). They have used a Saxon-Wood potential with a spin-orbit term, and have taken into account the particle-hole interactions. Their calculations yield two collective states, one at 12.9 MeV containing 72 per cent of the total dipole cross section and one at 13.6 MeV containing 17 per cent of the cross section. The relative strengths of the transitions are different for the two states. The strengths listed in the table are the sum of the transition strengths from the two states weighted in proportion to the percentage of the dipole cross section.

Table XIV lists the energies,  $E_1$ , of the known levels of  $\text{Pb}^{207}$ , taken from the Nuclear Data Sheets (66). Most of these levels are found by (d, t) pickup reactions to be single particle-hole states with the quantum number listed (Cohen et al (32)). It is just these single particle-hole states that the Wilkinson model predicts should be formed by a resonance direct emission. The other states which are not seen in (d, t) reactions are apparently more complicated configurations.  $S(E_n)$  for  $\text{Pb}^{208}$  was calculated from equation 74 using the  $f_\ell$ 's listed in Table XIV, and the  $T_j$ 's from ref 62. The  $(\gamma, n)$  cross section from ref 7 was used to calculate  $\rho_\Delta(E_\gamma)\sigma_C(E_\gamma)$ .  $S(E_n)$ , normalized to the data above 5.0 MeV, as described in Chapter IV, section E, is shown in Figs. 17 and 19 in the graphs labelled "Method I".

The solid curve in Fig. 17 is the direct spectrum calculated using the Wilkinson strengths, and the dashed curve is the direct spectrum calculated using the Pal et al strengths. The two curves are normalized to the data from



# BISMUTH - DIRECT SPECTRUM

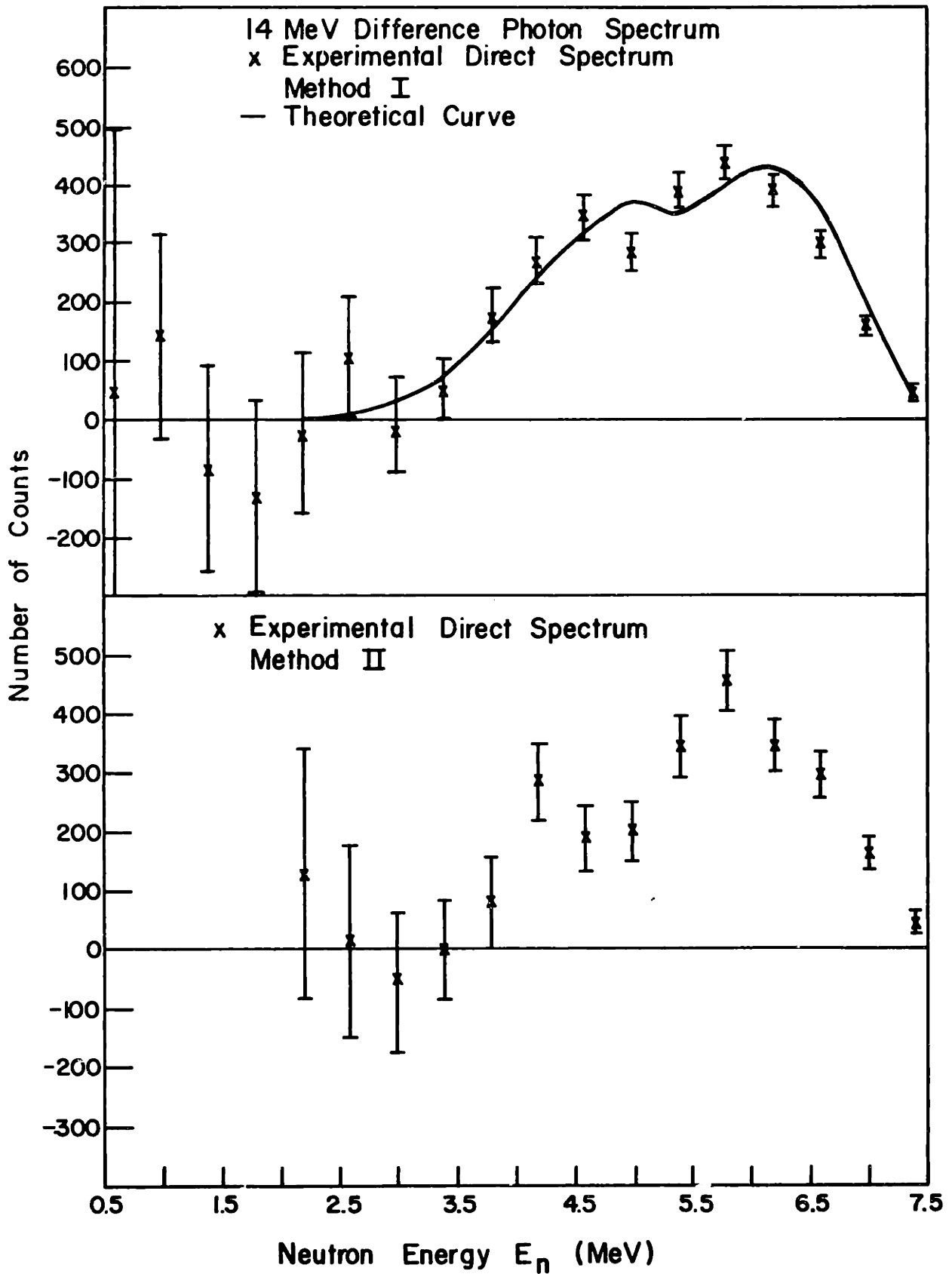


Fig. 18

# LEAD 208- DIRECT SPECTRUM

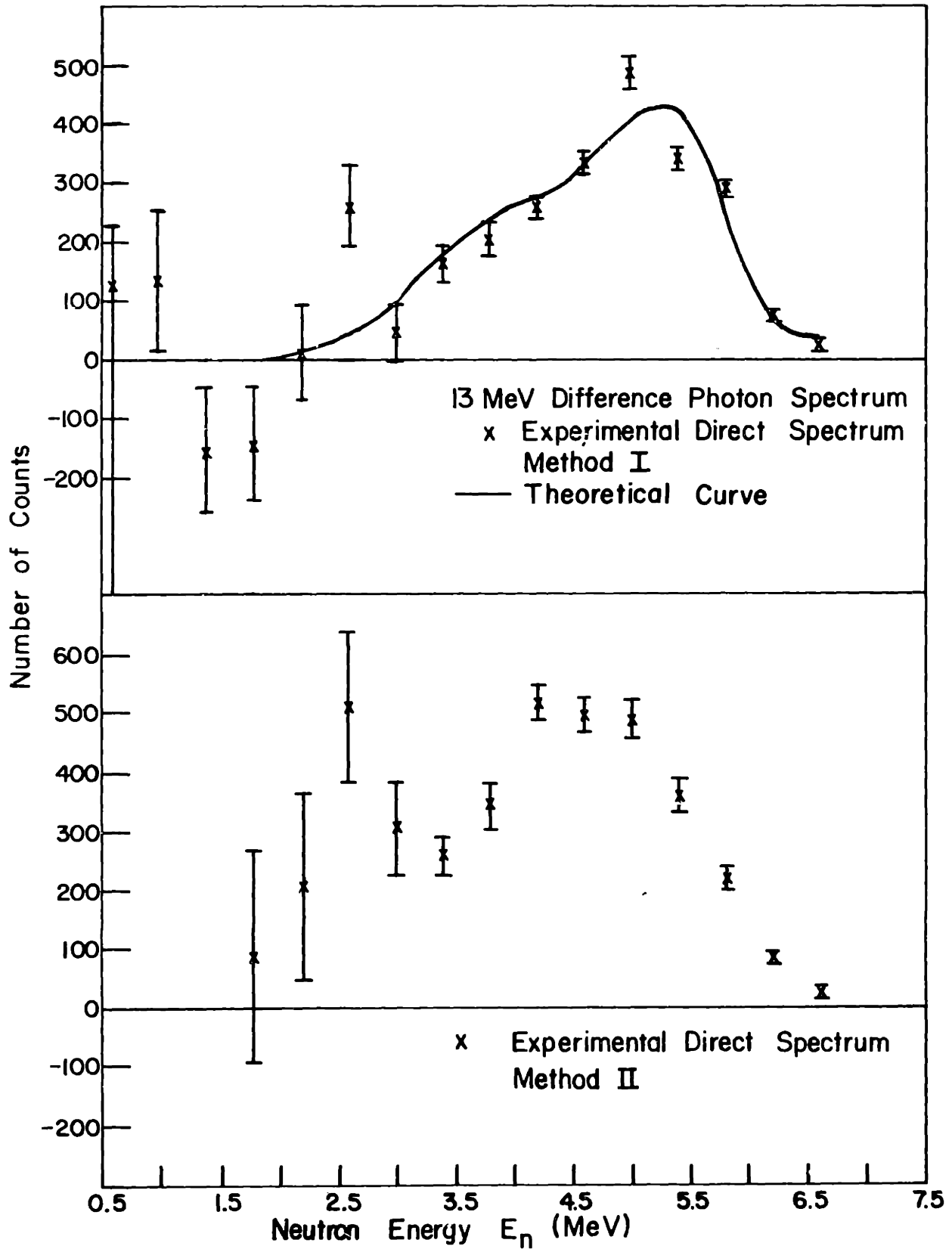


Fig. 19

# BISMUTH-DIRECT SPECTRUM

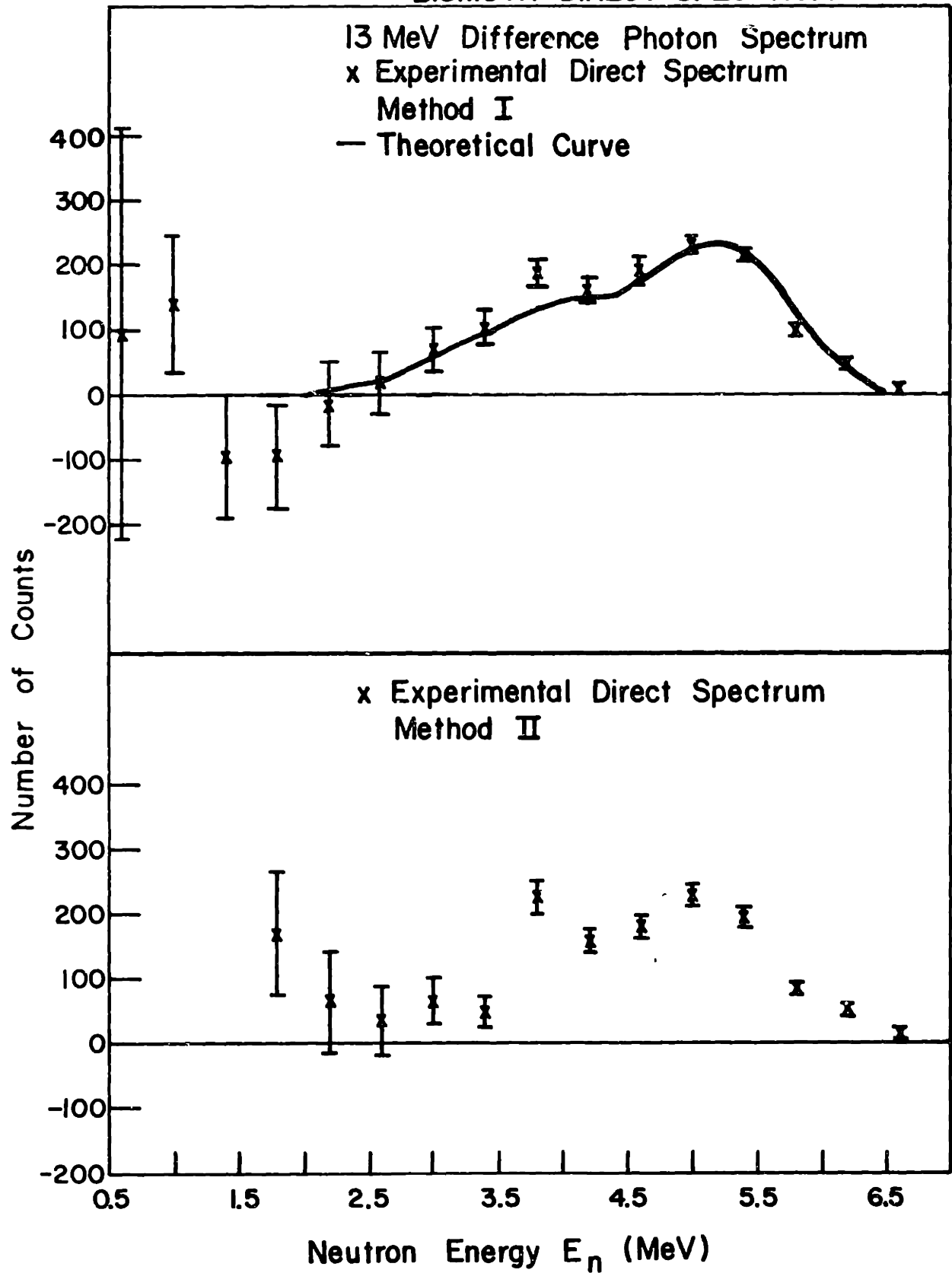


Fig. 20



5.0 to 8.0 MeV. (The data shown was obtained using the solid curve for  $S(E_n)$ .) Above 6.0 MeV the  $p^{1/2} \rightarrow d^{3/2}$ ,  $p^{3/2} \rightarrow d^{5/2}$  and  $f^{5/2} \rightarrow g^{7/2}$  transitions are dominant. Near 5.0 MeV, the  $2f^{7/2} \rightarrow 2g^{9/2}$  transition is dominant. The other transitions have small  $f_\ell$ 's or small  $T_\ell$ 's. Although it is not apparent from the figure (because of the method of normalization) the difference between the two results is due to the reduction of the  $3p^{1/2} \rightarrow 3d^{5/2}$  strength relative to the  $2f^{7/2} \rightarrow 2g^{9/2}$  strength in Pal's calculation (see Table XIII). Both calculations predict a direct fraction that is about 10 per cent of the experimental value. The possible reasons for this large discrepancy, which occurs for all of the targets, are discussed in section J of this Chapter.

$\text{Bi}^{208}$  consists of one  $h^{9/2}$  proton outside a closed shell, and one  $p^{1/2}$  neutron hole in a closed shell. Although the low lying levels are complicated mixtures of neutron-proton intrinsic states, the levels of  $\text{Bi}^{208}$  as found by Erskine (67) using a (d, t) reaction, tend to cluster around the energies where the single particle hole states of  $\text{Pb}^{207}$  fall (see Table XV). That is, the single particle character of the hole states persists despite the configuration mixing. The shell model configurations listed for  $\text{Bi}^{208}$  are taken from a calculation by Kim and Rasmussen (68). Their calculation predicts a multitude of levels composed of various proton and neutron intrinsic states. However many of the calculated levels consist of the various j values resulting from the coupling of an  $h^{9/2}$  proton and a given neutron hole. These are the states one would expect a ( $\gamma$ , n) or (d, t) reaction to populate. Erskine has tentatively assigned these configurations to the appropriate levels in his experimental level scheme. These configurations are listed in Table XV. Except for the missing  $i^{13/2}$  level, these states correspond closely to the  $\text{Pb}^{207}$  hole states. An isomeric level with  $J = 10, 9$ , or  $8$  at 1.43 MeV has been observed from (n, 2n) and ( $\gamma$ , n) work (66). Kim and Rasmussen predict a  $(h^{9/2})(i^{13/2})^{-1}$  state with  $J = 10^-$  at 1.75 MeV. Also levels near 1.6 MeV have been observed in other (d, t) experiments (32). Therefore the  $i^{13/2}$  levels calculated by Kim and Rasmussen were assigned to 1.43 MeV. Because of the excellent agreement between the experiment and theory, the levels calculated by Kim and Rasmussen were used for the residual states of  $\text{Bi}^{208}$ . The strength,  $f_\ell$ , for a given transition was divi-



Table XV  
Bi<sup>208</sup> Energy Levels

Experimental <sup>a</sup> Energy (MeV)	Shell Model Predictions <sup>b</sup>			Statistical Weighting
	Energy (MeV)	Spin	Configuration	
0.0	0.0	5 <sup>+</sup>	h <sup>9/2</sup> (p <sup>1/2</sup> ) <sup>-1</sup>	11/20
0.063	0.081	4 <sup>+</sup>	"	9/20
0.513	0.529	6 <sup>+</sup>	h <sup>9/2</sup> (f <sup>5/2</sup> ) <sup>-1</sup>	13/60
0.605	0.596	4 <sup>+</sup>	"	9/60
	0.622	5 <sup>+</sup>	"	11/60
0.634	0.630	3 <sup>+</sup>	"	7/60
0.651	0.664	7 <sup>+</sup>	"	15/60
0.890	0.916	5 <sup>+</sup>	h <sup>9/2</sup> (p <sup>3/2</sup> ) <sup>-1</sup>	11/40
0.929	0.920	2 <sup>+</sup>	h <sup>9/2</sup> (f <sup>5/2</sup> ) <sup>-1</sup>	5/60
0.963	0.981	4 <sup>+</sup>	h <sup>9/2</sup> (p <sup>3/2</sup> ) <sup>-1</sup>	9/40
1.074	1.046	3 <sup>+</sup>	"	7/40
1.098	1.079	6 <sup>+</sup>	"	13/40
(1.43) <sup>c</sup>	1.69-2.76	2 <sup>-</sup> -11 <sup>-</sup>	h <sup>9/2</sup> (i <sup>13/2</sup> ) <sup>-1</sup>	(1.0)
2.34 <sup>d</sup>	2.373	7 <sup>+</sup>	h <sup>9/2</sup> (f <sup>7/2</sup> ) <sup>-1</sup>	15/80
2.394 <sup>d</sup>	2.417	5 <sup>+</sup>	"	11/80
2.417 <sup>d</sup>	2.469	4 <sup>+</sup>	"	9/80
	2.482	3 <sup>+</sup>	"	7/80
	2.484	6 <sup>+</sup>	"	13/80
	2.531	2 <sup>+</sup>	"	5/80
	2.637	8 <sup>+</sup>	"	17/80
	2.850	1 <sup>+</sup>	"	3/80

<sup>a</sup>(d,t) reactions, Erskine (67)

<sup>b</sup>Suggested by Erskine; based on calculations by Kim and Rasmussen (68).

<sup>c</sup>Isomeric 10<sup>-</sup> state Nuclear Data Sheets (66)

<sup>d</sup>Angular distributions not measured, that is, J not known.

ded among the various levels resulting from coupling the neutron single particle state with the  $h^{9/2}$  proton single particle state according to the statistical weighting. These weights are listed in Table XV.  $S(E_n)$  was then calculated in the same manner as for  $Pb^{208}$ . The results of the calculation using Wilkinson's  $f_\ell$ 's are shown in Figs. 18 and 20. Good agreement with the experimental data is obtained.

The lower graphs in Figs. 17 to 20, which are labelled "Method II", are plots of the energy spectrum of the resonance direct component, calculated using the assumption that the evaporation component is isotropic and the direct component has a constant angular distribution, given by the high energy limit of the photoneutron angular distribution. The two methods agree quite well for bismuth and  $Pb^{208}$ .

The bismuth direct spectrum appears to have a dip at 5.0 MeV neutron energy for the 14 MeV photon spectrum data and at 4.2 MeV for the 13.2 MeV photon spectrum data. This feature has been observed by Kuchnir et al (69). They observed a deep dip in the photoneutron spectrum about  $1\frac{1}{2}$  MeV below the tip of the neutron spectrum, using a photon beam with a width of 0.250 MeV. The levels listed in Table XV indicate that a process which removes one neutron (such as  $(\gamma, n)$  or  $(d, t)$ ) does not strongly populate any levels that exist between the 1.1 and 2.35 MeV levels of  $Bi^{208}$ .  $S(E_n)$  exhibits a dip at 5.4 MeV neutron energy. The exact position of the dip in  $S(E_n)$  depends on the relative values of  $f_\ell$ .

The experimental  $Pb^{208}$  direct spectrum does not appear to contain this dip, although it is predicted by  $S(E_n)$ . This could be explained in several ways. For example, there is a level at 1.9 MeV in  $Pb^{207}$  that has not been included in the calculation. This level was excluded because it is not seen in  $(d, t)$  reactions (Cohen et al (32)) and is thought to be a core excitation rather than a single hole state. This interpretation may be in error, or the giant dipole state may couple strongly to this state even though it is not a simple hole state. This is mere conjecture, of course. Also the  $f_\ell$ 's may have different relative values than those used. The discussion in section J supports this view.

This would require substantially different  $f_{\ell}$ 's for Bi and Pb<sup>208</sup>.

### c) Evaporation Component

Once the direct component has been determined as described in detail in Chapter IV, section D, the evaporation component is found by subtracting  $S(E_n)$  from the experimental energy spectra. The results are plotted as  $\frac{dN}{dE_n} \frac{1}{E_n \sigma_C}$  vs  $E_n$  in Figs. 21 to 24. The solid curves in the figures are graphs of the quantity  $e^{2\sqrt{aU}/(U+t)^{3/2}}$  vs  $E_n$ . The fits are excellent up to 5.0 MeV in all four cases. Above this neutron energy,  $S(E_n)$  would have to reproduce the resonance direct spectrum in greater detail to improve the fit. Fig. 25 is a plot of the Pb<sup>208</sup> evaporation component derived using Method II to find the direct component spectrum. Again the theoretical curve fits the data quite well. Although these curves fit the data, it should not be taken as an indication that equation 57 is the best possible form for the level density. The data was also analyzed using the forms

$$\omega(U) = e^{-E_n/T} \quad (79)$$

and

$$\omega(U) = \frac{e^{2\sqrt{aU}}}{(U+t)^2} \quad (80)$$

Both of these formulas fit the data as well as equation 57, since the three forms differ very little in the region from 1.0 to 4.0 MeV, where the evaporation component dominates. Any differences at higher neutron energies are reflected in the normalization of  $S(E_n)$ . The temperature and the two level density parameters for all the targets are listed in Tables XXIX, XXX, and XXXI.

The low energy points in Figs. 21 to 25, specifically the points at 0.6 and 1.0 MeV, are subject to several distortions which are negligible at higher neutron energies. The first distortion is the scattering correction which increases rapidly at lower neutron energies. This correction was as large as 20 per cent at 0.6 MeV for bismuth and lead. The second distortion is the effect of the negative tail in the 14 MeV photon difference spectrum (Fig. 10). This might reduce the total neutron difference spectrum for Pb<sup>208</sup> and Bi by as much as 3 per cent. This effect is negligible for isotopes with  $(\gamma, n)$  thresh-

Fig. 21 Neutron Evaporation Spectrum

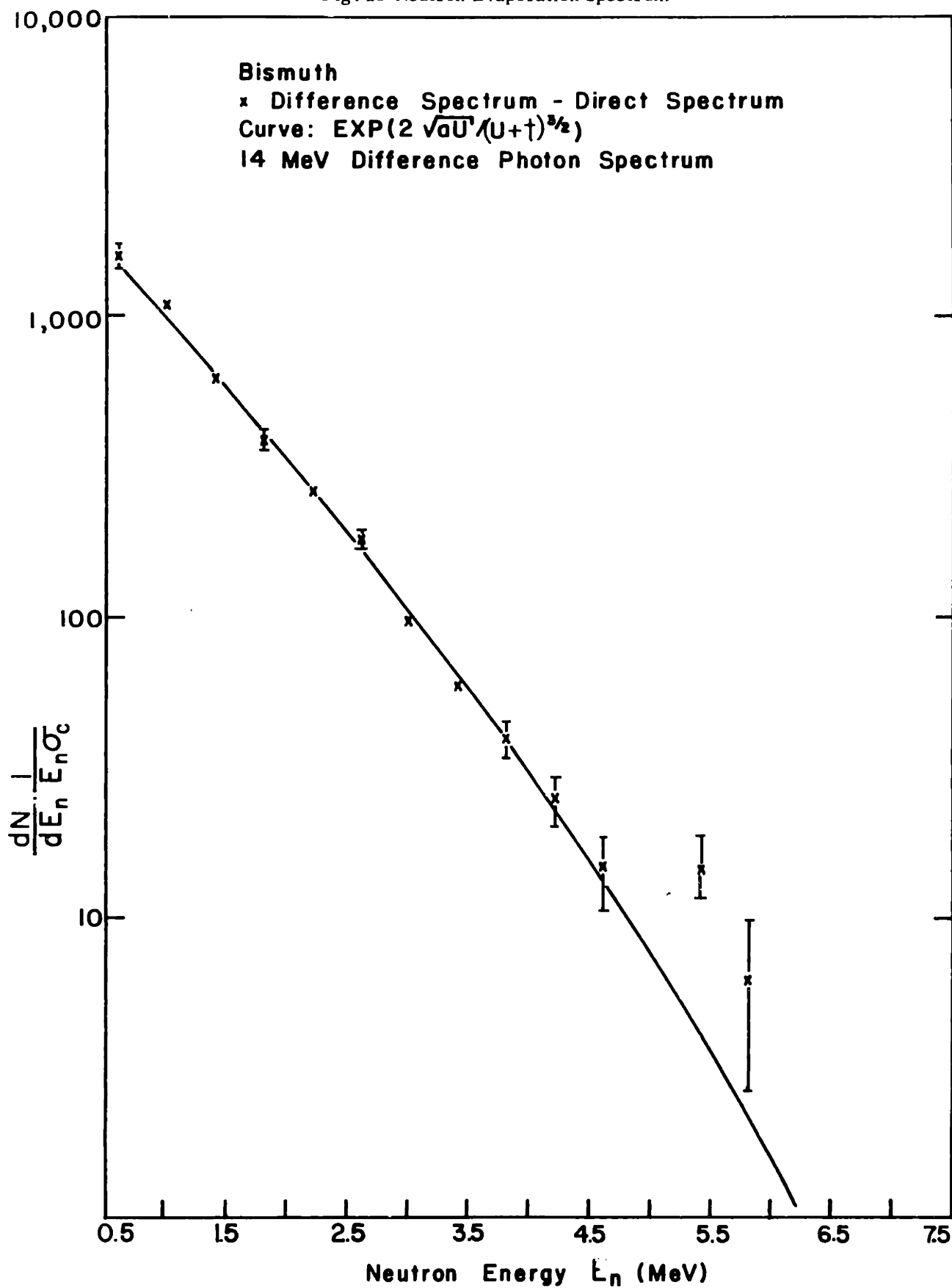


Fig. 22 Neutron Evaporation Spectrum

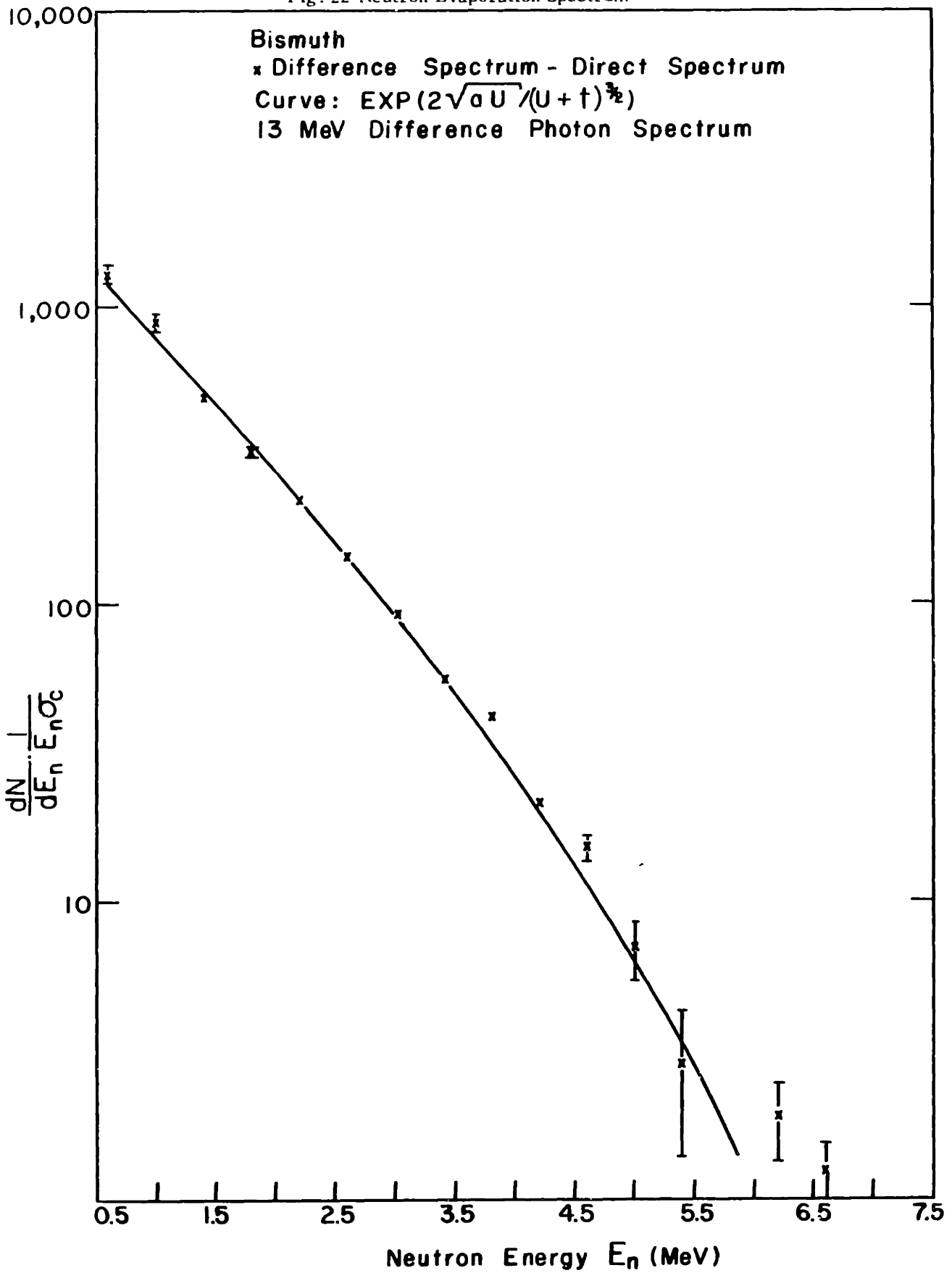
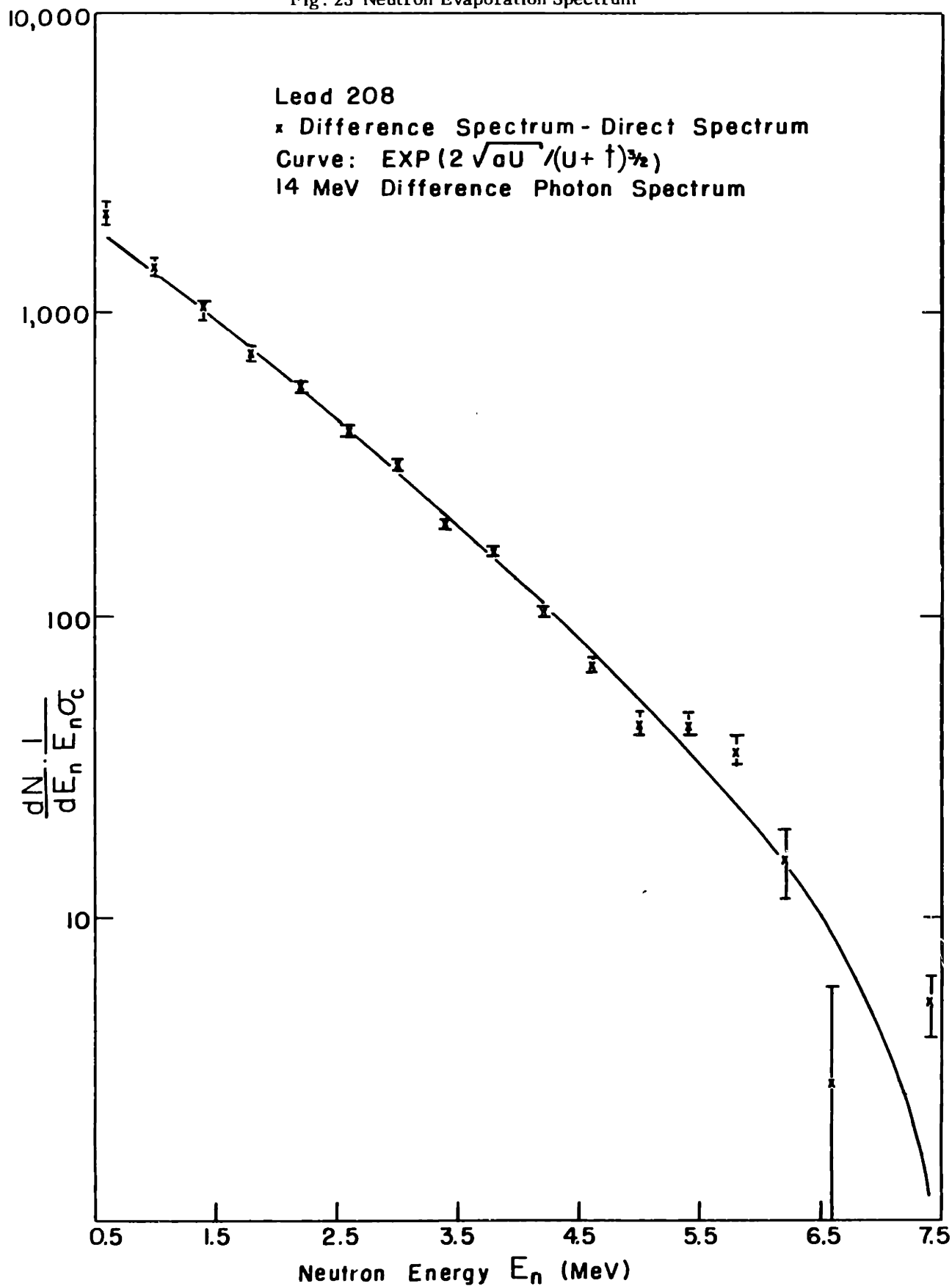


Fig. 23 Neutron Evaporation Spectrum



10,000

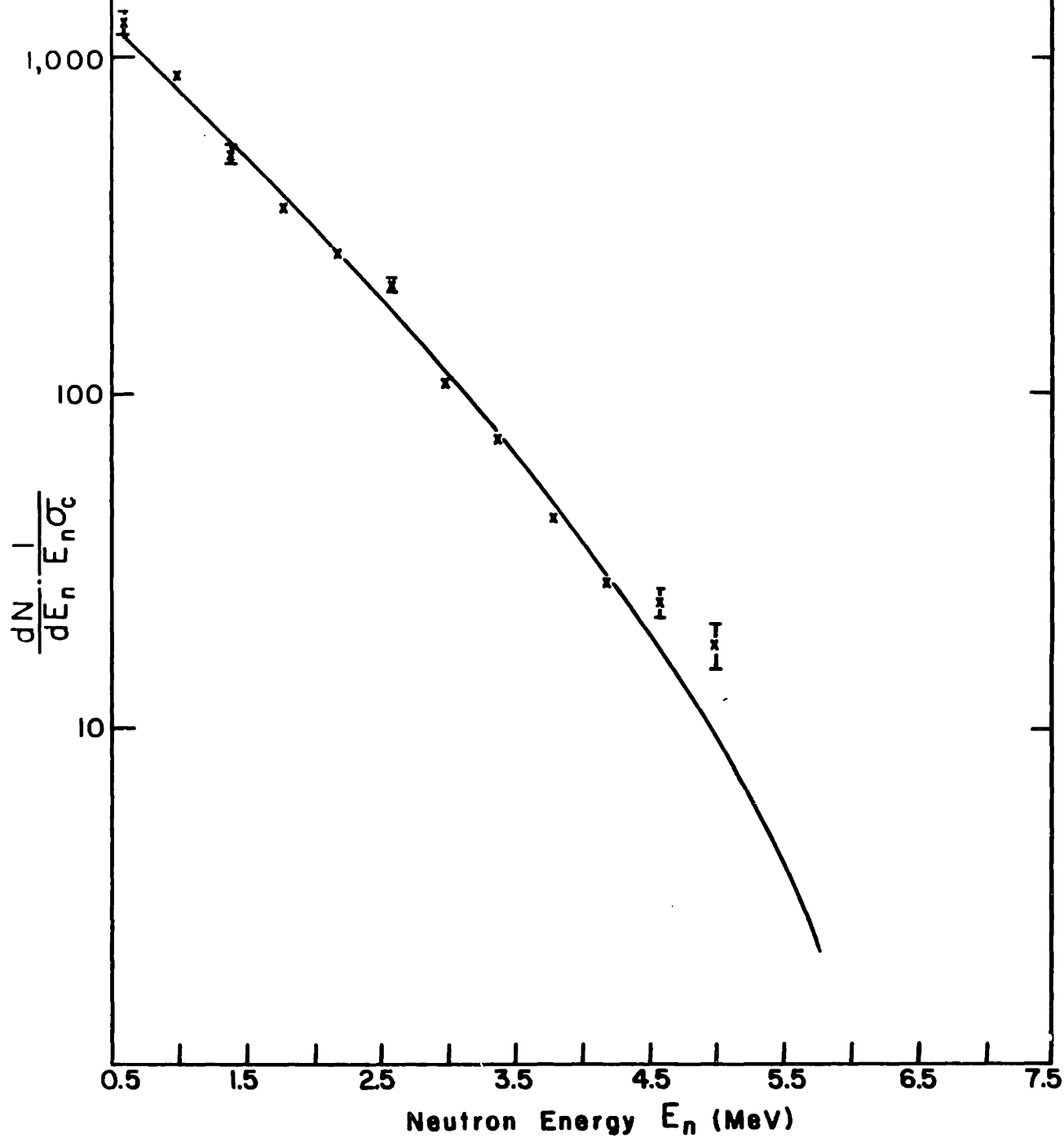
Fig. 24 Neutron Evaporation Spectrum

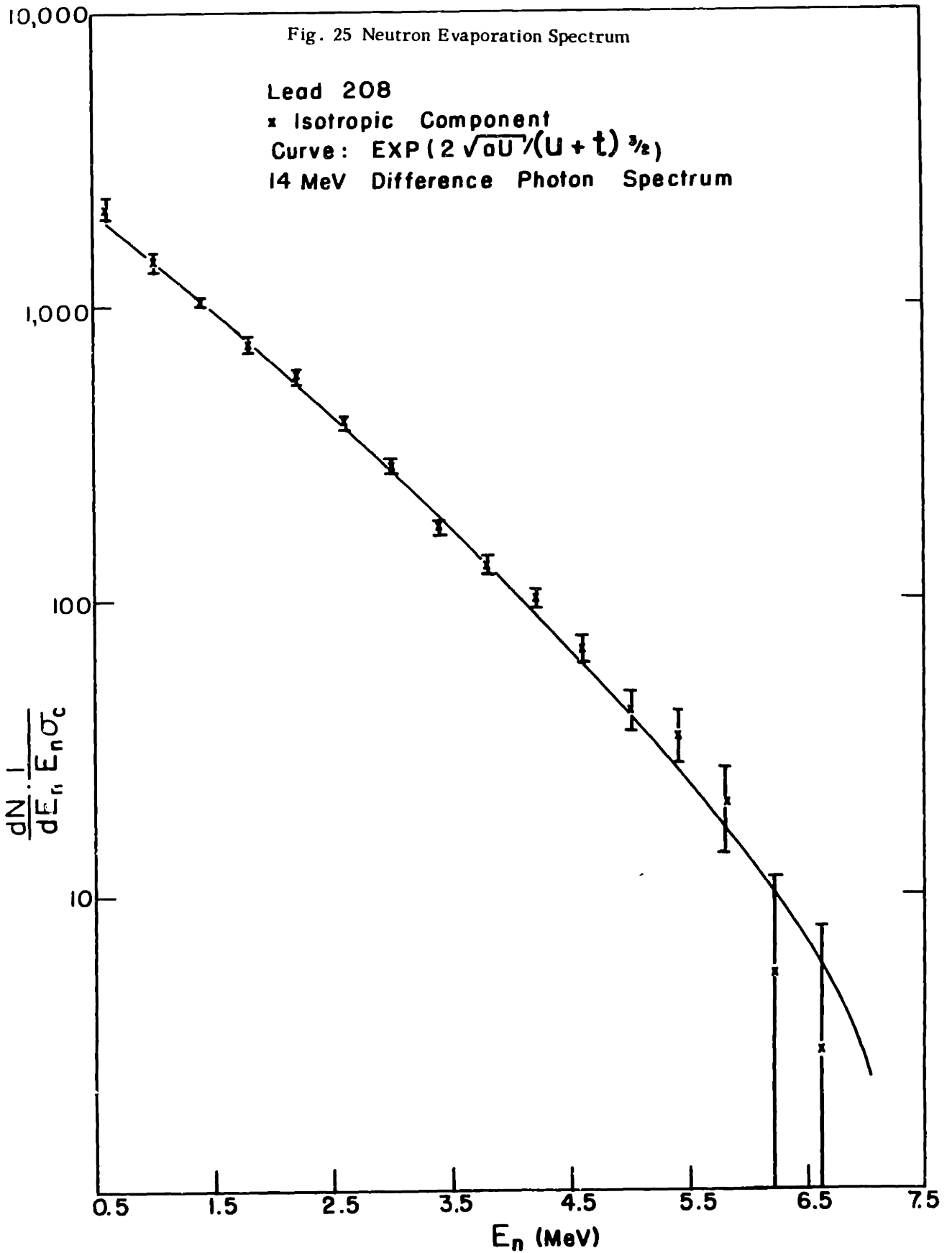
Lead 208

x Difference Spectrum - Direct Spectrum

Curve:  $\text{EXP}(2\sqrt{aU}/(U+t)^{3/2})$

13 MeV Difference Photon Spectrum







holds above 9 MeV. The negative tail of the 13 MeV photon difference spectrum occurs below 9 MeV, and therefore is less than 1 per cent. The third distortion is  $(\gamma, 2n)$  contamination of the neutron spectrum. The  $(\gamma, 2n)$  threshold for  $\text{Pb}^{208}$  is 14.11 MeV and 14.33 MeV for Bi (70). Therefore a second neutron can be emitted with energies up to 1.4 and 1.2 MeV respectively for the 14 MeV difference spectrum. Since the photon spectrum decreases rapidly at the tip, the second neutron will appear primarily in the 0.6 MeV bin. Using the  $(\gamma, n)$  and  $(\gamma, 2n)$  cross sections measured by Harvey et al (7), the photon spectrum shown in Fig. 10, and the level density parameters measured in this experiment, the  $(\gamma, 2n)$  yield was estimated to be about 14 per cent of the  $(\gamma, n)$  yield for  $\text{Pb}^{208}$ , and about 6 per cent for Bi. Approximately 10 per cent of the  $(\gamma, n)$  neutron spectrum is contained in the first bin (0.6 MeV), and therefore the  $(\gamma, 2n)$  neutrons could account for as much as 60 per cent of this data for  $\text{Pb}^{208}$  and 40 per cent for Bi. They also account for 17 per cent and 2 per cent respectively of the data in the 1.0 MeV bin. In the case of the 13 MeV data the  $(\gamma, 2n)$  contribution is negligible in both bins.

The result of these three distortions in the  $\text{Pb}^{208}$  and Bi data is to:

- increase the uncertainty of the low energy data because of the scattering calculation;
- increase the number of 0.6 MeV neutrons by 40 to 60 per cent for the 14 MeV data because of the  $(\gamma, 2n)$  contamination and
- reduce the number of 0.6 MeV neutrons by about 30 per cent due to the negative portion of the photon spectrum.

These effects cause the largest errors in the  $(\gamma, n)$  spectrum in the lowest energy bin, 0.6 MeV. This point was excluded from the calculation of the evaporation component. That is,  $j = 1$  in equation 66 of Chapter IV, section D, refers to the 1.0 MeV energy bin rather than the 0.6 MeV energy bin. This was done for all the targets. Referring to Figs. 21 to 24, it is seen that the  $\text{Pb}^{208}$  data seems qualitatively to confirm these conclusions. The 0.6 MeV point for the 14 MeV data is 18 per cent higher than the solid curve while in the 13 MeV data it is less than 10 per cent higher, and still within the estimated error. The bismuth data is about 5 per cent higher than the curve for both energies, which is within the estimated error.

#### d) Neutron Energy Spectra

The solid curve in Figs. 13 to 16 is the sum of the calculated evaporation component and direct component. Comparing Figs. 13 to 16 with Figs. 21 to 24, it is immediately evident from equation 78 that  $\sigma_C$  has a profound effect on the evaporation component. In fact if  $\sigma_C$  had been approximated by a constant, as it often is in the literature, the excellent fit achieved in Figs. 13 to 16 and 21 to 24 would be impossible. The values of  $\sigma_C$  are taken from a recent optical model calculation by Auerbach and Moore (62).

Glazunov et al (14) have measured the photoneutron spectra of Bi, Pb (natural abundance), Pt, and U from a 16 MeV bremsstrahlung spectrum with time-of-flight techniques at  $90^\circ$ . They fit their data with  $\frac{dN}{dE_n} \propto \frac{E_n}{T} e^{-E_n/T}$  (ie,  $\sigma_C = 1.0$ ) over the region 0.2 to 1.3 MeV. They find that the Pb and Bi photoneutron spectra exceed this curve at 2.0 MeV and above 3.0 MeV. They attempt to explain a broad peak at 2.0 MeV by invoking single particle transitions between excited levels of the compound nucleus. However if the  $\sigma_C$  from ref 62 had been included in the evaporation spectrum, this peak would be eliminated. The Bi photoneutron energy spectra data measured in other experiments, Bertozzi (50) and Kuchnir (69), were fit quite well using  $\omega(U) \propto e^{-E_n/T}$  with  $\sigma_C = \text{constant}$  for the level density of the residual nucleus. The disagreement between these data and the present data (and the data in ref 14) might be due to neutron scattering in the  $(\gamma, n)$  target. Neither of the above sets of data (50, 69) were corrected for neutron scattering. Such a correction would reduce the neutron spectra at low energies and improve the agreement with the present data. In yet other experiments on Pb and Bi (71, 72, 73, and 74) the neutron spectra were measured with emulsions. These experiments did not have sufficient statistics or low energy resolution to allow an evaluation of the role of  $\sigma_C$ .

#### e) Angular Distribution

The angular distributions for Bi and Pb<sup>208</sup> at three different bremsstrahlung endpoints -- 15, 14 and 13 MeV -- are plotted in Figs. 26 and 27. The three sets of data coincide within statistics. In the region where the evapora-

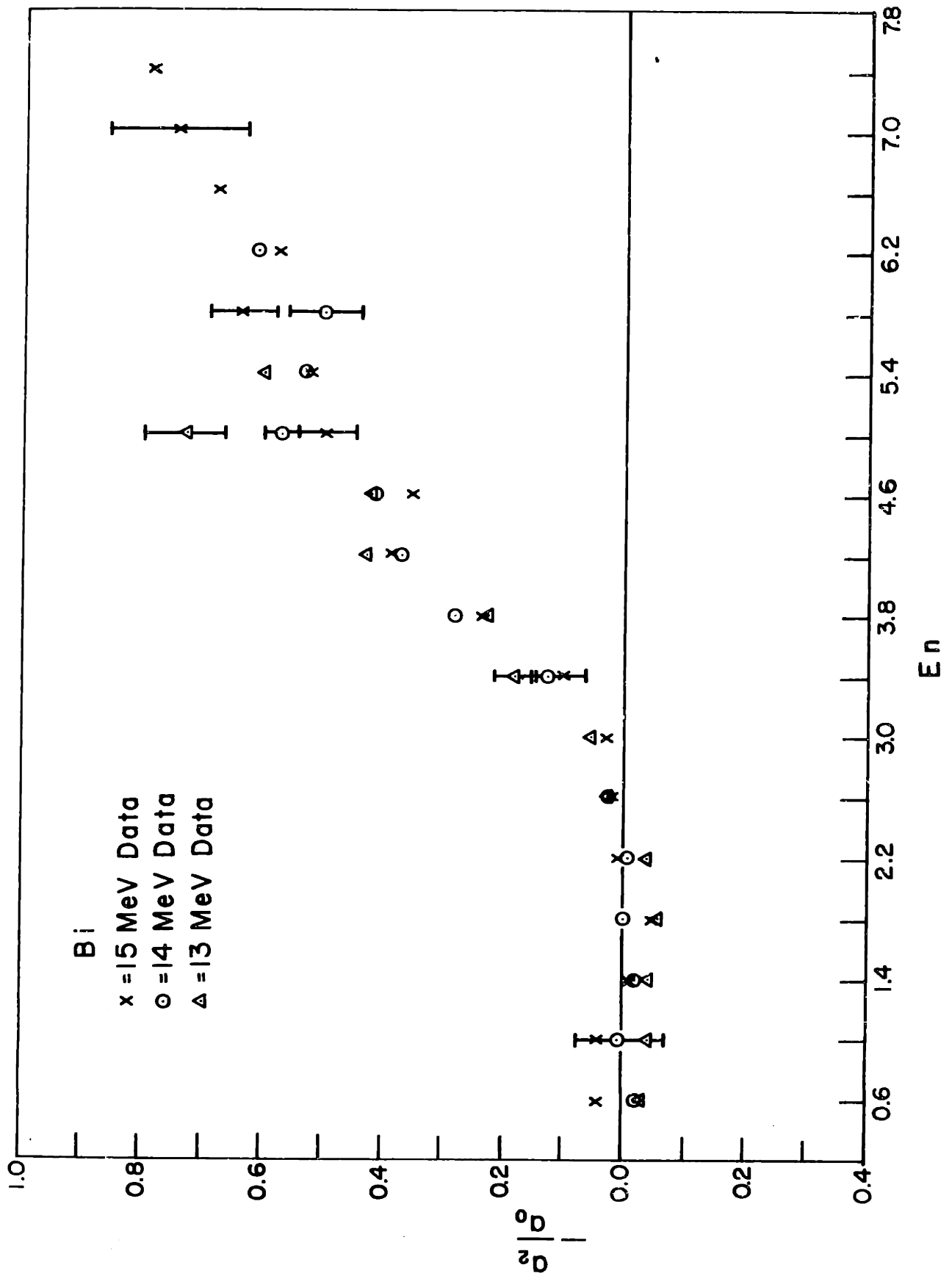


Fig. 26 Photoneutron Angular Distributions

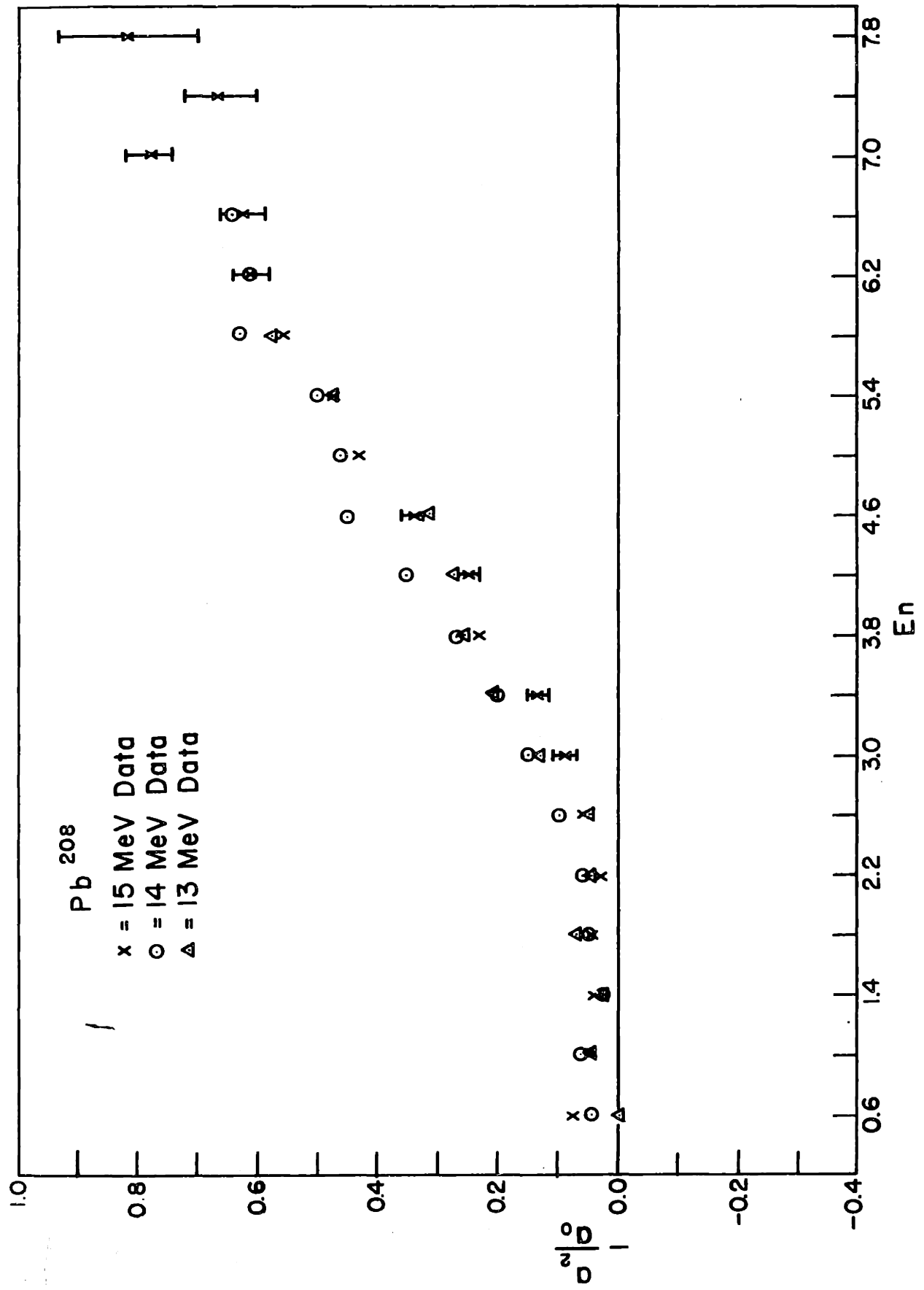


Fig. 27 Photoneutron Angular Distributions

tion component dominates (0.6 to 3.0 MeV) the Bi angular distribution is isotropic as expected, except for the 13 MeV run which tends to be backward peaked in this region. The 13 MeV data was collected using a thick Bi disk as a  $(\gamma, n)$  target. Neutron scattering in this target resulted in a large distortion of the neutron spectrum at low neutron energies. This backward peaking may be an underestimation of the scattering correction. The higher counting rates encountered at 15 and 14 MeV allowed the use of a small Bi cylinder as a target, which reduced the distortion of the energy spectra due to neutron scattering. The  $\text{Pb}^{208}$  data shows an anisotropy at low energies of about  $0.04 \pm 0.02$ . One would expect the statistically emitted neutrons to be isotropic. However the residual nucleus,  $\text{Pb}^{207}$ , unlike the other elements studied in this experiment, has only a few levels in the first three MeV of excitation (about 7 levels). Therefore the neutrons produced by a low energy gamma ray will be making transitions to discrete, widely-separated levels, and could have an average non-isotropic distribution. Thus the statistically emitted neutrons may be contaminated by non-isotropic neutrons from low energy gammas.

For example compare the yield of 1 MeV neutrons from 14 and 10 MeV photons. At 10 MeV the photon absorption cross section is about  $\frac{1}{5}$  of that at 14 MeV and the photon intensity is larger by a factor of three (Fig. 10). About 15 per cent of the neutrons produced by the 14 MeV photons will appear in a 0.5 MeV bin at 1.0 MeV. The 10 MeV photons will produce neutrons with energies of 0.26, 0.5, 1.0, 1.7, 2.03, and 2.6 MeV (see Table XIV). If these levels are approximately equally populated, about 10 per cent of these neutrons will appear in the 0.5 MeV bin at 1.0 MeV. The ratio of anisotropic to statistical neutrons is nearly  $\frac{2}{5}$ . Therefore the neutrons produced by 10 MeV photons would only require an angular distribution of  $-a_2/a_0 \approx 0.1$  to account for the observed  $-a_2/a_0 = 0.04$ . Angular distribution measurements made with 10 MeV bremsstrahlung spectra (not included in this thesis) indicate that such values of  $-a_2/a_0$  are reasonable.

As the neutron energy increases, the anisotropy increases, reaching a maximum of  $-a_2/a_0 \approx 0.7$  for both  $\text{Pb}^{208}$  and Bi. The angular distribution for single particle transitions are listed in Table XIII. The largest  $-a_2/a_0$  listed

is 0.5 ( $p \rightarrow d$ ). These values are calculated from equations 11a and 11b which do not take into account the possibility of interference between different final states. For example, consider the transition  $p^{1/2} \rightarrow d^{3/2}$  or  $s^{1/2}$ . Both s and d wave neutrons are possible and the angular distribution is given by equation 14 as

$$\frac{B}{A} = \frac{3}{2} \left[ \frac{|K_D|^2 - 2|K_D K_S| \cos \delta_{SD}}{|K_D|^2 + |K_S|^2 + 2|K_D K_S| \cos \delta_{SD}} \right] \quad (81)$$

where the K's are the appropriate matrix elements,  $\delta_{SD}$  is the sum of the phase shifts of the s and d wave functions, and  $W(\Theta) = A + B \sin \Theta$ . Converting to  $W(\Theta) = a_0 + a_2 P_2(\cos \Theta)$ , one finds

$$-\frac{a_2}{a_0} = \frac{\frac{2B}{3A}}{1 + \frac{2B}{3A}} \quad (82)$$

$$-\frac{a_2}{a_0} = \frac{|K_D|^2 - 2|K_D K_S| \cos \delta_{SD}}{2|K_D|^2 + |K_S|^2} \quad (83)$$

If  $|K_S|^2 = 0$ ,  $-\frac{a_2}{a_0} = 0.5$  in agreement with equation 11a; if  $|K_D|^2 = 0$ ,  $-\frac{a_2}{a_0} = 0$  in agreement with equation 11b; but if  $\cos \delta_{SD} = -1$  and  $|K_D|^2 = |K_S|^2$ , then  $-a_2/a_0$  can reach a maximum value of 1.0. Thus a  $p^{1/2}$  hole ( $Pb^{207}$  ground state) can be reached by a transition having  $-a_2/a_0$  equal to 0.0 to 1.0.

Heiss (46) has attempted to calculate the angular distribution including the interference terms using a Saxon-Wood potential and spin orbit coupling. He dealt with only one gingle particle transition for each nucleus, however. His results, for the angular distribution of a neutron directly emitted from the  $2f^{5/2}$  shell of bismuth, are listed below in Table XVI.

Table XVI  
Angular Distribution of Photoneutrons from the  $2f^{5/2}$  Level of Bi

$E_n$	B/A	$-a_2/a_0$
7.0	1.5	0.5
8.0	1.9	0.55
9.0	2.4	0.615
10.0	2.7	0.645
11.0	3.3	0.69

Comparing this with Table XIII, where the  $2f^{5/2}$  transition is listed as having a maximum  $-a_2/a_0$  of 0.4, it can be seen that the interference effects have increased the angular distribution considerably. The present experimental results for Bi only extend up to 8.0 MeV and have a larger anisotropy than the values calculated by Heiss. However the inclusion of the  $p^{1/2}$  and  $p^{3/2}$  transitions should increase  $-a_2/a_0$ .

## B. Lead 207

### a) Experimental Data

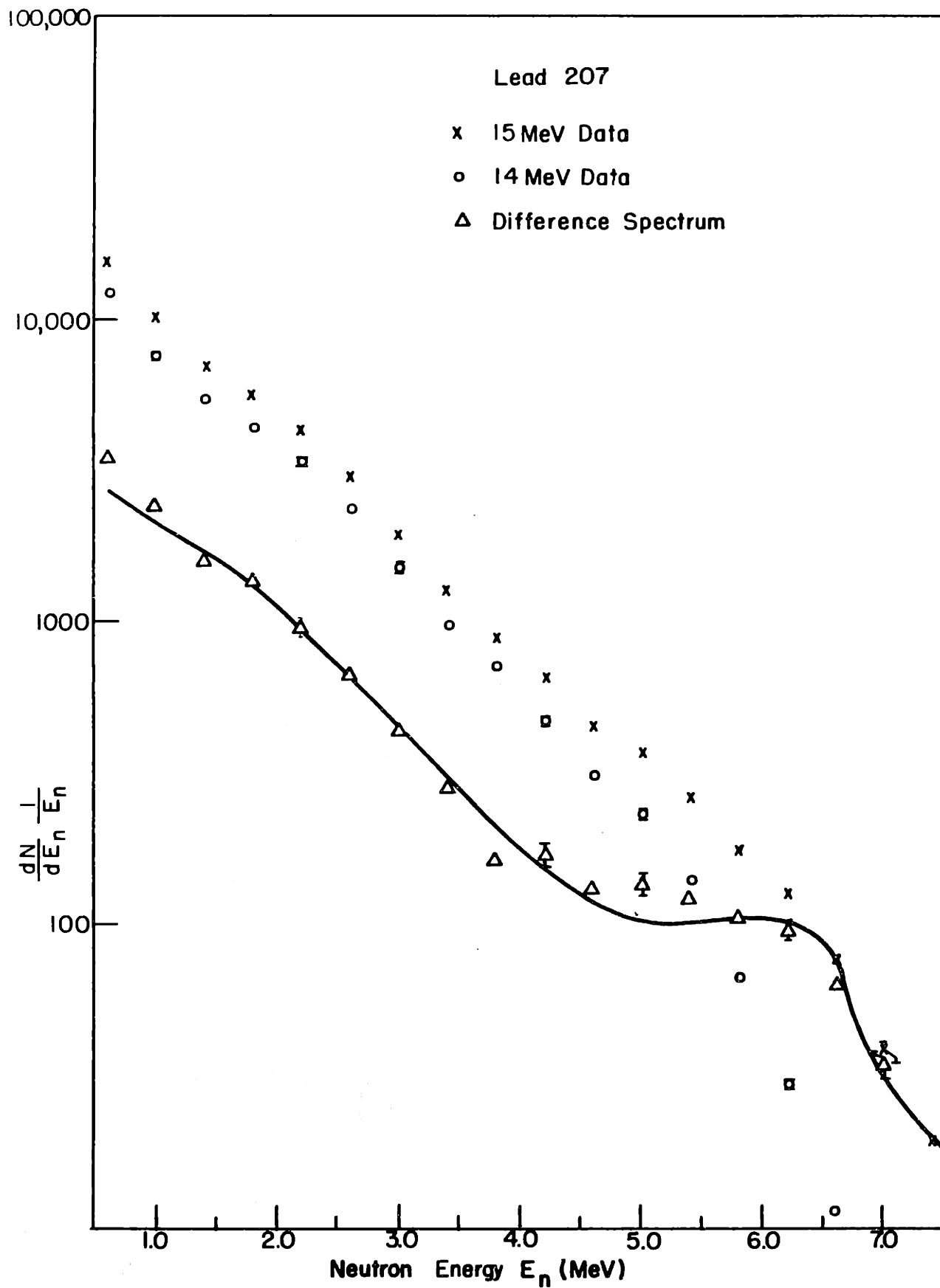
The photoneutron energy spectra  $\frac{dN}{dE_n} \frac{1}{E_n}$  for  $Pb^{207}$  are plotted vs  $E_n$  in Figs. 28 and 29. The information contained in these graphs is the same as that described for  $Pb^{208}$  (see section (a) of part A of this chapter).

### b) Direct Spectrum

The energies and  $j$  values of the  $Pb^{206}$  levels (66) are listed in Table XVII. Guman et al (75) have calculated the levels of  $Pb^{206}$  taking into account pair correlations. They list the wave functions of each level as a linear combination of the single particle hole states. The squares of the coefficients of the configurations consisting of a hole in the  $p^{1/2}$  shell (the ground state of  $Pb^{207}$ ) and a hole in one other shell are listed in Table XVII. (The wave functions for the ground state and the first  $1^+$  state were taken from the results of the  $Pb^{207}(p,d)Pb^{206}$  measurements of Cohen et al (32, 76, 77).)  $S(E_n)$  was calculated for  $Pb^{207}$  from equation 73 of Chapter IV using the relative transition strengths,  $f_{\ell}$ , calculated by Wilkinson\* from Table XIII; the  $T_j$ 's from ref 61; and the parentage of the residual nuclear levels given in Table XVII. If more than one level is made up of a given configuration, the transition strength for this configuration was then divided amongst those levels in proportion to the coefficients listed in Table XVII. In the case of the  $p^{1/2} p^{1/2}$  configuration, the transition strength was reduced by a factor of two to take into account the missing  $p^{1/2}$  neutron. The results of the calculation are shown in Figs. 30 and 31. The agreement of the shape of  $S(E_n)$  and the data

\*The relative transition strengths calculated by Wilkinson will be used for the remaining targets, since Pal's calculations are specifically for  $Pb^{208}$ .

Fig. 28 Neutron Energy Spectra





# LEAD 207

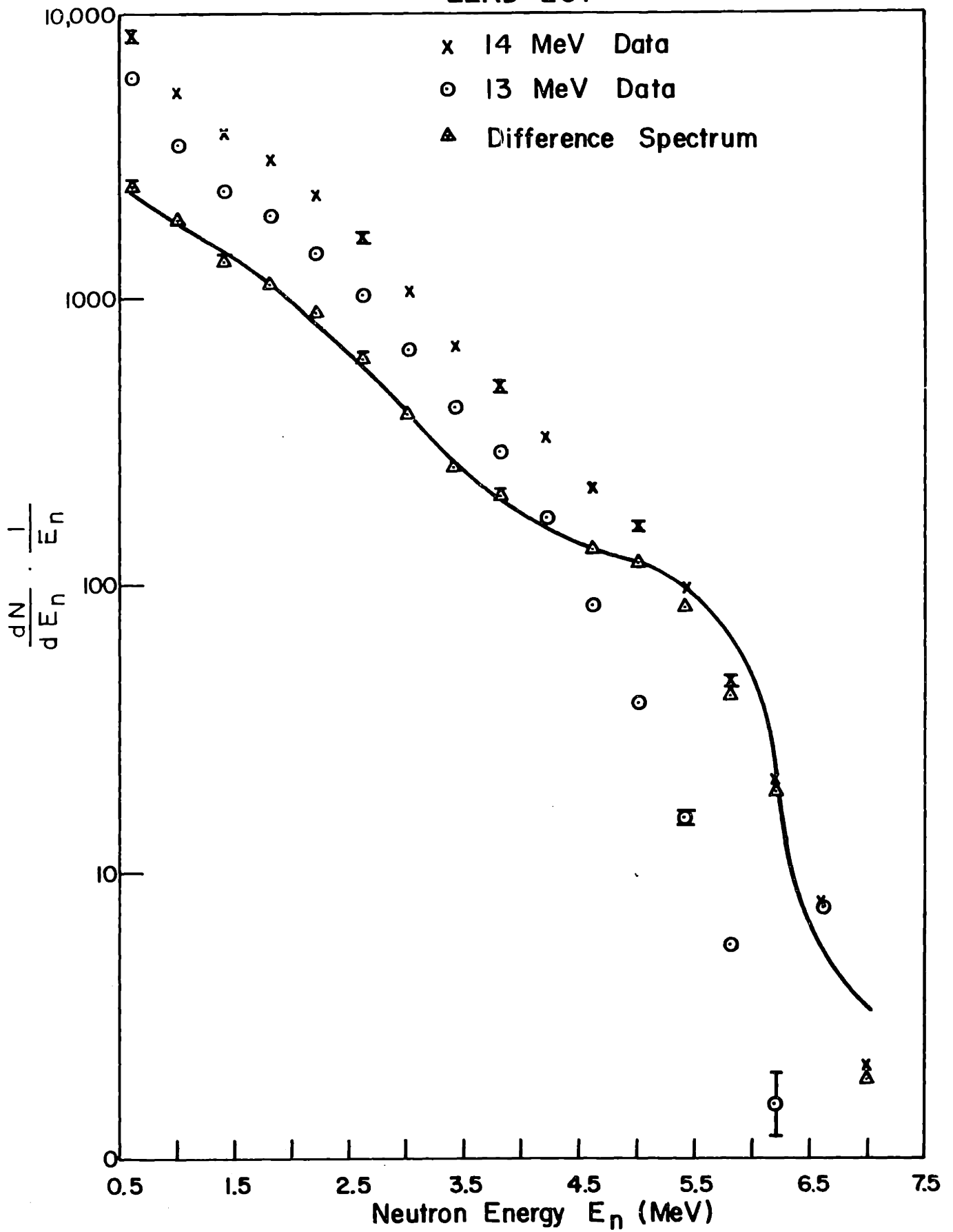


Fig. 29 Neutron Energy Spectra

Table XVII  
Excited States of Pb<sup>206</sup>

Energy* (MeV)	Spin*	Configuration**											
		p <sup>1/2</sup>	p <sup>1/2</sup>	p <sup>1/2</sup>	p <sup>3/2</sup>	p <sup>1/2</sup>	f <sup>5/2</sup>	p <sup>1/2</sup>	f <sup>7/2</sup>	p <sup>1/2</sup>	i <sup>13/2</sup>	p <sup>1/2</sup>	h <sup>9/2</sup>
0.0	0 <sup>+</sup>	0.5											
0.8	2 <sup>+</sup>			0.2		0.6							
1.15	0 <sup>+</sup>	0.12											
1.34	3 <sup>+</sup>					0.94							
1.47	2 <sup>+</sup>			0.64		0.26							
1.71	1 <sup>+</sup>			1.0									
1.78	0 <sup>+</sup>	0.09											
2.19	7 <sup>-</sup>									1.0			
2.39	6 <sup>-</sup>									1.0			
2.93	4 <sup>+</sup>							1.0					
3.11	3 <sup>+</sup>							1.0					
4.07	?												1.0

\* Nuclear Data Sheets (66)

\*\* Guman et al (75)

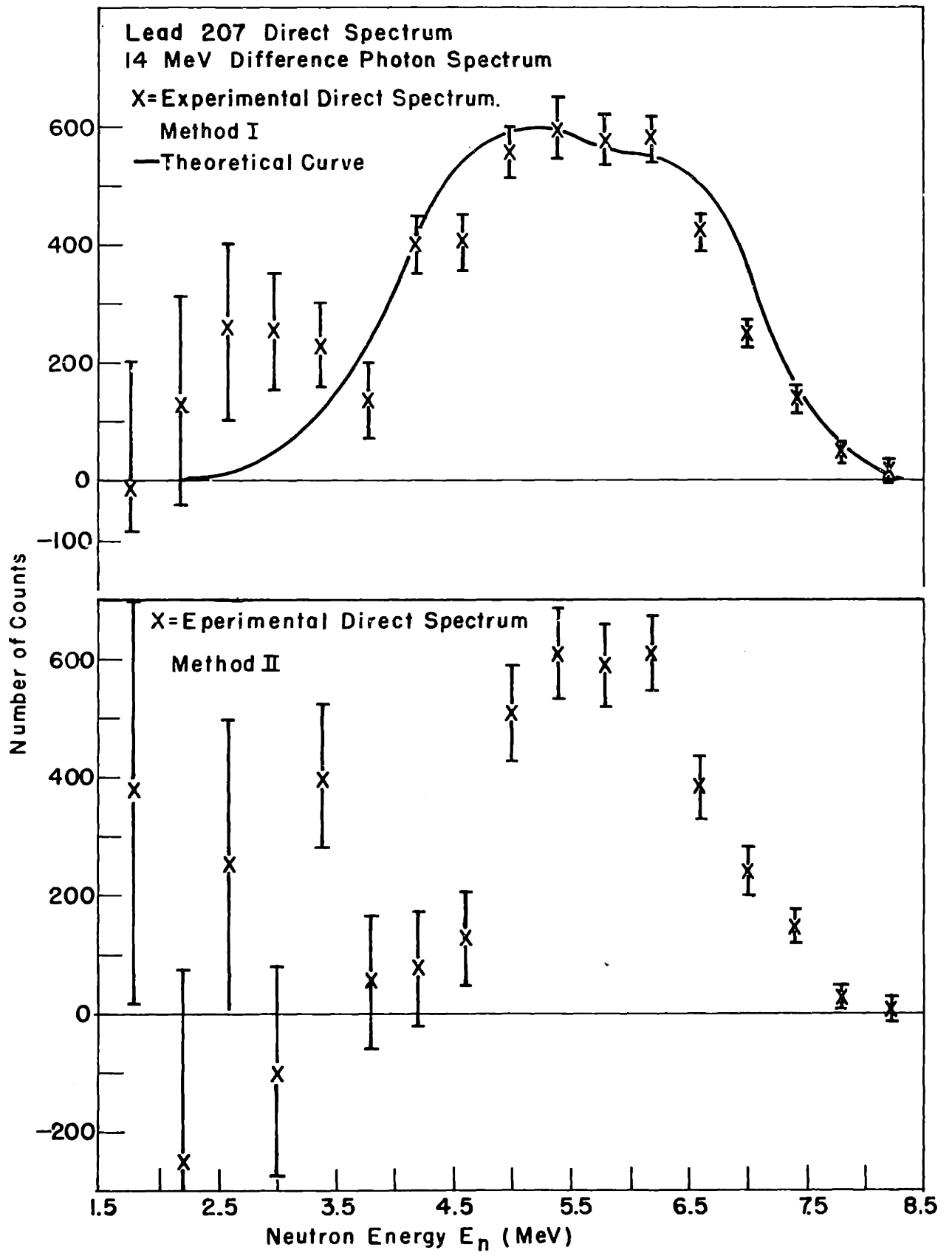


Fig. 30

# LEAD 207 DIRECT SPECTRUM

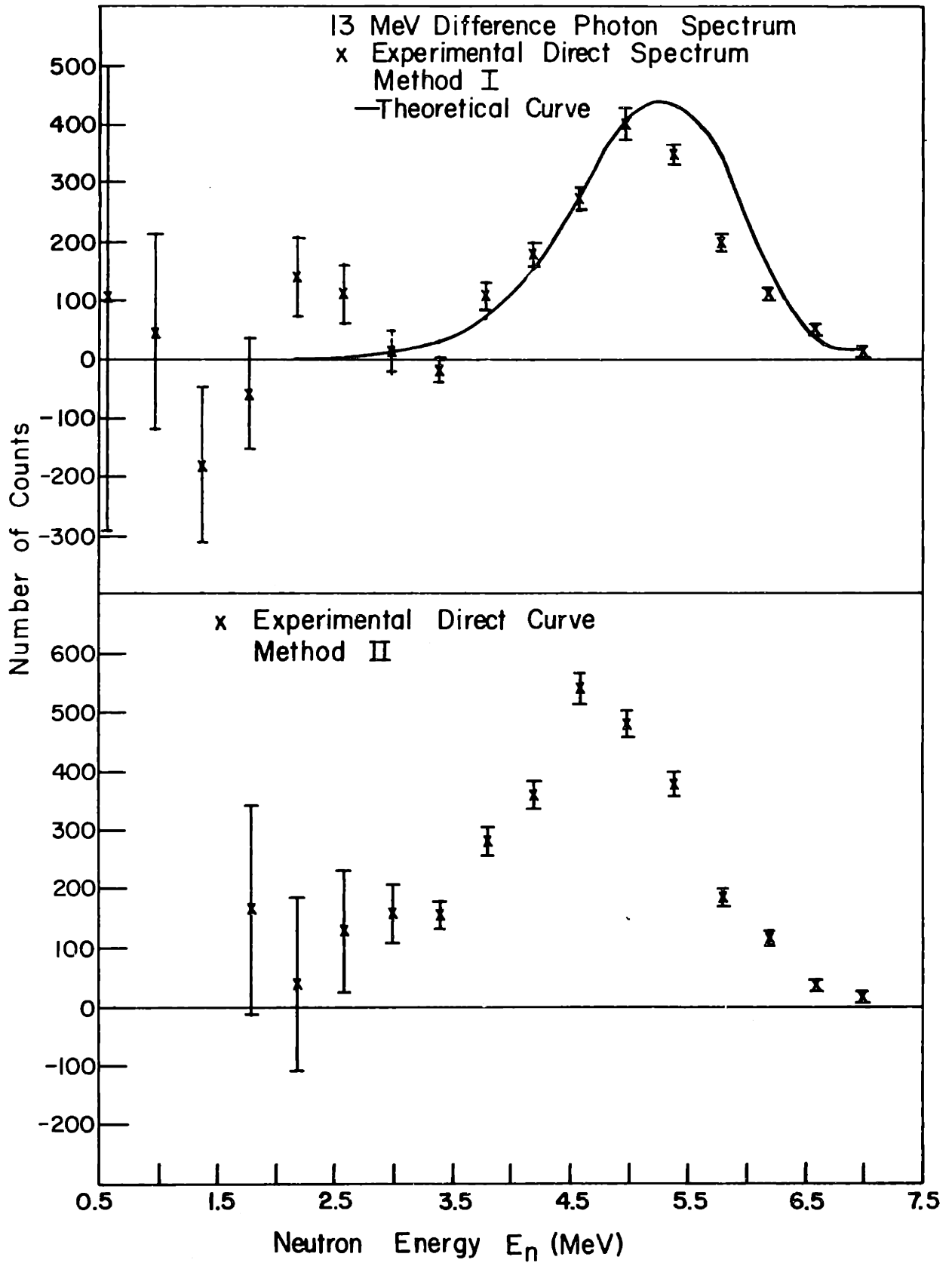


Fig. 31

is quite good. However, as in all the targets used, the calculated direct fraction is about 10 per cent of the experimental value.

An interesting feature of this spectrum is the fact that the  $\text{Pb}^{206}$  ground state configuration is only 70 per cent  $p^{1/2} p^{1/2}$  and the rest two holes in other shells. Since the  $\text{Pb}^{207}$  ground state is a  $p^{1/2}$  hole, direct emission to the  $\text{Pb}^{206}$  ground state is predicted to be 25 per cent of that for the  $\text{Pb}^{208}$  to  $\text{Pb}^{207}$  ground state transition, for the first 0.8 MeV below the neutron endpoint. Although the resolution at 8.0 MeV neutron energy is poor (about 0.6 MeV), the data does seem to agree with  $S(E_n)$ . When the data is analyzed channel by channel instead of in 0.4 MeV bins, this low cross section for the ground state transitions is more evident.

#### c) Evaporation Spectrum

The photoneutron evaporation spectra and the theoretical curves for  $\text{Pb}^{207}$  are shown in Figs. 32 and 33. The theoretical fit to the 13 MeV difference spectrum is excellent up to 5.0 MeV. The 0.6 and 1.0 MeV points of the 14 MeV difference spectrum are substantially above the theory. Since the  $(\gamma, 2n)$  threshold is 14.85 MeV (7, 70), this will affect only the 0.6 MeV point. Using the  $(\gamma, 2n)$  cross section from ref 7, the photon spectrum from Fig. 10, and the level density parameter measured in this experiment, the  $(\gamma, 2n)$  contamination was estimated to be 4 per cent of the  $(\gamma, n)$  data at 0.6 MeV, which is a factor of ten too small to account for the discrepancy between theory and experiment. In view of the agreement found for the 13 MeV data, it is difficult to explain this discrepancy.

#### d) Angular Distribution

The angular distribution of the photoneutrons from 15, 14 and 13 MeV bremsstrahlung spectra for  $\text{Pb}^{207}$  are shown in Fig. 34. The angular distributions are quite similar to the angular distributions of the  $\text{Pb}^{208}$  data. The absence of one  $p^{1/2}$  neutron seems to have little effect. The low energy neutrons are isotropic, unlike the situation for  $\text{Pb}^{208}$ . This could be explained by the larger number of levels below 3.0 MeV in  $\text{Pb}^{206}$  compared to  $\text{Pb}^{207}$ .

10,000

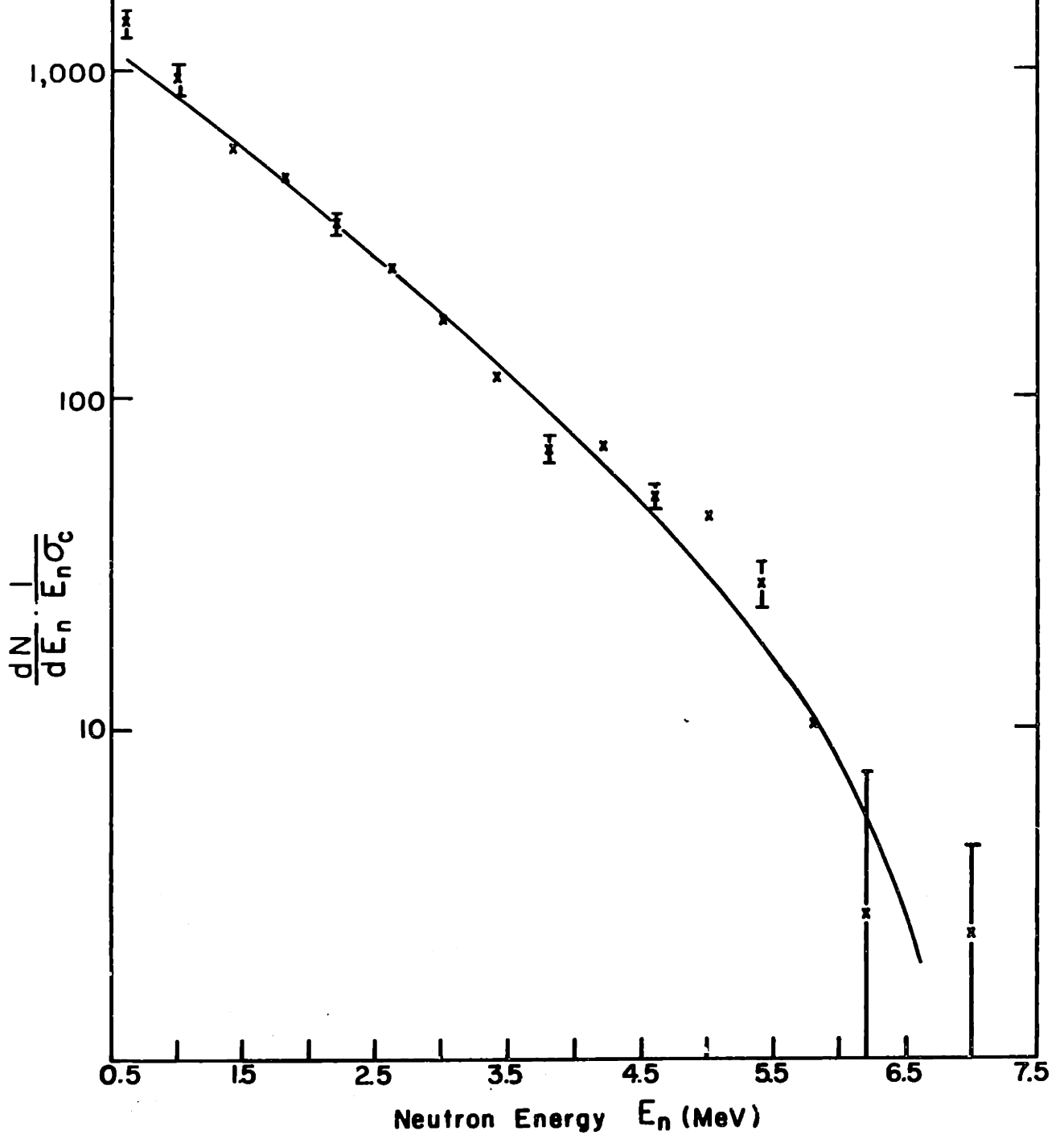
Fig. 32 Neutron Evaporation Spectrum

Lead 207

x Difference Spectrum - Direct Spectrum

Curve:  $\text{EXP}(2\sqrt{aU}(U+t)^{3/2})$

14 MeV Difference Photon Spectrum



10,000

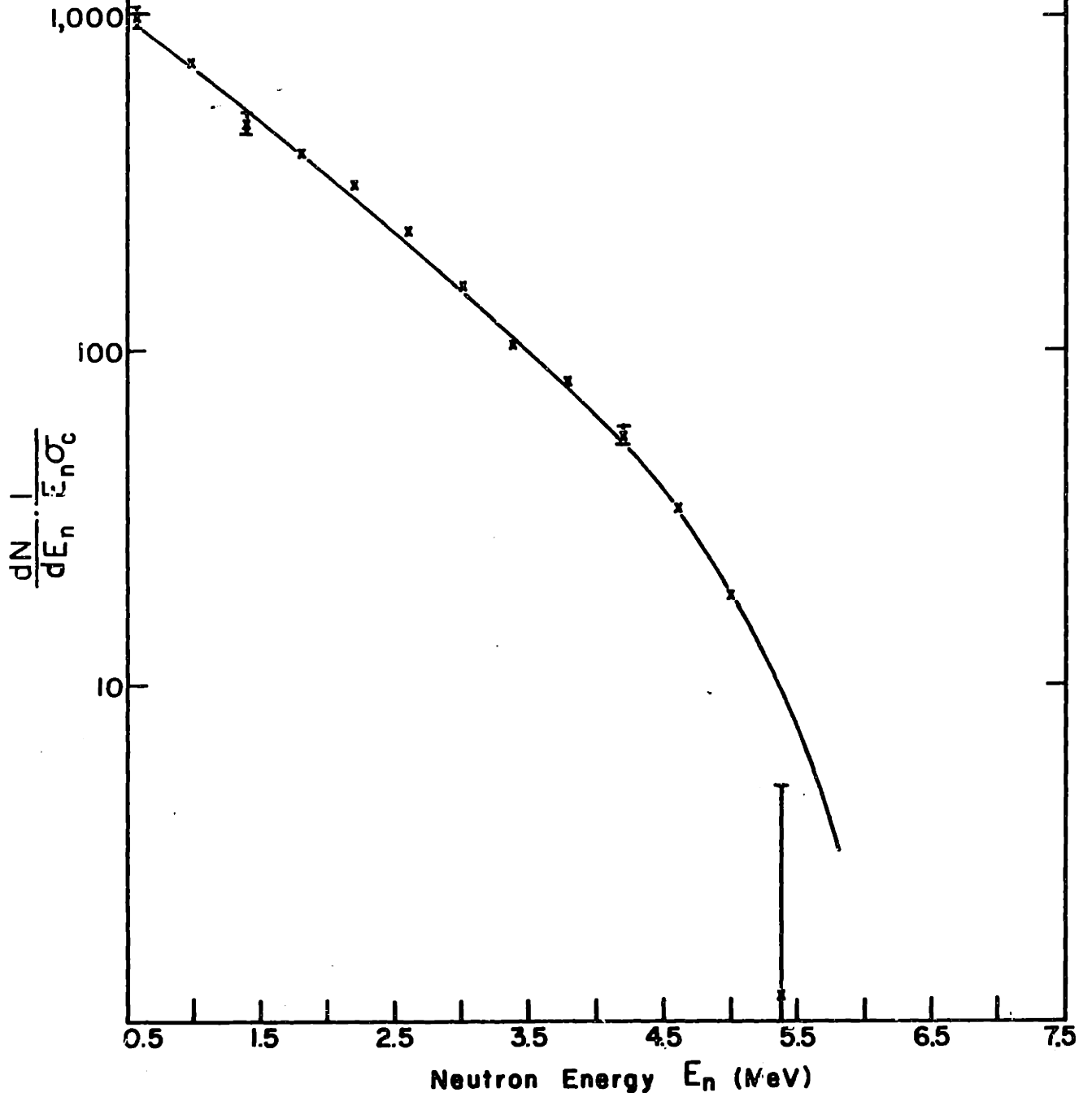
Fig. 33 Neutron Evaporation Spectrum

Lead 207

x Difference Spectrum - Direct Spectrum

Curve:  $\text{EXP}(2\sqrt{aU}/(U+t)^{3/2})$

13 MeV Difference Photon Spectrum



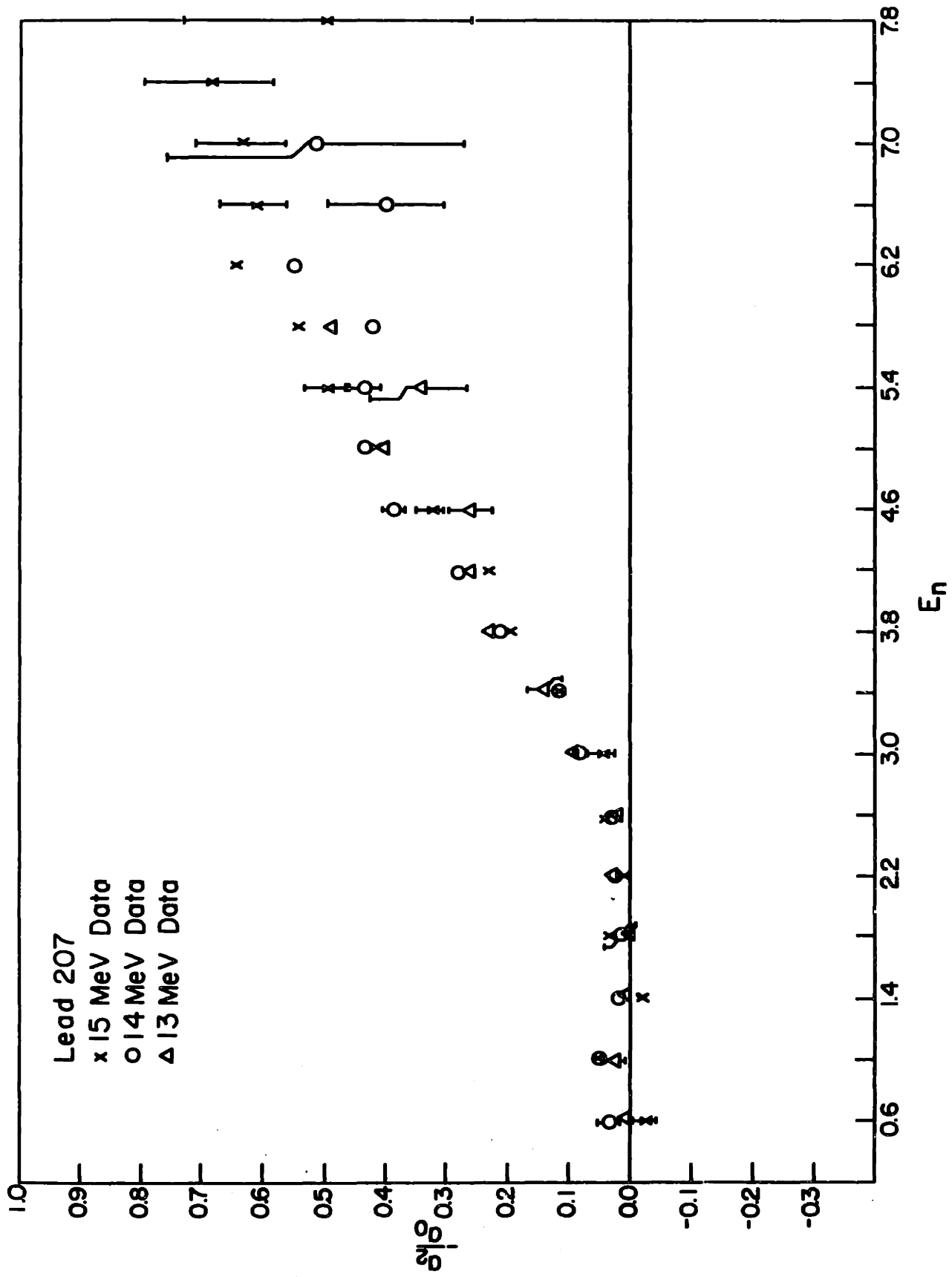


Fig. 34 Photoneutron Angular Distributions



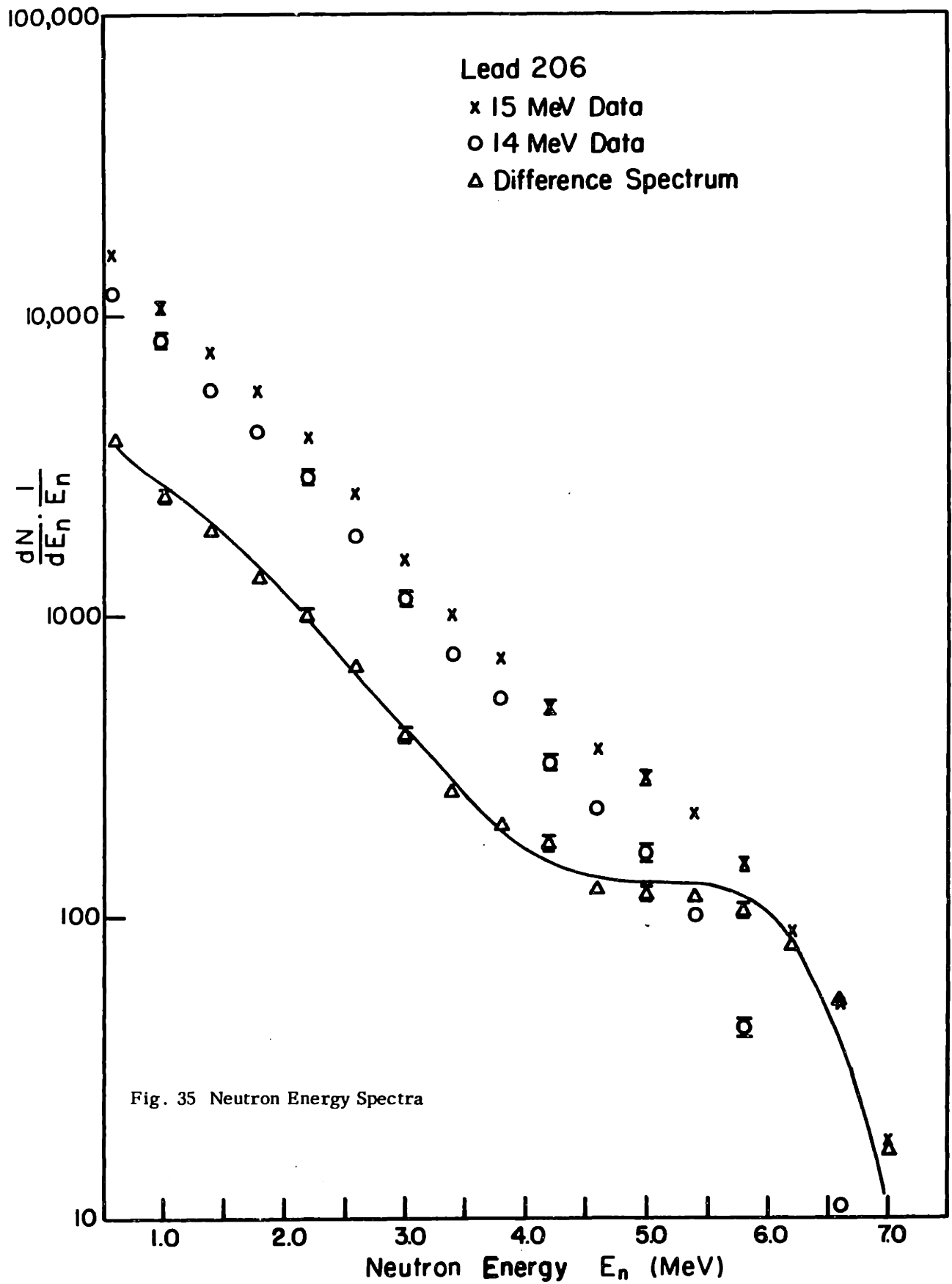
## C. Lead 206 and Thallium

### a) Experimental Data

The photoneutron energy spectra  $\frac{dN}{dE_n} \frac{1}{E_n}$  vs  $E_n$  for  $\text{Pb}^{206}$  is plotted in Figs. 35 and 36. As before, each graph contains two experimental photoneutron spectra and their difference. The two neutron spectra were generated by two bremsstrahlung spectra with endpoints of either 15 and 14 MeV or 14 and 13 MeV. The difference represents the photoneutron spectrum resulting from a photon spectrum peaked at 14 MeV or 13 MeV respectively, which is the difference of the corresponding bremsstrahlung spectra. In the case of thallium, the neutron data from the 14 MeV bremsstrahlung run was lost due to electronic problems. Therefore the photoneutron energy spectra for thallium, plotted in Fig. 37, contains two experimental spectra generated by two bremsstrahlung spectra with endpoints of 15 and 13 MeV, and their difference, which represents the photoneutron spectrum resulting from a photon spectrum peaked at 13.5 MeV with a 3 MeV FWHM. The significance of the solid curves and error bars has been discussed in section A of this chapter.

### b) Direct Spectrum

Since the configurations of the levels of  $\text{Pb}^{205}$ , the residual nucleus, are not as well known as those of  $\text{Pb}^{207}$  and  $\text{Pb}^{206}$ , one is forced to make some assumptions about the character of the hole states. Table XVIII lists the known levels of  $\text{Pb}^{205}$  (66). The first column lists the spins of the levels and the second column lists their energies. (Doubtful spin assignments are bracketed.) The next two columns list a level scheme of intrinsic single particle states taken from a shell model calculation by Ross et al (64). The  $f^{5/2}$  shell was assigned zero excitation energy to account for the missing  $p^{1/2}$  shell neutrons. (The ground state of  $\text{Pb}^{206}$  was assumed to have two  $p^{1/2}$  holes.) The interaction between the holes will mix the intrinsic states, but as can be seen from Table XVIII, levels of the appropriate spin appear at approximately the energies predicted by the shell model. The single particle character of the levels appears to persist despite the configuration mixing. Therefore  $S(E_n)$  for  $\text{Pb}^{206}$  and thallium were calculated using the shell model states listed in Table XVIII, the



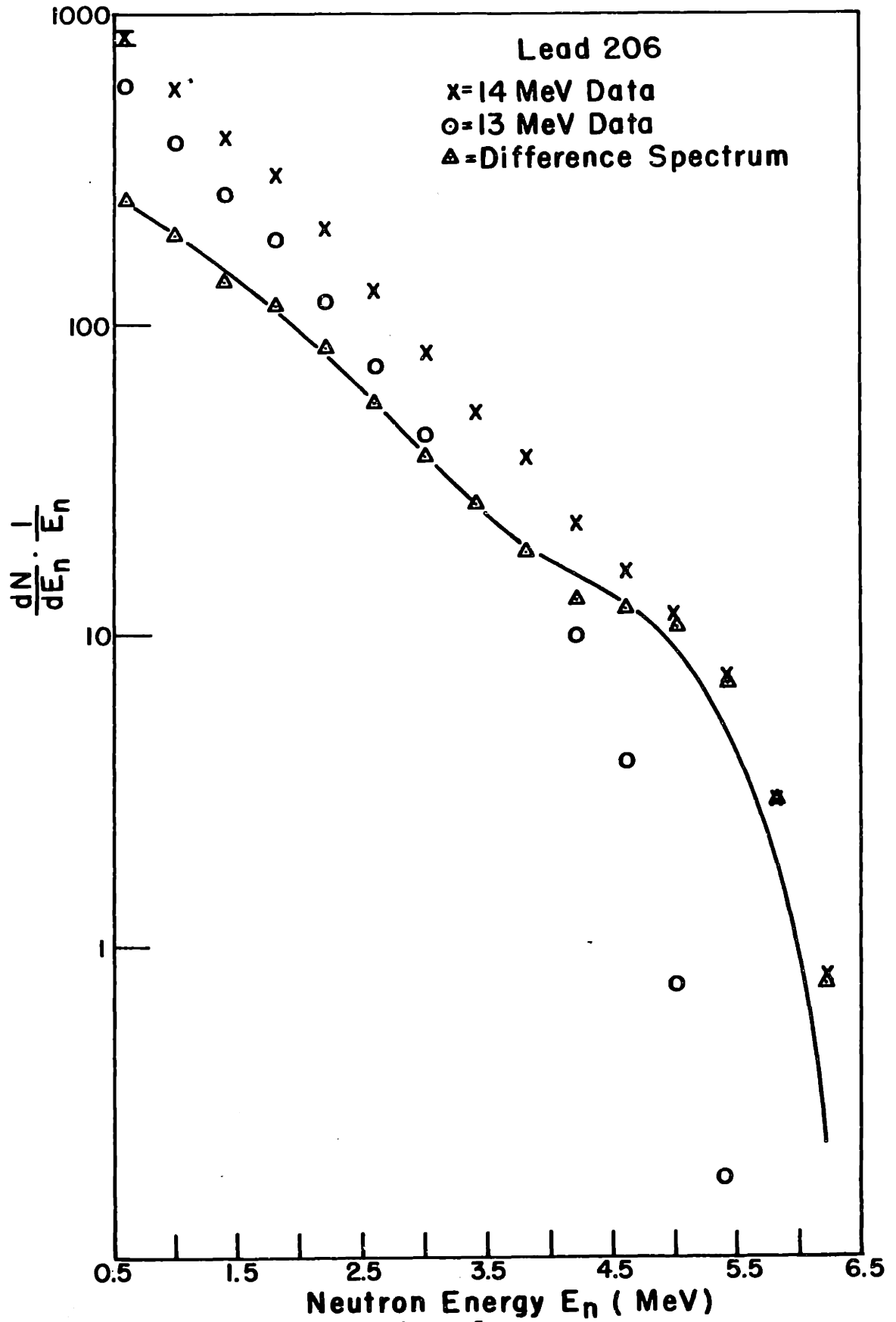


Fig. 36 Neutron Energy Spectra

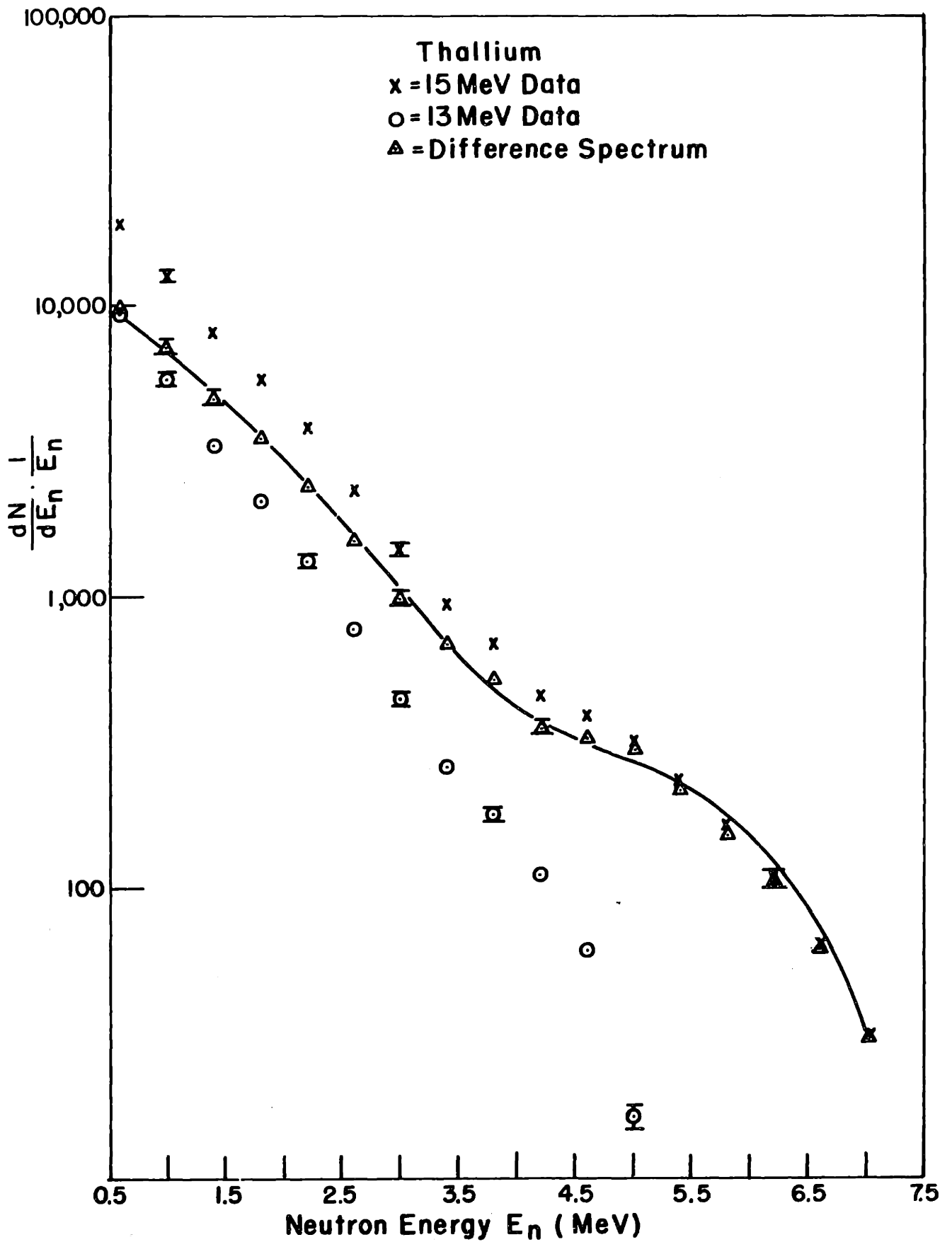


Fig. 37 Neutron Energy Spectra

Table XVIII  
Excited States of Pb<sup>205</sup>

Spin*	Energy (MeV)*	Shell Model States**		
		Energy (MeV)	Used for Thallium	Used for Pb <sup>205</sup>
$\frac{5}{2}^-$	0.0	0.0	$2f^{5/2}$	$2f^{5/2}$
$\frac{1}{2}^-$	0.002			
$\frac{3}{2}^-$	0.26	0.32	$3p^{3/2}_+$	$3p^{3/2}$
?	0.41			
?	0.58			
$\frac{7}{2}^-$	0.703			$2f^{7/2}$
?	0.761			
?	0.79			
$\frac{9}{2}^-$	0.988			$h^{9/2}$
$\frac{13}{2}^+$	1.014	1.06	$i^{13/2}_+$	$i^{13/2}$
$[\frac{5}{2}^-, \frac{7}{2}^-]$	1.044			
?	1.499			
?	1.615			
$\frac{7}{2}^-$	1.766	1.77	$2f^{7/2}_-$	$2f^{7/2}$
?	1.777			
$\frac{9}{2}^+$	2.566			
$\frac{9}{2}^+$	2.610			
$\frac{9}{2}^-$	2.72	2.9	$h^{9/2}_-$	$h^{9/2}$

\* Nuclear Data Sheets (66)

\*\* Ross, Mark and Lawson (64)

transition strengths,  $f_{\ell}$ , from Table XIII column two, the  $T_j$ 's from ref 61, and equation 73. In both cases the target nuclei were assumed to have two holes in the  $p^{1/2}$  shell. The  $Pb^{205}$  level structure was modified by assuming that the  $f^{7/2}$  hole configuration was equally divided between the 1.77 MeV level, which corresponds to the level predicted by the shell model, and the  $\frac{7}{2}$ -level found at 0.703 MeV. Also the  $h^{9/2}$  hole configuration was divided between the 2.7 MeV level, which corresponds to the level predicted by the shell model, and the  $\frac{9}{2}$ -level found at 0.99 MeV. This was an attempt to make  $S(E_n)$  more realistic by including some levels in the large gap between the  $p^{3/2}$  shell and the  $f^{7/2}$  shell. (The  $i^{13/2}$  shell, which occurs between these two shells, contributes very little to  $S(E_n)$  due to the small  $T_j$  for  $\ell = 7$  neutrons.) The level scheme used for  $Pb^{205}$  is listed in the last column of Table XVIII. The unmodified shell model level scheme listed in column four was used for thallium. The results are shown in Figs. 38, 39, and 40. The  $S(E_n)$  calculated for  $Pb^{206}$  appears to be narrower than the direct spectrum obtained with the second method (assuming an isotropic evaporation component, and a constant angular distribution for the direct component). This would indicate that the direct emission is not exhausted by the low lying levels of the residual nucleus, and that there is a sizable resonance direct decay to levels above 2 MeV. On the other hand, the experimental points found by the first method agree quite well with the  $S(E_n)$  calculated for the 14 MeV photon spectrum and are even narrower than the  $S(E_n)$  calculated for the 13 MeV photon spectrum. This seems to indicate that  $S(E_n)$  might be a reasonable approximation, and that the second method is incorrect. This would require that  $-a_2/a_0$  increase with decreasing neutron energy in the region from 3.0 to 5.0 MeV neutron energy.

The thallium data agrees with the calculated  $S(E_n)$  and the two methods of determining the direct component agree within the statistical uncertainty of the data.

### c) Evaporation Spectrum

The photoneutron evaporation spectra and the theoretical curves fitted to the data are shown in Figs 41, 42, and 43. The experimental data and the

# LEAD 206 - DIRECT SPECTRUM

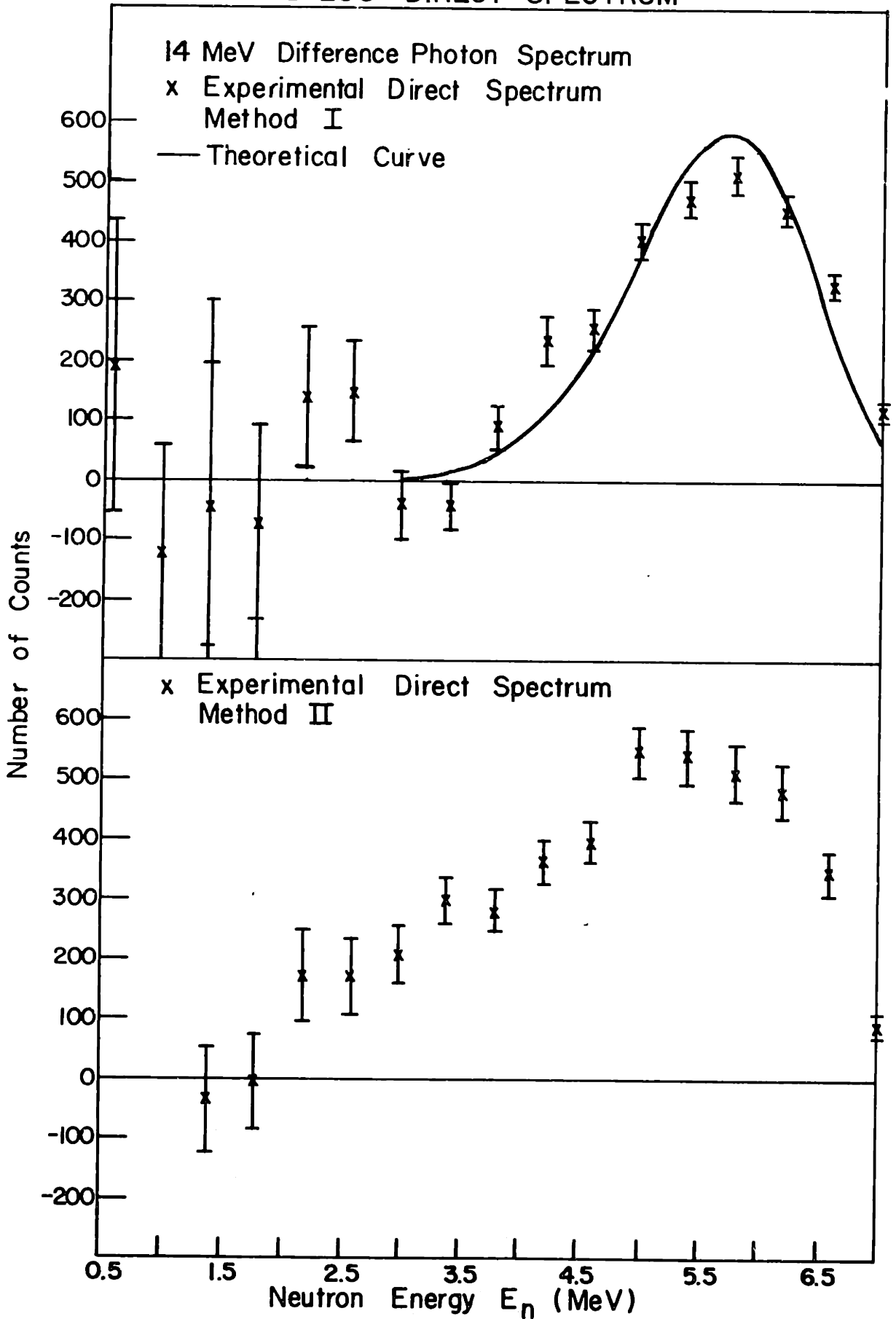


Fig. 38

# LEAD 206 - DIRECT SPECTRUM

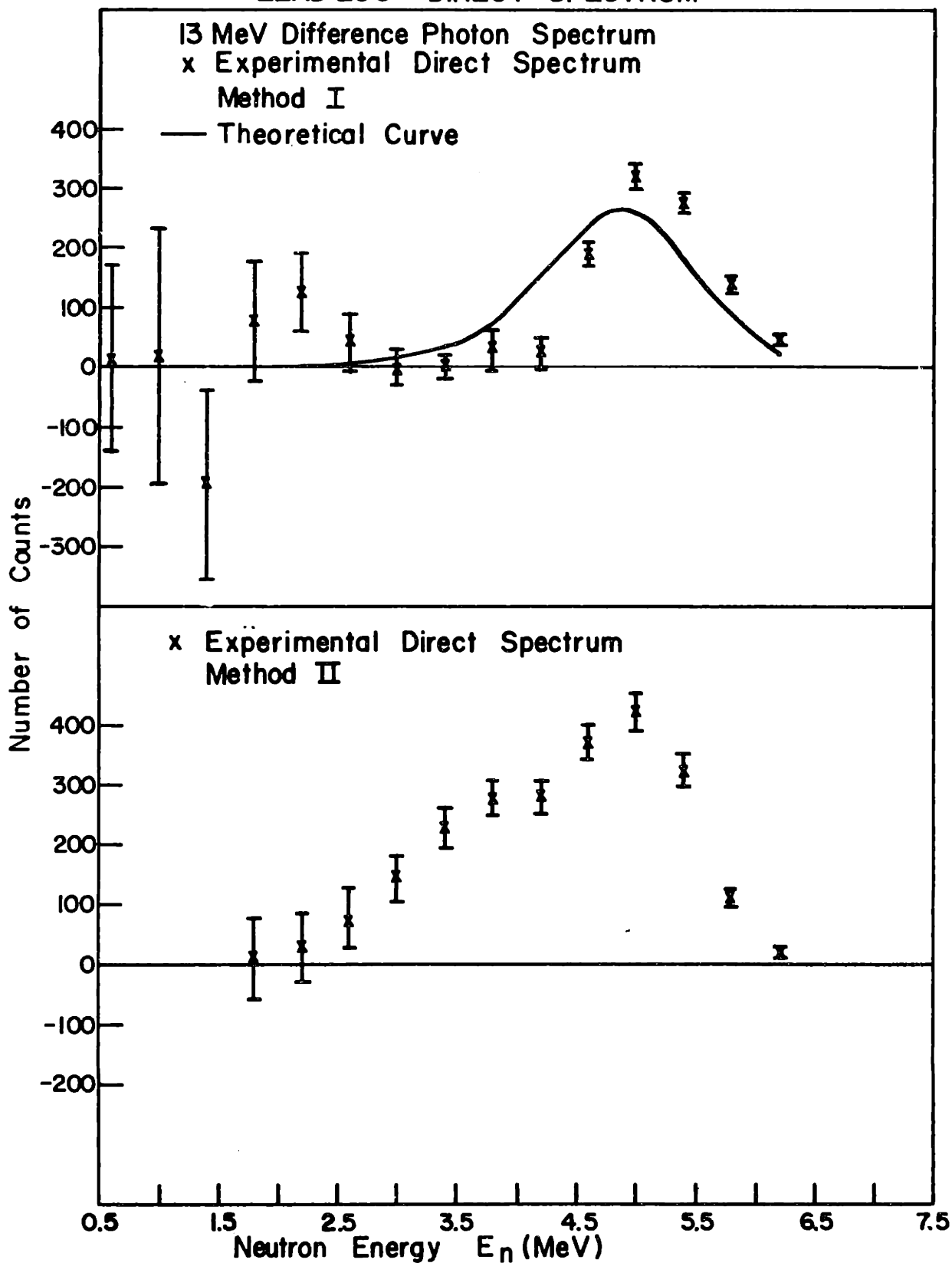


Fig. 39



# THALLIUM - DIRECT SPECTRUM

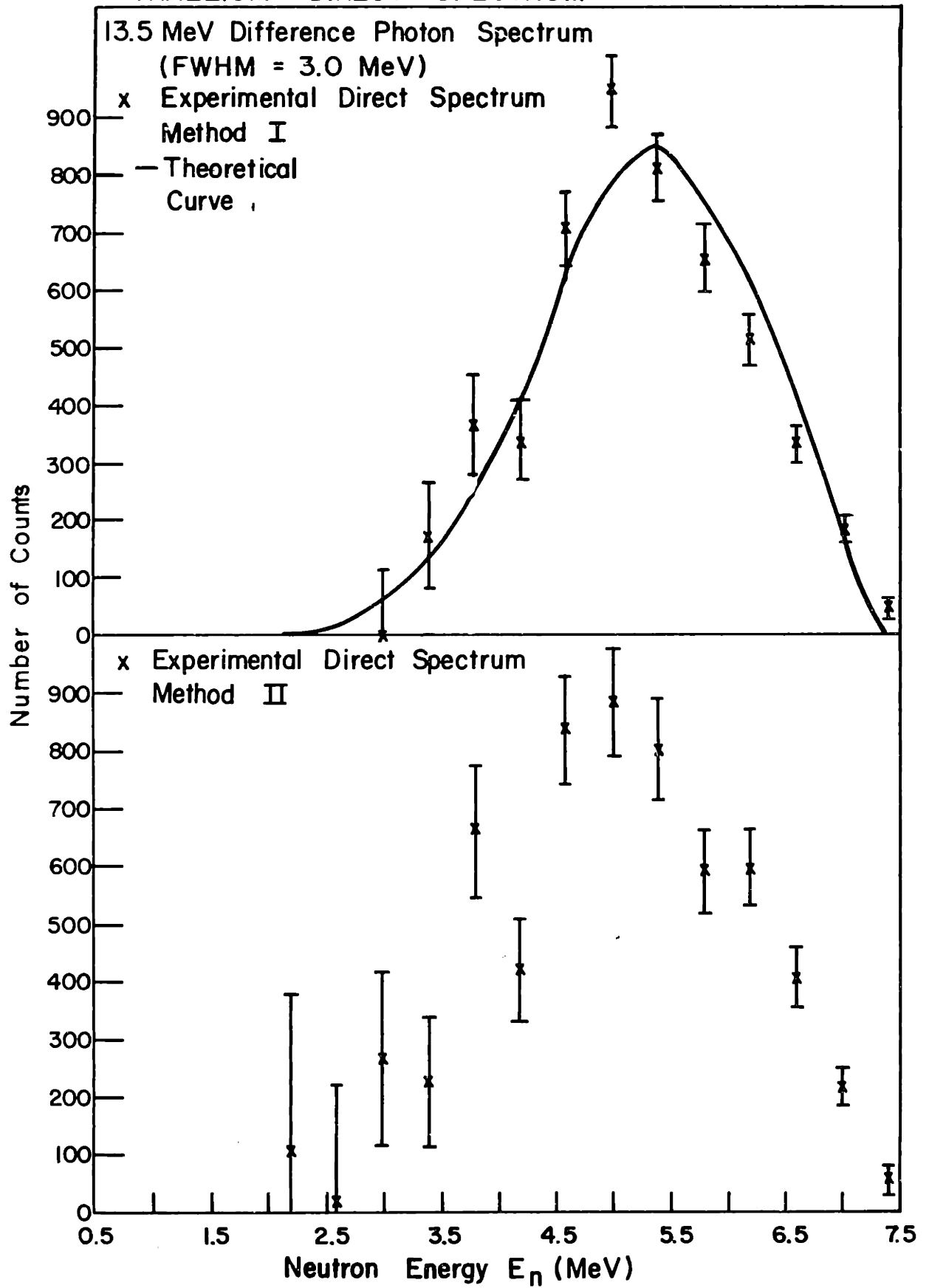


Fig. 40

LEAD 206

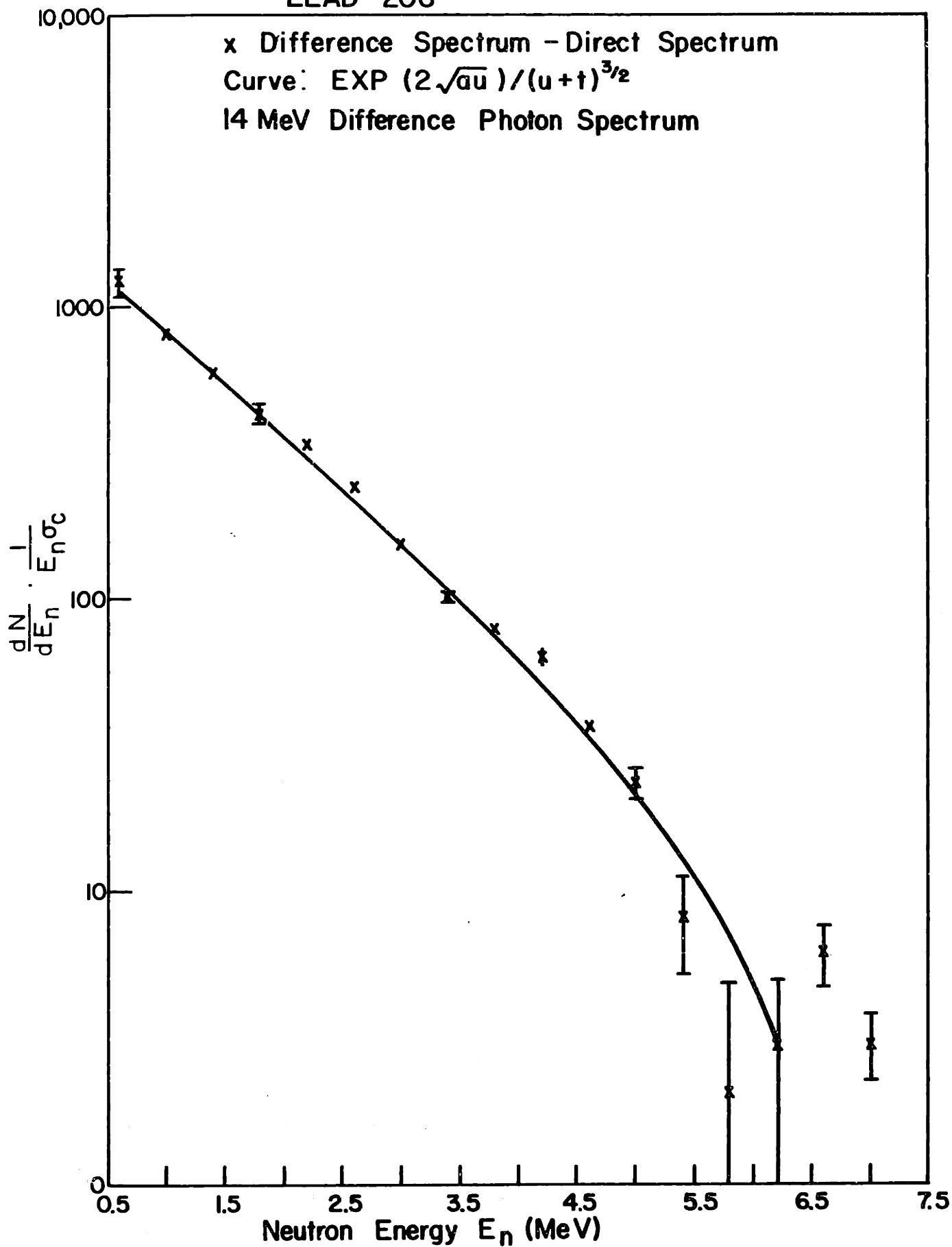


Fig. 41 Neutron Evaporation Spectrum

10,000

Fig. 42 Neutron Evaporation Spectrum

Lead 206

x Difference Spectrum - Direct Spectrum

Curve:  $\text{EXP}(2\sqrt{aU}/(U+t)^{3/2})$

13 MeV Difference Photon Spectrum

1,000

$\frac{dN}{dE_n} \cdot \frac{1}{E_n \sigma_c}$

100

10

0.5

1.5

2.5

3.5

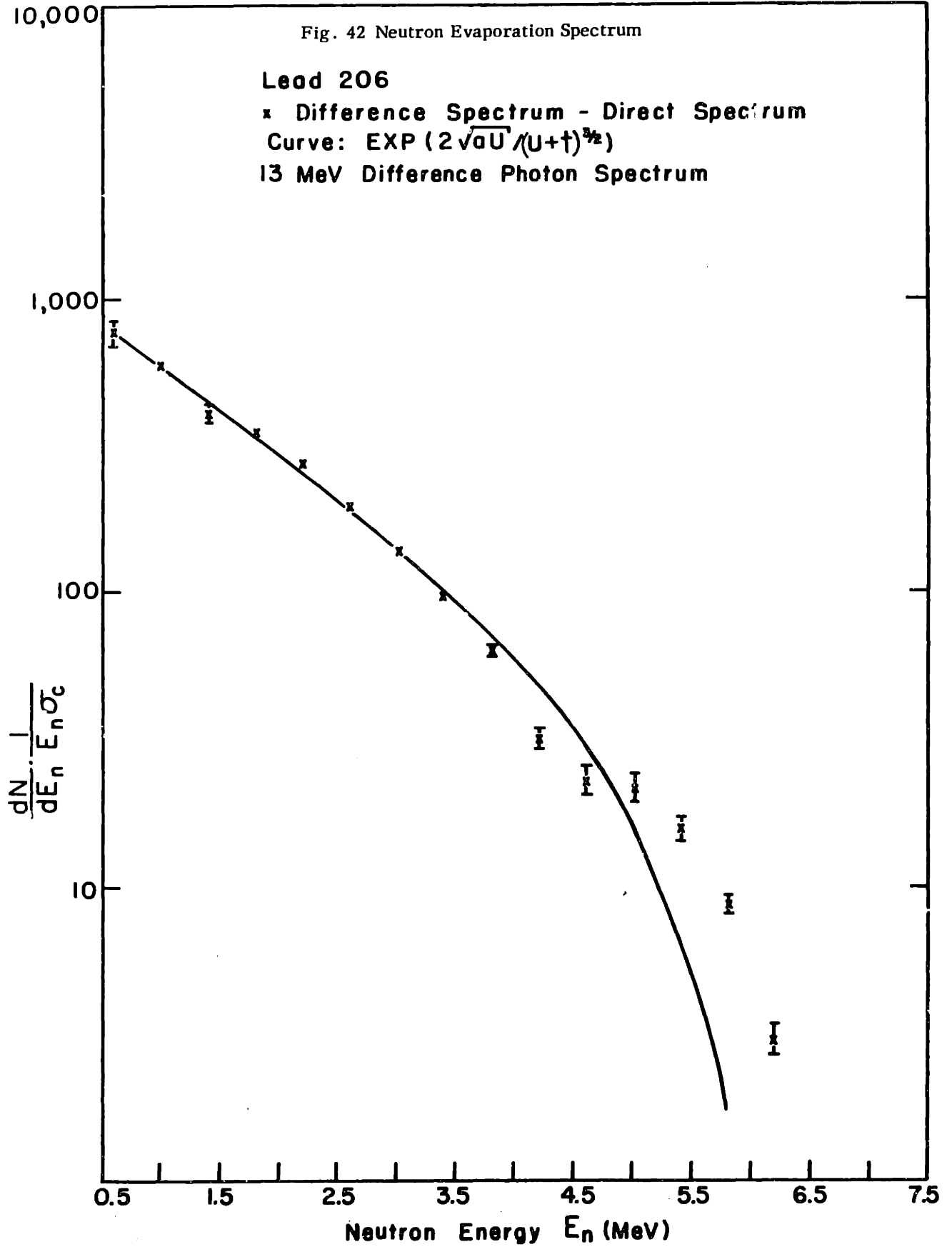
4.5

5.5

6.5

7.5

Neutron Energy  $E_n$  (MeV)



# THALLIUM

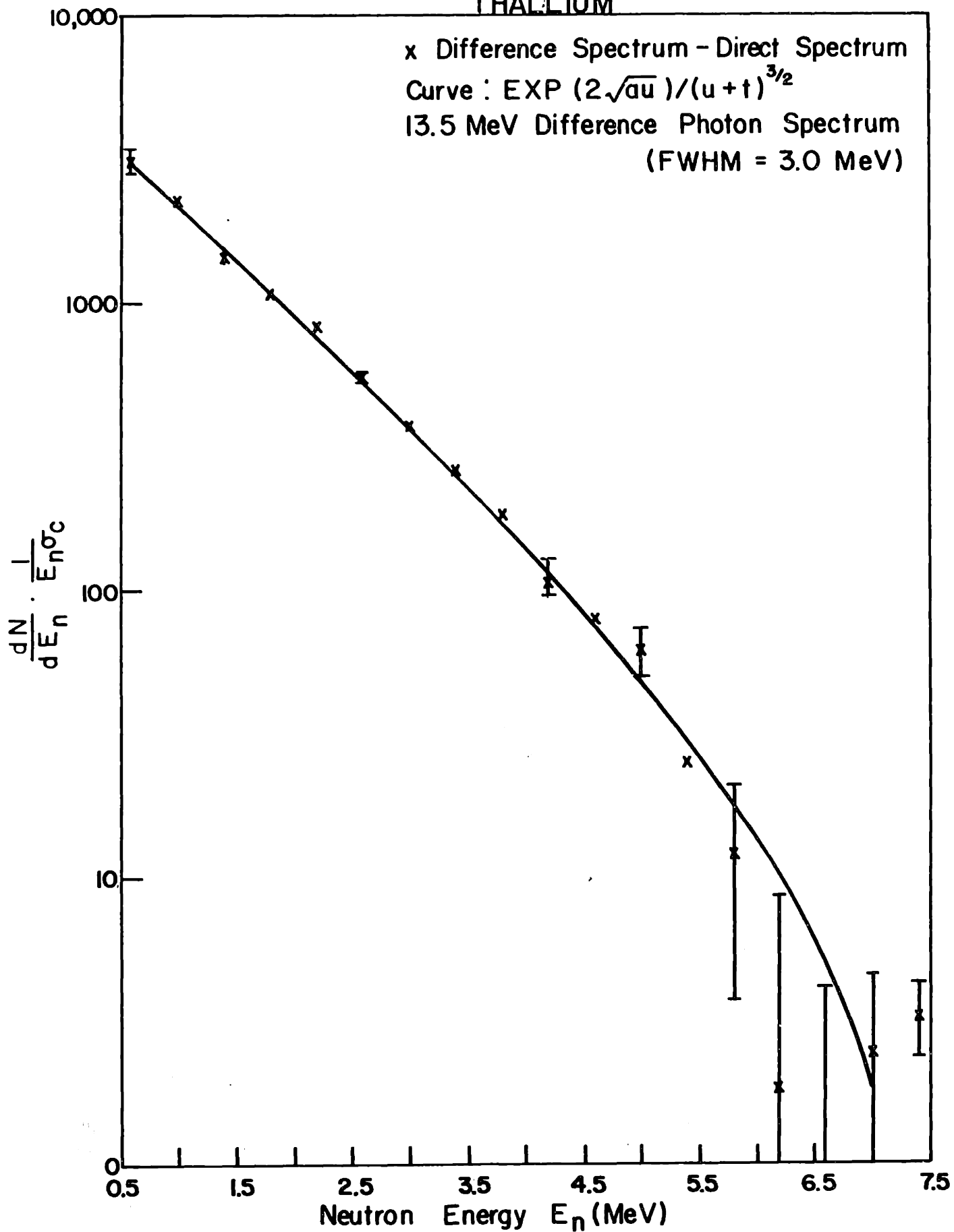


Fig. 43 Neutron Evaporation Spectrum

theoretical curve agree within the error bars up to 5.0 MeV neutron energy for thallium and the 14 MeV  $\text{Pb}^{206}$  data. The 13 MeV  $\text{Pb}^{206}$  data deviates from the theoretical curve at 4.0 MeV neutron energy, because  $S(E_n)$  is wider than the experimental direct spectrum. The evaporation component was calculated using Method II to determine the direct spectrum for  $\text{Pb}^{206}$  (not shown). The data was a noticeably poorer fit to the evaporation theory. This tends to support the direct spectrum found using  $S(E_n)$  by means of Method I.

The  $(\gamma, 2n)$  contamination of the low energy neutrons was estimated to be negligible for  $\text{Pb}^{206}$ , using the  $(\gamma, 2n)$  and  $(\gamma, n)$  cross sections measured by Harvey et al (7), and the level densities parameters measured in this experiment. The  $(\gamma, n)$  threshold for  $\text{Tl}^{205}$  (70 per cent abundance) is 14.2 MeV, and for  $\text{Tl}^{203}$  (30 per cent abundance) it is 14.7 MeV. The  $(\gamma, 2n)$  contamination was estimated to be 18 per cent of the  $(\gamma, n)$  contribution in the 0.6 MeV bin. The negative tail of the photon spectrum was negligible for Tl.

#### d) Angular Distribution

The angular distributions of the  $\text{Pb}^{206}$  and Tl photoneutrons from bremsstrahlung spectra with endpoints of 15, 14 and 13 MeV are plotted in Figs. 44 and 45.\* Both are isotropic at low neutron energies. The anisotropy increases to about  $-a_2/a_0 = 0.6$  at the neutron endpoint, a somewhat lower value than found in the case of  $\text{Pb}^{208}$ . Presumably this is due to the absence of the two  $p^{1/2}$  neutrons.

### D. Mercury and Gold

#### a) Experimental Data

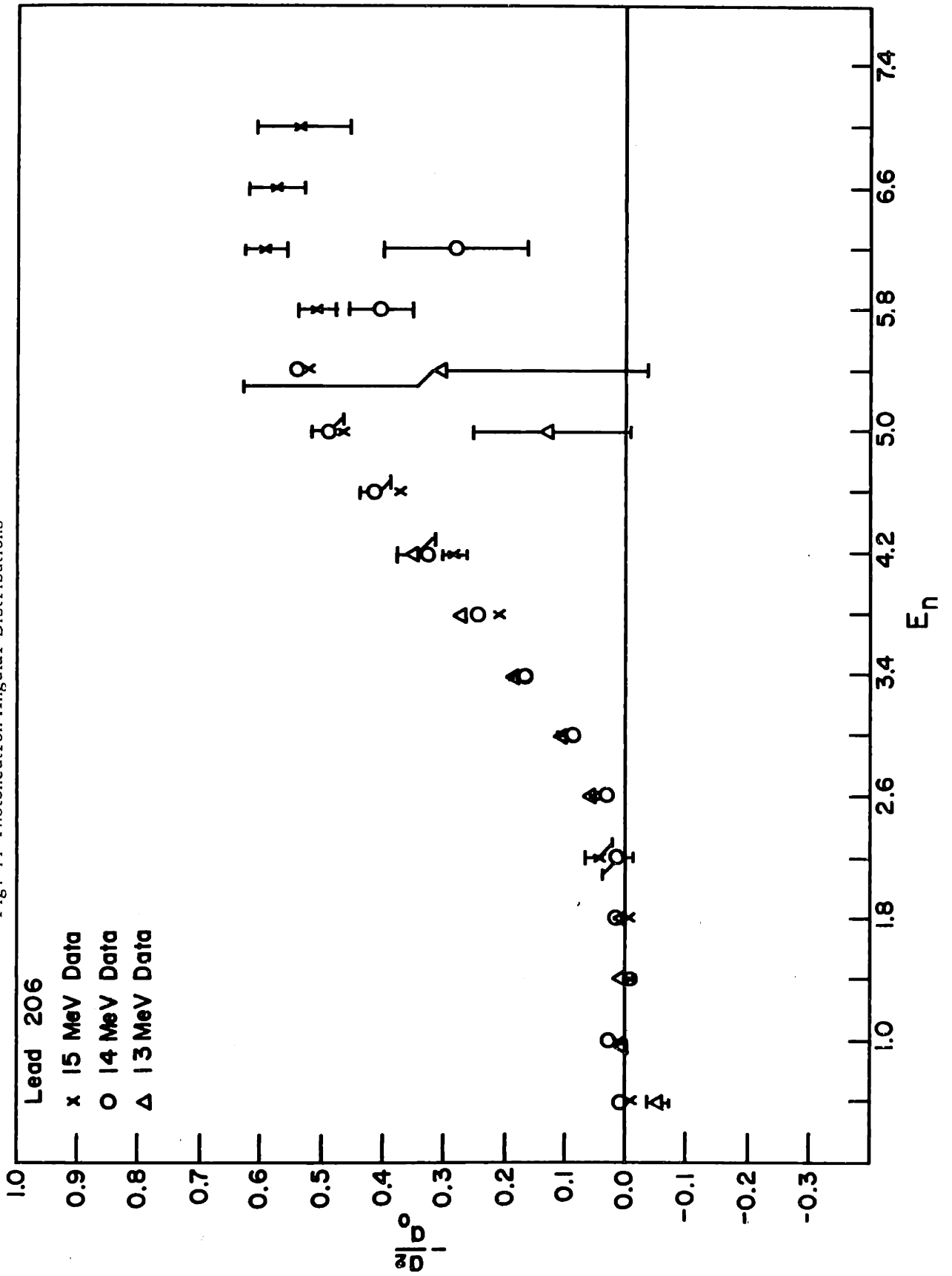
The photoneutron energy spectra  $\frac{dN}{dE_n} \frac{1}{E_n}$  vs  $E_n$  for mercury and gold are plotted in Figs. 46 to 49. The information contained in these graphs is the same as that described for  $\text{Pb}^{208}$  (section a of part A of this chapter).

#### b) Direct Spectrum

In the case of mercury and gold, both the neutron and proton shells are no longer filled. As a result there are a large number of levels in the

\*The defective 14 MeV thallium run has been included in Fig. 45.

Fig. 44 Photoneutron Angular Distributions



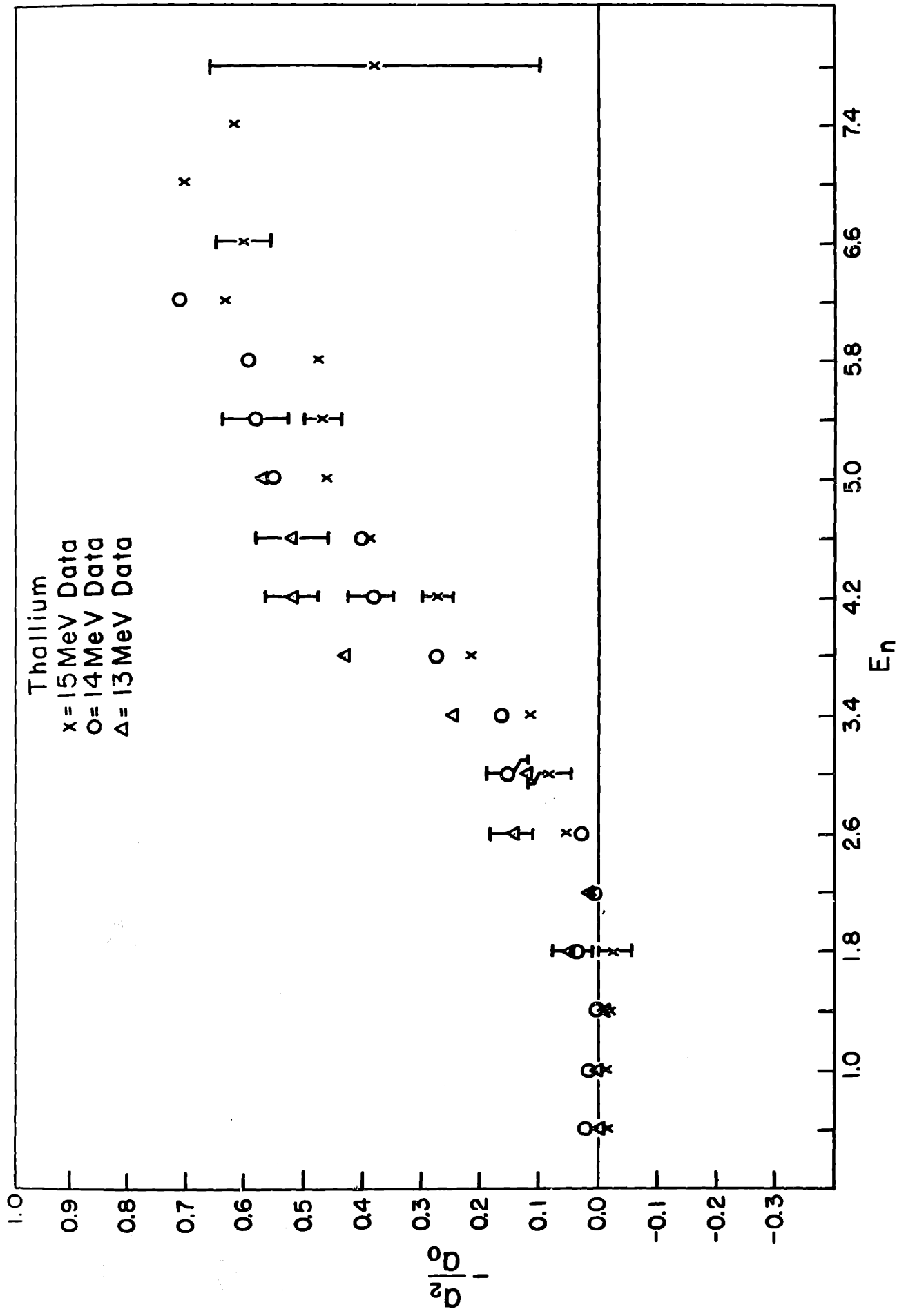


Fig. 45 Photoneutron Angular Distributions

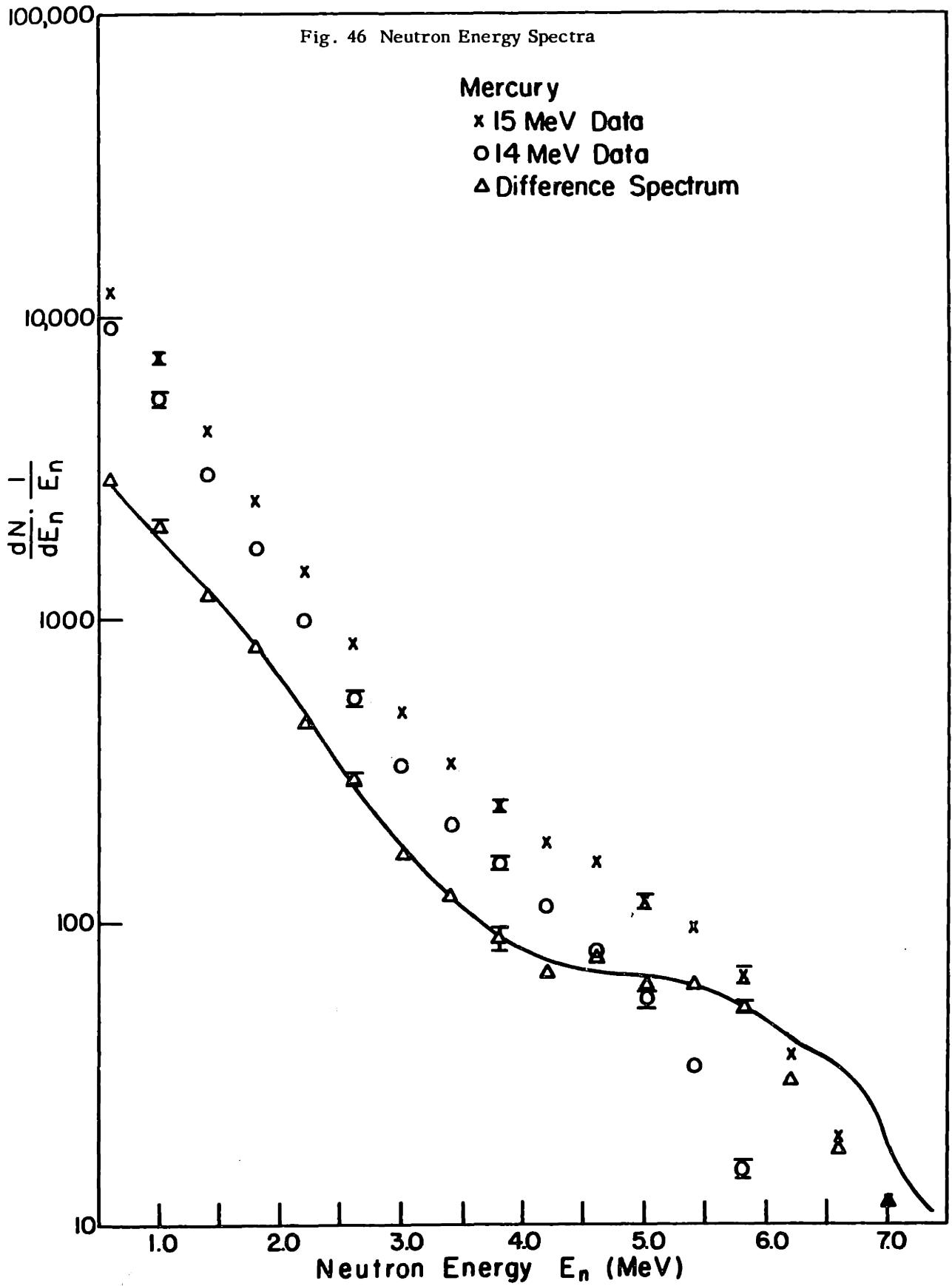




Fig. 47 Neutron Energy Spectra

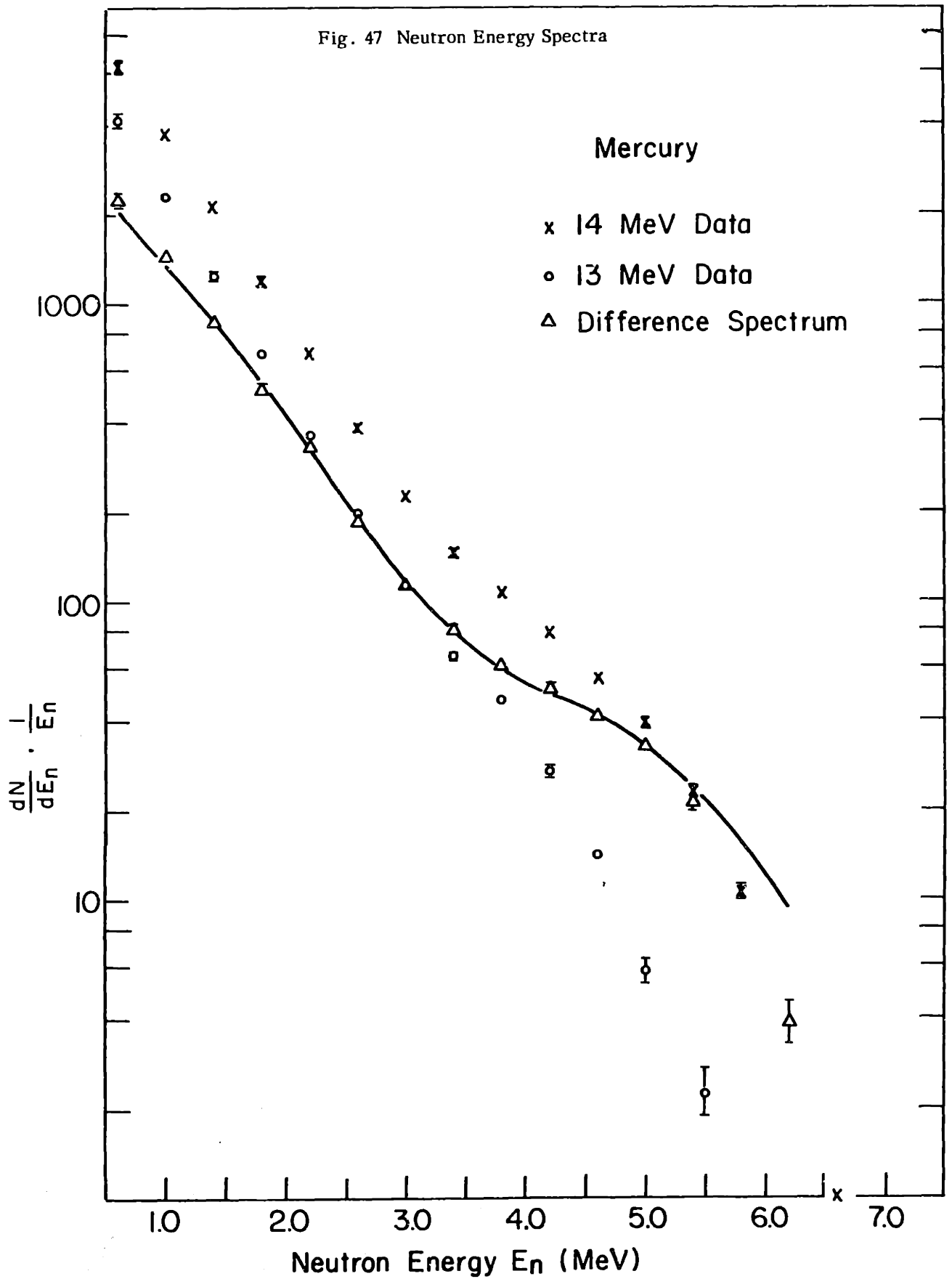
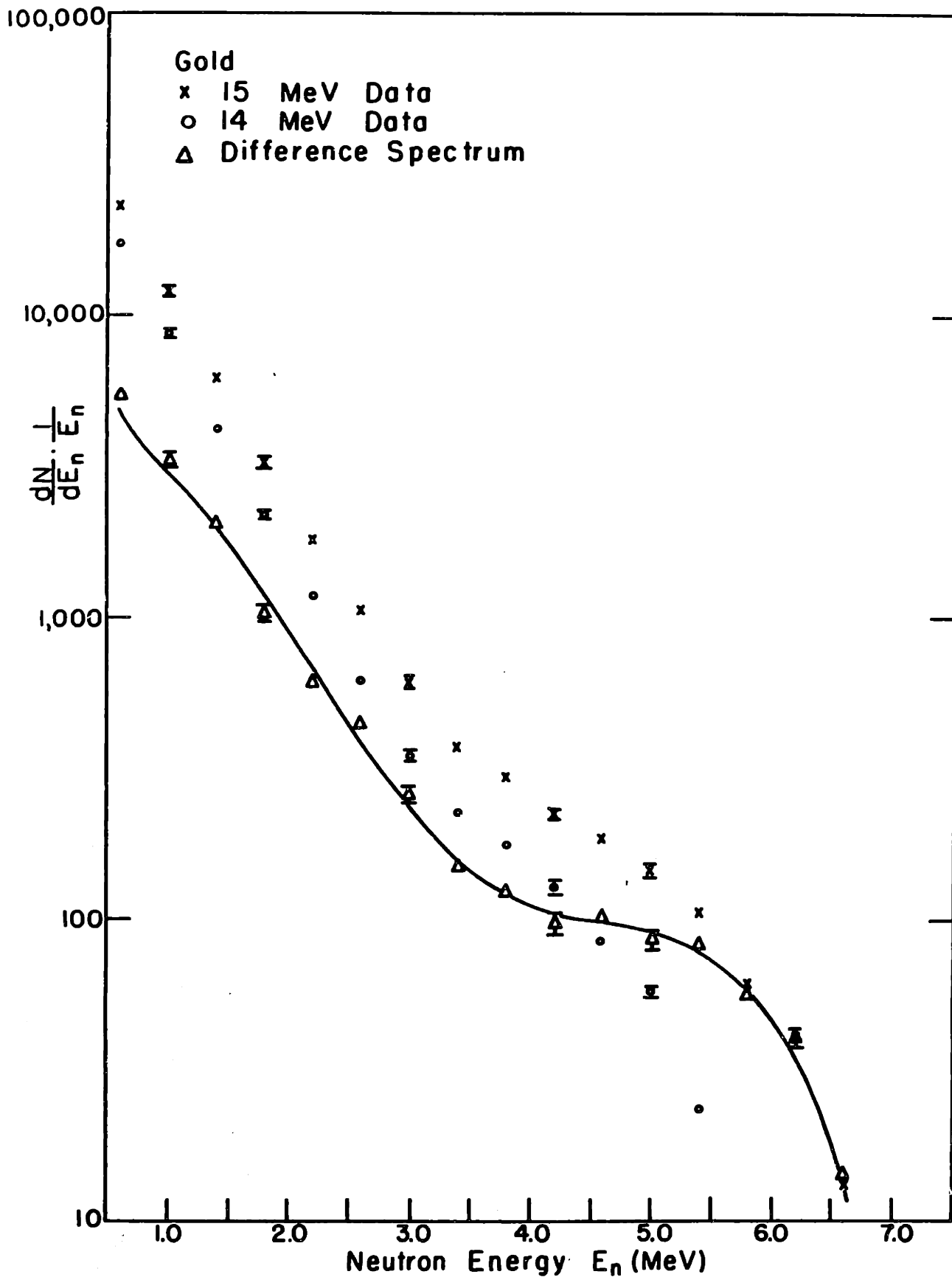


Fig. 48 Neutron Energy Spectra



GOLD

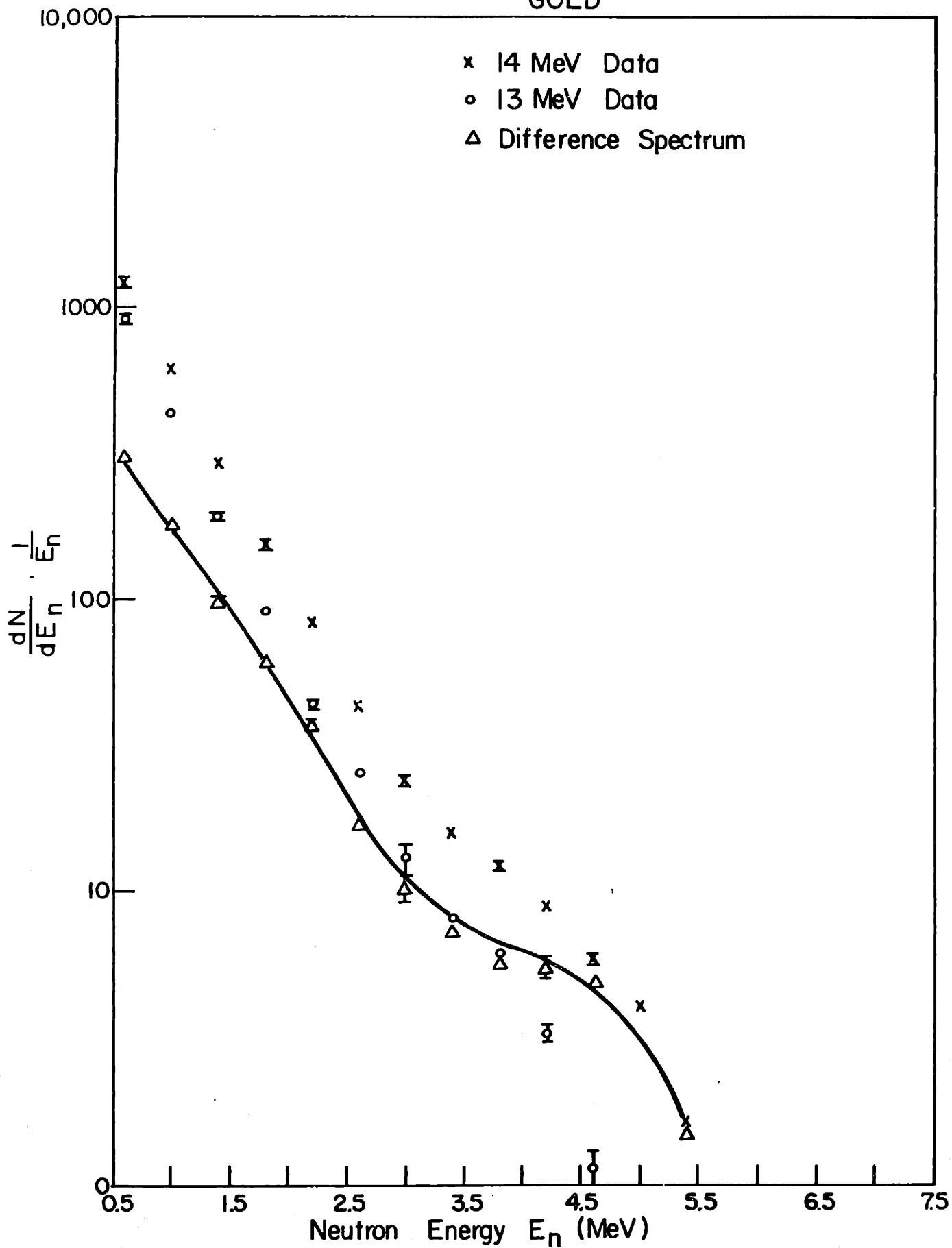


Fig. 49 Neutron Energy Spectra

first few MeV of the residual nuclei composed of a complicated mixture of intrinsic neutron and proton single particle states. Therefore the second method of calculating  $S(E_n)$  outlined in Chapter IV, section E, was used. That is, the hole states were assumed to be uniformly distributed in the residual nucleus. Since the neutron shells are not filled, transitions can take place from a lower shell (ie, the levels listed in Table XXII). However since the single particle residual states for these transitions are at a very high excitation energy (5 to 8 MeV), these levels were not included in the residual states. The transition strengths were included in the calculation of  $S(E_n)$ . That is, these transitions were allowed to absorb photons, but not emit neutrons. This reduces the theoretical estimate of the direct fraction as the shell empties. This point is discussed further in section J of this chapter. The shape of  $S(E_n)$  is then determined primarily by the transmission coefficients,  $T_j$ , at low neutron energies, and by the shape of the photon difference spectrum at the high end of the neutron spectrum. The single particle states in the  $N = 126$  shell were taken from the shell model calculations of Ross et al (64) (see Table XVIII), and the stripping experiments of Cohen et al (32). Gold was assumed to have all of the shells up to and including the  $p^{3/2}$  shell occupied, with the  $f^{5/2}$  and  $p^{1/2}$  shells empty. The ground state configuration of  $Hg^{200}$  was assumed to be two holes in the  $p^{3/2}$  shell, four holes in the  $f^{5/2}$  shell, two holes in the  $i^{13/2}$  shell and the other levels occupied. The two  $p^{1/2}$  and two  $f^{5/2}$  neutrons were retained because some of the Hg isotopes have  $\frac{1}{2}$ - ground states and  $\frac{5}{2}$ - low lying states. The configuration will vary for each mercury isotope but  $S(E_n)$  is not sensitive to the exact configuration because of the assumption of uniformly distributed hole states. The relative transition strengths,  $f_l$ , taken from Table XIII column two, were reduced in proportion to the number of holes in a given shell.  $S(E_n)$  was calculated from equation 74 of Chapter IV, section E. The  $T_j$ 's were taken from ref 61 as usual. To account for the different isotopes of mercury, the element was assumed to be composed of two isotopes,  $Hg^{200}$  with a threshold of 8.0 MeV and 70 per cent isotopic abundance, and  $Hg^{119}$  with a threshold of 6.4 MeV and an isotopic abundance of 30 per cent. An  $S(E_n)$  was calculated for each of the above isotopes and weighted according to the "pseudo-isotopic abundance".

The results are shown in Figs. 50 to 53.  $S(E_n)$  lies above the experimental data at the high energy end of the mercury direct spectrum. This overestimation of the directly emitted neutrons is reasonable since the method used requires that all hole states of the residual nucleus be present down to the ground state, whereas the first  $\frac{7}{2}$ - and  $\frac{9}{2}$ - levels lie much higher (about 1.0 to 2.0 MeV excitation energy). If the contribution of these states corresponding to direct emission of neutrons from the  $f^{7/2}$  and  $h^{9/2}$  shell were extended only up to 2.0 MeV from the neutron endpoint,  $S(E_n)$  would be reduced by 40 to 50 per cent in the region  $\frac{1}{2}$  MeV below the neutron endpoint. This would improve the fit. The gold data is in excellent agreement with the calculated  $S(E_n)$ . Since  $Au^{196}$  is an odd-odd isotope, one would expect a large number of levels of all spins even at low excitation energies. Hence the approximations are better than in the case of mercury where the proton pairing energy reduces the number of levels available in the first few MeV.

The direct spectrum calculated from the angular distribution method presents much the same picture as the first method for both gold and mercury, except for a deep dip at about 5.0 MeV in some of the data. This dip is generated by a large difference in the angular distributions for the 15 and 14 MeV data which occurs in many runs at 4.6 or 5.0 MeV regardless of the isotope involved. This dip does not appear at a lower energy in the 13 MeV mercury difference spectrum, and it appears at the same energy in both gold difference spectra. It also does not appear in other runs made with a different experimental configuration (2 ns/channel instead of 4 ns/channel) which are not presented here. Therefore it seems that this fluctuation in the angular distribution is an artifact of the equipment, although its origin has not been traced. On the other hand, the dip observed in the Bi spectra (section A) was considered to be a real effect. In that case the dip appeared in the direct spectra found using both Methods I and II. It was found approximately 1 MeV lower in both direct spectra for the 13 MeV difference spectra, and it was found in the 2 ns/channel runs (not shown). Furthermore the angular distributions of the Bi photoneutrons do not exhibit the sharp fluctuation that is associated with the spurious dips in the direct spectrum derived from Method II.

Fig. 50

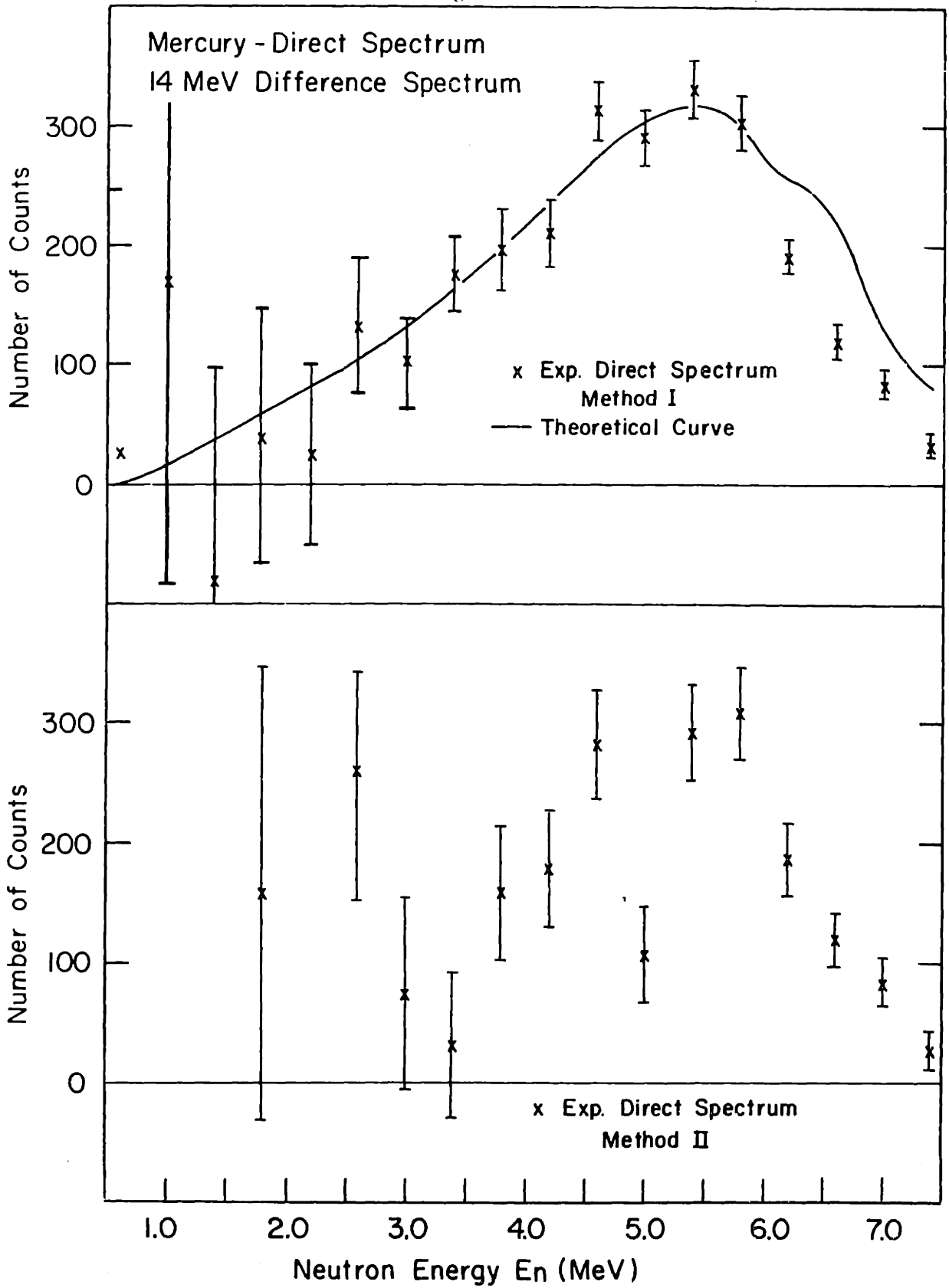
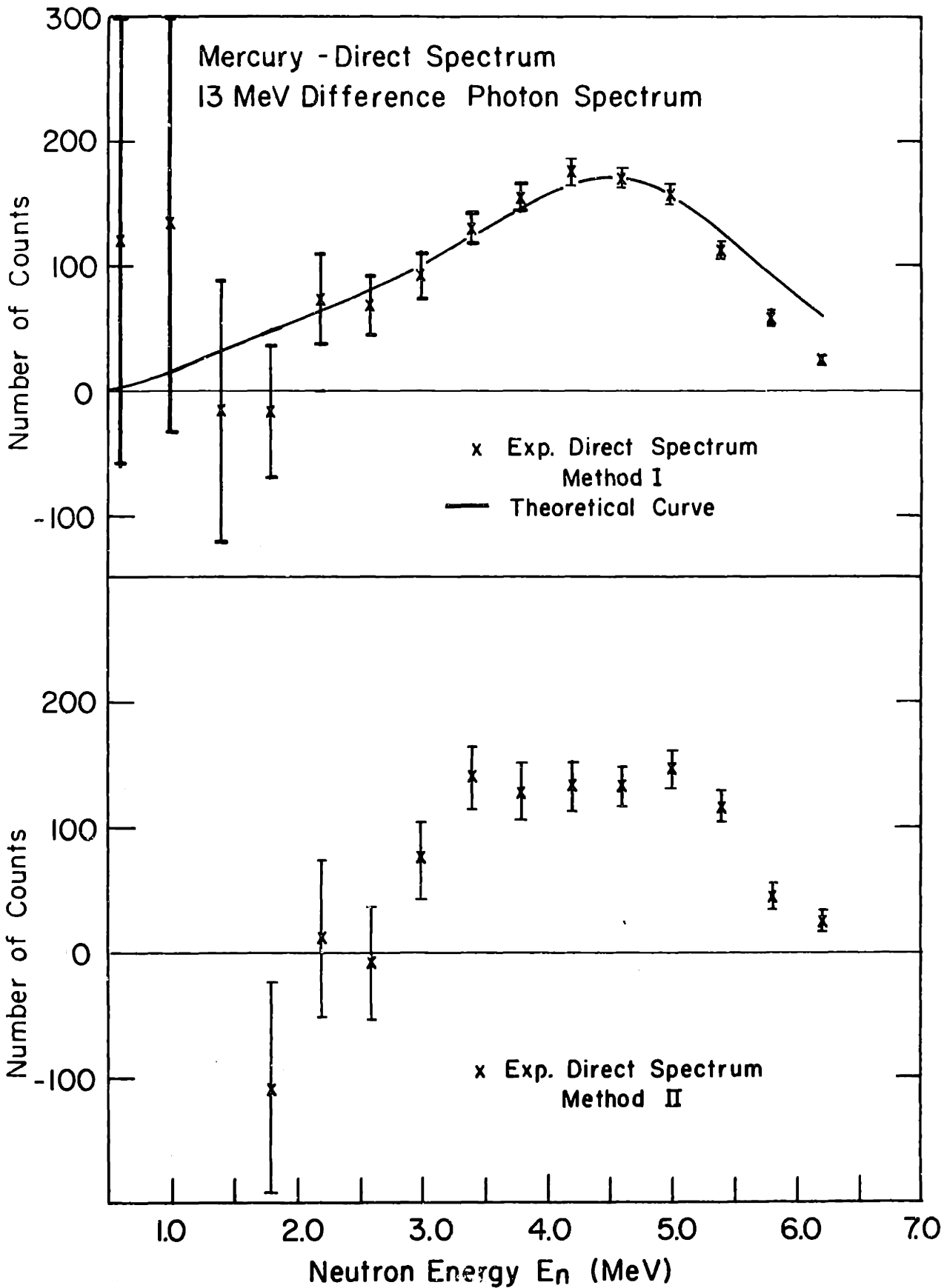


Fig. 51



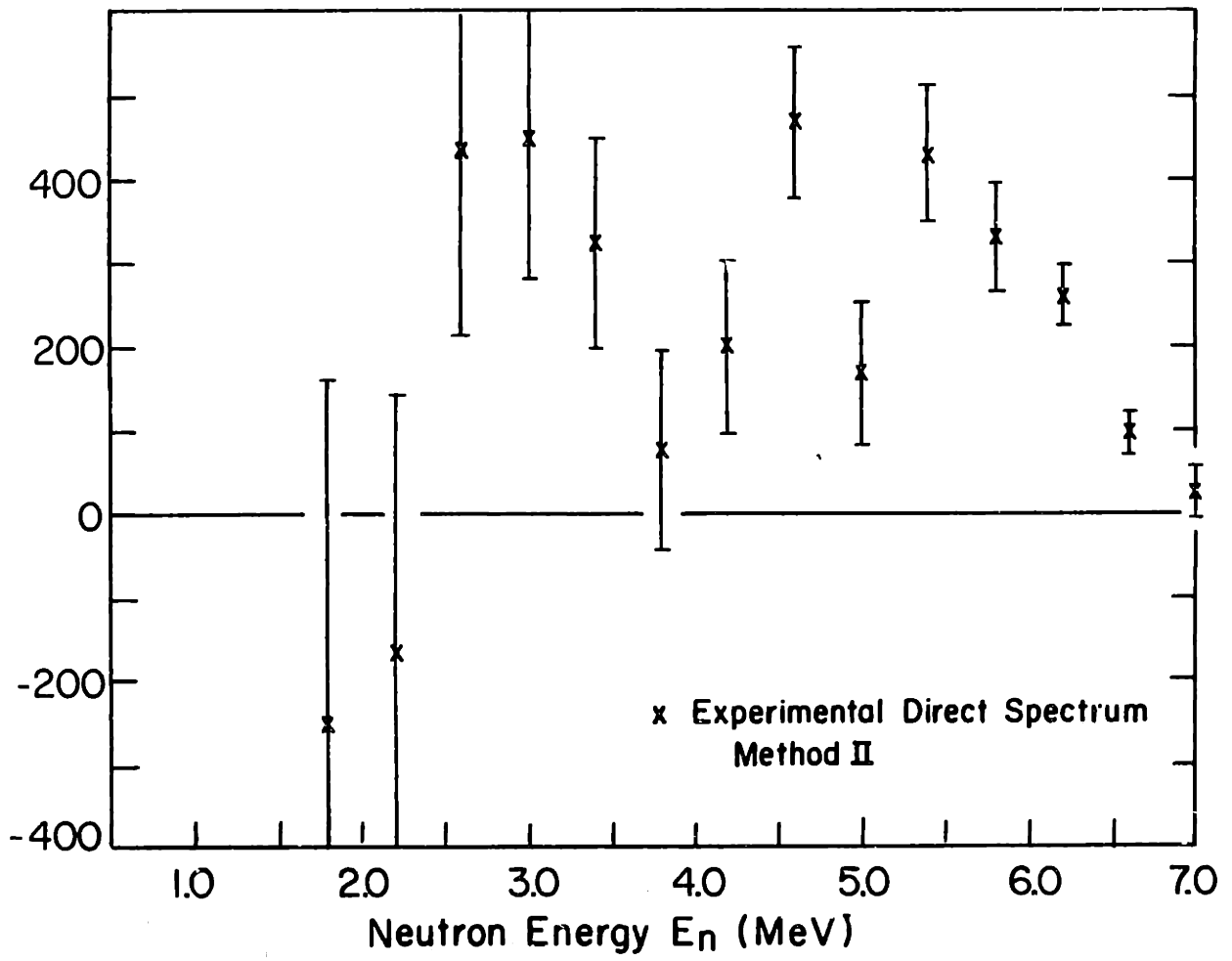
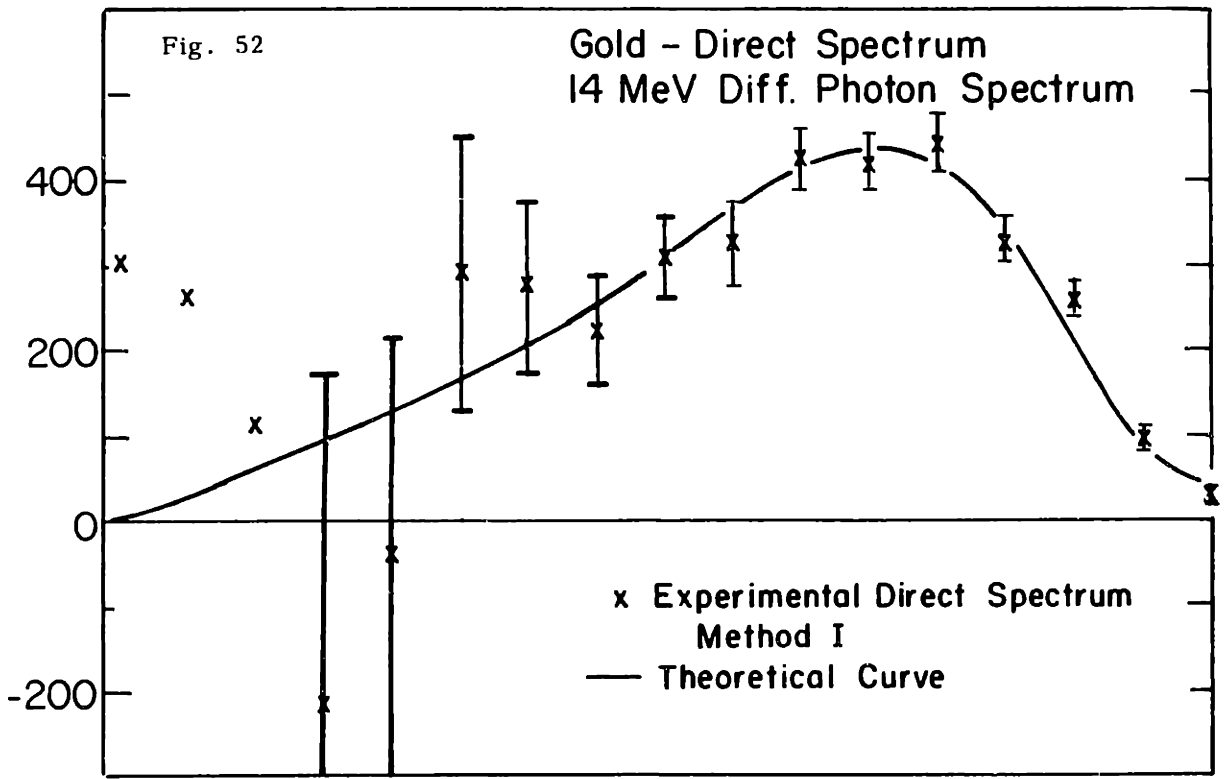
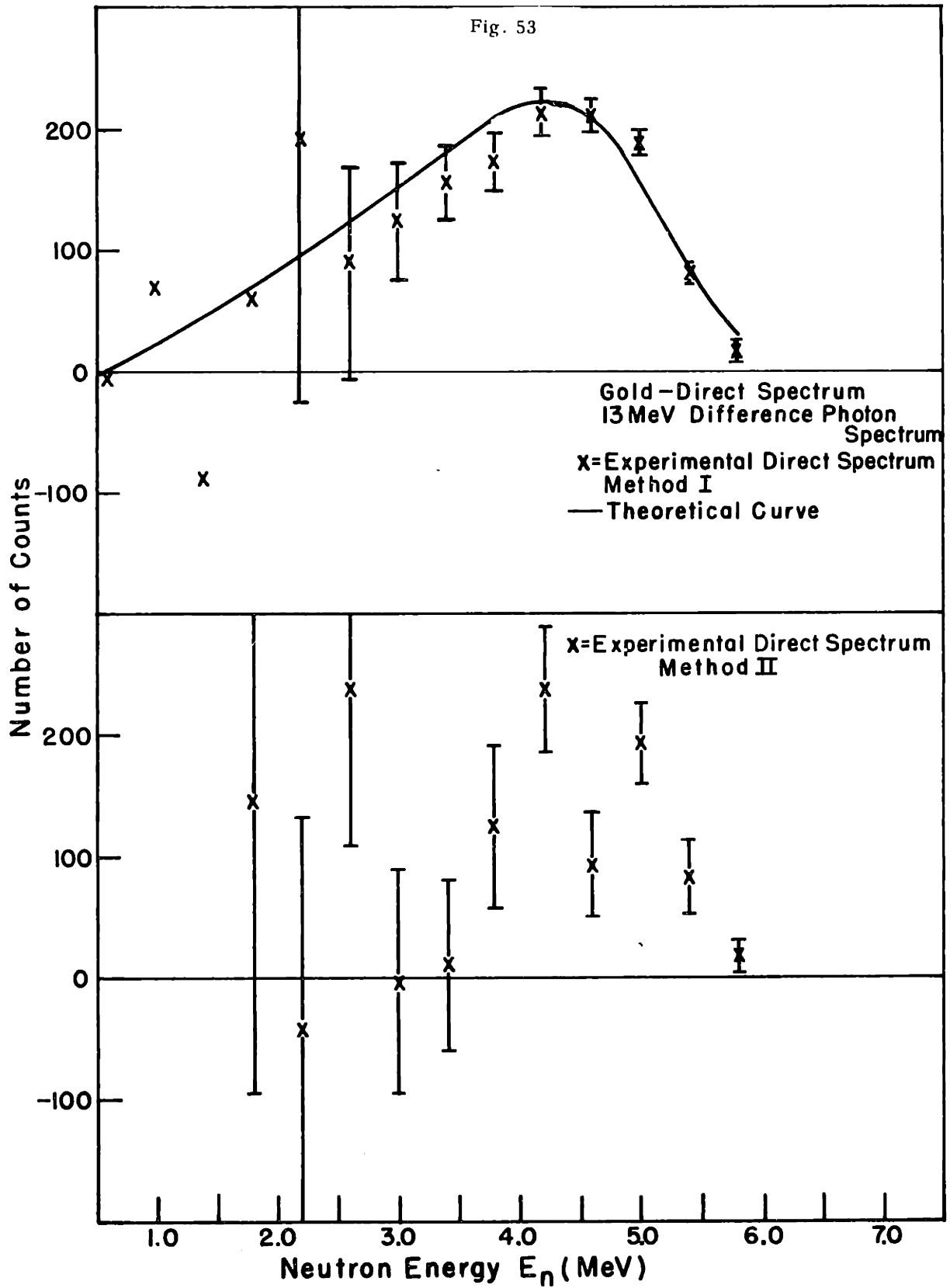




Fig. 53



### c) Evaporation Spectrum

The evaporation component and the theoretical curves fitted to the data are shown in Figs. 54 to 57. The experimental data lies within one standard deviation of the theoretical curves up to 4.0 MeV in all four cases. The  $(\gamma, 2n)$  threshold for gold is given as 14.75 MeV in ref 70; using the  $(\gamma, 2n)$  and  $(\gamma, n)$  cross sections measured in ref 5, the  $(\gamma, 2n)$  component is estimated to be about 1 per cent of the total neutron spectrum. The negative tail of the 14 MeV photon difference spectrum should reduce the  $(\gamma, n)$  data by about  $\frac{1}{2}$  per cent. Therefore the two effects are expected to cancel in the case of the 14 MeV data. The  $(\gamma, 2n)$  contamination and the negative tail of the 13 MeV photon difference spectrum are estimated to be negligible for the 13 MeV data. The experimental data lies slightly above the theoretical prediction at 0.6 MeV (Fig. 56) but still within the uncertainty of the data. The  $(\gamma, 2n)$  thresholds for the mercury isotopes range from 14.0 MeV ( $\text{Hg}^{202}$ , 29.8 per cent) to 15.3 MeV ( $\text{Hg}^{198}$ , 10 per cent) (70). Therefore the  $(\gamma, 2n)$  contamination of the low energy mercury data is expected to be somewhat less than that for gold. Since the  $(\gamma, n)$  cross sections for each mercury isotope are not available, this is the best estimate that can be made. The  $(\gamma, n)$  thresholds range from 6.7 MeV ( $\text{Hg}^{199}$ , 17 per cent) to 7.8 MeV ( $\text{Hg}^{202}$ , 29.8 per cent). Thus the negative tail of the photon difference spectrum should reduce the mercury  $(\gamma, n)$  spectrum somewhat more than in the case of gold. From these two estimates, one would expect that the 0.6 MeV point might lie lower than the theoretical curve for the 14 MeV data. Fig. 54 shows that the data point falls on the curve. The two effects apparently cancel. In the case of the 13 MeV difference spectrum, the two effects are expected to be negligible, as in the case of gold. The data plotted in Fig. 55 support this conclusion.

### d) Angular Distributions

The angular distributions of the photoneutrons from mercury and gold are plotted in Figs. 58 and 59. The graphs are quite similar. The low energy data is isotropic within the estimated errors. The anisotropic component

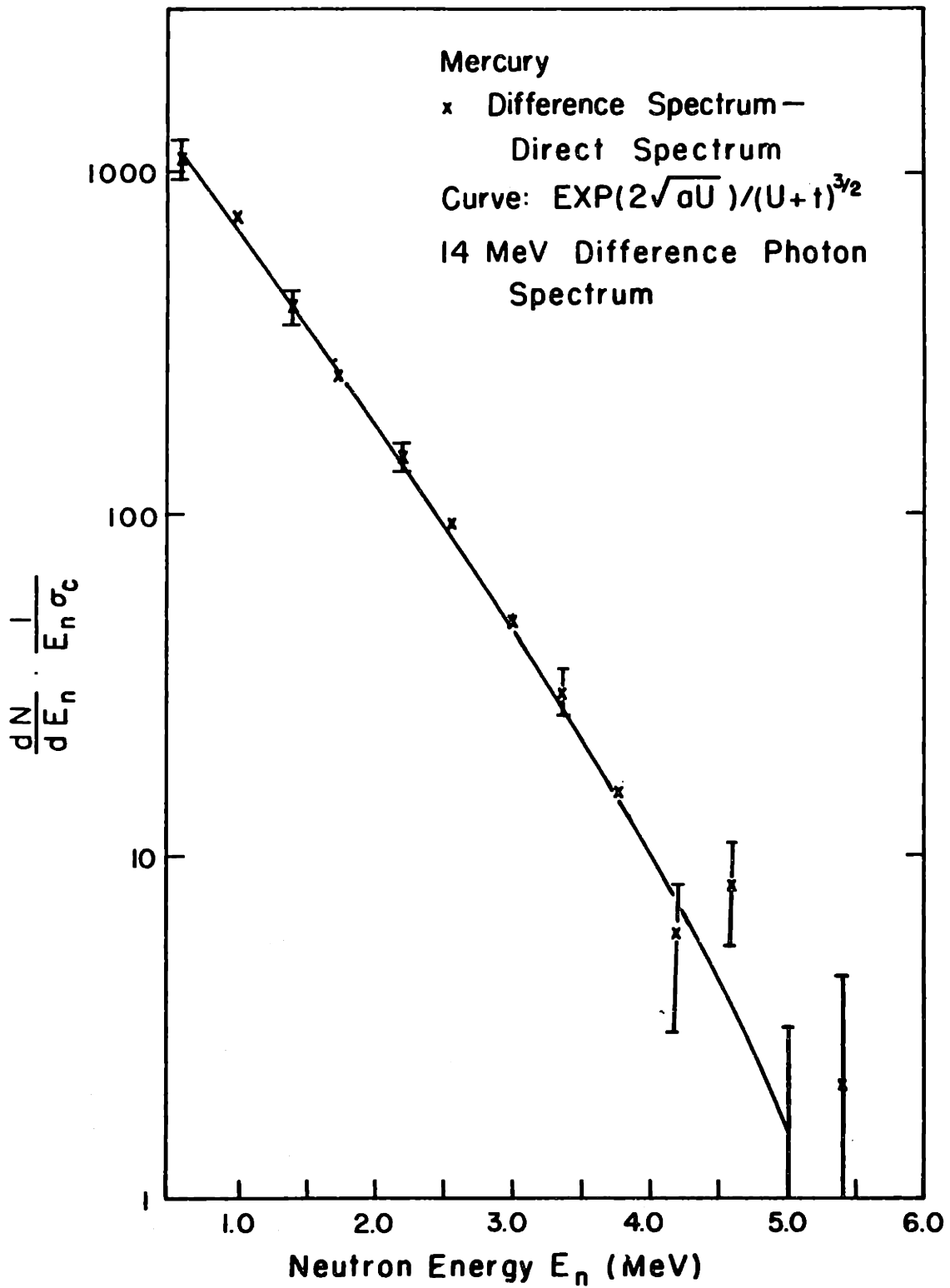


Fig. 54 Neutron Evaporation Spectrum

# MERCURY

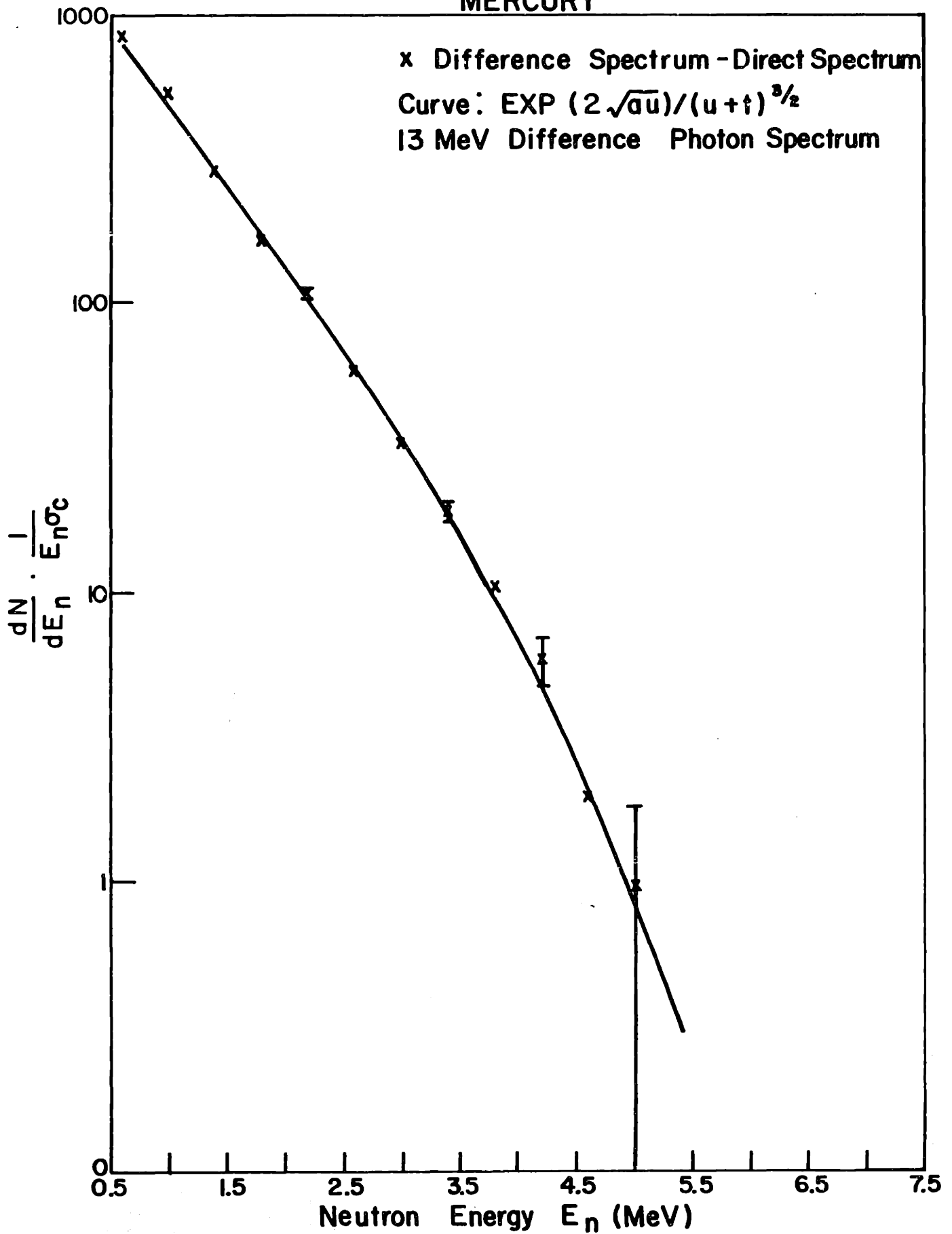
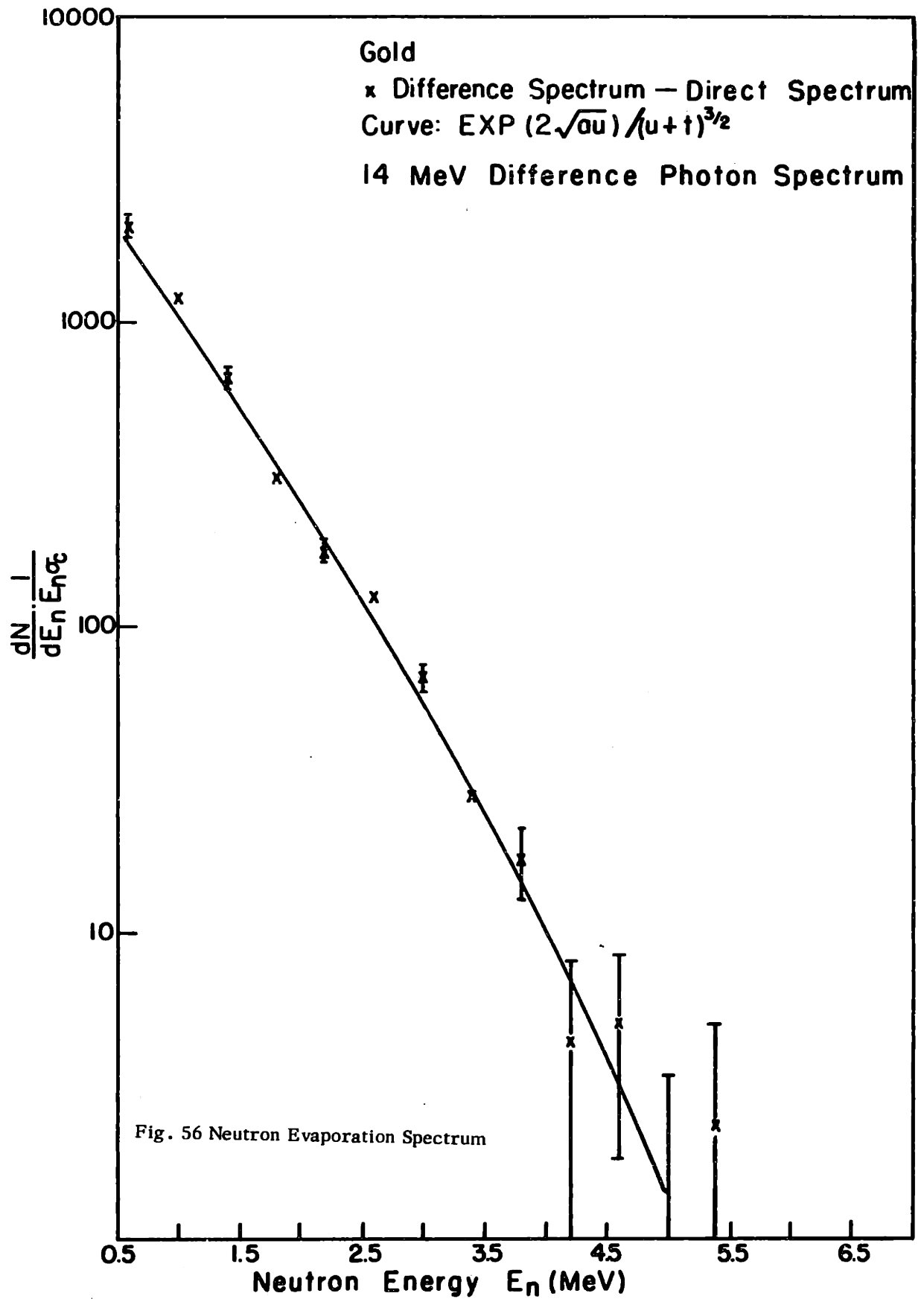


Fig. 55 Neutron Evaporation Spectrum



10,000

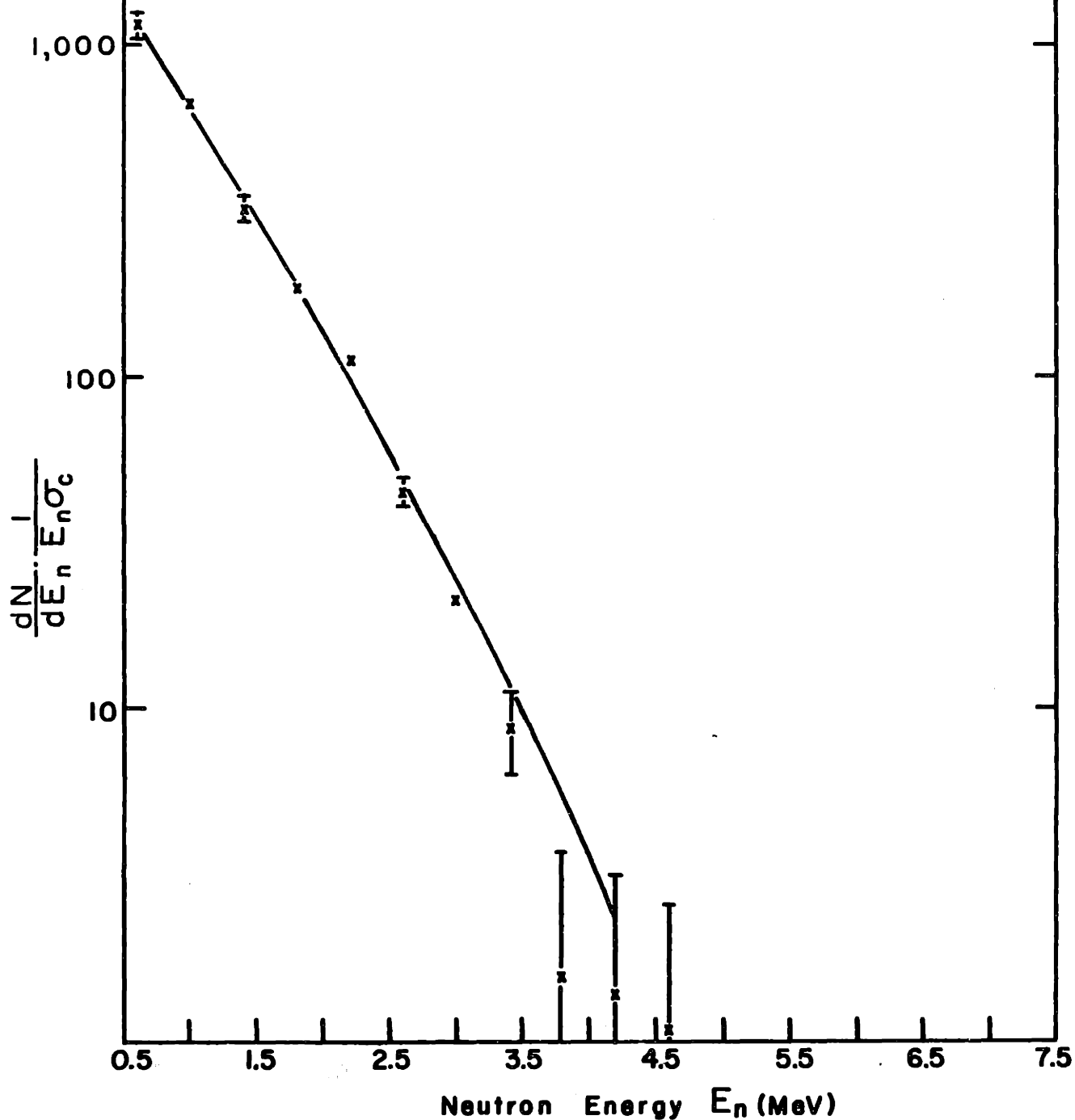
Fig. 57 Neutron Evaporation Spectrum

Gold

x Difference Spectrum - Direct Spectrum

Curve:  $\text{EXP}(2\sqrt{aU})/(U+t)^{3/2}$

13 MeV Difference Photon Spectrum



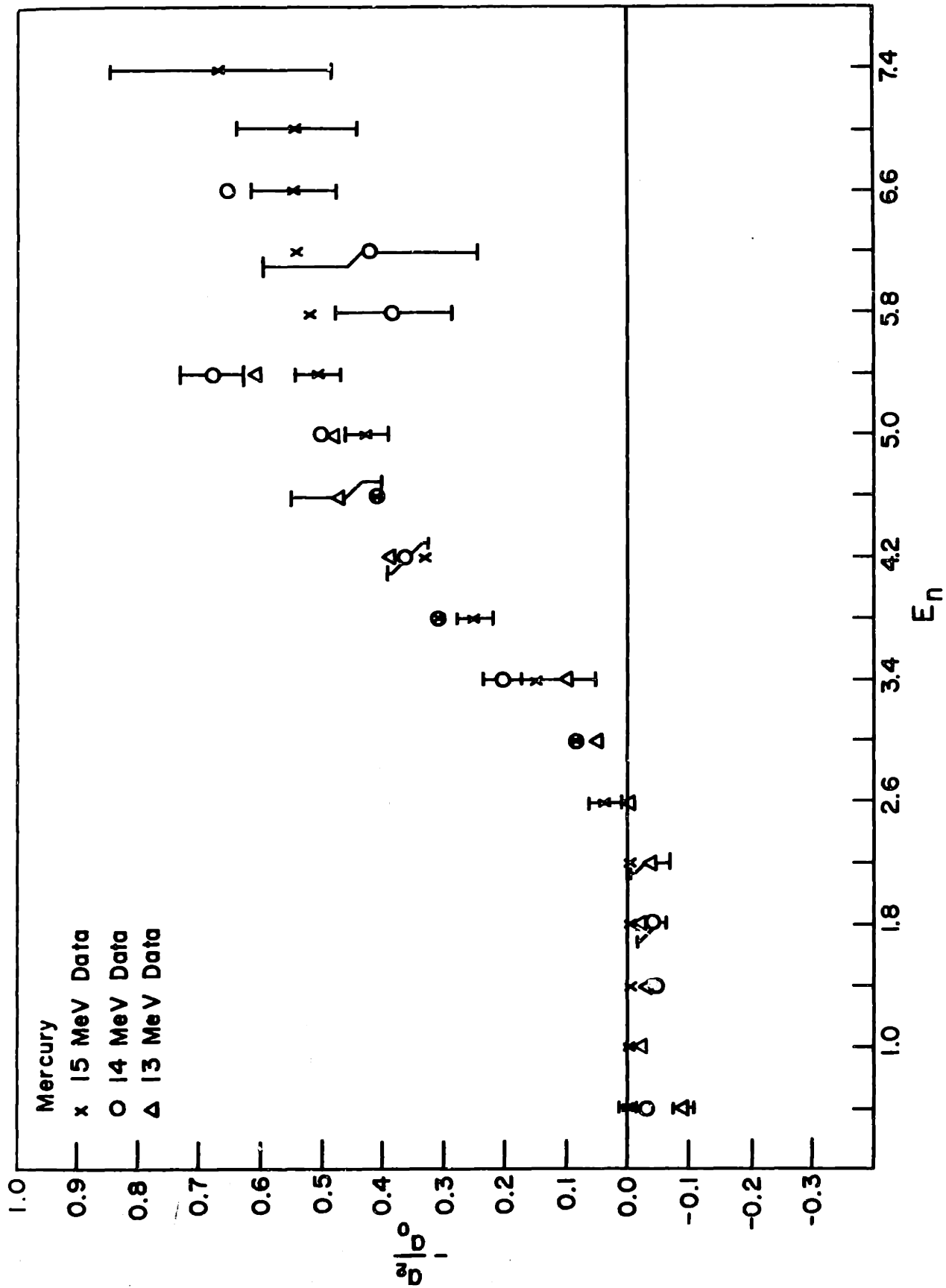


Fig. 58 Photoneutron Angular Distributions

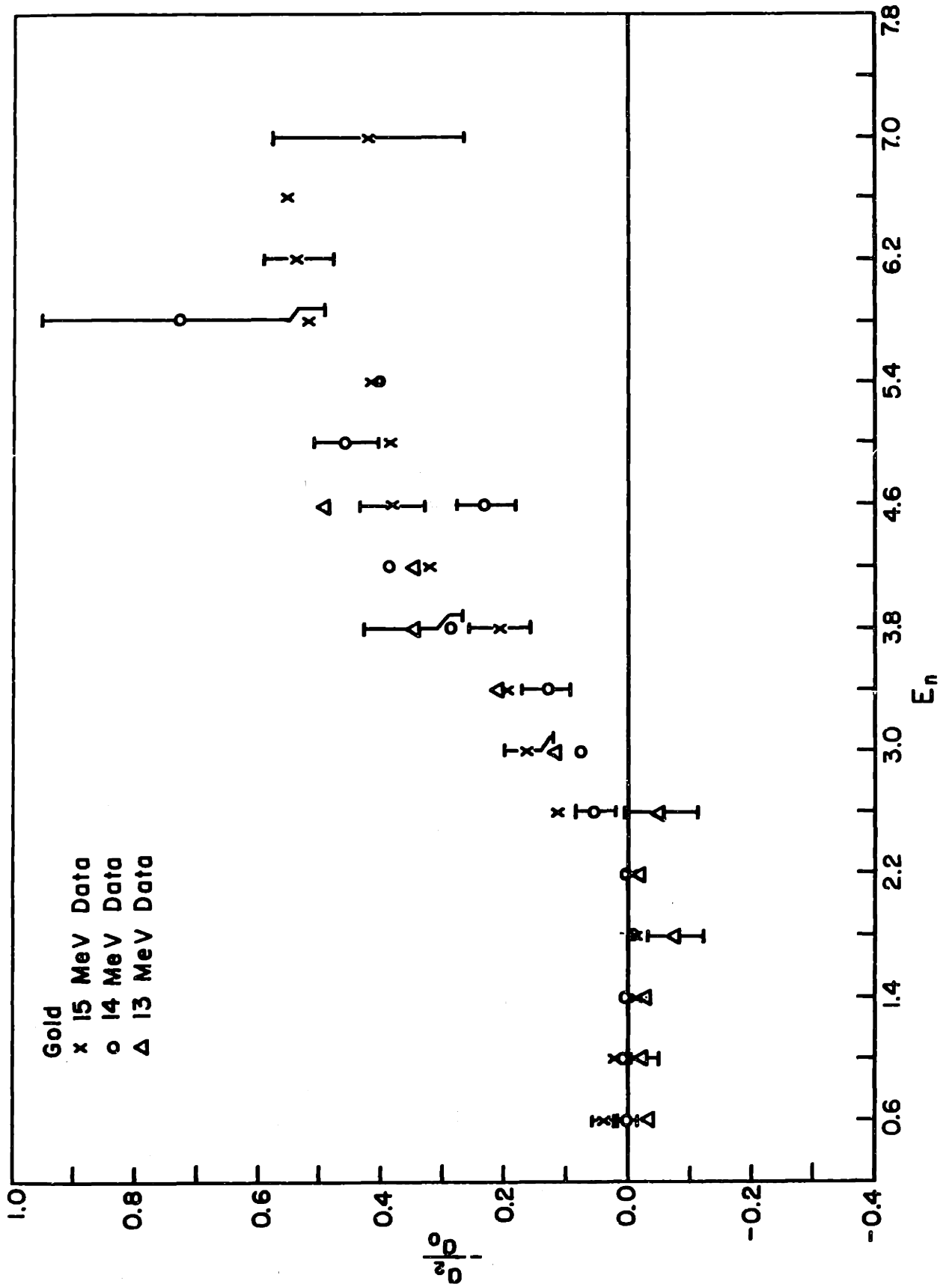


Fig. 59 Photoneutron Angular Distributions



begins to increase at about  $2\frac{1}{2}$  MeV, rises to about  $-a_2/a_0 \approx 0.55$ , and is virtually flat above this. This lower value of the high energy limit of  $-a_2/a_0$  (as compared to the value of 0.7 reached by  $\text{Pb}^{208}$  photoneutrons) is apparently due to the loss of the highly anisotropic  $p^{1/2}$  and  $f^{5/2}$  neutrons in gold. The two  $p^{1/2}$  neutrons and two  $f^{5/2}$  neutrons were retained in the case of mercury. It is possible that these two  $p^{1/2}$  neutrons should have been placed in the  $i^{13/2}$  shell, which would reduce the expected anisotropy without appreciably affecting  $S(E_n)$ . (These assignments are of course only crude approximations. The ground state configuration of the  $\text{Hg}^{200}$  and  $\text{Hg}^{199}$  are linear combinations of the  $p^{1/2}$ ,  $p^{3/2}$ ,  $f^{5/2}$ ,  $f^{7/2}$ ,  $i^{13/2}$ , and  $h^{9/2}$  neutron states and the appropriate proton states.)

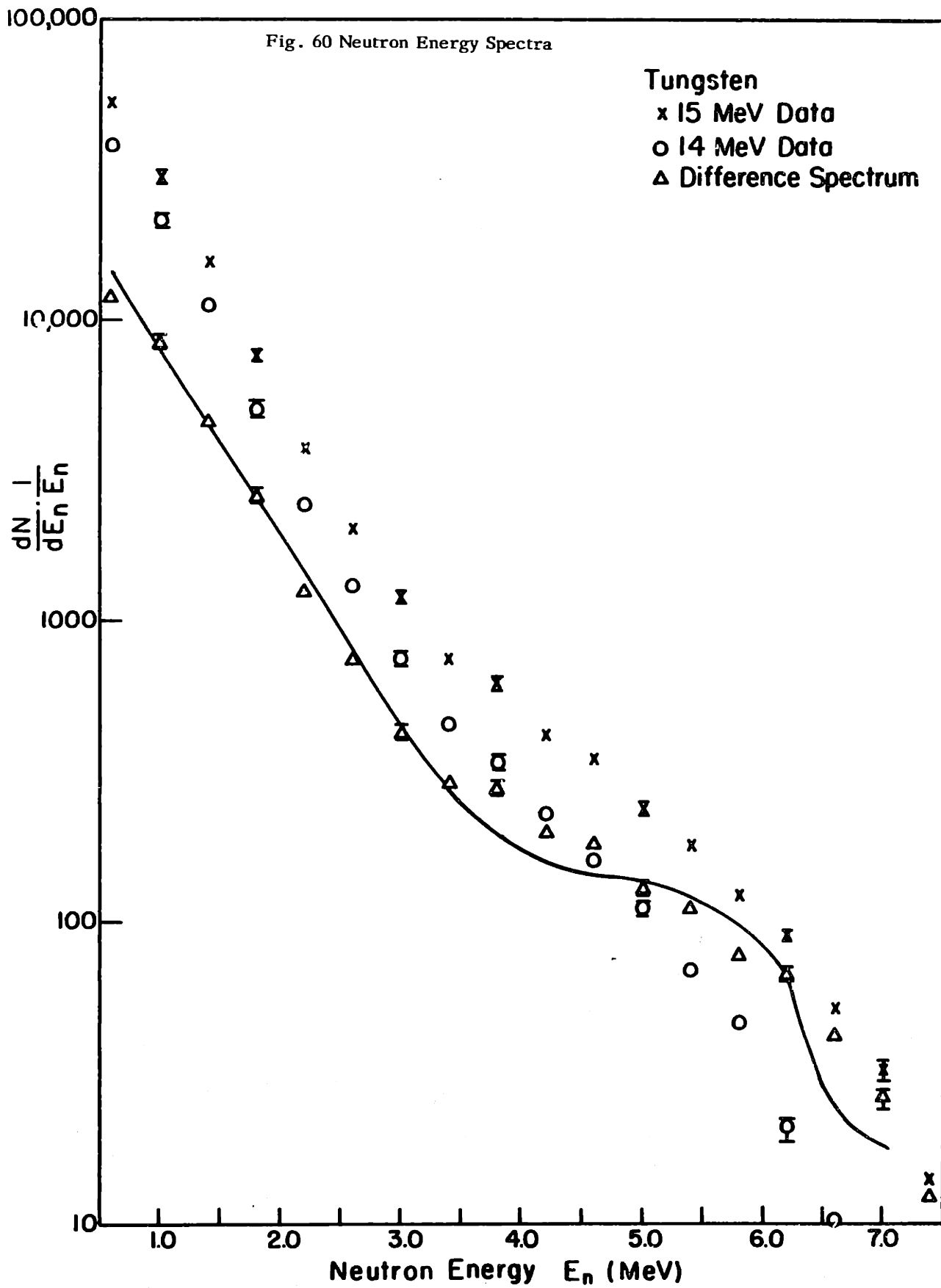
#### E. Deformed Nuclei: Tungsten, Tantalum, Erbium, Holmium, and Samarium

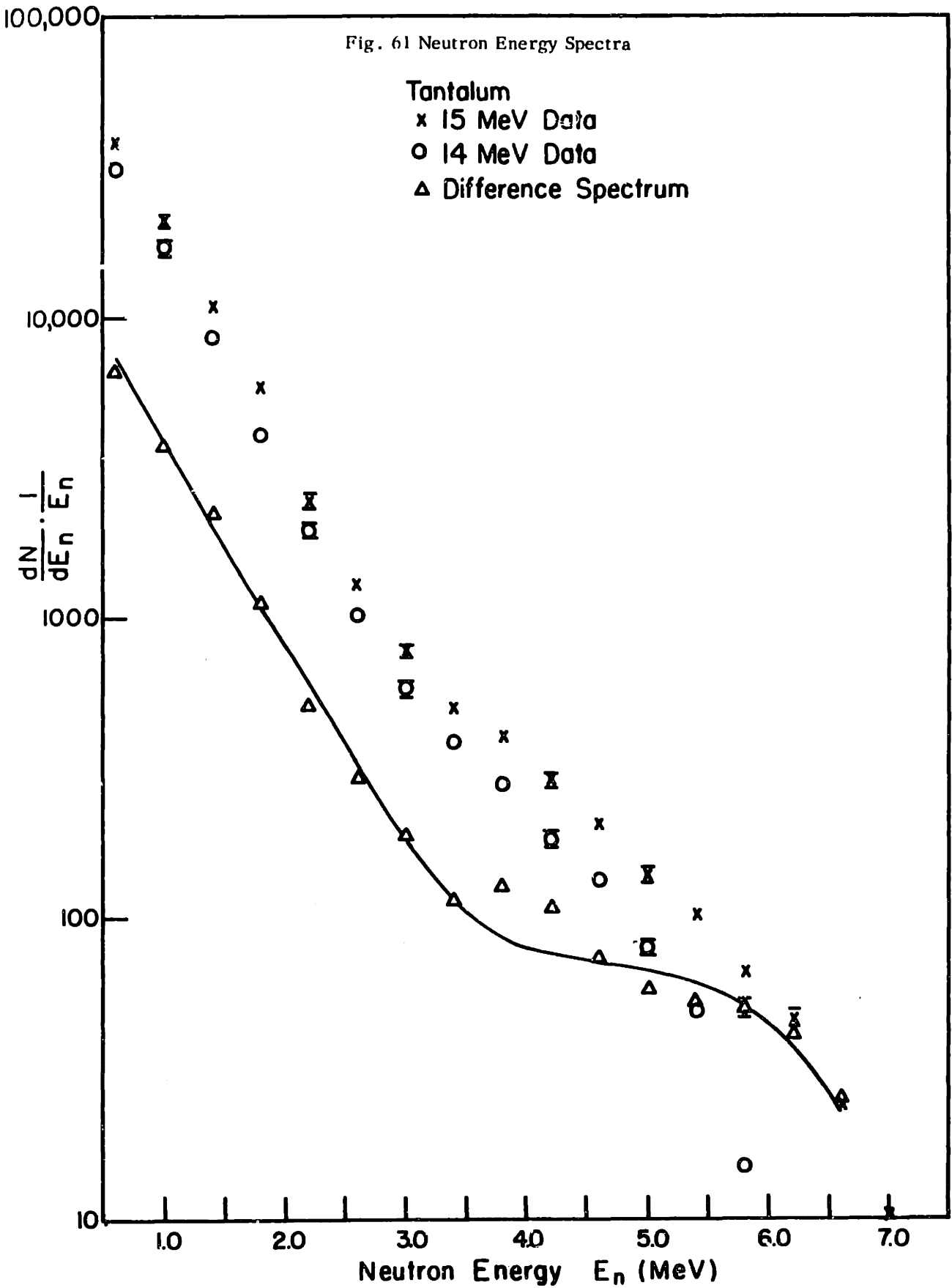
##### a) Experimental Data

The photoneutron energy spectra  $\frac{dN}{dE_n} \frac{1}{E_n}$  vs  $E_n$  for W, Ta, Er, Ho, and Sm are plotted in Figs. 60 to 65. Each graph contains two experimental photoneutron spectra and their difference. The two neutron spectra are generated by two bremsstrahlung spectra with endpoints of 15 and 14 MeV respectively. The difference represents the photoneutron spectrum resulting from a photon spectrum peaked at 14 MeV. In addition a second set of tantalum data is shown (Fig. 63), which contains the photoneutron spectrum resulting from a photon difference spectrum peaked at 13 MeV. Because of the splitting of the giant resonance in the deformed region, the photon difference spectrum times the photon absorption cross section is somewhat wider than in the case of the targets near lead (see Fig. 11).

##### b) Direct Spectrum

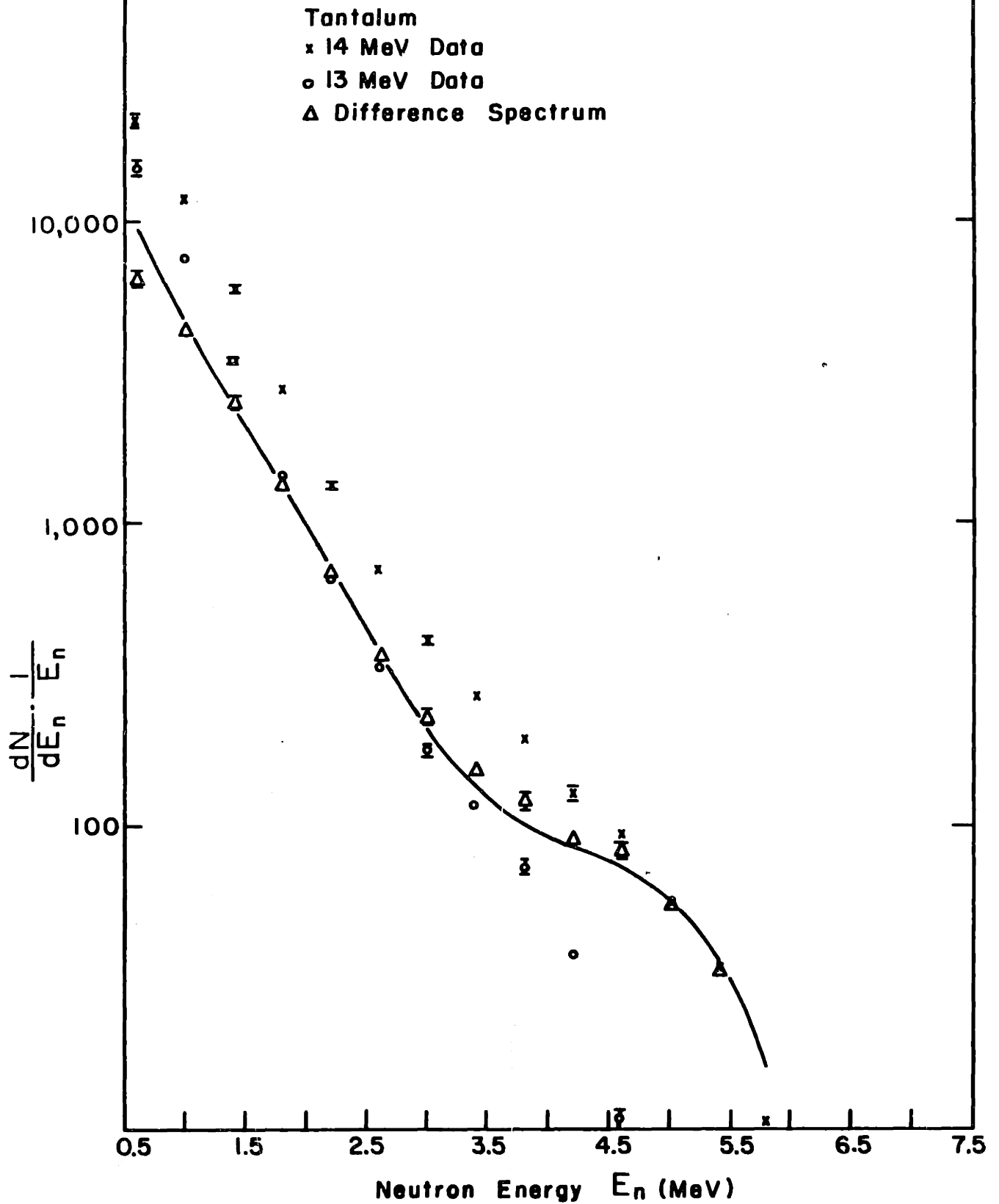
The relative transition strengths,  $f_{\rho}$ , given in Table XIII were calculated for a spherically symmetric square well (30). These values may not be applicable in the region of the deformed nuclei, W to Sm, because of the mixing of the single particle states in a deformed well. The calculations on deformed nuclei available in the literature are for nuclei with much lower mass





100,000

Fig. 62 Neutron Energy Spectra



100000

Fig. 63 Neutron Energy Spectra

Erbium  
x 15 MeV Data  
o 14 MeV Data  
Δ Difference Spectrum

$$\frac{dN}{dE_n} \cdot \frac{1}{E_n}$$

10,000

1000

100

10

1.0

2.0

3.0

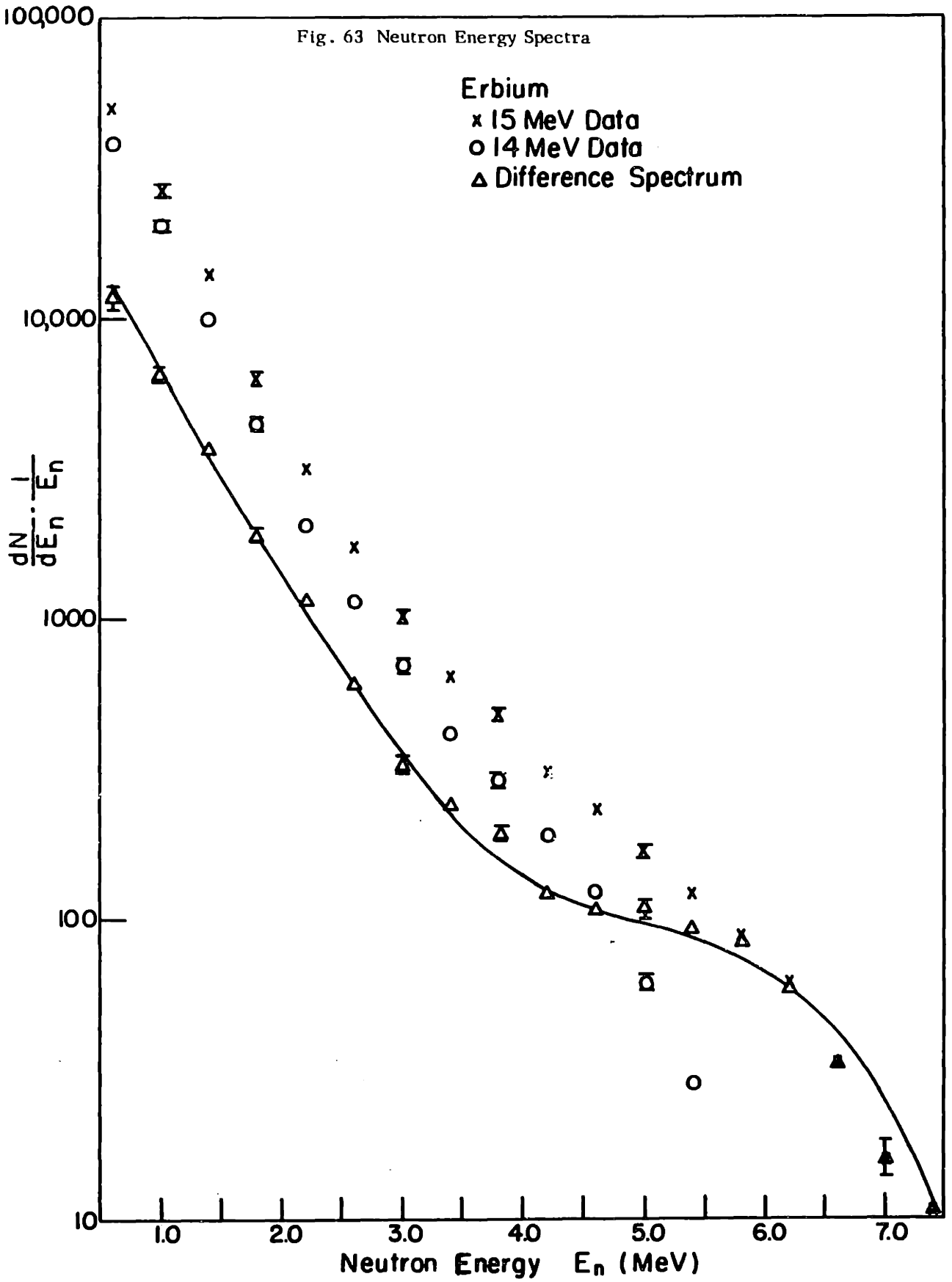
4.0

5.0

6.0

7.0

Neutron Energy  $E_n$  (MeV)



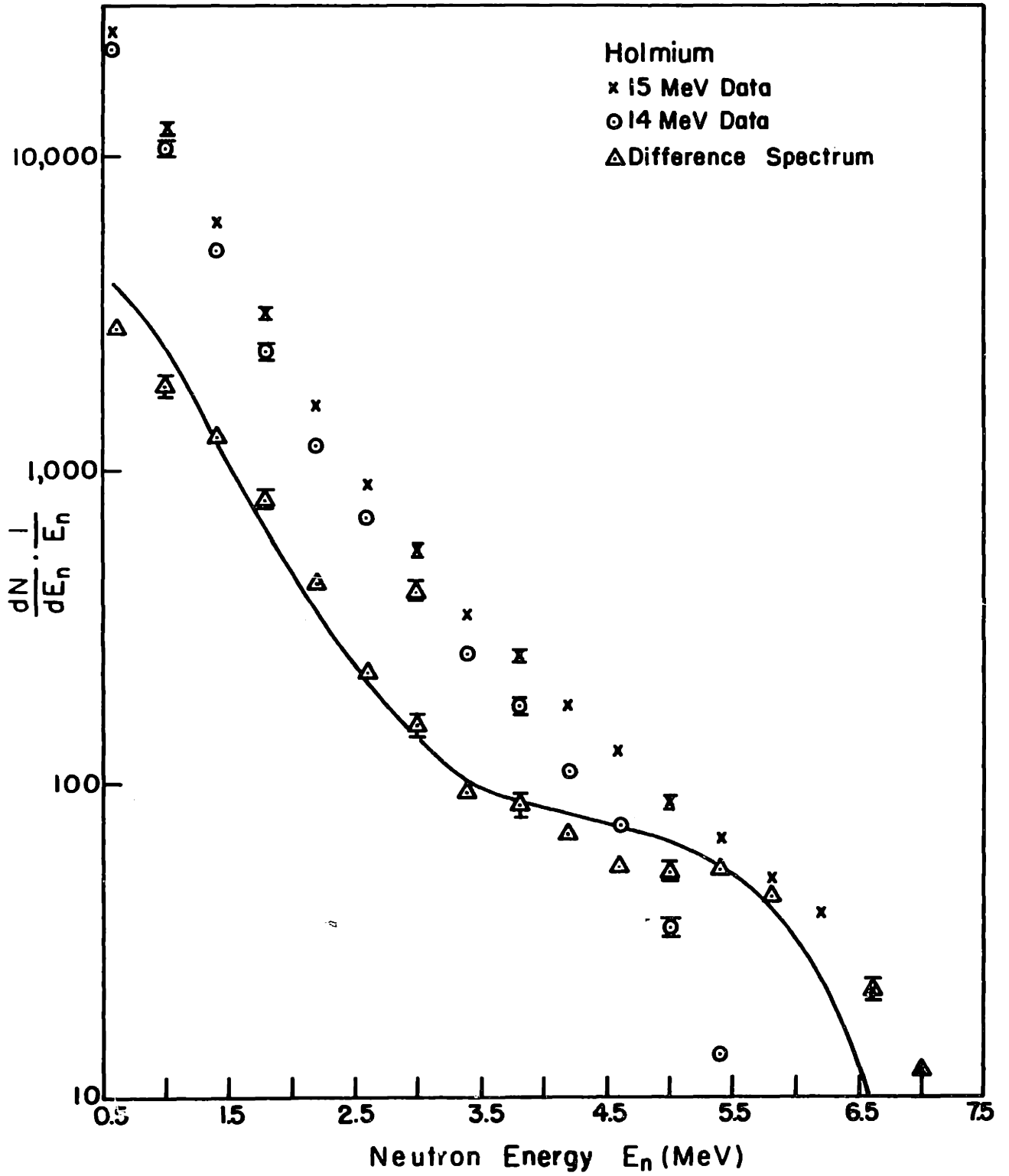
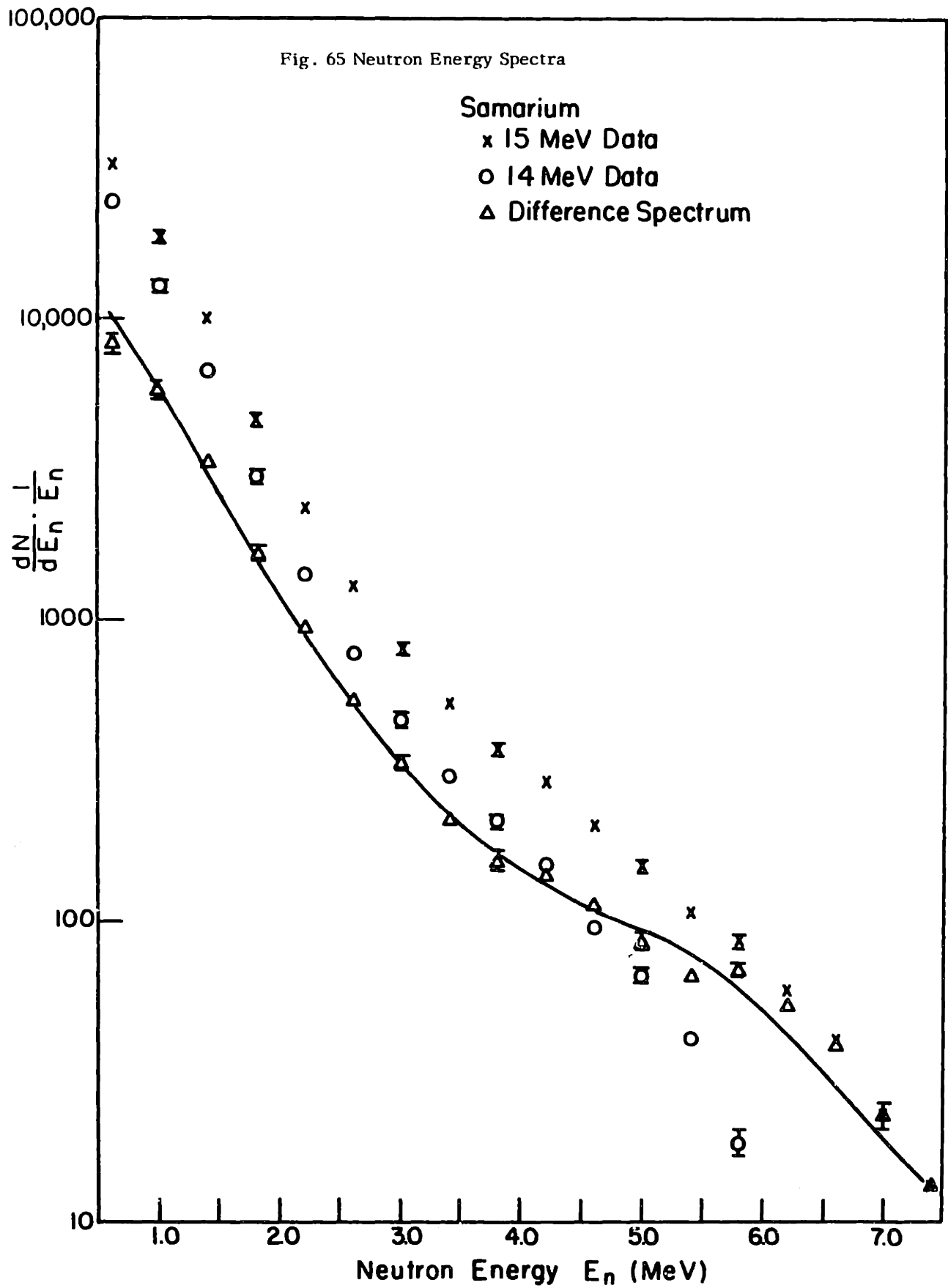


Fig. 64 Neutron Energy Spectra



number A than the rare earth region. For example, Nilsson et al (41) have performed the necessary calculations for  $Mg^{24}$ . Their calculations show that the  $\Delta\Omega = 0$  transitions favor the  $\Delta N = \Delta n_z = +1$  transitions, and the  $\Delta\Omega = \pm 1$  transitions favor the  $\Delta N = \Delta \Lambda = +1$  transitions.

In the deformed nuclei  $n$  and  $\ell$  are no longer good quantum numbers. Instead the states are labelled  $|Nn_z\Lambda\Omega\rangle$  where  $N$  is the total number of nodes in the radial nucleonic wave function,  $n_z$  is the number of nodal planes perpendicular to the symmetry axis,  $\Lambda$  is the component of the nucleon orbital angular momentum along the symmetry axis, and  $\Omega$  is the component of the total nucleon angular momentum along the symmetry axis. (These are good quantum numbers in the limit of large deformations (78).) There are two types of E1 transitions possible,  $\Delta\Omega = 0$ , which corresponds to the multipole operator  $z$  and is associated with the energy  $\hbar\omega_z$ , ie, oscillations along the  $z$  axis, and  $\Delta\Omega = \pm 1$  which corresponds to the multipole operator  $2^{-1/2}(x + iy)$  and is associated with the energy  $\hbar\omega_\perp$ , ie, oscillations perpendicular to the symmetry axis.  $\hbar\omega_z < \hbar\omega_\perp$  for prolate nuclei (the rare earth region). Therefore the  $\Delta\Omega = 0$  transition will occur at a lower energy.

An examination of Nilsson's level diagram for deformed nuclei (40) shows that these transitions are generally E1 transitions between states that correspond to the  $n\ell \rightarrow n\ell+1$  transitions in the case of an undeformed nucleus. Although the square well calculations of  $f_\ell$  are not quantitatively correct, they will at least tend to pick out the important transitions. Lacking a calculation of overlap integrals for a deformed potential, the  $f_\ell$ 's calculated from the square well potential (and listed in Table XIII, column two) will be used.

Therefore  $S(E_n)$  was calculated using the Wilkinson transition strengths and assuming a continuous distribution of the hole states in the residual nucleus. The neutron ground state configuration of the deformed nuclei were determined by placing the appropriate number of neutrons in the Nilsson diagram. These configurations are listed in Table XIX. Also shown are the  $n\ell \rightarrow n\ell+1$  transition strengths for a filled shell. In addition to transitions from the  $N = 126$  shell, transitions from the  $N = 82$  to the  $N = 126$  shell are possible. These tran-



Table XIX

## Ground State Configuration for Deformed Nuclei\*

Subshell	No. of Neutrons in a Filled Shell	$f_{\ell}$	A = 180	A = 165	A = 152	$-a_2/a_0$
3p <sup>1/2</sup>	2	0.17	0	0	0	0.5
3p <sup>3/2</sup>	4	0.33	2	0	0	0.5
2f <sup>5/2</sup>	6	0.63	0	0	0	0.357
i <sup>13/2</sup>	14	2.16	8	6	2	0.30
2f <sup>7/2</sup>	8	0.84	8	6	4	0.357
1h <sup>9/2</sup>	10	1.53	6	4	2	0.318
N=82 shell filled	82		82	82	82	
Total No. of neutrons	126		106	98	90	

\*Nilsson (40)

Table XX

## Isotopic Abundance and Thresholds for the Deformed Nuclei\*

Isotope	Abundance Per Cent	$E_{th}$	$E_{2n}$	Isotope	Abundance Per Cent	$E_{th}$	$E_{2n}$
W <sup>186</sup>	28.4	7.28	12.96	Er <sup>170</sup>	14.9	17.19	13.18
W <sup>184</sup>	30.6	7.46	13.64	Er <sup>168</sup>	27.1	7.78	14.32
W <sup>183</sup>	14.4	6.19	14.19	Er <sup>167</sup>	22.9	6.54	14.99
W <sup>182</sup>	26.4	8.0	14.93	Er <sup>166</sup>	33.4	8.55	15.19
Ta <sup>181</sup>	100	7.65	14.4	Sm <sup>154</sup>	22.53	7.90	13.79
Ho <sup>165</sup>	100	8.12	14.6	Sm <sup>152</sup>	26.63	8.22	13.83
				Sm <sup>149</sup>	13.84	5.86	13.99
				Sm <sup>148</sup>	11.27	8.13	14.47
				Sm <sup>147</sup>	15.07	6.33	14.77

\*Wapstra et al (70)

sitions have been included, and the necessary hole states evenly distributed in the residual nucleus. This procedure was used for the deformed nuclei, even though it was not used for Hg and Au, because the deformation mixes the single particle states more thoroughly. The transition strengths,  $f_{\ell}'$ , for an unfilled shell were assumed to be the  $f_{\ell}$ 's times the ratio of the number of neutrons in the shell to the number of neutrons that a filled shell could contain. The  $T_j$ 's were taken from ref 61 as usual. The product  $\rho_{\Delta}(E_n)\sigma(\gamma, n)$  was calculated for Ta and Ho using the parameters from ref 6. The photon absorption cross section for W was assumed to be similar to that for Ta, and the cross sections for Er and Sm were assumed to be similar to the one for Ho. The isotopic abundance and  $(\gamma, n)$  thresholds for W, Er and Sm are shown in Table XX.  $S(E_n)$  was calculated separately for each isotope and weighted by the isotopic abundance.

The results are shown in Figs. 66 to 71. The fit to the experimental direct spectrum is not as good as that obtained with nuclei near a closed shell. Due to the approximations that have been used, this method can only be expected to estimate the shape of the direct spectrum at low neutron energies where the  $T_j$ 's dominate and near the neutron endpoint where the photon spectrum dominates. It should not reproduce any effects due to the splitting of the giant resonance.

Any effects due to the double photon absorption peaks would probably be seen in the monoisotopic targets, Ta and Ho. Bramblett et al (6) have measured the  $(\gamma, n)$  and  $(\gamma, 2n)$  cross sections for Ta and Ho. They find that these cross sections have two peaks, at about 12.1 MeV and 15.8 MeV photon energy for Ho, and 12.8 MeV and 15.5 MeV for Ta. Since the  $(\gamma, n)$  threshold for Ho is 8.1 MeV, neutrons from the first peak should appear near 4.0 MeV and those from the second peak near 8.0 MeV neutron energy. The photon difference spectrum is small at 12 MeV and is peaked at 14 MeV photon energy, which corresponds to 6.0 MeV neutron energy. Fig. 70 shows that the neutron difference spectrum for Ho has a definite peak at 5.8 MeV and appears to have a peak at 4.2 MeV. Both the tungsten and tantalum data

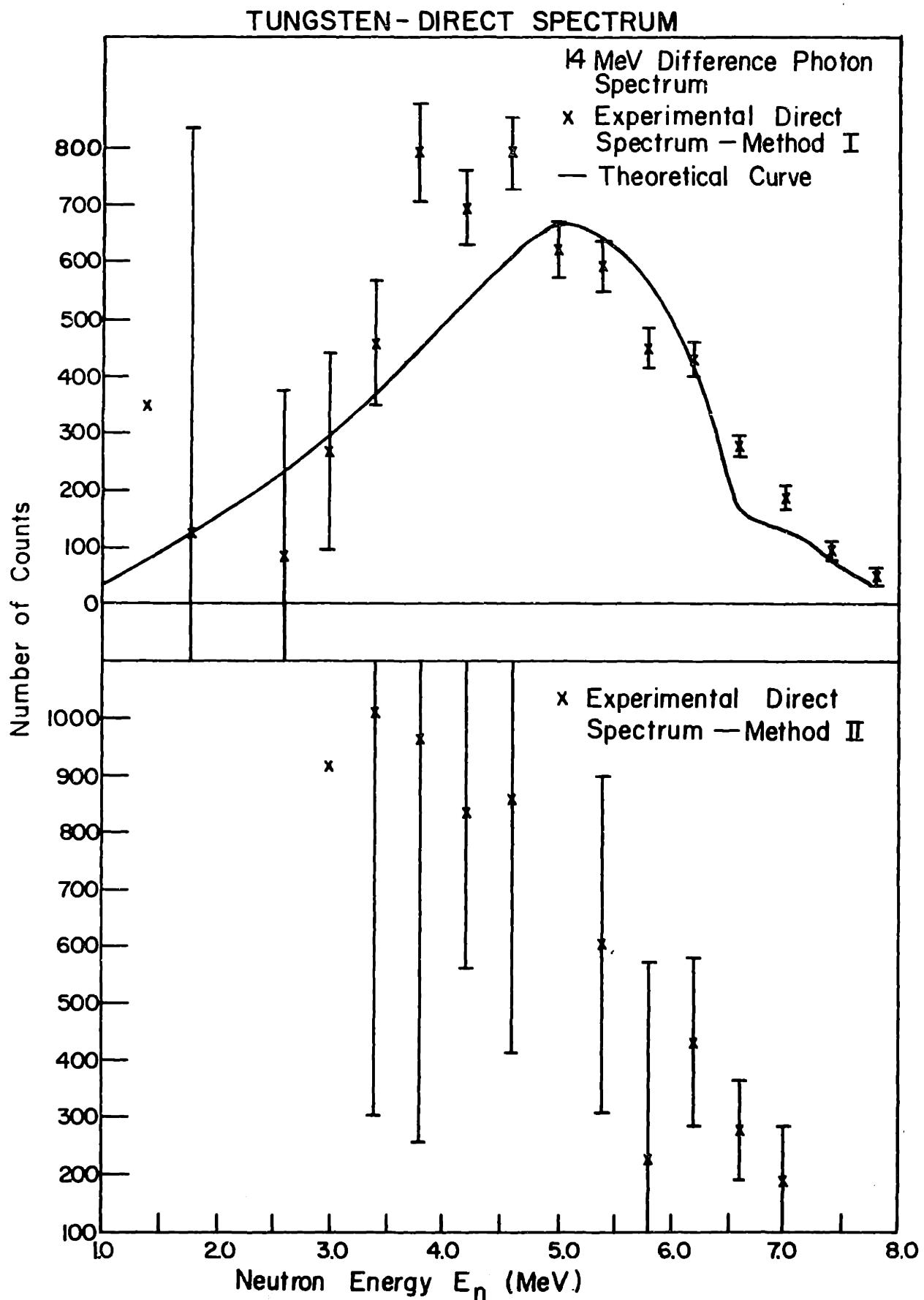


Fig. 66

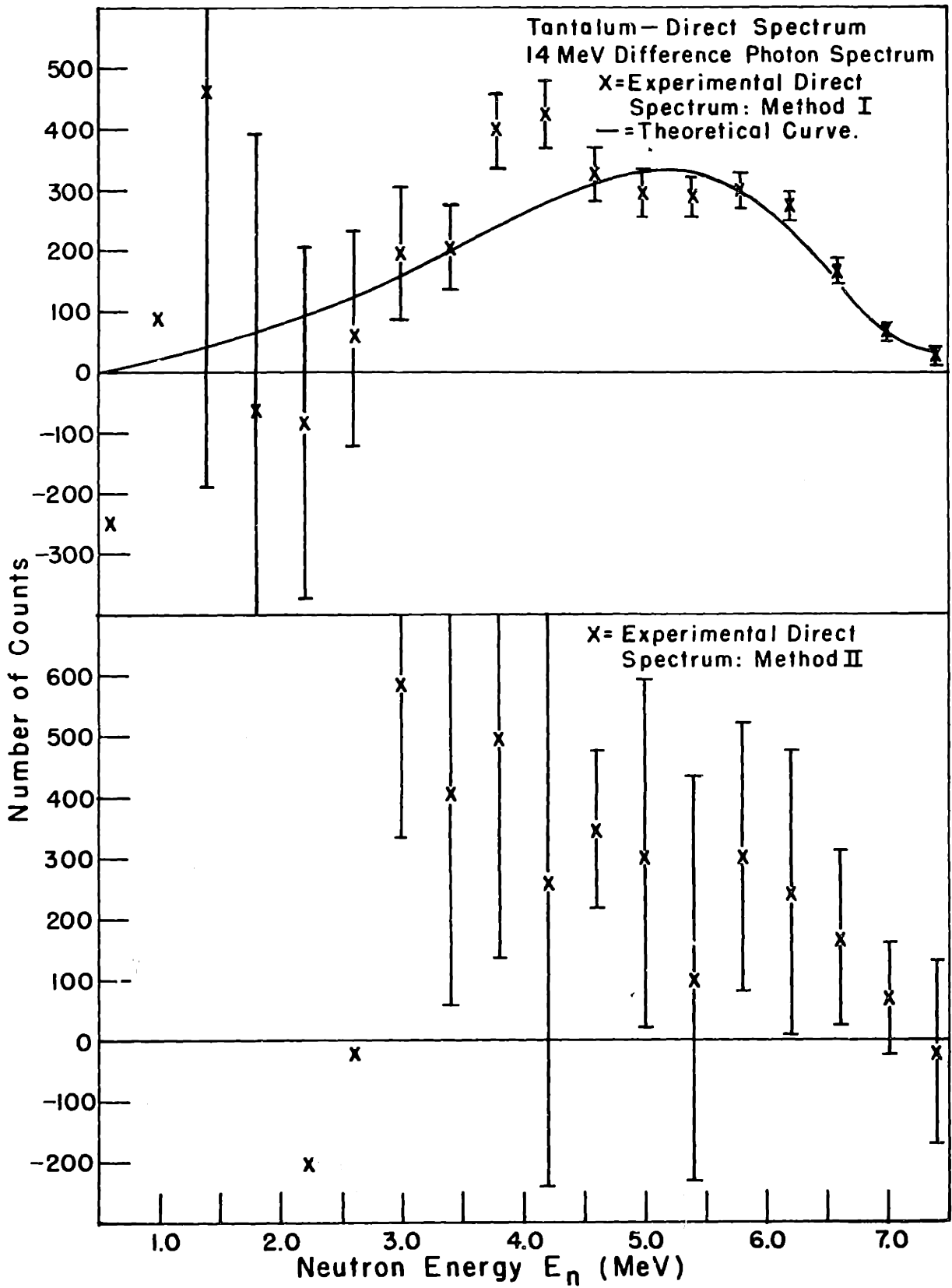
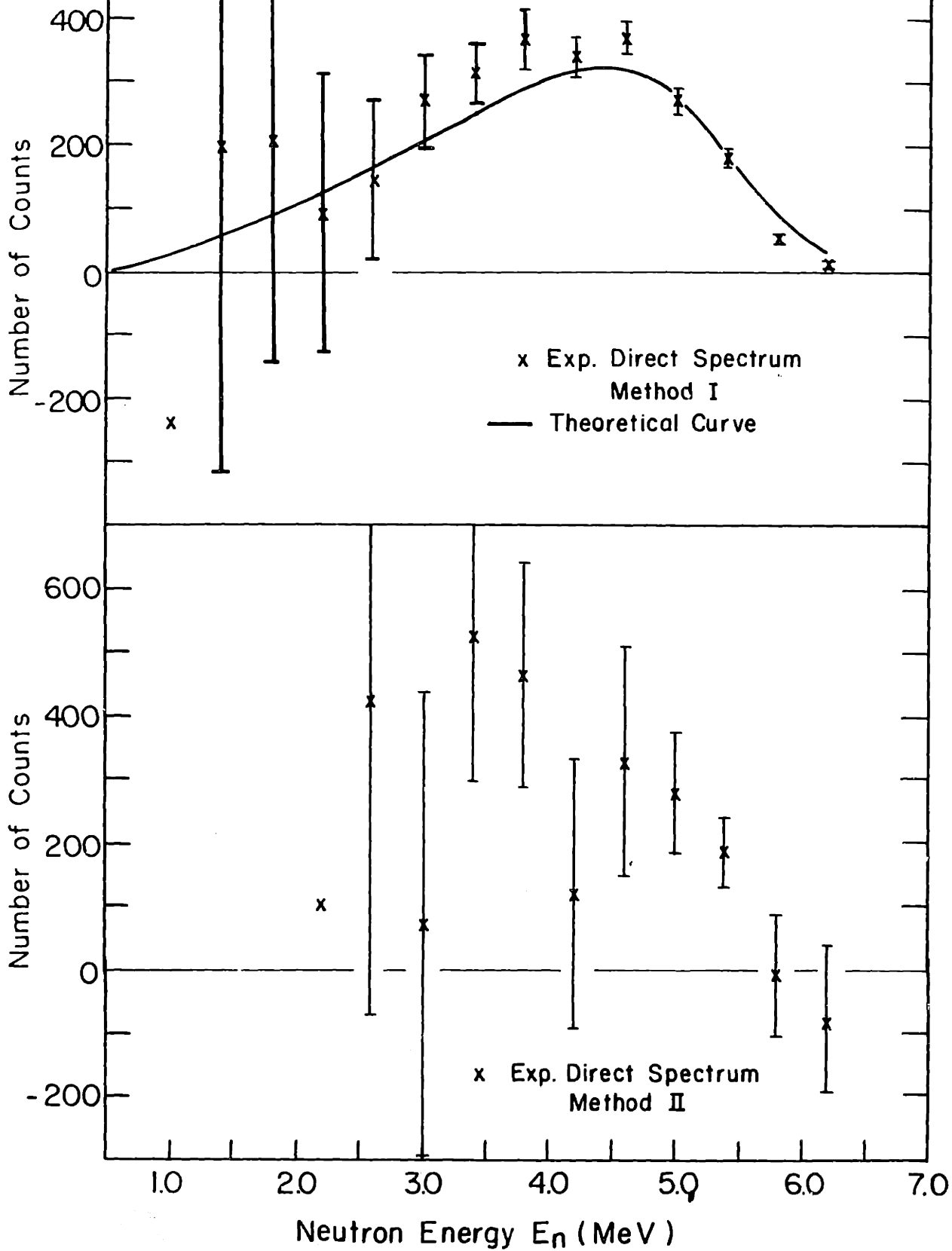


Fig. 67

Tantulum - Direct Spectrum  
13 MeV Difference Photon Spectrum

Fig. 68



# ERBIUM - DIRECT SPECTRUM

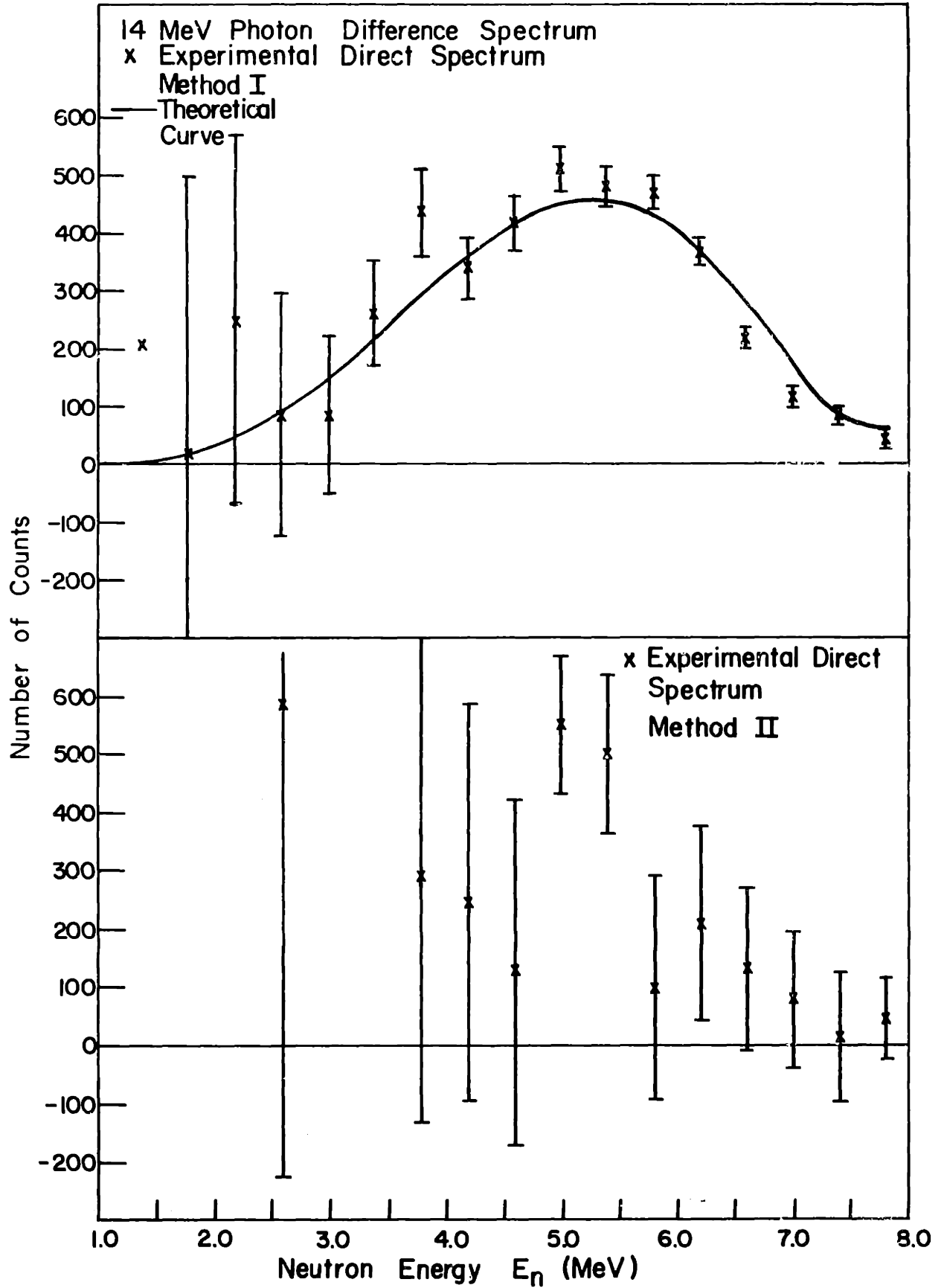


Fig. 69

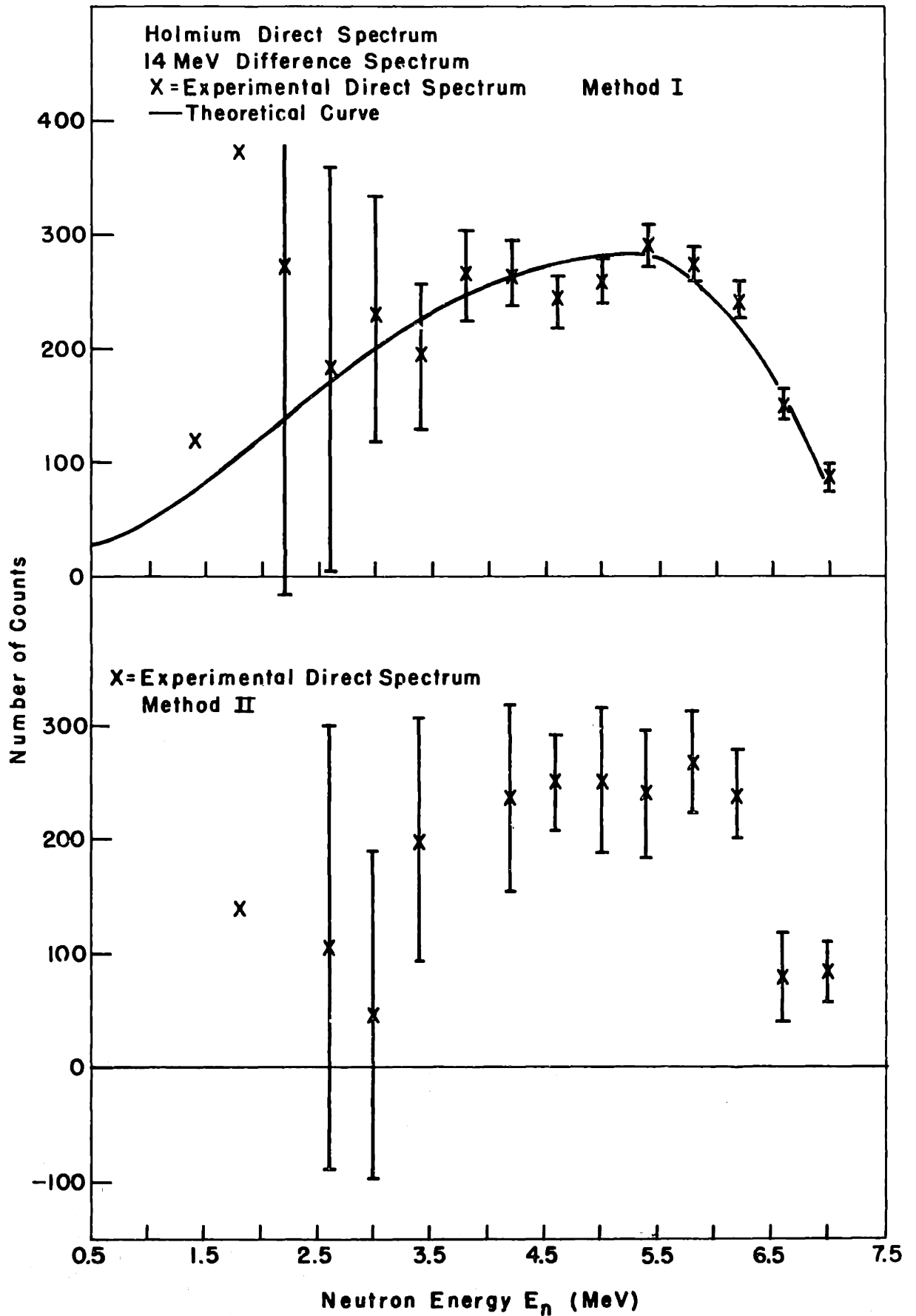


Fig. 70

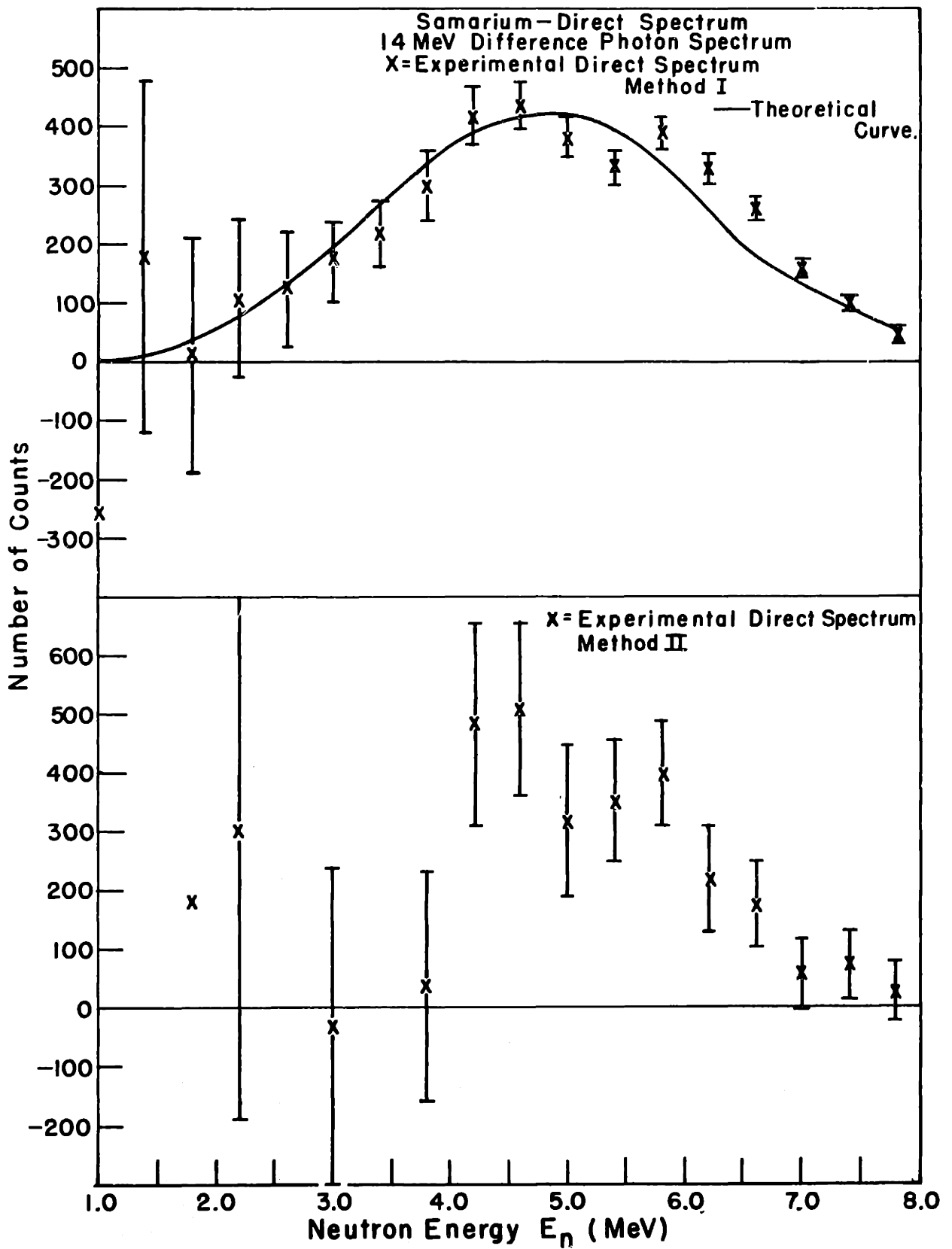


Fig. 71

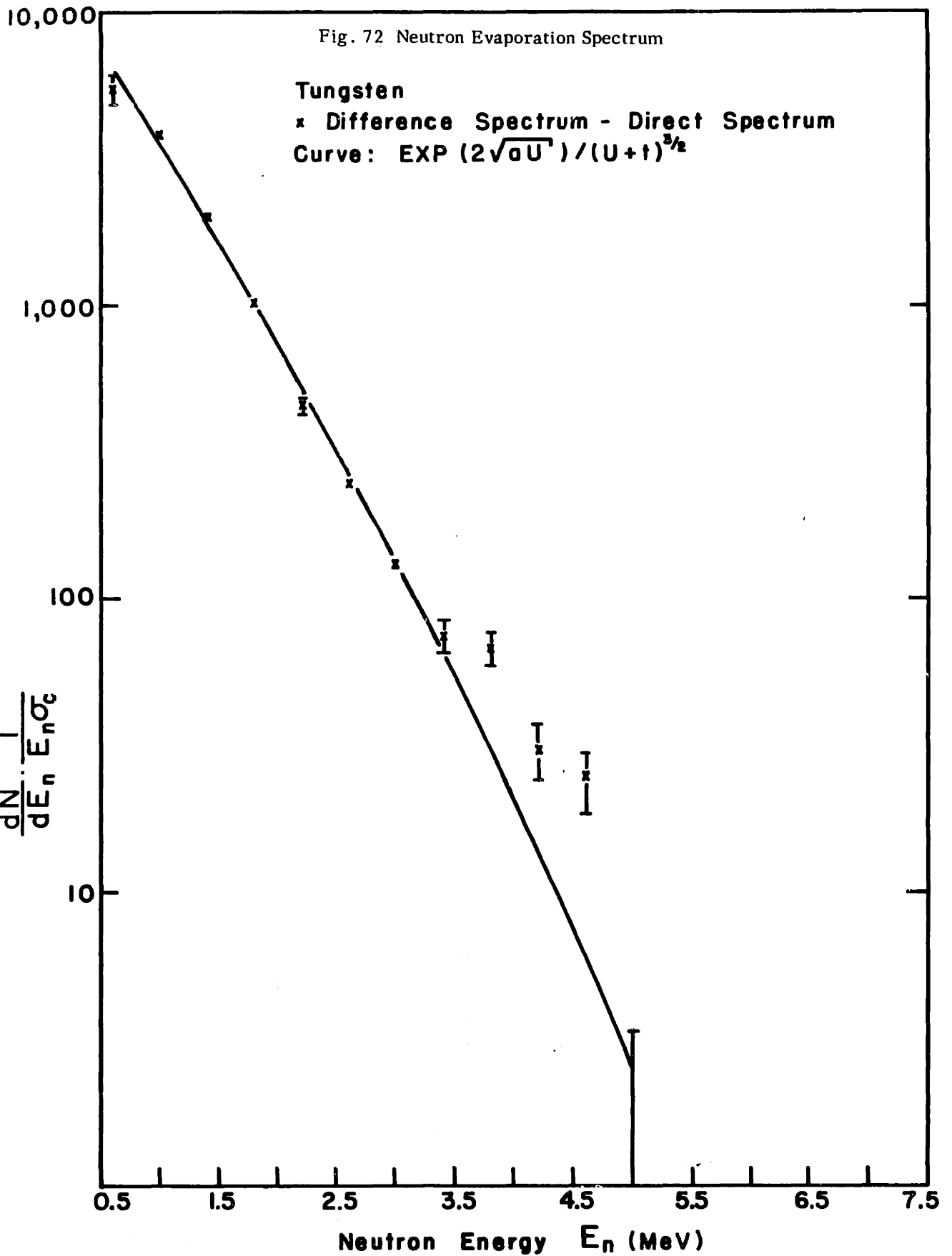


show peaks at about 3.0 to 4.0 MeV (Figs. 66, 67 and 68), which is somewhat lower than the 7.8 MeV ( $\gamma, n$ ) threshold for Ta and about 7.5 MeV ( $\gamma, n$ ) threshold for W would have led one to expect. The direct neutron spectra from Ho and Ta thus seem to indicate that the assumption of uniformly distributed hole states is weak. One can see a suggestion of the same peaks in Sm, but the low threshold isotopes (see Fig. 71) tend to obscure them. In Er, the isotopes have thresholds about 1 MeV apart, which would cause the peaks of one isotope to fall in the valley of another, which may explain the relatively featureless direct spectrum (Fig. 69).

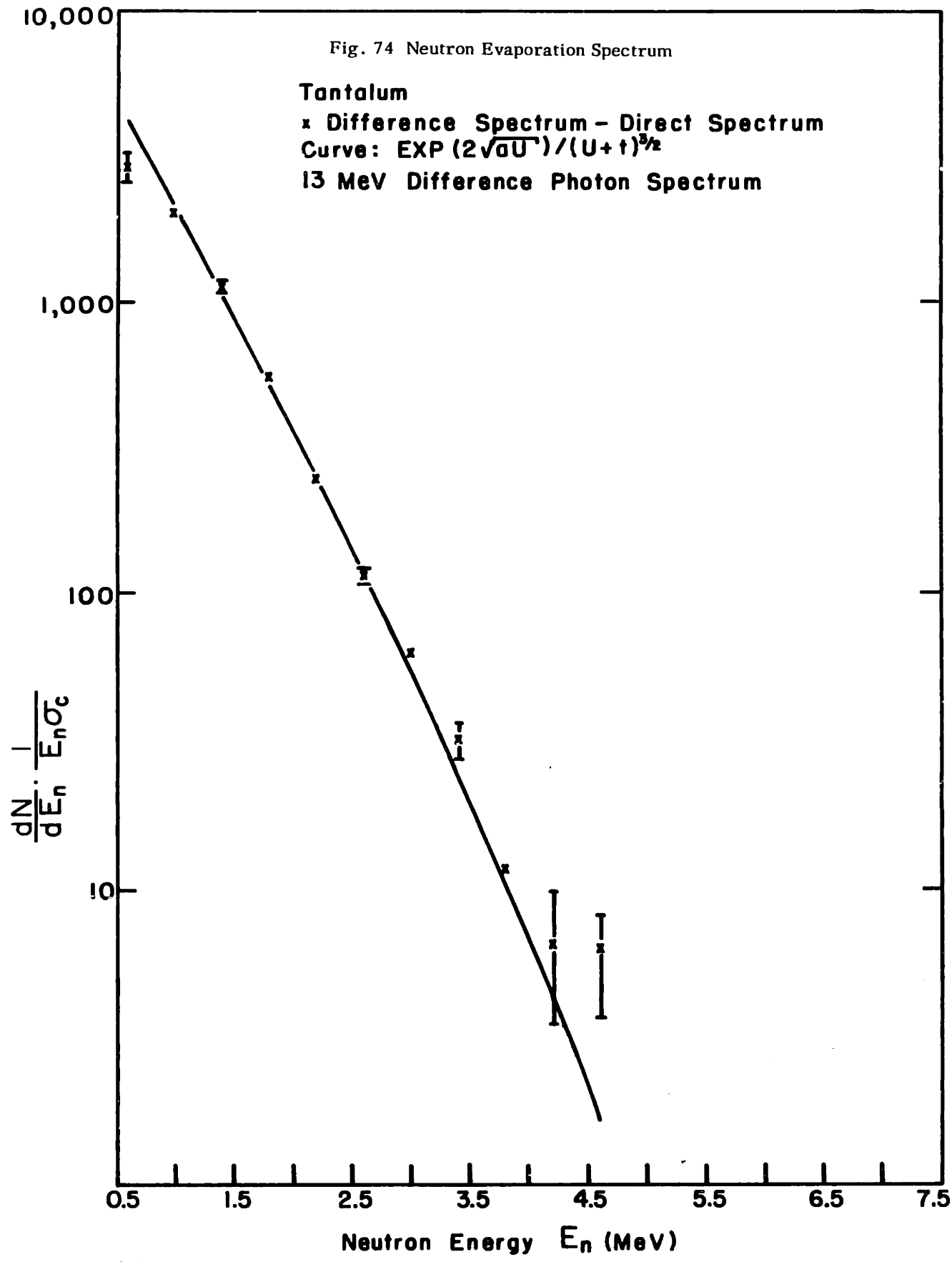
The above discussion has perhaps not been too informative. Because of the complexity of the unfilled, deformed shells, one cannot make simple predictions about the direct spectrum. Also the direct neutron spectra determined by Method II has very large errors, especially for W, Ta, and Er, because the angular distributions are small. As a result the resonance direct spectrum is poorly determined.

### c) Evaporation Spectrum

The experimental evaporation data and the theoretical curves are plotted in Figs. 72 to 77. The ( $\gamma, 2n$ ) contribution to the data can be considerable, as W, Er and Sm all have isotopes with ( $\gamma, 2n$ ) thresholds below 14.0 MeV. (See Table XX.) In the case of Ho, the ( $\gamma, 2n$ ) threshold is 14.6 MeV therefore the ( $\gamma, 2n$ ) contamination is expected to be negligible (about 3 per cent). Using the ( $\gamma, 2n$ ) and ( $\gamma, n$ ) cross sections from ref 6, the ( $\gamma, 2n$ ) contribution to the ( $\gamma, n$ ) spectrum of Ta is estimated to be about 6 per cent. This corresponds to about 18 per cent of the data at 0.6 MeV. On the other hand the negative portion of the 14 MeV photon difference spectrum is estimated to reduce the Ta neutron production by about 2 per cent. This would again be concentrated in the 0.6 MeV bin. Therefore the two effects tend to cancel in the 14 MeV difference spectrum. The 13 MeV difference data is not expected to have any ( $\gamma, 2n$ ) contamination and the effect of the negative tail of the 13 MeV photon spectrum is negligible. The data shown in Figs. 73 and 74 confirm these predictions qualitatively. If the 0.6 MeV point is excluded, the data and the-







# ERBIUM

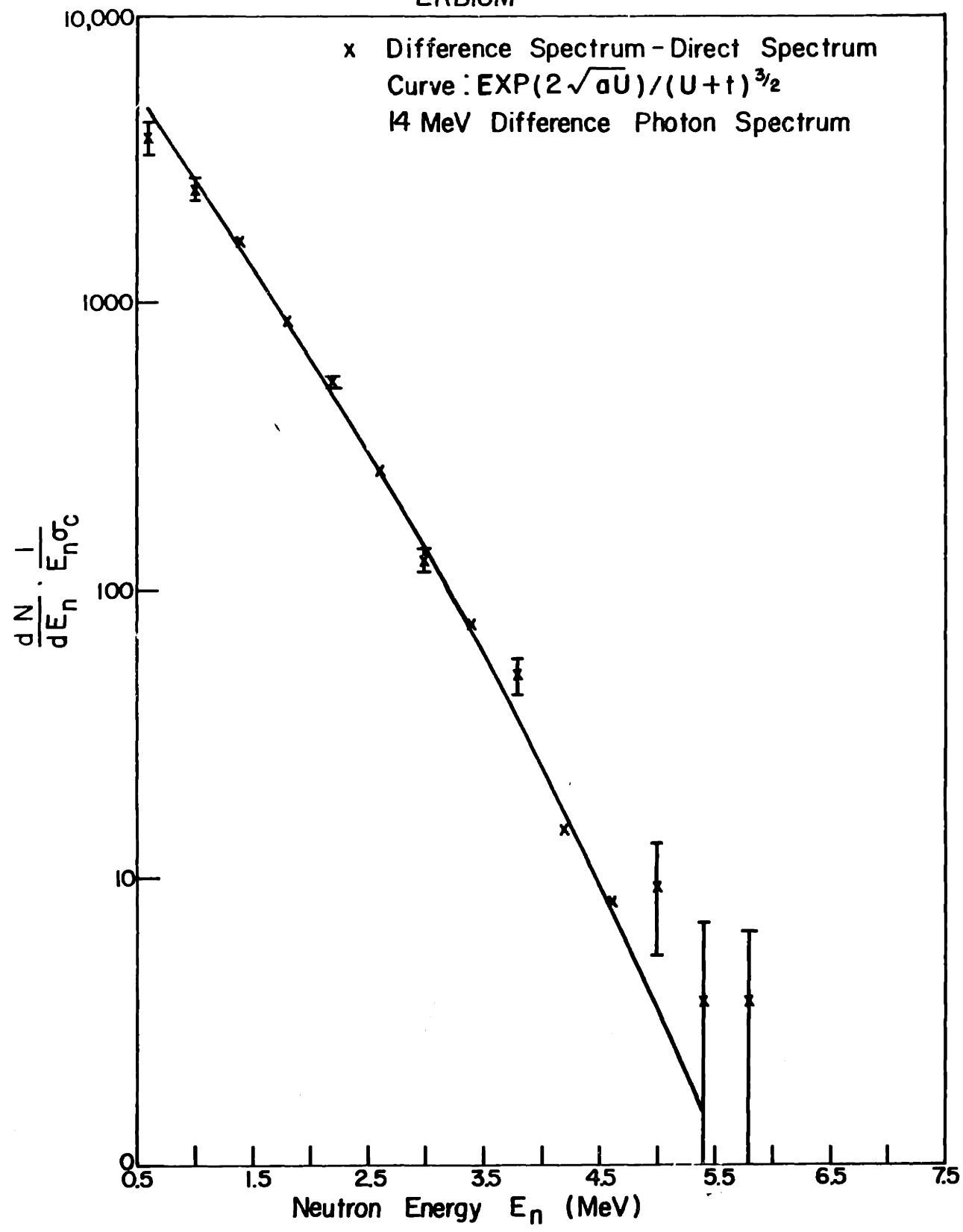


Fig. 75 Neutron Evaporation Spectrum

10,000

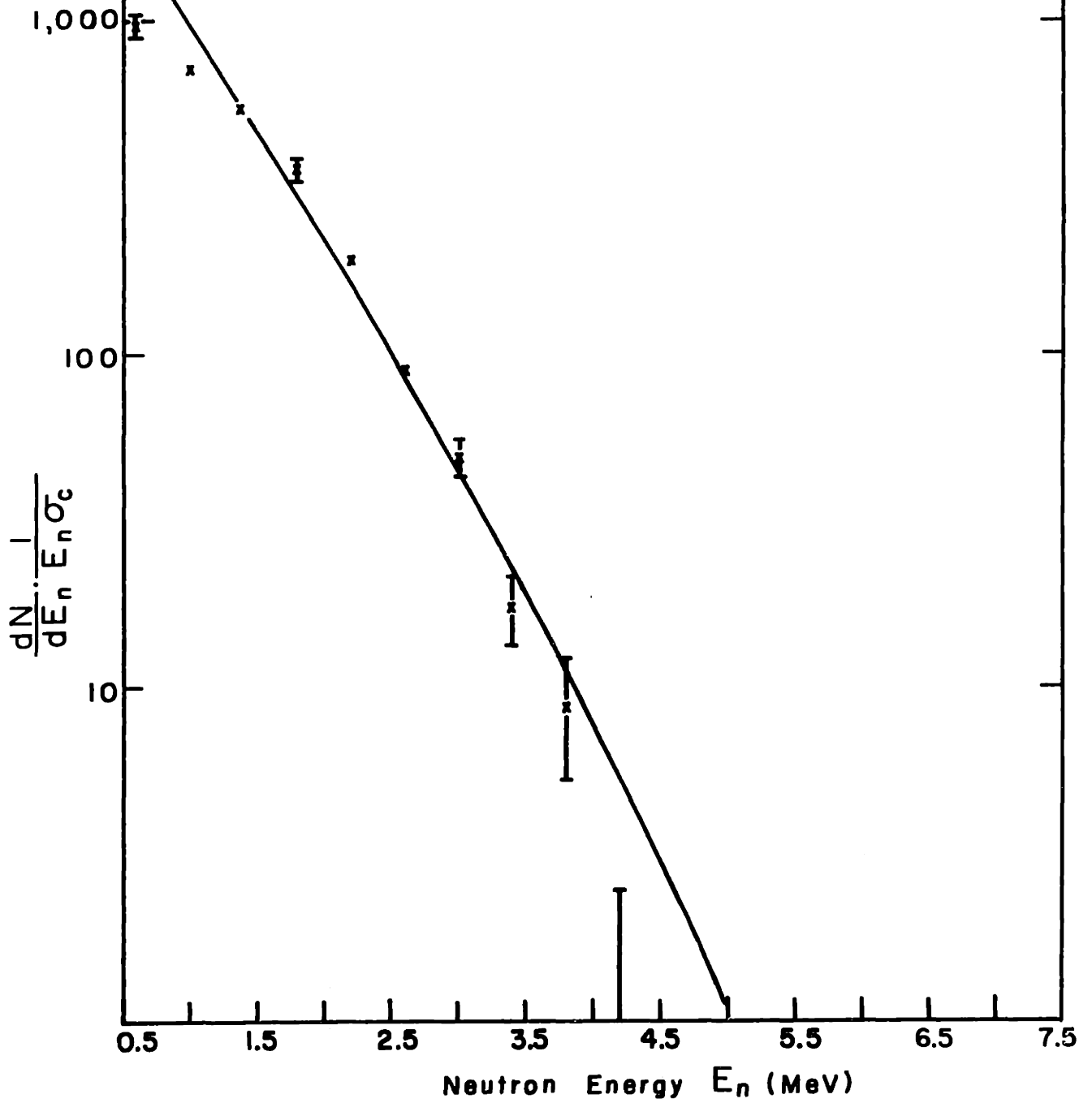
Fig. 76 Neutron Evaporation Spectrum

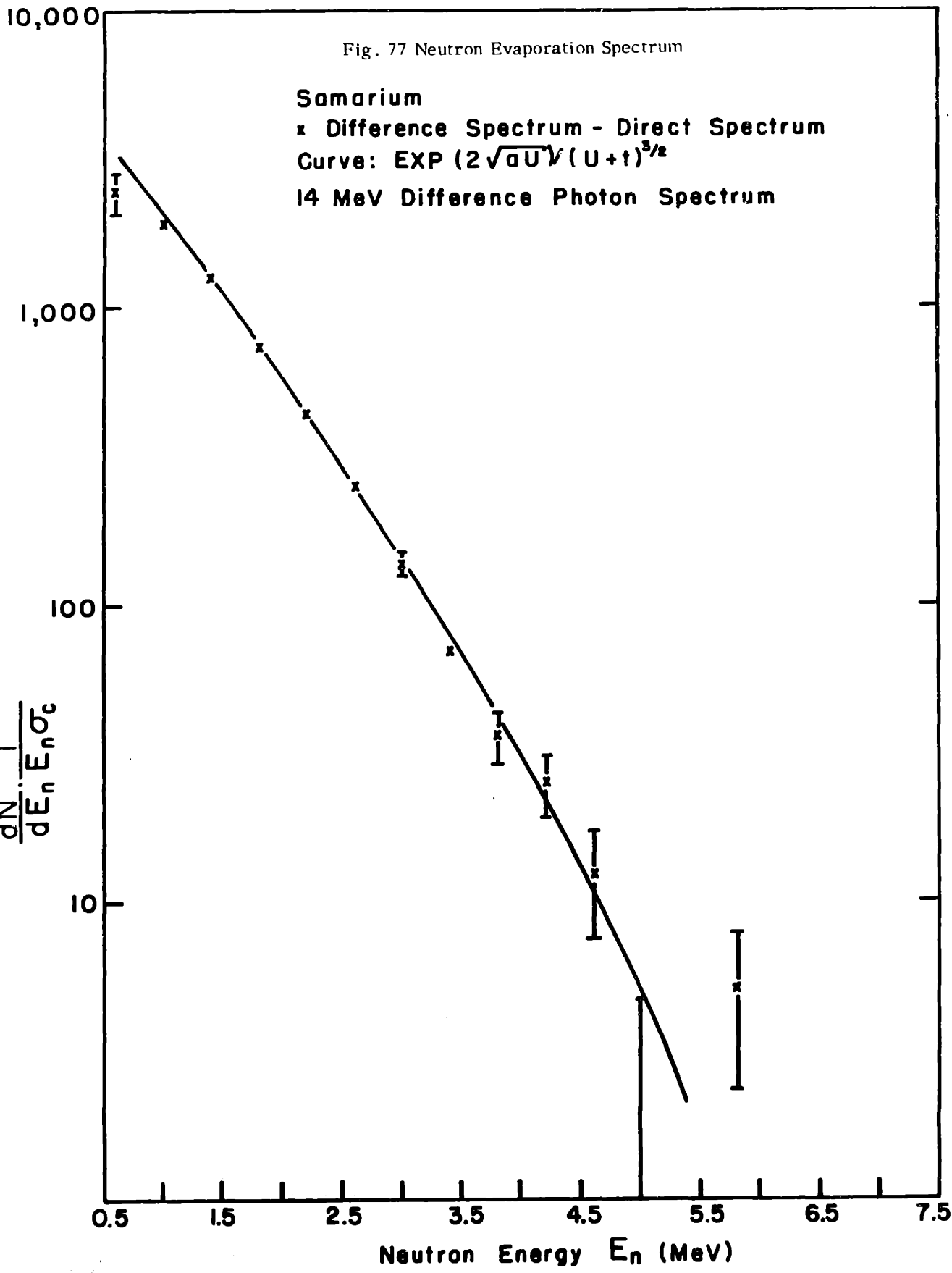
Holmium

x Difference Spectrum - Direct Spectrum

Curve:  $\text{EXP}(2\sqrt{aU})/(U+t)^{3/2}$

14 MeV Difference Photon Spectrum





ory are in excellent agreement from 1 to 3.5 MeV. Since the  $(\gamma, 2n)$  cross section for each isotope of W, Er and Sm is not available, the  $(\gamma, 2n)$  contribution cannot be calculated accurately. However, using the level density parameters measured in this experiment and the thresholds listed in Table XX, the  $(\gamma, 2n)$  contamination for these elements was estimated. In each case the  $(\gamma, 2n)$  contamination of the total spectrum is sizable, W = 23 per cent, Er = 9 per cent, and Sm = 15 per cent. The negative portion of the photon difference spectrum is a smaller effect, W = 3 per cent, Er = 3 per cent, and Sm = 4 per cent of the total spectrum. The  $(\gamma, 2n)$  contamination is a large contribution to the 0.6 MeV bin, W = 67 per cent, Er = 25 per cent and Sm = 50 per cent. In addition the  $(\gamma, 2n)$  contribution is no longer negligible in the 1.0 MeV bin, W = 19 per cent, Er = 7 per cent and Sm = 11 per cent. The contribution to the 1.4 MeV bin is negligible in all three cases. Thus the level density parameters have been increased to some degree by the  $(\gamma, 2n)$  contamination. (However, remember that the 0.6 MeV bin has been excluded from the calculation of the level density parameters.)

However from Figs. 72 to 77 it is seen that the data fits the theory quite well excluding the 0.6 MeV bin. The data lies below the curve for the 0.6 MeV point, although the Er and W data are almost within one standard deviation, while Sm is almost two standard deviations away. This surprising agreement suggests that the  $(\gamma, 2n)$  contamination has been overestimated. Since the actual  $(\gamma, n)$ ,  $(\gamma, 2n)$  cross sections are not known, this is quite possible. Also the  $(\gamma, 2n)$  thresholds may be too low for a few isotopes. (The values used were taken from mass tables compiled by Wapstra et al (70).) A third possible explanation is suggested by the Ho data. This data is a very poor fit to the theoretical curve. The  $(\gamma, 2n)$  contamination is small, and the effect of the negative portion of the photon spectrum is small (about 3 per cent) because of the high  $(\gamma, n)$  threshold (about 8.1 MeV) (70). The inverse capture cross section  $\sigma_C$  used for Ho has a large peak at 0.6 MeV (see Table XII). If  $\sigma_C$  had a different behavior at low neutron energy (for instance, if  $\sigma_C \approx \text{constant}$ ) the fit could be improved. Since the  $\sigma_C$  from ref 62 was calculated for a spherical potential, it would not be surprising to find the  $\sigma_C$  for a deformed



nucleus differing from the calculated value. In the same manner the  $\sigma_C$ 's for W, Ta, Er and Sm may be too large at low neutron energies and tending to mask the  $(\gamma, 2n)$  contamination. For these reasons, the level density parameters derived from the deformed nuclei data may be less reliable than those derived from the nondeformed nuclei data.

#### d) Angular Distributions

The angular distribution of the photoneutrons from W, Ta, Er, Ho and Sm are plotted in Figs. 78 to 82. The graphs are plots of  $-a_2/a_0$  vs  $E_n$ , where  $W(\Theta) = a_0 + a_2 P_2(\cos \Theta)$ . It is immediately obvious that the maximum values of  $-a_2/a_0$  reached by these data are much lower than the  $-a_2/a_0$  obtained with the nuclei at closed shells. The W photoneutrons reach a maximum  $-a_2/a_0$  of about 0.2 at 5.0 MeV, and then decrease with increasing neutron energy. The Ta photoneutrons reach a maximum  $-a_2/a_0$  of  $> 0.2$  at about 4.5 MeV, after which the spectrum remains flat. The Er photoneutrons have a maximum  $-a_2/a_0$  of about 0.3 at 5.0 MeV, and then the spectrum decreases with increasing neutron energy. The Sm photoneutrons have a maximum  $-a_2/a_0$  of about 0.25 at 5.0 MeV and then their spectrum remains flat. Only the Ho photoneutrons appear to have an increasing  $-a_2/a_0$  with increasing neutron energy, and even here, the statistics are such that one could claim that  $-a_2/a_0$  reaches a maximum of about 0.3 at 0.6 MeV and remains flat above this. In all five elements the low energy photoneutrons are isotropic.

The direct spectrum neutrons are predominately from the  $f^{7/2}$  shell according to the simplified model employed here. The neutrons from the  $i^{13/2}$  and  $h^{9/2}$  shells are suppressed by the small  $T_j$ 's. According to equation 11 the neutrons from the  $f^{7/2}$  shell can have an angular distribution ranging from  $-a_2/a_0 = 0.1$  for  $2f^{7/2} \rightarrow 3d^{5/2}$ , to 0.47 for  $2f^{7/2} \rightarrow 2g^{9/2}$ . All of the observed  $-a_2/a_0$ 's lie between these wide limits.

### F. Praseodymium and Lanthanum

#### a) Experimental Data

The photoneutron energy spectra  $\frac{dN}{dE_n} \frac{1}{E_n}$  vs  $E_n$  for Pr and La are plotted in Figs. 83 and 84. Each graph contains two neutron spectra and their

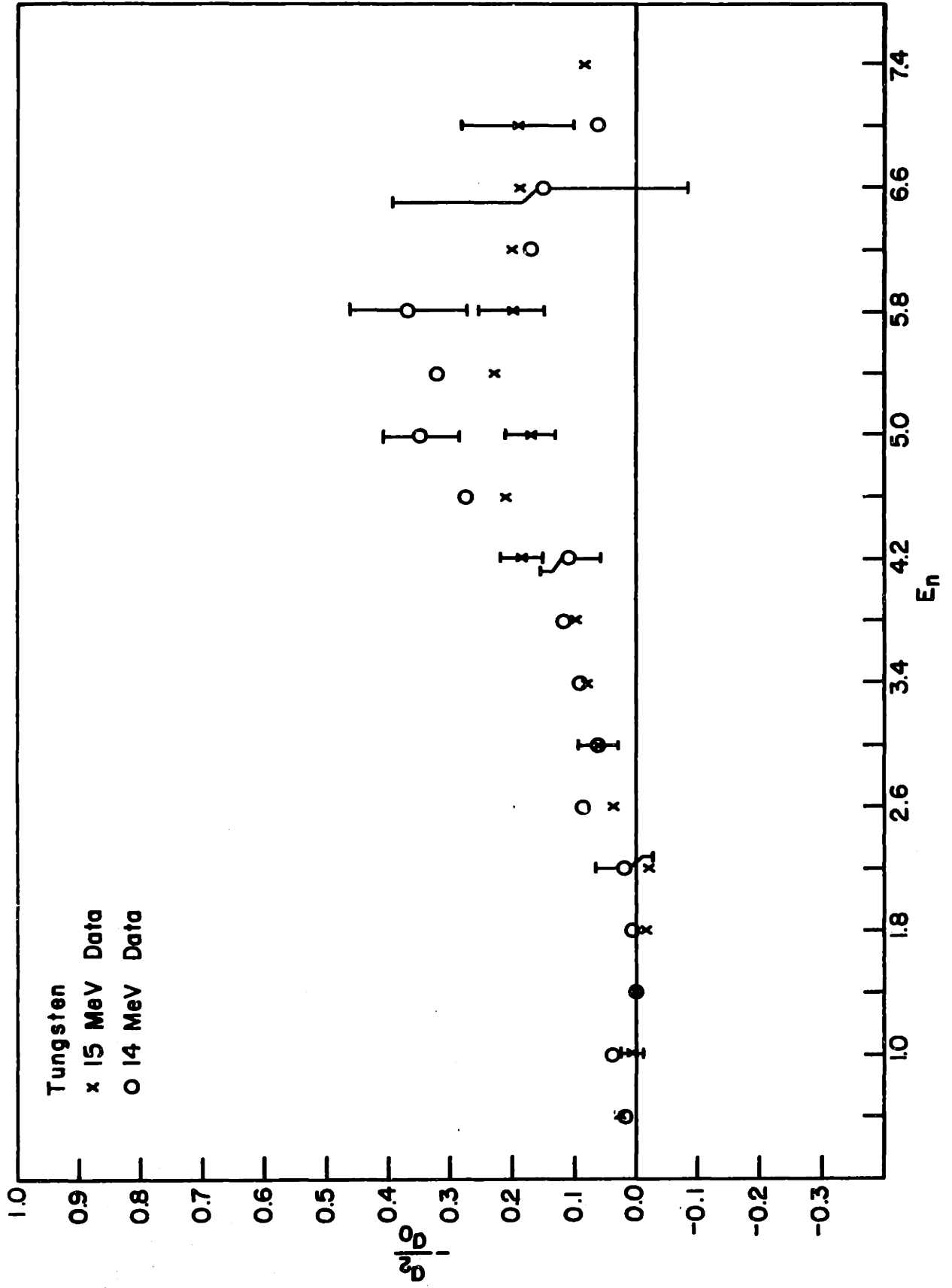


Fig. 78 Photoneutron Angular Distributions

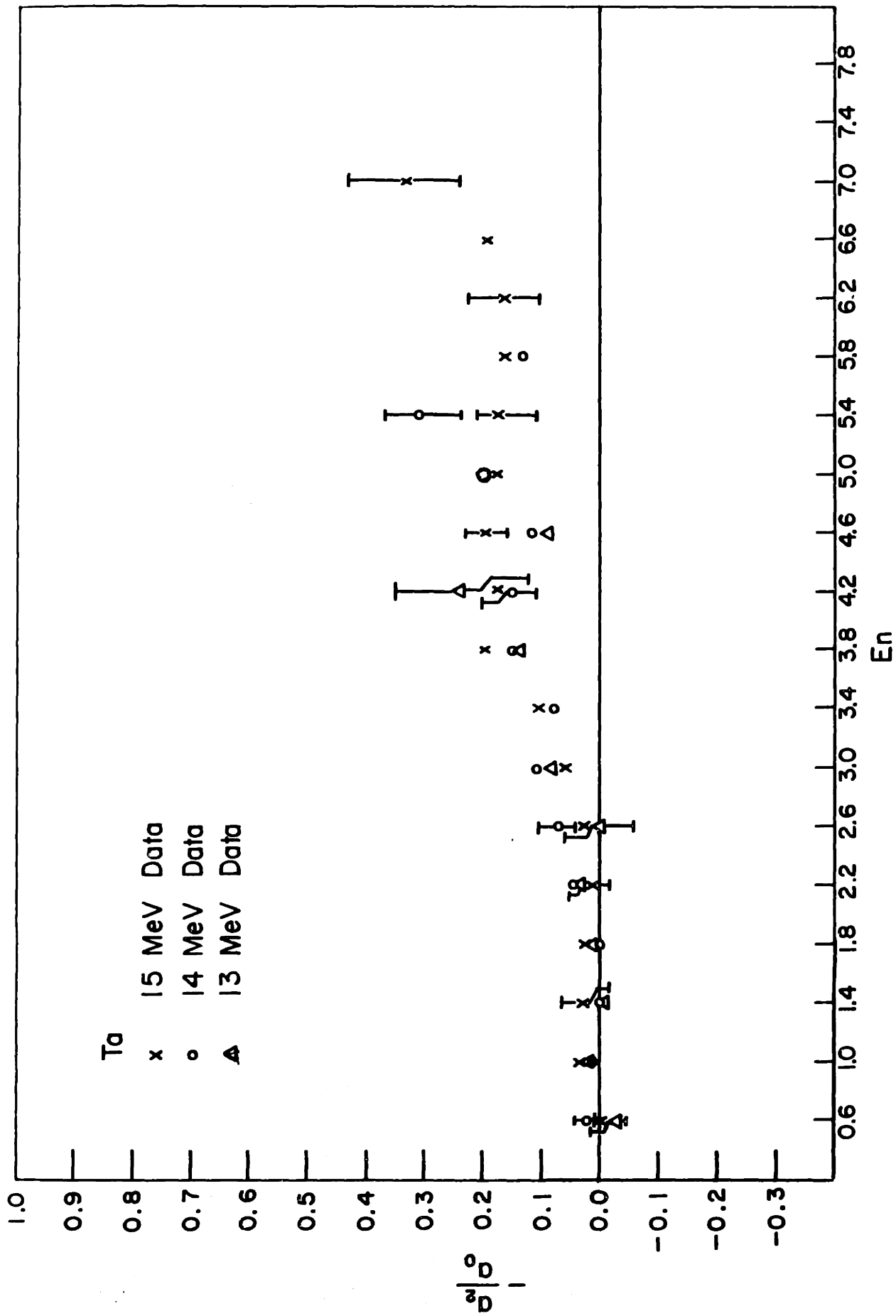
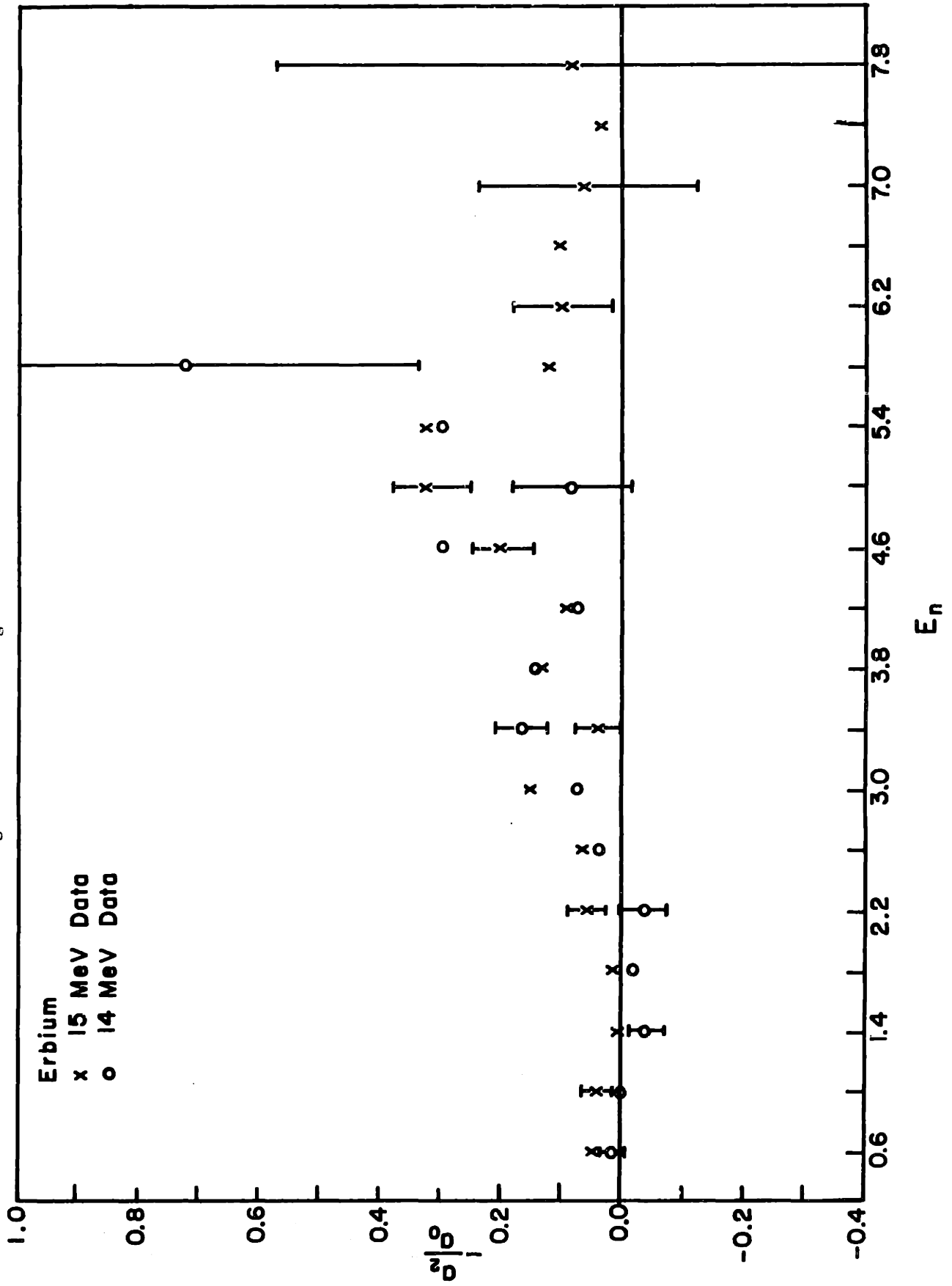


Fig. 79 Photoneutron Angular Distribution

Fig. 80 Photoneutron Angular Distributions



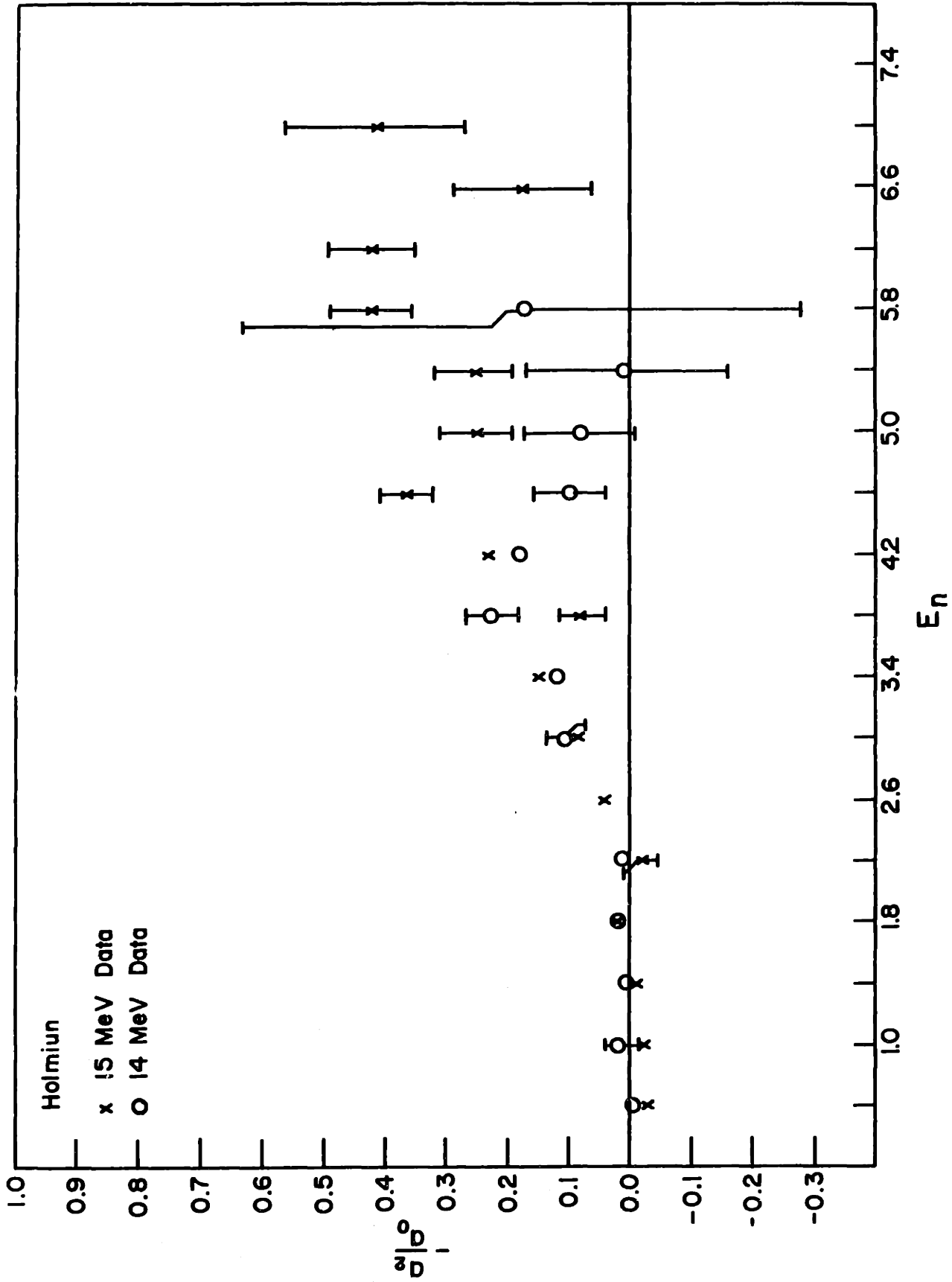
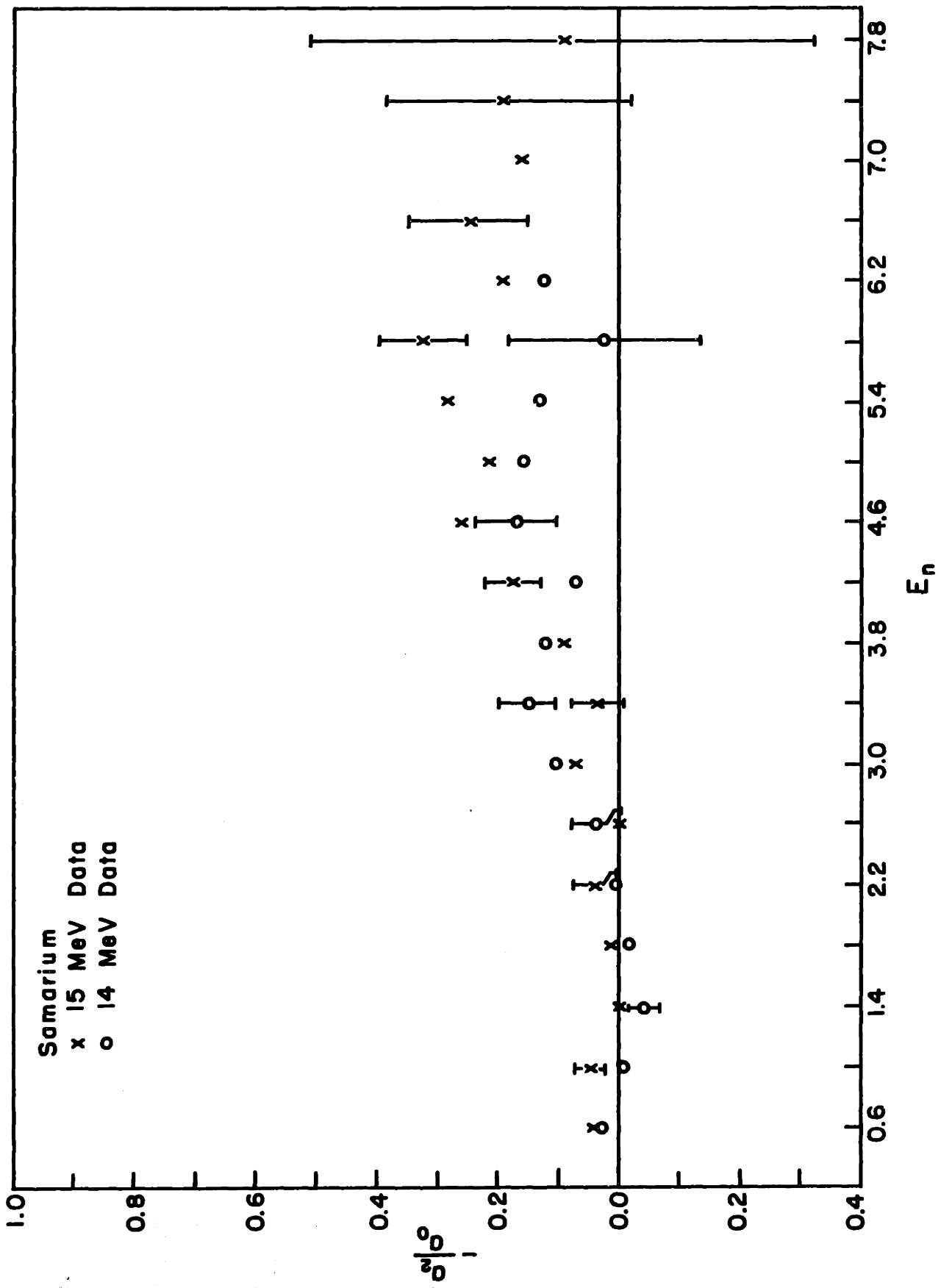
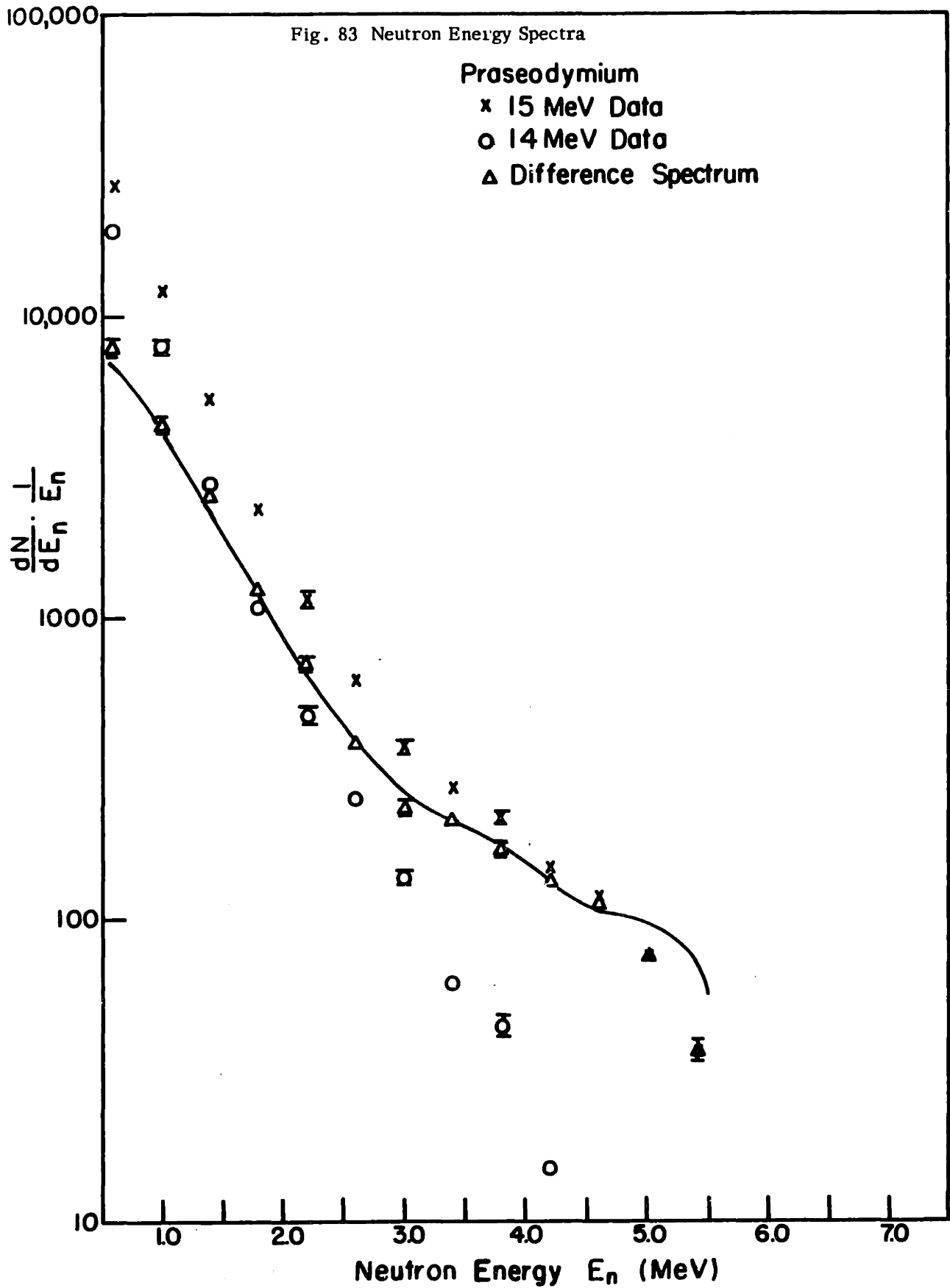


Fig. 81 Photoneutron Angular Distributions

Fig. 82 Photoneutron Angular Distributions





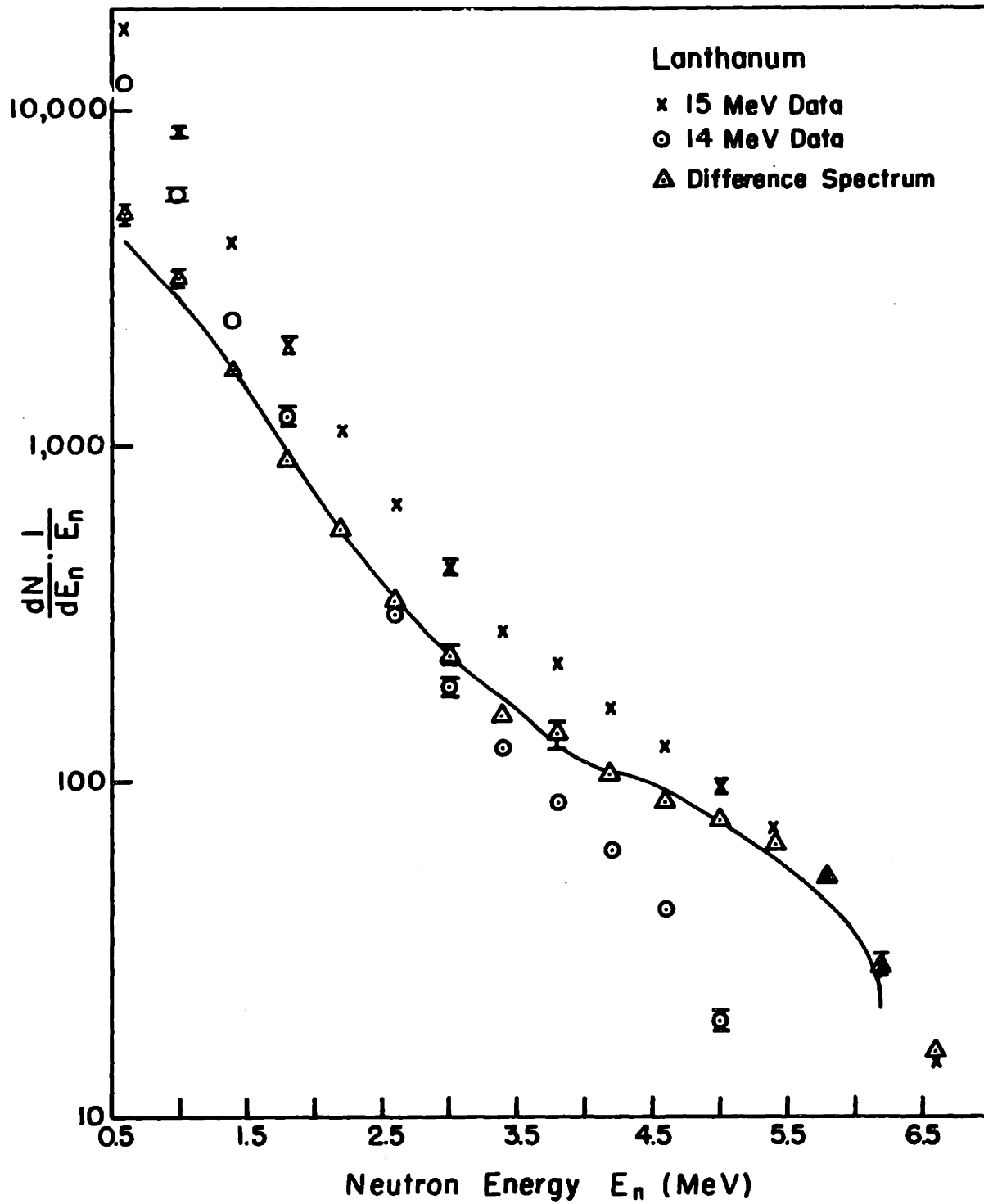


Fig. 84 Neutron Energy Spectra



difference. The two neutron spectra are generated by two bremsstrahlung spectra with endpoints of 15 and 14 MeV. The difference represents the photon-neutron spectrum resulting from a photon difference spectrum peaked at 14.4 MeV with a FWHM of  $1\frac{3}{4}$  MeV.

#### b) Direct Spectrum

Table XXI lists the important single particle dipole transitions for the closed neutron shell at  $N = 82$ . These levels were taken from the stripping data in ref 32. The last column lists the angular distributions of the directly emitted neutrons using equation 11 of Chapter I.

$\text{Pr}^{141}$  and  $\text{La}^{139}$  have closed neutron shells but an odd number of protons. Thus  $\text{Pr}^{140}$  and  $\text{La}^{138}$  are odd-odd nuclei and will have many low lying levels with complicated configurations. As in the case of  $\text{Bi}^{208}$  and  $\text{Pb}^{205}$ , the assumption was made that the single particle neutron hole states will persist despite the configuration mixing caused by the unpaired proton. Therefore the level structure of the residual nuclei were taken from the levels of  $\text{Cs}^{139}$  and  $\text{Ba}^{137}$  found from stripping reactions (32). A composite list of these levels is given in Table XXII. These are the discrete hole states used to calculate  $S(E_n)$  for La and Pr.  $S(E_n)$  was calculated from equation 73 of Chapter IV, using the  $f_l$ 's listed in Table XXI, the  $E_i$ 's listed in Table XXII, the  $(\gamma, n)$  cross section from Rice et al (57), and the  $T_j$ 's from ref 61. The results are shown in Figs. 85 and 86. The calculated curves fit the data well for La. The calculated curve lies higher than the experimental data at the high energy end of the Pr spectrum. There are several possible explanations for this: the low lying states of  $\text{Pr}^{140}$  may not be fed as strongly as the calculation predicts; or the  $(\gamma, n)$  cross section may be lower at 15 MeV than that given by ref 57. The first reason is the more likely because of the configuration mixing of the neutron hole states.

In general the direct component for both La and Pr derived from Method II agrees quite well with that derived from Method I. However the direct spectrum derived from Method II for La, shown in Fig. 86, does seem to indicate more direct neutrons at about  $2\frac{1}{2}$  MeV than the first method does.

Table XXI

Possible Dipole Transitions for a Closed Shell at  $N = 82$ 

Transitions	Strength $f_l^*$	$-a_2/a_0^{**}$
$2d^{3/2} \rightarrow 2f^{5/2}$	0.39	0.40
$\rightarrow 3p^{3/2}$	0.01	0.10
$\rightarrow 3p^{1/2}$	0.06	0.10
$3s^{1/2} \rightarrow 3p^{3/2}$	0.15	0.67
$\rightarrow 3p^{1/2}$	0.07	0.67
$h^{11/2} \rightarrow i^{13/2}$	1.81	0.32
$g^{7/2} \rightarrow h^{9/2}$	1.18	0.33
$\rightarrow 2f^{7/2}$	0.003	0.17
$\rightarrow 2f^{5/2}$	0.07	0.17
$2d^{5/2} \rightarrow 2f^{7/2}$	0.57	0.40
$\rightarrow 2f^{5/2}$	0.02	0.40
$\rightarrow 3p^{3/2}$	0.11	0.10

\*Wilkinson (30)

\*\*Courant (45)

Table XXII

Energy Levels\* for a Nucleus with  $N = 82$ 

Level	Energy (MeV)
$2d^{3/2}$	0.0
$3s^{1/2}$	0.25
$h^{11/2}$	0.75
$g^{7/2}$	1.34
$2d^{5/2}$	1.9

\*Cohen et al (32)

# PRASEODYMIUM - DIRECT SPECTRUM

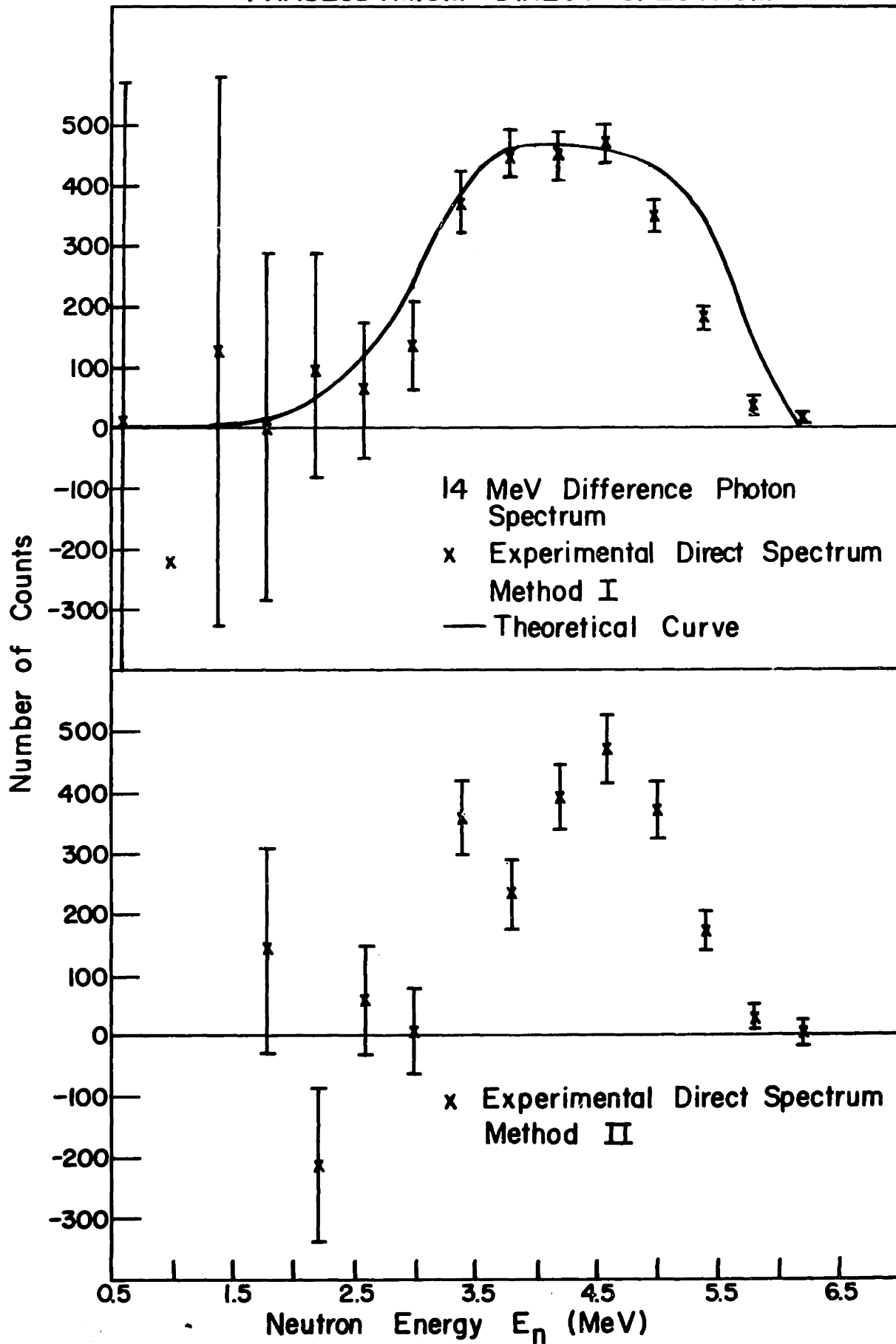


Fig. 85

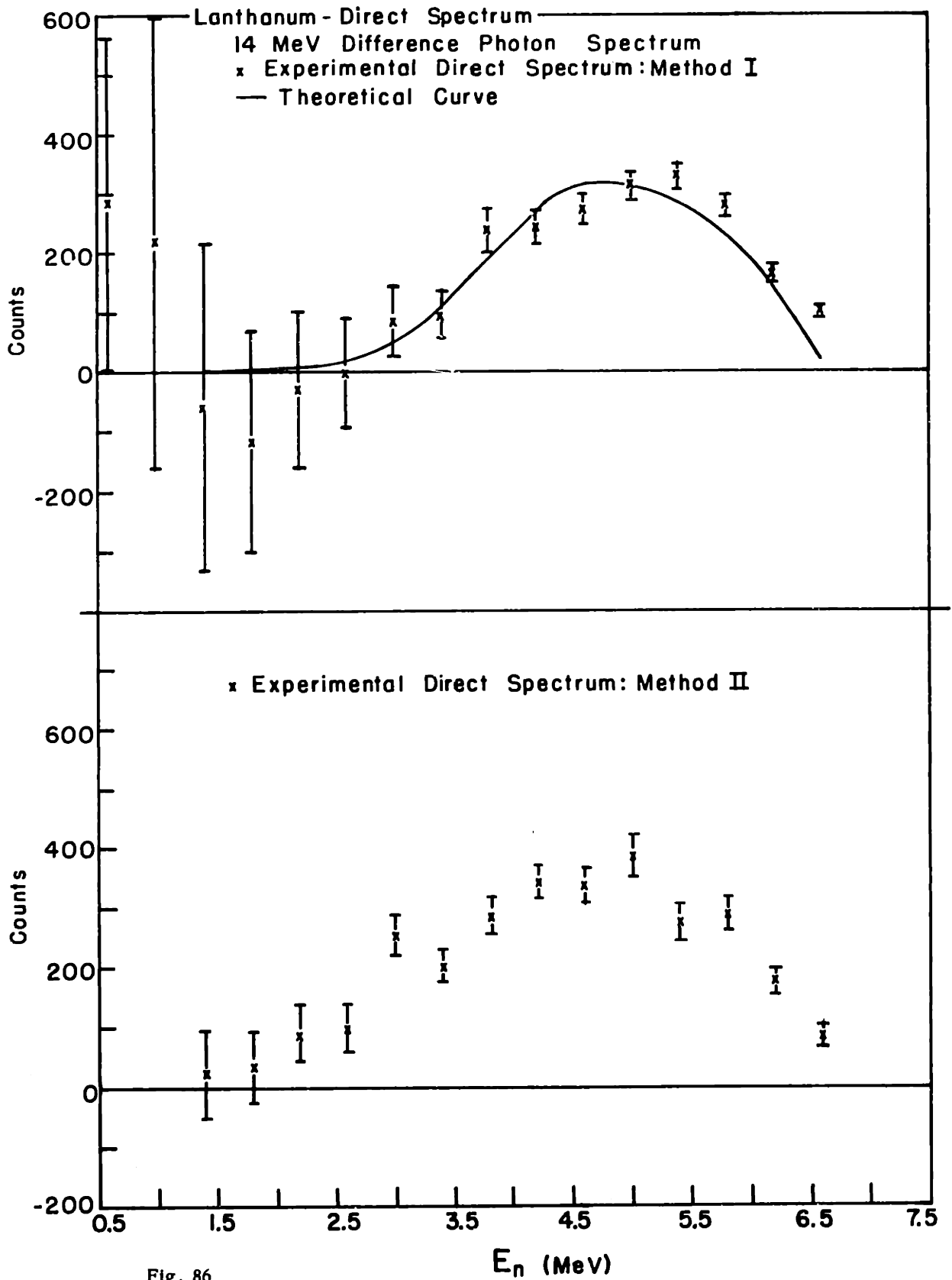


Fig. 86

This is quite possible because of the simplified level structure used.

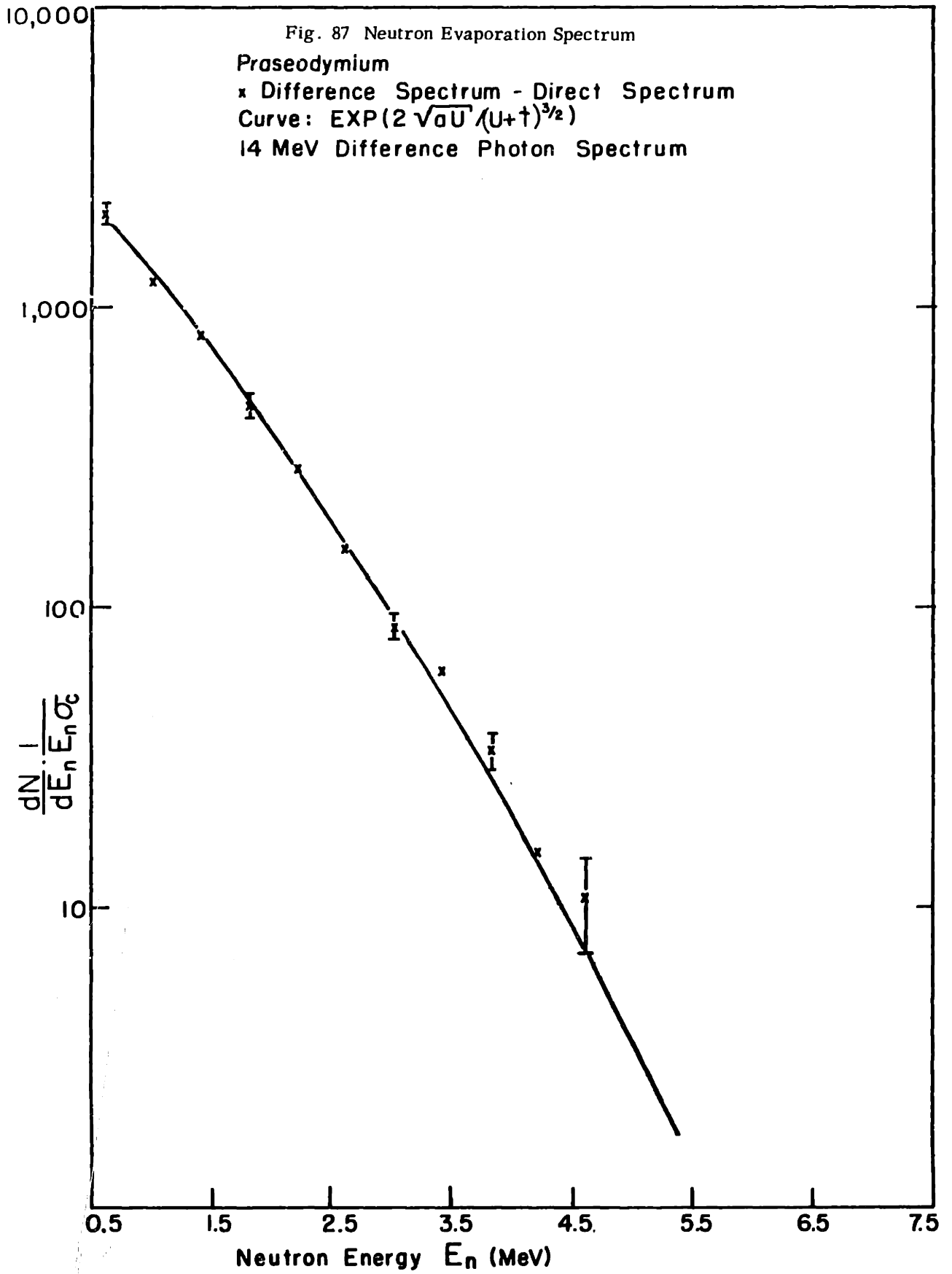
### c) Evaporation Spectrum

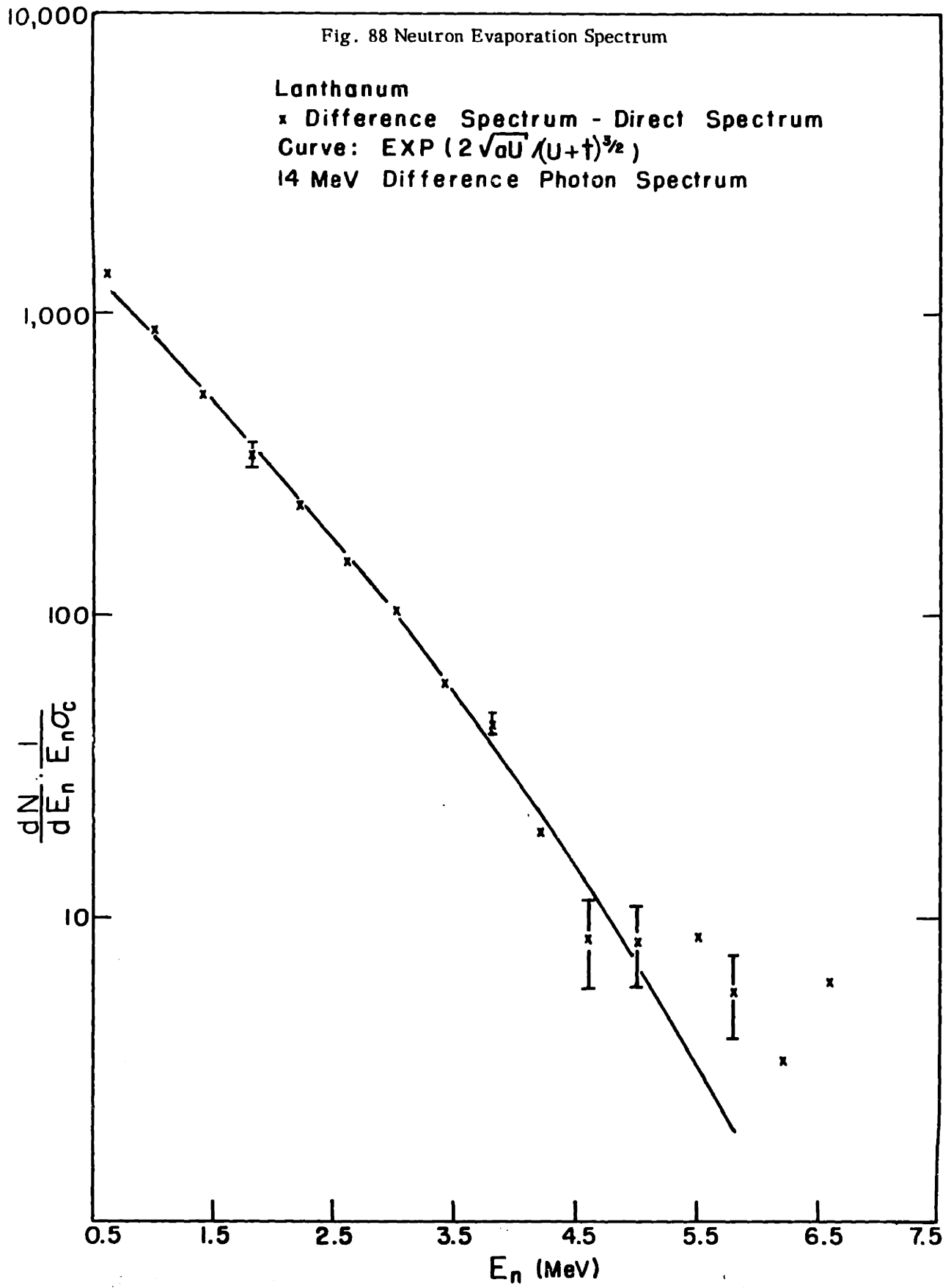
The evaporation energy spectrum and the theoretical curve for Pr and La are shown in Figs. 87 and 88. The data fits the theoretical curve from 0.6 to 4.5 MeV for Pr, and from 1.0 to 4.5 for La. The negative portion of the photon spectrum has a negligible effect because of the high  $(\gamma, n)$  threshold for both elements. Since the  $(\gamma, 2n)$  threshold is 16.25 MeV for Pr and 16.05 MeV for La (70), the  $(\gamma, 2n)$  contamination is zero.

### d) Angular Distributions

The angular distributions of the photoneutrons from Pr and La are shown in Figs. 89 and 90. The low energy data portions of the curves are not quite isotropic, having values of  $-a_2/a_0$  of about  $0.03 \pm 0.03$  for La and  $0.05 \pm 0.03$  for Pr. It is difficult to determine if this is a real effect for the following reason. The Pr and La targets had a coating of plastic about  $\frac{1}{16}$ " thick to prevent their oxidation. This coating attenuates the neutrons and affects the angular distributions. The ratio of the  $156^\circ$  data to the  $76^\circ$  data was increased by about 0.08 to take this scattering into account (see Appendix IV). This scattering correction may have been overestimated. Since the targets were dipped into liquid plastic, the coatings are not uniform, and may be thinner for these two targets than for others used in this experiment. Another possible explanation of the anisotropy is that the low energy portion of the energy spectrum may contain a small admixture of direct neutrons with a strong angular distribution. This was postulated in the case of  $\text{Pb}^{208}$  because neutrons ejected by low energy photons could only make transitions to widely separated, discrete levels, and thus could show a strong angular distribution (see section A). Because of the configuration mixing due to the unpaired protons in Pr and La, this explanation seems less likely for these two elements. The first argument presented above (incorrect scattering correction) seems to be preferable.

The angular distribution of both Pr and La increases with increasing neutron energy, reaching  $-a_2/a_0 \approx 0.65$  at  $E_n \approx 6.0$  MeV. This is a much





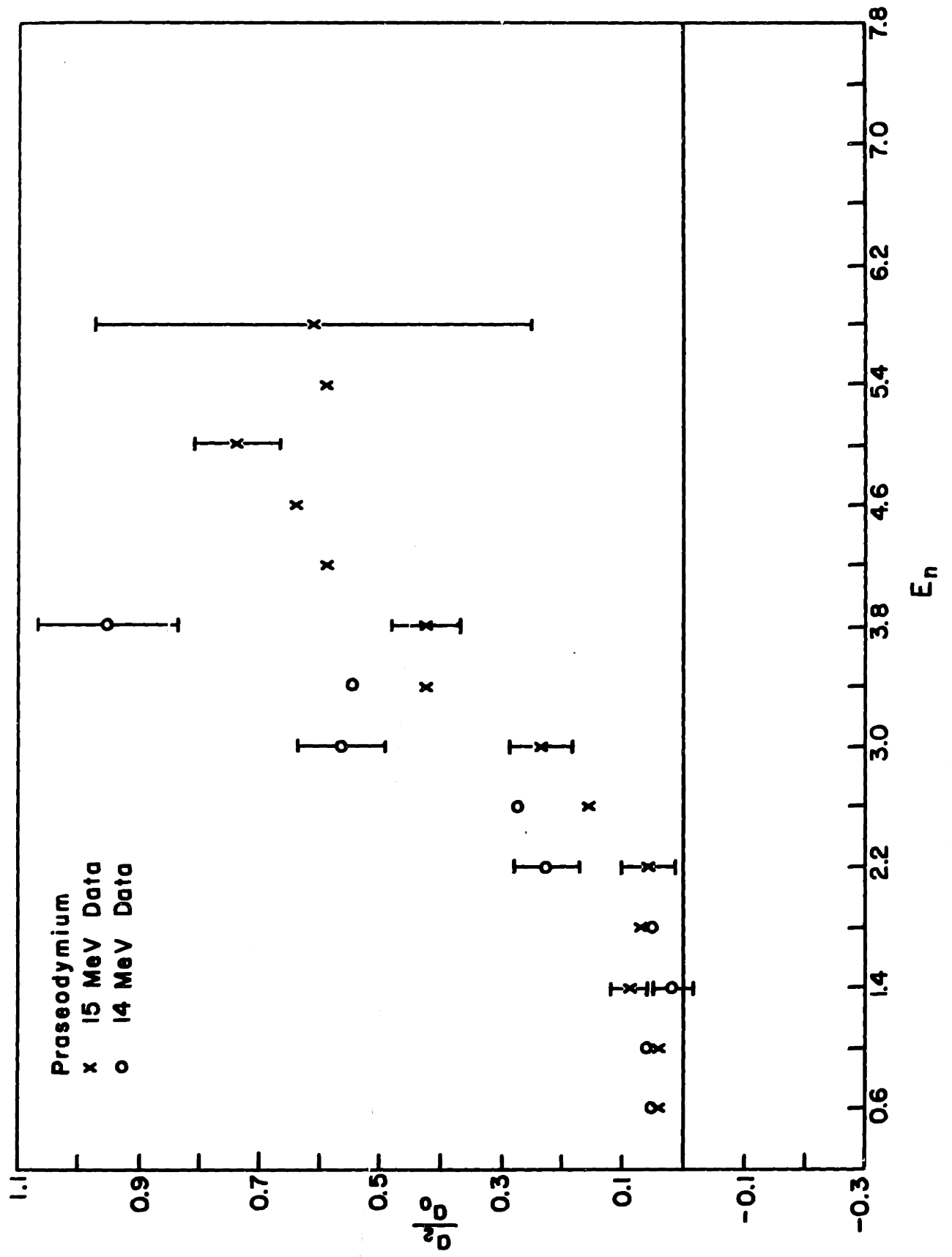


Fig. 89 Photoneutron Angular Distributions



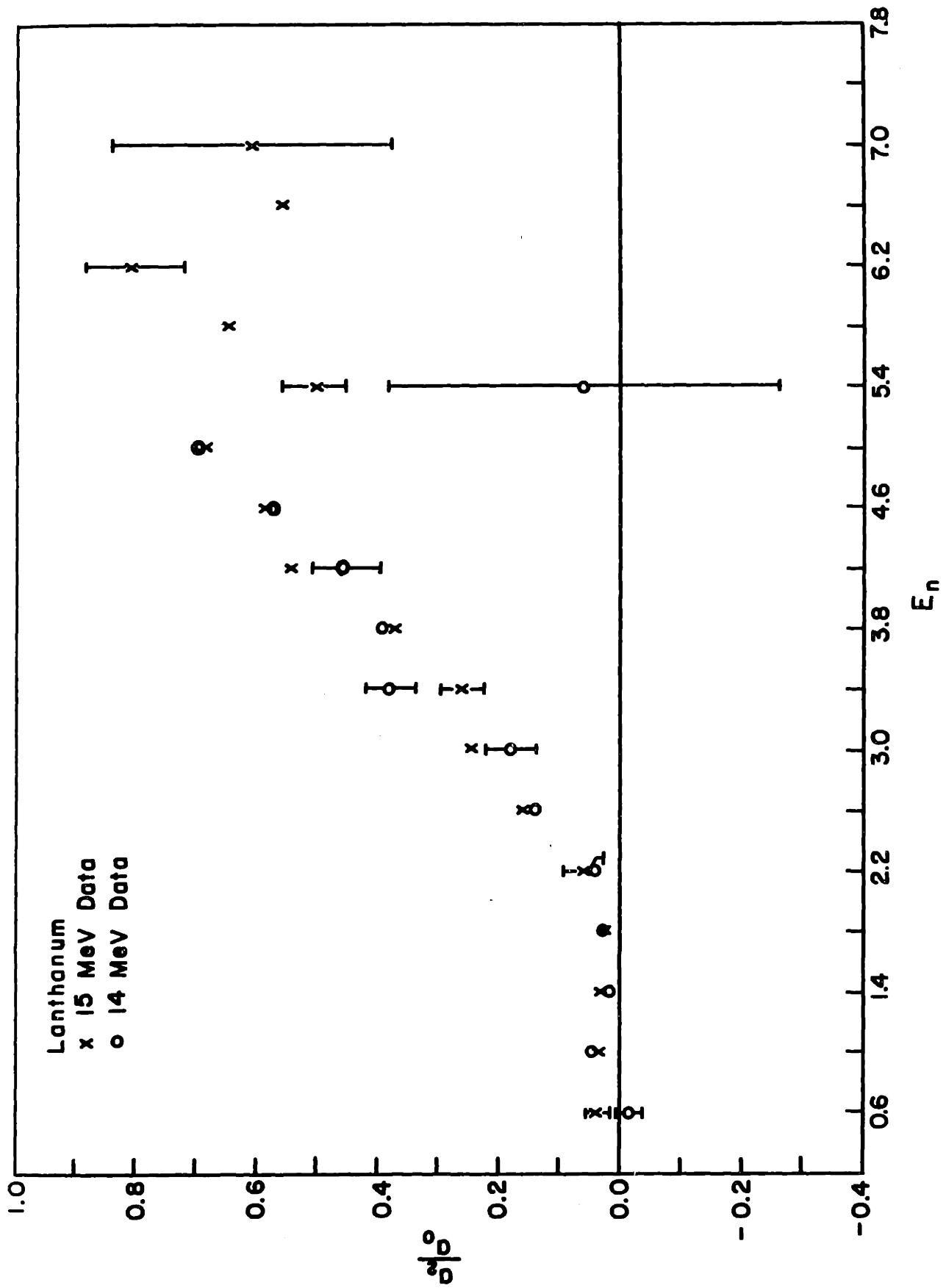


Fig. 90 Photoneutron Angular Distributions

larger value of  $-a_2/a_0$  than was found in the rare earth region, and probably reflects the influence of the highly anisotropic neutrons emitted from the  $2d^{3/2}$  and  $3s^{1/2}$  shells. Heiss (46) has calculated the angular distribution for La for neutrons emitted from the  $2d^{3/2}$  level which dominates the direct region near the neutron endpoint. The results are shown in Table XXIII from 7.0 to 11.0 MeV neutron energy. Although the data presented here does not extend above 7.0 MeV, the agreement at 7.0 MeV is striking.

Table XXIII  
Angular Distribution\* of Photoneutrons from La

$E_n$	B/A	$-a_2/a_0$
7	2.7	0.64
8	3.1	0.675
9	3.5	0.700
10	3.8	0.72
11	3.9	0.725

\*Heiss (46)

## G. Iodine

### a) Experimental Data

The photoneutron energy spectrum  $\frac{dN}{dE_n} \frac{1}{E_n}$  vs  $E_n$  for Iodine is plotted in Fig. 91. The graph contains two neutron spectra and their difference. The two spectra are generated by two bremsstrahlung spectra with endpoints of 15 and 14 MeV. The difference represents the photoneutron spectrum resulting from a photon difference spectrum peaked at 14.4 MeV.

### b) Direct Spectrum

Iodine is eight neutrons away from the closed neutron shell at  $N = 82$ , and three protons away from the closed proton shell at  $Z = 50$ . Furthermore  $I^{126}$  is an odd-odd nucleus. Therefore the assumption was made that the hole states in the residual nucleus are uniformly distributed.

The assumed ground state configuration for  $I^{127}$  is two neutrons in the  $2d^{3/2}$  shell, two neutrons in the  $3s^{1/2}$  shell, six neutrons in the  $h^{11/2}$

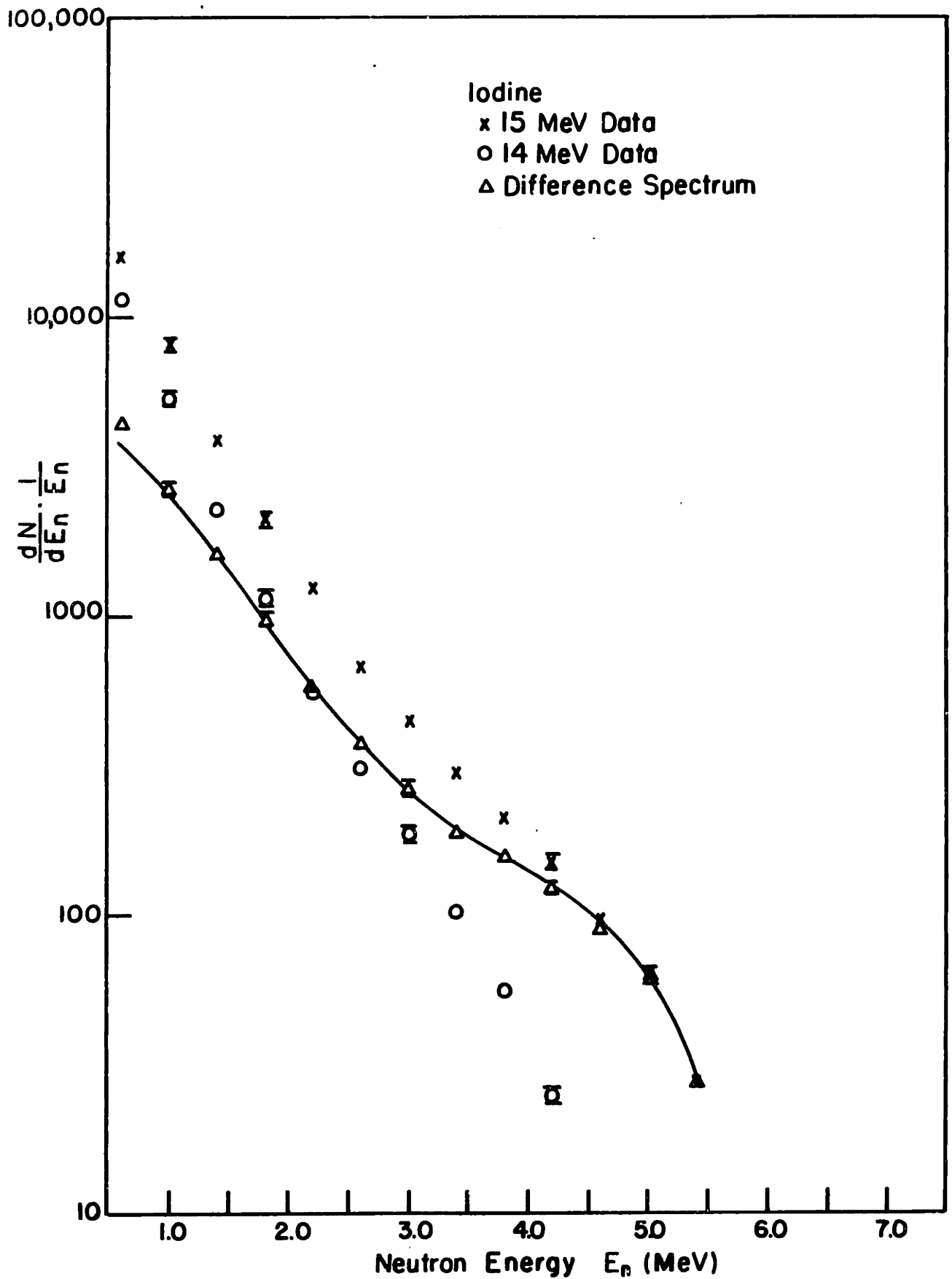


Fig. 91 Neutron Energy Spectra

shell and the remaining shells filled (see Table XXII). The  $3s^{1/2}$  and  $2d^{3/2}$  neutrons were retained because nearby even proton isotopes ( $Xe^{127}$  and  $Te^{125}$ ) have  $\frac{1}{2}+$  and  $\frac{3}{2}+$  low lying states.  $S(E_n)$  is not sensitive to the exact configuration.  $S(E_n)$  was then calculated using equation 74 in Chapter IV, the  $f_\ell$ 's listed in Table XXI reduced in proportion to the number of holes in a given shell, the  $T_j$ 's from ref 61, and the photon cross section taken from Montalbetti et al (79). Transitions from the  $N = 50$  shell to the  $N = 82$  shell were taken into account. The results are shown in Fig. 92. The calculated curve is an excellent fit to the experimental direct spectrum. The direct spectrum derived from Method II agrees with that from Method I within the large errors.

### c) Evaporation Spectrum

The photoneutron evaporation spectrum and the theoretical curve are shown in Fig. 93. The data fits the theoretical prediction from 1.0 to 5.0 MeV. The  $(\gamma, 2n)$  threshold for  $I^{127}$  is given in ref 70 as 16.36 MeV. Therefore the  $(\gamma, 2n)$  contamination is zero. The contribution of the negative portion of the photon spectrum is negligible because of the high  $(\gamma, n)$  threshold for  $I^{127}$ . Despite these facts, the 0.6 MeV data lies about 15 per cent above the theoretical prediction.

### d) Angular Distribution

The angular distribution of the photoneutrons from I are shown in Fig. 94. The maximum value of  $-a_2/a_0$  is about 0.4 and occurs at 4.5 MeV. The spectrum appears to remain flat above this energy, however the errors are such that the exact shape at high energies cannot be determined. This angular distribution is smaller than the 0.68 found for Pr and La. This is probably a reflection of the emptying of the  $2d^{3/2}$  shell. Indeed, the ground state configuration may contain too many  $2d^{3/2}$  and  $3s^{1/2}$  neutrons. If transitions from the  $2d^{3/2}$  and  $3s^{1/2}$  shells were reduced, the  $g^{7/2} \rightarrow h^{9/2}$  transition would dominate the direct spectrum. According to equation 11 of Chapter I, this transition would have an angular distribution of  $-a_2/a_0 = 0.33$ . This averaged with the 0.66 expected from the reduced  $2d^{3/2}$  and  $3s^{1/2}$  subshells, could easily result in the observed maximum value of  $-a_2/a_0$  of 0.4.

# IODINE - DIRECT SPECTRUM

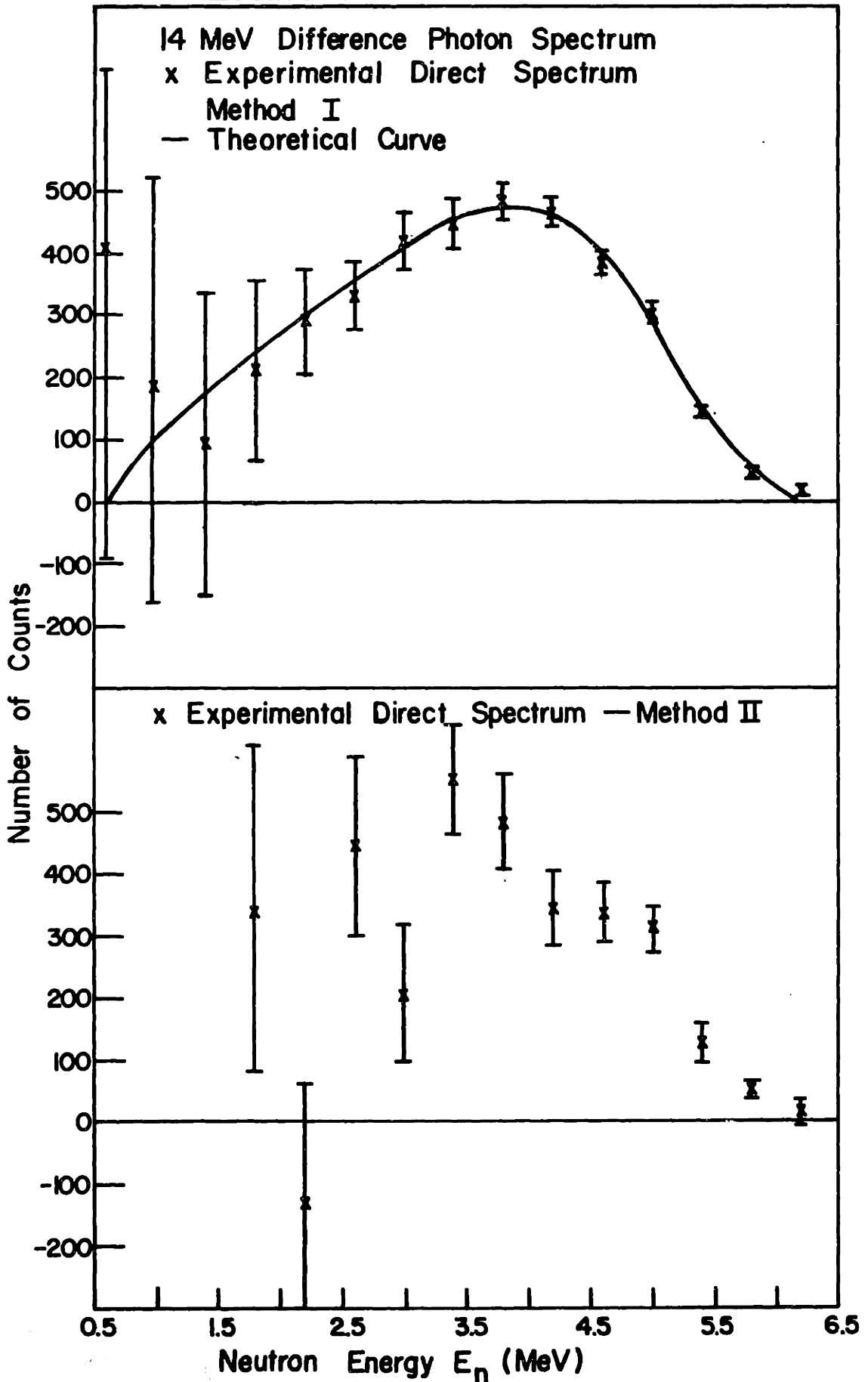


Fig. 92

# IODINE

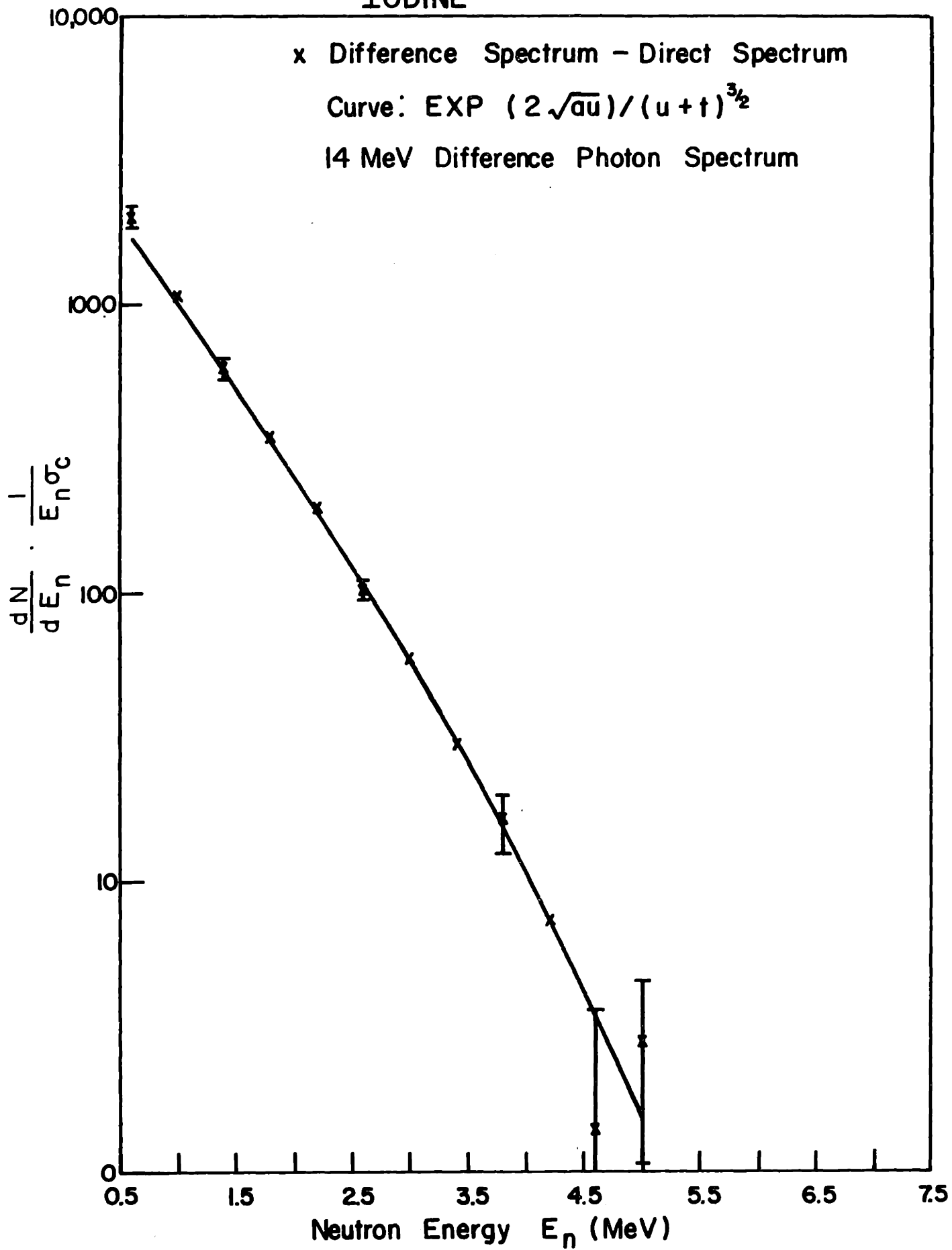


Fig. 93 Neutron Evaporation Spectrum

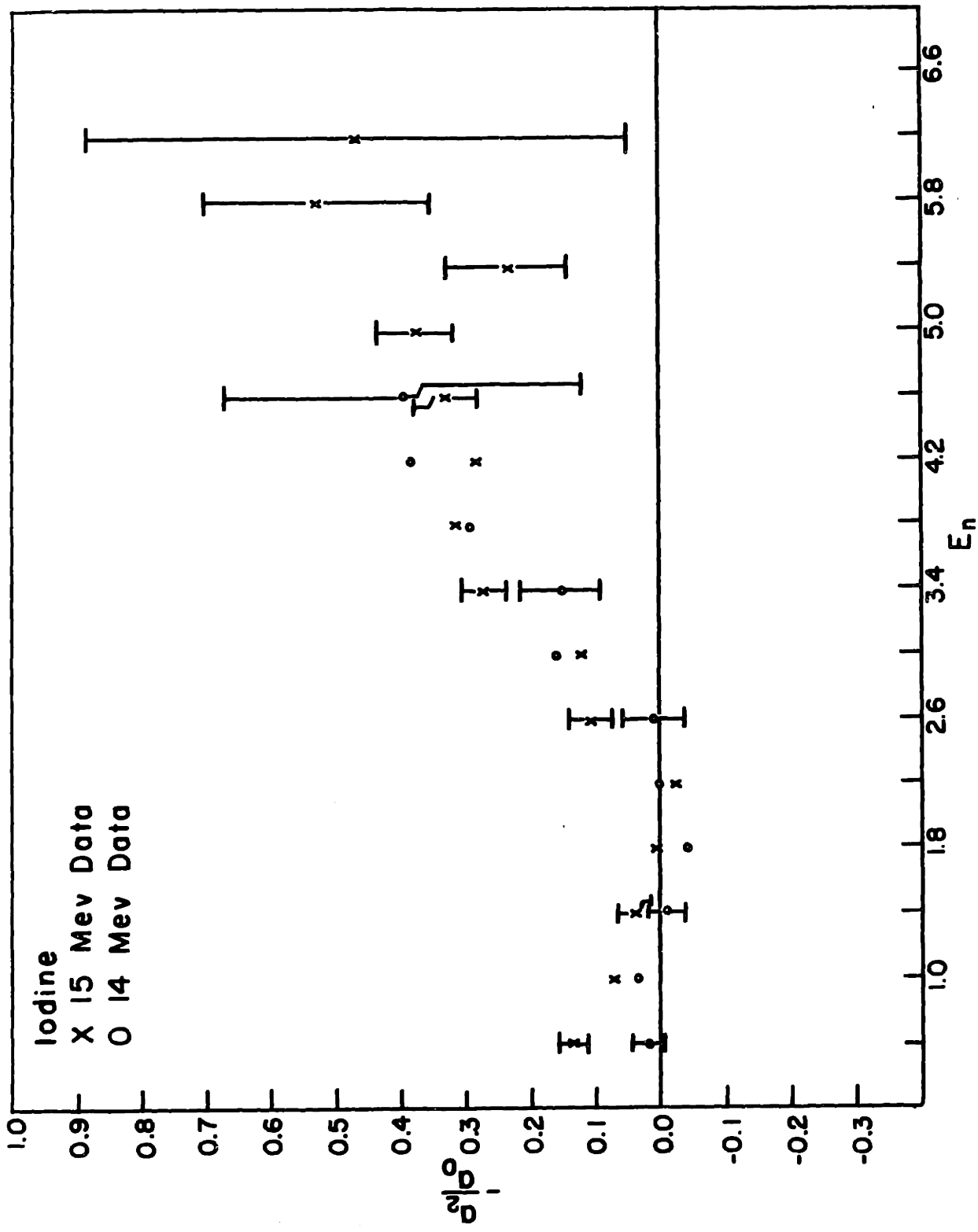


Fig. 94 Photoneutron Angular Distributions

The low energy photoneutrons from the 14 MeV bremsstrahlung spectrum are isotropic. However the 15 MeV bremsstrahlung data is not isotropic at low neutron energies. One possible explanation lies in the difficulties encountered with the electronics during the experiments using the I, Sn, and In targets as discussed in Chapter IV, section B. A faulty coincidence circuit misrouted coincidence pulses. As a result the information required to calculate the coincidence correction was lost, and this correction is undoubtedly inaccurate. This would be a more severe problem in the higher energy run, which of course had a higher counting loss due to coincidences between two counters.

#### H. Tin and Indium

##### a) Experimental Data

The photoneutron energy spectrum  $\frac{dN}{dE_n} \frac{1}{E_n}$  vs  $E_n$  for Sn and In are plotted in Figs. 95 and 99. The two neutron spectra are generated by bremsstrahlung spectra with endpoints of 15 and 14 MeV. Their difference represents the photoneutron spectrum resulting from a photon difference spectrum peaked at 14.4 MeV.

##### b) Direct Spectrum

In Sn the  $N = 50$  proton shell is filled, but the  $N = 82$  neutron shell is not. Since the neutron shell is not magic, the energy levels of tin are mixtures of the single particle neutron states, which makes it difficult to estimate  $S(E_n)$  using discrete hole states in the residual nucleus. On the other hand the closed shell proton core is not easily excited, which weakens the assumption that the hole states are uniformly distributed in the residual nucleus, for the first few MeV of excitation especially in the even-even residual nuclei. Because a shell model calculation by Sanders (80) affords some insight into the structure of the ground state and first few excited states of the Sn isotopes,  $S(E_n)$  was calculated assuming discrete hole states for the residual nucleus.



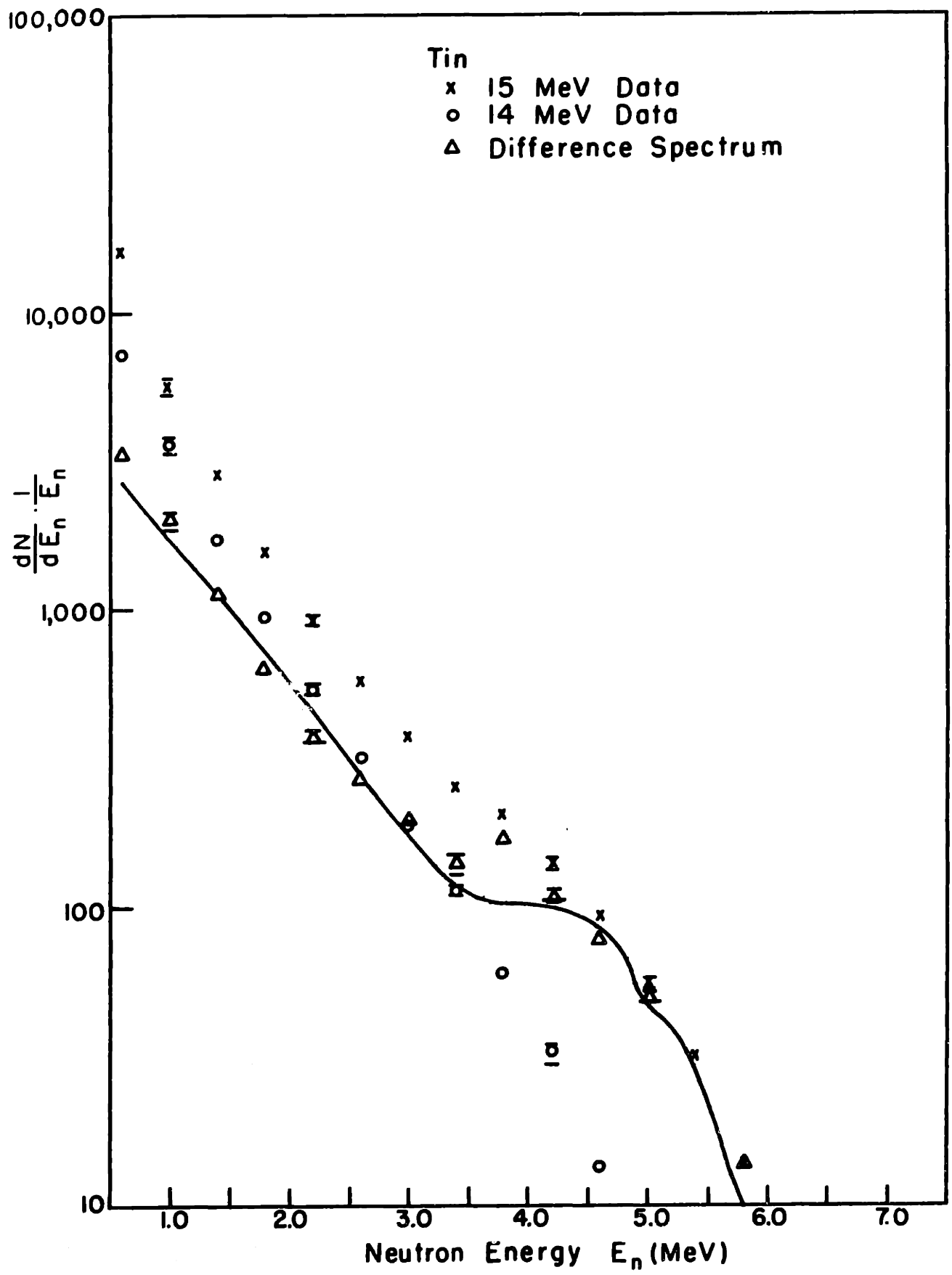


Fig. 95 Neutron Energy Spectra

Since tin has 10 stable isotopes (see Table XXIV) the calculation was first simplified by choosing four representative isotopes. It was assumed that tin consists of 8.9 per cent  $\text{Sn}^{117}$  with a  $(\gamma, n)$  threshold of 7.0 MeV, 39 per cent  $\text{Sn}^{118}$  with a  $(\gamma, n)$  threshold of 9.4 MeV, 8.6 per cent  $\text{Sn}^{119}$  with a  $(\gamma, n)$  threshold of 9.0 MeV. The known levels of isotopes 116, 117, 118, and 119 are listed in Table XXV. The configuration of the first three levels of  $\text{Sn}^{117}$  and  $\text{Sn}^{119}$ , and the ground states of  $\text{Sn}^{116}$ ,  $\text{Sn}^{118}$  and  $\text{Sn}^{120}$ , calculated by Sanders (80) are given in Table XXVI. The single particle levels employed are  $3s^{1/2}$ ,  $2d^{3/2}$  and  $h^{11/2}$ . Standard spectroscopic notation has been used. The remaining single particle states of the major shells,  $g^{7/2}$  and  $2d^{5/2}$ , are assumed to be filled. The percentages listed refer to the percentage of the given configuration in the wave function. As can be seen from Table XXVI, removing one  $s^{1/2}$  neutron from the ground state configuration of  $\text{Sn}^{119}$ , for example, does not result in the exact ground state configuration of  $\text{Sn}^{118}$ . Instead only a small percentage of the resulting configuration overlaps the  $\text{Sn}^{118}$  ground state. That is, if the initial state is given by

$$\psi_i = \sum_n c_{ni} \phi_{ni} \quad (84)$$

and the final state by

$$\psi_f = \sum_{n'} c_{n'f} \phi_{n'f} g_f \quad (85)$$

where  $\phi_n = s^j d^k h^m \dots$  etc, for  $j, k, m, \dots$  etc being the number of neutrons in the  $s$  state,  $d$  state,  $h$  state,  $\dots$  etc.

$g_f$  = wave function of the outgoing neutron

Then the dipole overlap integral is given by

$$D^2 = |\langle \psi_f | 0 | \psi_i \rangle|^2 \quad (86)$$

$$D^2 = \sum_{nn'} \langle (c_{n'f} s^{j'} d^{k'} h^{m'} \dots) g_f | 0 | (c_{ni} s^j d^k h^m \dots) \rangle \quad (87)$$

$$D^2 = f_l \left| \sum_n c_{ni} c_{nf} \delta_{j, j'+1} \right|^2 \quad (88)$$

where  $0$  is the dipole operator,  $f_l$  is the square of the dipole radial overlap integral between the neutron in a given initial single particle state ( $s^{1/2}$  in this example) and the outgoing neutron in the final state, and  $\sum_n c_{ni} c_{nf} \delta_{j, j'+1}$

Table XXIV

## Isotopic Abundance and Neutron Thresholds of Tin\*

Isotope	Abundance Per Cent	$E_{th}$	$E_{2n}$
112	0.96	11.1	?
114	0.66	10.0	18.0
115	0.35	7.5	17.5
116	14.3	9.6	17.1
117	7.6	6.9	16.6
118	24.0	9.3	16.4
119	8.6	6.5	15.8
120	33.9	9.1	15.6
122	4.7	8.8	15.0
124	6.0	8.5	14.4

\*Wapstra et al (70)

Table XXV

Energy Levels\* of  $Sn^{116}$ ,  $Sn^{117}$ ,  $Sn^{118}$ ,  $Sn^{119}$ 

$Sn^{116}$ Spin	Energy (MeV)	$Sn^{117}$ Spin	Energy (MeV)	$Sn^{118}$ Spin	Energy (MeV)	$Sn^{119}$ Spin	Energy (MeV)
0+	0.0	$\frac{1}{2}+$	0.0	0+	0.0	$\frac{1}{2}+$	0.0
2+	1.27	$\frac{3}{2}+$	0.16	2+	1.22	$\frac{3}{2}+$	0.034
2+	2.09	$\frac{11}{2}-$	0.32	(0, 1)+	1.75	$\frac{11}{2}-$	0.089
?	2.20	$\frac{7}{2}+$	0.73	(0, 1)+	2.03	$\frac{7}{2}+$	0.84
?	2.31	$(\frac{1}{2}, \frac{3}{2})+$	0.82	4+	2.25	$\frac{3}{2}+$	0.907
4+	2.35	$(\frac{3}{2}, \frac{5}{2})+$	0.86	(0, 1)+	2.48		
?	2.45	$(\frac{3}{2}, \frac{5}{2})+$	1.03	5+	2.51		
4+	2.49			?	2.55		
4+	2.76						
?	2.85						
4+	3.04						

\*Nuclear Data Sheets (66)

Table XXVI

Configuration of Levels\* of Sn<sup>116</sup>, Sn<sup>117</sup>, Sn<sup>118</sup>, Sn<sup>119</sup>, Sn<sup>120</sup>

Isotope	Spin	Configuration**
Sn <sup>116</sup>	0+	s <sup>2</sup> (28) d <sup>2</sup> (7) h <sup>2</sup> (65)
Sn <sup>117</sup>	$\frac{1}{2}+$	sd <sup>2</sup> (40) sh <sup>2</sup> (60)
	$\frac{3}{2}+$	s <sup>2</sup> d (90) h <sup>2</sup> d (7) d <sup>3</sup> (3)
	$\frac{11}{2}-$	s <sup>2</sup> h (20) d <sup>2</sup> h (7) h <sup>3</sup> (73)
Sn <sup>118</sup>	0+	s <sup>2</sup> d <sup>2</sup> (22) s <sup>2</sup> h <sup>2</sup> (4) d <sup>4</sup> (2) d <sup>2</sup> h <sup>2</sup> (12) h <sup>4</sup> (60)
Sn <sup>119</sup>	$\frac{1}{2}+$	d <sup>4</sup> s (20) d <sup>2</sup> h <sup>2</sup> s (73) h <sup>4</sup> s (7)
	$\frac{3}{2}+$	s <sup>2</sup> d <sup>3</sup> (35) h <sup>2</sup> d <sup>3</sup> (1) s <sup>2</sup> h <sup>2</sup> d (22) h <sup>4</sup> d (43)
	$\frac{11}{2}-$	s <sup>2</sup> d <sup>2</sup> h (15) s <sup>2</sup> h <sup>3</sup> (2) d <sup>4</sup> h (5) d <sup>2</sup> h <sup>3</sup> (72) h <sup>5</sup> (6)
Sn <sup>120</sup>	0+	s <sup>2</sup> d <sup>4</sup> (5) s <sup>2</sup> d <sup>2</sup> h <sup>2</sup> (5) s <sup>2</sup> h <sup>4</sup> (1) d <sup>2</sup> h <sup>4</sup> (33) h <sup>6</sup> (56)

\*Sanders (80)

\*\*Figures in parentheses are percentages.

is the parentage coefficients between the initial and final states. As usual  $f_{\ell}$  was estimated using the square well calculations of Wilkinson (30). The parentage coefficients for the Sn<sup>119</sup>→Sn<sup>118</sup> ground state transition is about 0.01 (see Table XXVII).

The parentage coefficients for transitions between the ground states of Sn<sup>120</sup> and Sn<sup>118</sup> and the first three levels of Sn<sup>119</sup> and Sn<sup>117</sup> are calculated as outlined above for the s<sup>1/2</sup> neutrons emitted from the ground state of Sn<sup>119</sup>. The configurations of the remaining levels of Sn<sup>119</sup> and Sn<sup>117</sup> were not calculated in ref (80). Therefore each of the remaining levels of Sn<sup>119</sup> or Sn<sup>117</sup> was assumed to be the ground state configuration of Sn<sup>120</sup> or Sn<sup>118</sup> with one neutron removed from the single particle state indicated by the spin of the level in question. The resulting parentage coefficients are listed in Table XXVII. In Sn<sup>117</sup> the levels at 0.82 and 0.86 MeV have been grouped

Table XXVII  
 Parentage Coefficients\* for Sn<sup>116</sup>, Sn<sup>117</sup>, Sn<sup>118</sup>, and Sn<sup>119</sup>

Isotope	Spin	Energy	Hole State	Parentage Coefficient
Sn <sup>116</sup>	0+	0.0	s <sup>1/2</sup>	0.33
	2+	1.27	d <sup>3/2</sup>	0.08
	"	"	d <sup>5/2</sup>	0.5
	2+	2.09	d <sup>3/2</sup>	0.08
	"	"	d <sup>5/2</sup>	0.5
	4+	2.50	g <sup>7/2</sup>	1.0
		3.0 ?	h <sup>11/2</sup>	0.06
Sn <sup>117</sup>	$\frac{1}{2}+$	0.0	s <sup>1/2</sup>	0.02
	$\frac{3}{2}+$	0.16	d <sup>3/2</sup>	0.04
	$\frac{11}{2}-$	0.32	h <sup>11/2</sup>	0.09
	$\frac{7}{2}+$	0.73	g <sup>7/2</sup>	1.0
	$\frac{3}{2}+$ *	0.82	d <sup>3/2</sup>	0.03
	$\frac{5}{2}+$	1.03	d <sup>5/2</sup>	1.0
Sn <sup>118</sup>	0+	0.0	s <sup>1/2</sup>	0.01
	2+	1.22	d <sup>5/2</sup>	1.0
	(0, 1) +	1.9	s <sup>1/2</sup>	0.12
	4+	2.25	d <sup>3/2</sup>	0.12
	"	"	g <sup>7/2</sup>	1.0
	(0, 1) +	2.5	s <sup>1/2</sup>	0.12
	"	"	d <sup>3/2</sup>	0.12
		3.0 ?	h <sup>11/2</sup>	0.06
Sn <sup>119</sup>	$\frac{1}{2}+$	0.0	s <sup>1/2</sup>	0.002
	$\frac{3}{2}+$	0.03	d <sup>3/2</sup>	0.03
	$\frac{11}{2}-$	0.089	h <sup>11/2</sup>	0.04
	$\frac{7}{2}+$	0.84	g <sup>7/2</sup>	1.0
	$\frac{3}{2}+$	0.907	d <sup>3/2</sup>	0.11
	$\frac{5}{2}+$ *	~1.0	d <sup>5/2</sup>	1.0

\*See text.

into a  $\frac{3}{2}^+$  level at 0.84 MeV in analogy with the  $\frac{3}{2}^+$  level at 0.91 MeV of  $\text{Sn}^{119}$ . Also a  $\frac{5}{2}^+$  level at 1.0 MeV has been added to  $\text{Sn}^{119}$  in analogy to the  $\frac{5}{2}^+$  level at 1.03 MeV in  $\text{Sn}^{117}$ . In this manner at least one level of each spin was used for both isotopes. In the case of the  $\text{Sn}^{119}(\frac{1}{2}^+) \rightarrow \text{Sn}^{118}(0^+, 2^+, \text{etc})$  and  $\text{Sn}^{117}(\frac{1}{2}^+) \rightarrow \text{Sn}^{116}(0^+, 2^+, \text{etc})$  transitions, the spin of the levels in the residual nucleus do not uniquely define the single particle state from which the neutron was emitted. Instead two single particle states are possible. Therefore each excited state of  $\text{Sn}^{118}$  and  $\text{Sn}^{116}$  were assumed to be composed of equal amounts of two configurations. The first is the ground state configuration of  $\text{Sn}^{119}$  with one neutron removed from the single particle state indicated by the spin of the level plus one half, the other is the ground state configuration of  $\text{Sn}^{119}$  with one neutron removed from the single particle state indicated by the spin of the level minus one half. Having made these assumptions about the excited states of  $\text{Sn}^{117}$  and  $\text{Sn}^{118}$ , the parentage coefficients for this transition were calculated as outlined above and these coefficients are listed in Table XXVII.

Transitions from lower shells into the unfilled  $N = 82$  neutron shell were included in all four isotopes. These states have very high excitation energies (5.0 to 8.0 MeV), and therefore they do not contribute appreciably to the direct spectrum,  $S(E_n)$ .

$S(E_n)$  was calculated using equation 73 of Chapter IV, the transition strengths,  $f_{\rho}$ , from ref 30, Table XXI, for the discrete levels listed in Table XXVII, multiplied by the parentage coefficients listed in the table. The  $T_j$ 's were taken from ref 61 and the  $(\gamma, n)$  cross section from ref 115. The calculation was performed for  $\text{Sn}^{117}$  and  $\text{Sn}^{118}$ ,  $\text{Sn}^{119}$  and  $\text{Sn}^{120}$ , and weighted by the assumed isotopic abundance. The results are shown in Fig. 96. The calculated curve fits the experimental data above 4.5 MeV; below this, it is much lower than the experimental points. This poor fit is a direct consequence of not using any levels above 1.0 MeV in  $\text{Sn}^{117}$  and  $\text{Sn}^{119}$ . Specifically only a small fraction of the available  $s^{1/2}$  strength has been exhausted and the  $g^{7/2}_+$  and  $d^{5/2}$  strengths are undoubtedly spread out over more than the

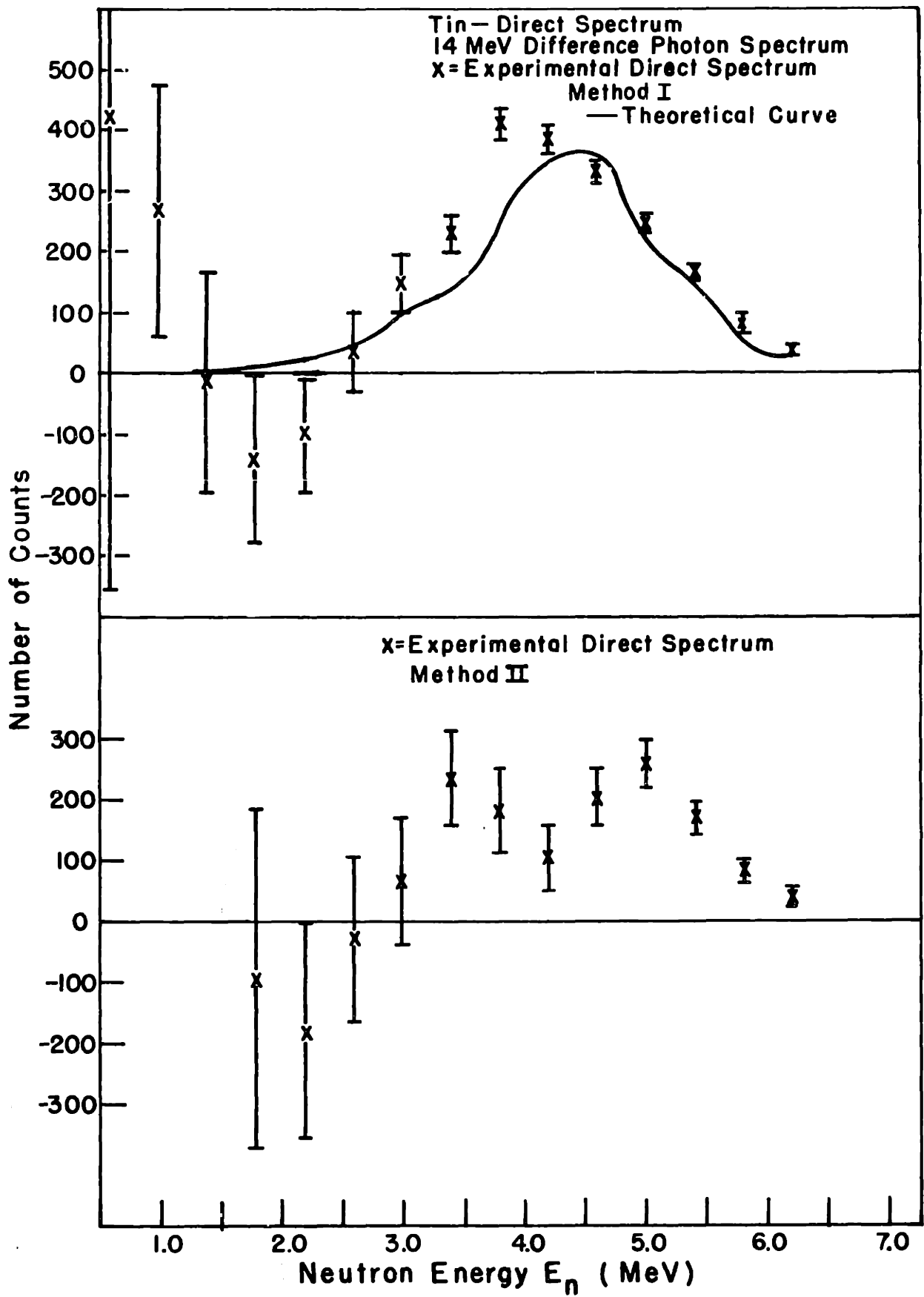


Fig. 96

two levels listed.  $\text{Sn}^{117}$ ,  $\text{Sn}^{118}$ ,  $\text{Sn}^{119}$ , and  $\text{Sn}^{120}$  would yield neutron endpoints of 8.4, 6.0, 8.9, and 6.4 MeV respectively if the ground states were strongly fed. Instead the 1.27 MeV excited state of  $\text{Sn}^{116}$ , the 0.73 MeV excited state of  $\text{Sn}^{117}$ , the 1.22 MeV excited state of  $\text{Sn}^{118}$  and the 0.84 MeV excited state of  $\text{Sn}^{119}$  are the lowest states to have any appreciable strength (under the assumptions used) and the neutron endpoints are reduced to 7.3, 5.3, 7.7 and 5.6 MeV respectively. The observed endpoint is even lower (about 6.0 MeV), however since  $\text{Sn}^{119}$  and  $\text{Sn}^{117}$  have only a total abundance of 16 per cent, the actual endpoint is difficult to separate from the background.

The direct spectrum derived from Method II has a different shape than that found from the first method. The angular distributions shown in Fig. 97 tend to explain this. The 14 MeV bremsstrahlung run has a much higher anisotropy near the neutron endpoint than the 15 MeV run. As a result the angular distribution of the difference spectrum has a dip at about 4.0 MeV, resulting in the dip in the direct spectrum seen in Fig. 97. This difference in angular distributions between the two runs is probably due to the fact that the background level is difficult to determine. Since the isotopes with low thresholds ( $\text{Sn}^{119}$ ,  $\text{Sn}^{117}$ , etc) also have low isotopic abundances, it is therefore difficult to determine where the neutron spectrum endpoint is.

When  $S(E_n)$  for In was calculated, problems similar to those found in the case of Sn were encountered. Indium has one proton less than a closed shell, but this does not justify the assumption of a uniform distribution of hole states in the residual nucleus. On the other hand, knowledge of the structure and position of the actual levels is meagre. A calculation was made assuming a uniform distribution of hole states, but the results fit the data badly. Instead the  $S(E_n)$  shown in Fig. 100 was calculated with the same levels, parentage coefficients, and hole states used to calculate  $S(E_n)$  for  $\text{Sn}^{118}$ , as a rough approximation. The resulting  $S(E_n)$  is larger than the experimental data above 4.0 MeV, and smaller than this data below 4.0 MeV. The direct spectrum derived from Method II agrees with that found by the first method.



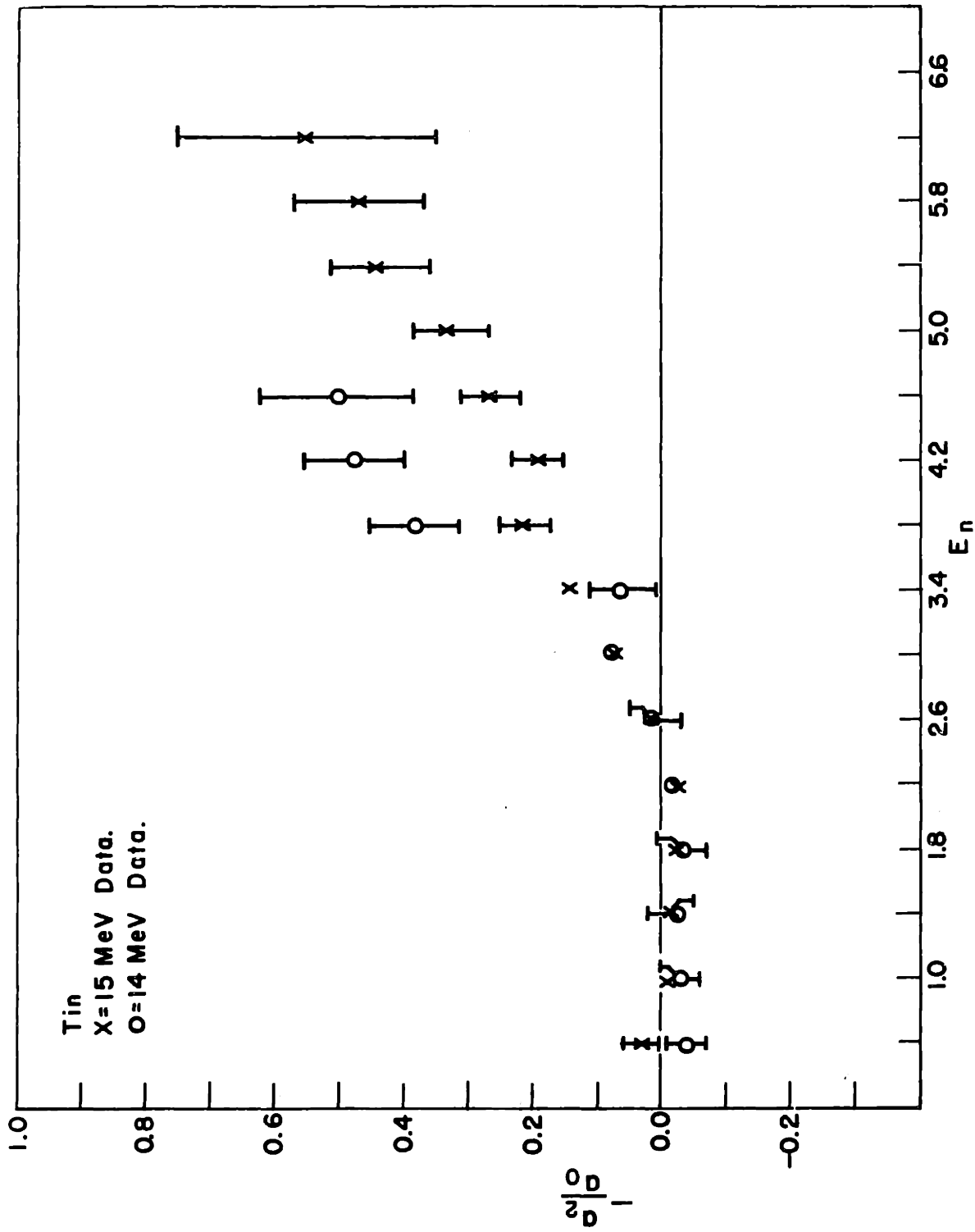
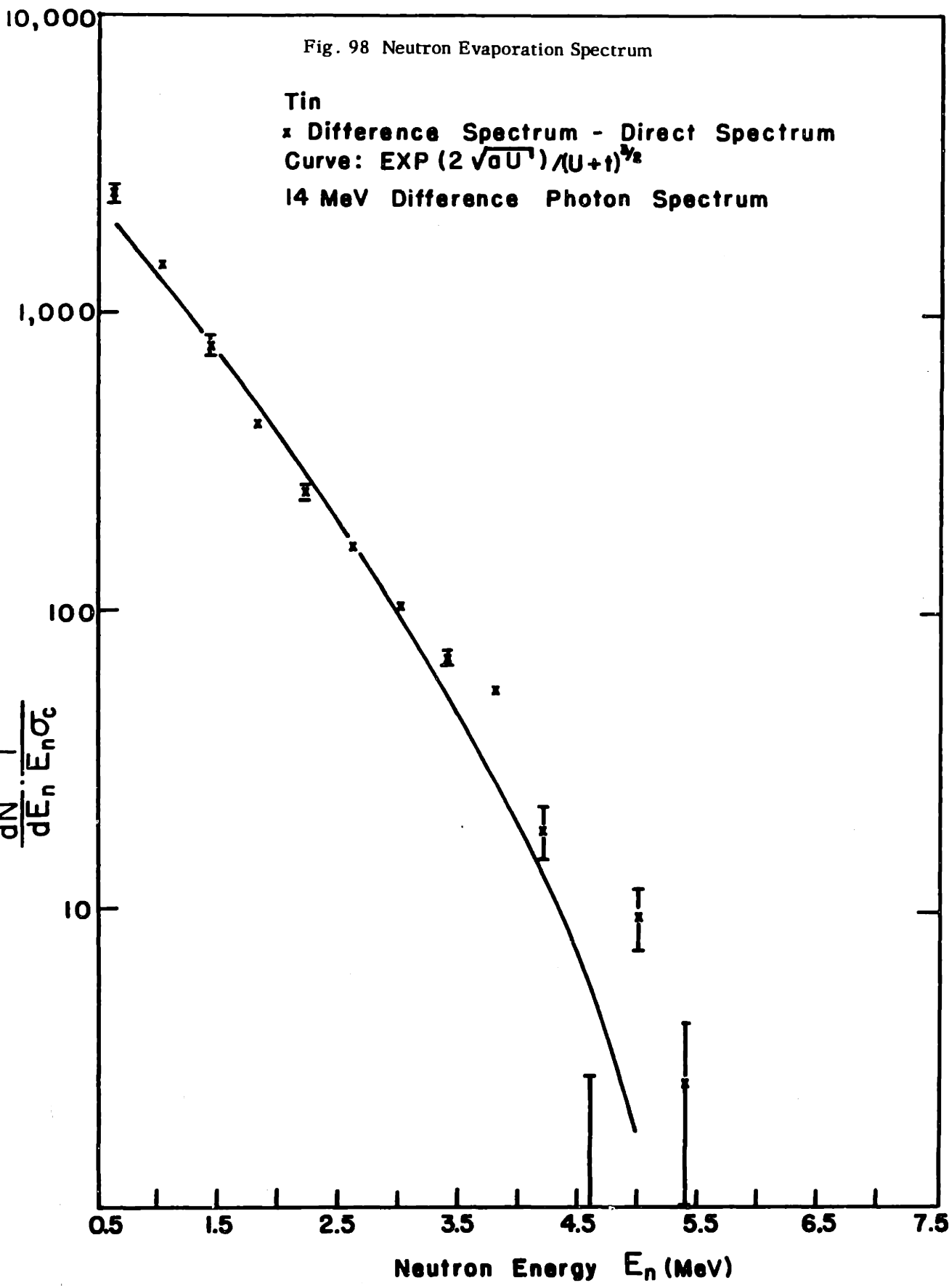


Fig. 97 Photoneutron Angular Distributions



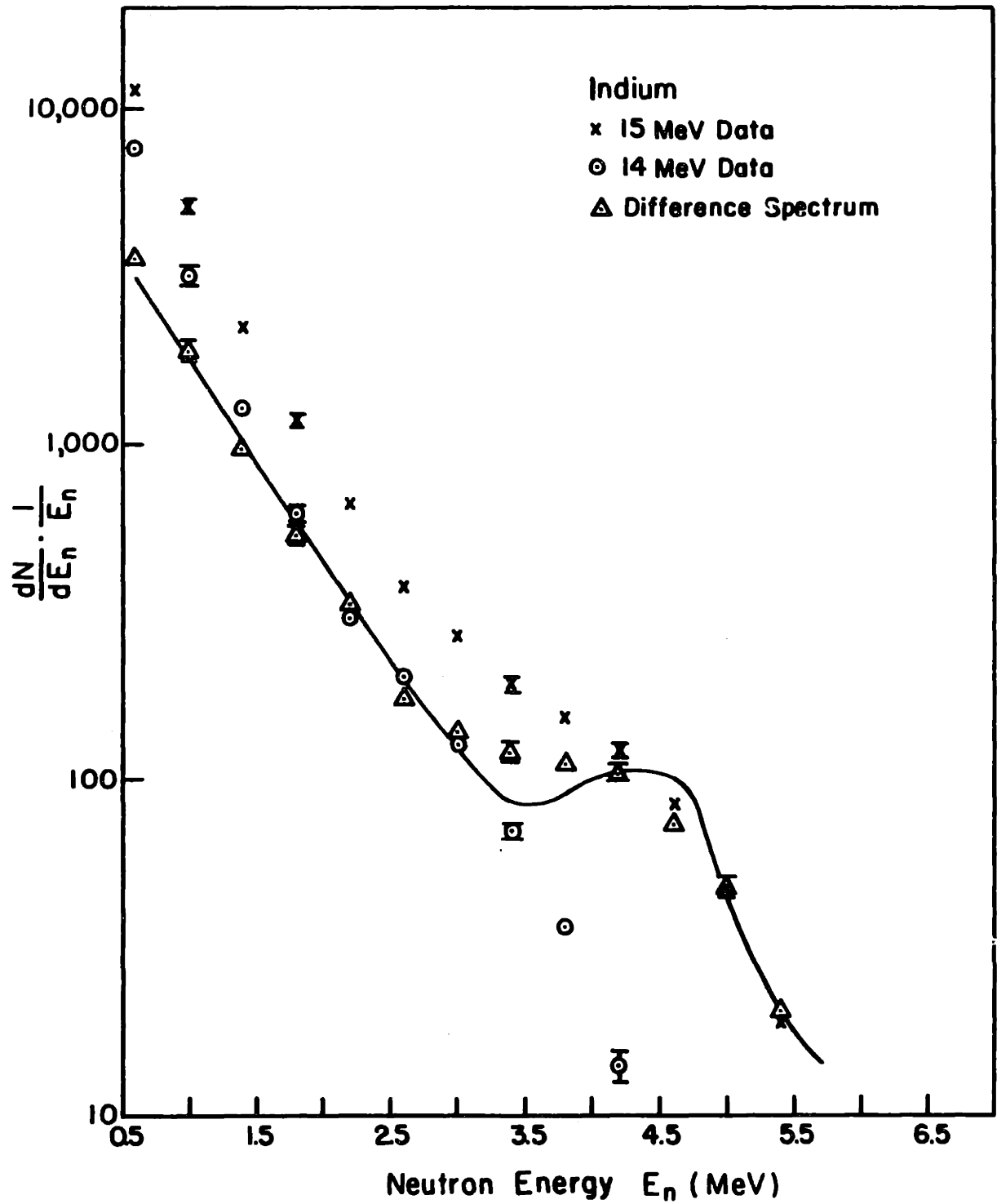


Fig. 99 Neutron Energy Spectra

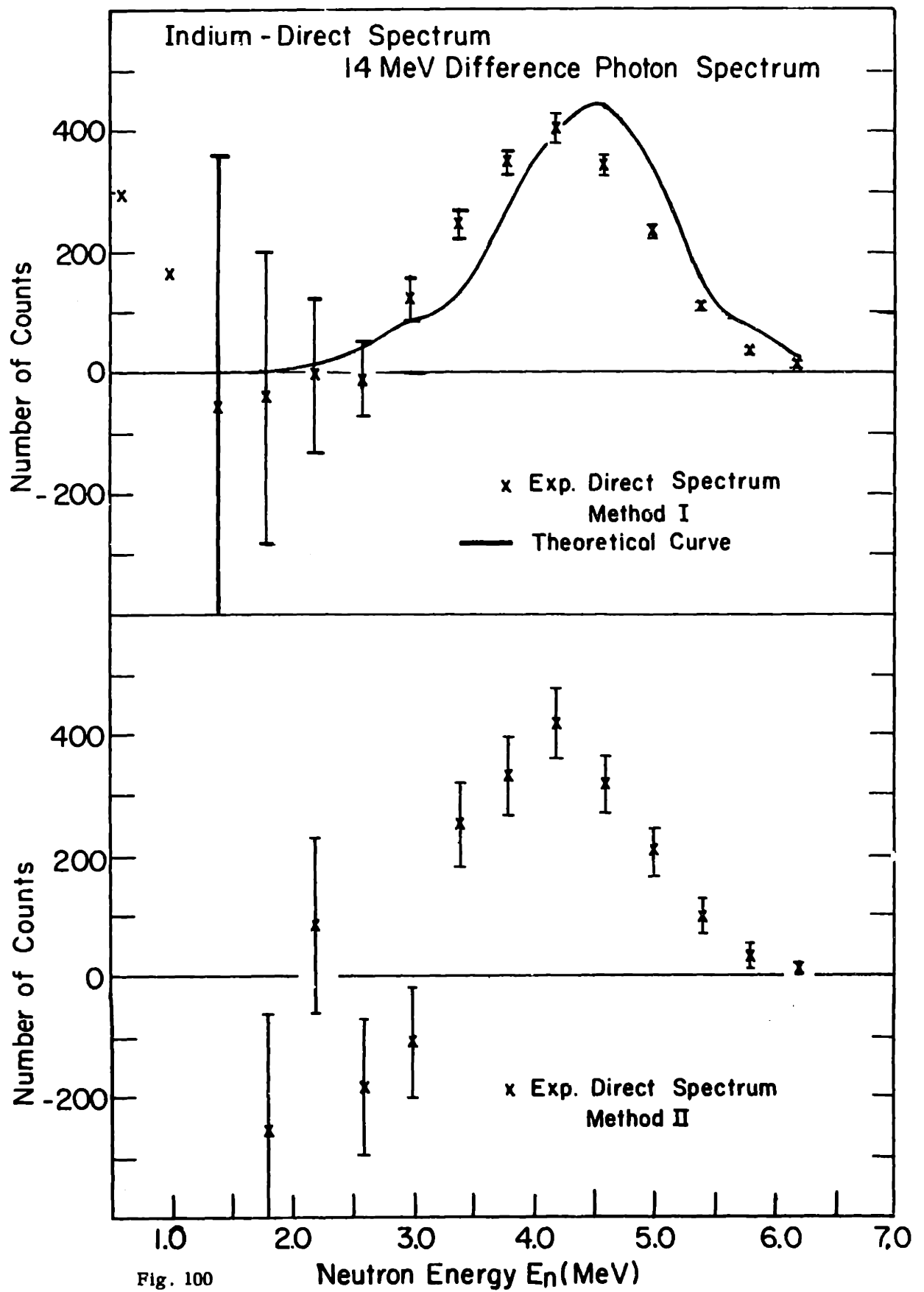


Fig. 100

### c) Evaporation Spectrum

The experimental evaporation spectrum and theoretical curve are shown in Figs. 98 and 101. The  $(\gamma, 2n)$  contamination is expected to be zero as the  $(\gamma, 2n)$  thresholds for  $\text{In}^{115}$  and the Sn isotopes are greater than 15 MeV. The theoretical curve fits the data for In from 0.6 to 3.0 MeV. However in the case of Sn the fit is not as good. If the region over which the fit is performed (1.0 to 3.0 MeV) is reduced (to 1.0 to 2.2 MeV) the fit is improved. The same effect could be achieved by increasing  $S(E_n)$  in the region around 3.0 MeV. As was noted in the last section, the direct spectrum has probably been underestimated in this region. Therefore it is felt that if a better calculation of  $S(E_n)$  were available, the experimental evaporation spectrum and theoretical curve for Sn would be in much better agreement than obtained here.

### d) Angular Distributions

The angular distribution of the photoneutrons from Sn and In are shown in Figs. 97 and 102. The two elements are isotropic at low neutron energies. The anisotropy of tin increases with increasing neutron energy to about  $-a_2/a_0 = 0.5$ . In the case of In,  $-a_2/a_0$  seems to reach a maximum value of 0.35, and then decreases with increasing neutron energies. The low lying levels in the residual nuclei of the tin isotopes are primarily  $d^{3/2}$  and  $h^{11/2}$  states. These could explain an anisotropy of about 0.4. On the other hand, the low lying levels of  $\text{In}^{115}$  should be primarily  $h^{11/2}$  and  $g^{7/2}$  states. These transitions would produce angular distributions of about 0.33 (equation 11). At higher energies of excitation, the  $d^{5/2}$  states may become dominant, which could explain the increase in  $-a_2/a_0$ . These statements cannot be confirmed without a better knowledge of the structure of the levels of  $\text{In}^{114}$  and the tin isotopes.

The angular distribution of the photoneutrons from the 14 MeV bremsstrahlung spectrum differ from those from the 15 MeV spectrum for tin, as was explained in the last section above. It could be explained by the fact that the electronics were faulty during this run (see section B of Chapter IV), which

# INDIUM

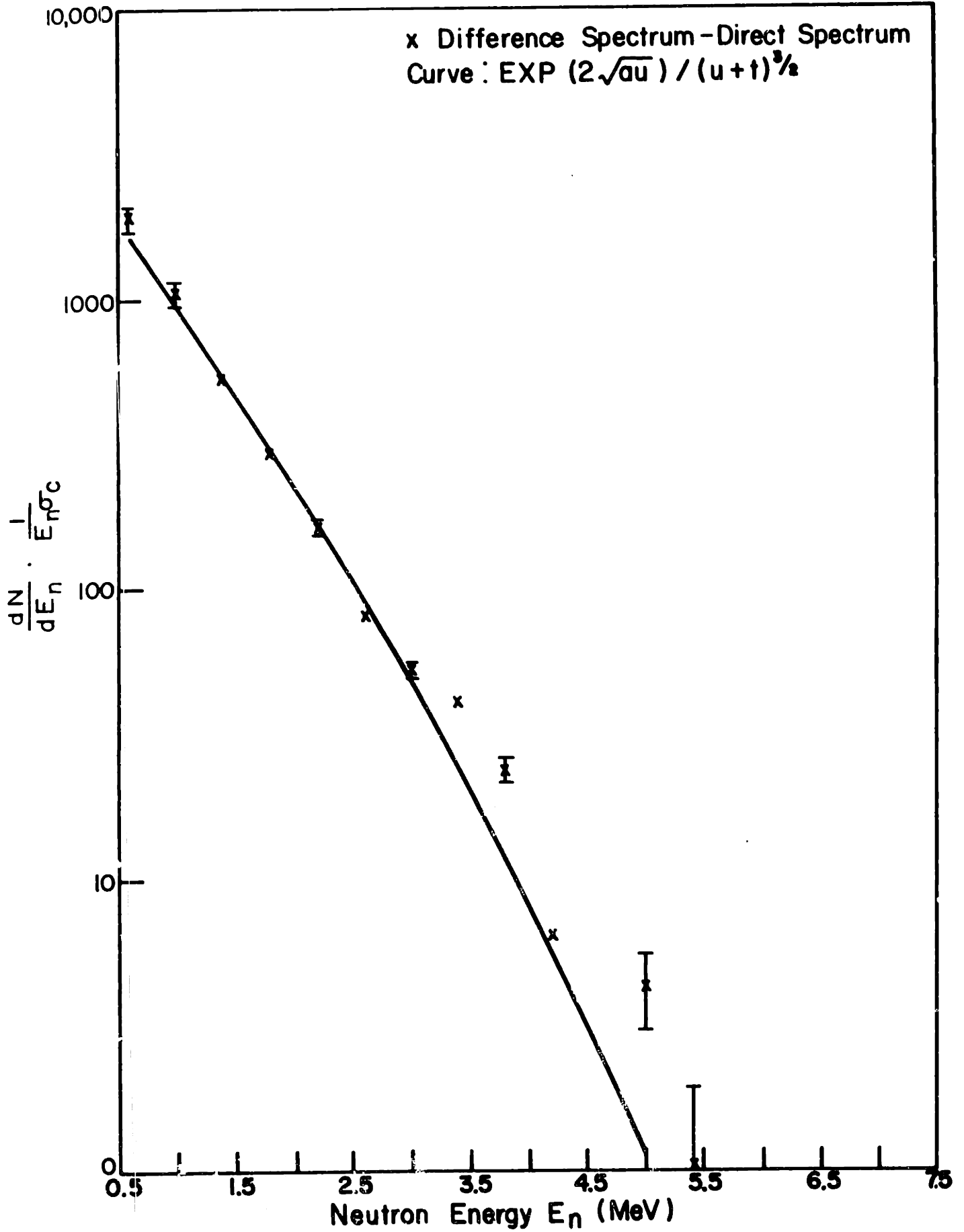


Fig. 101 Neutron Evaporation Spectrum

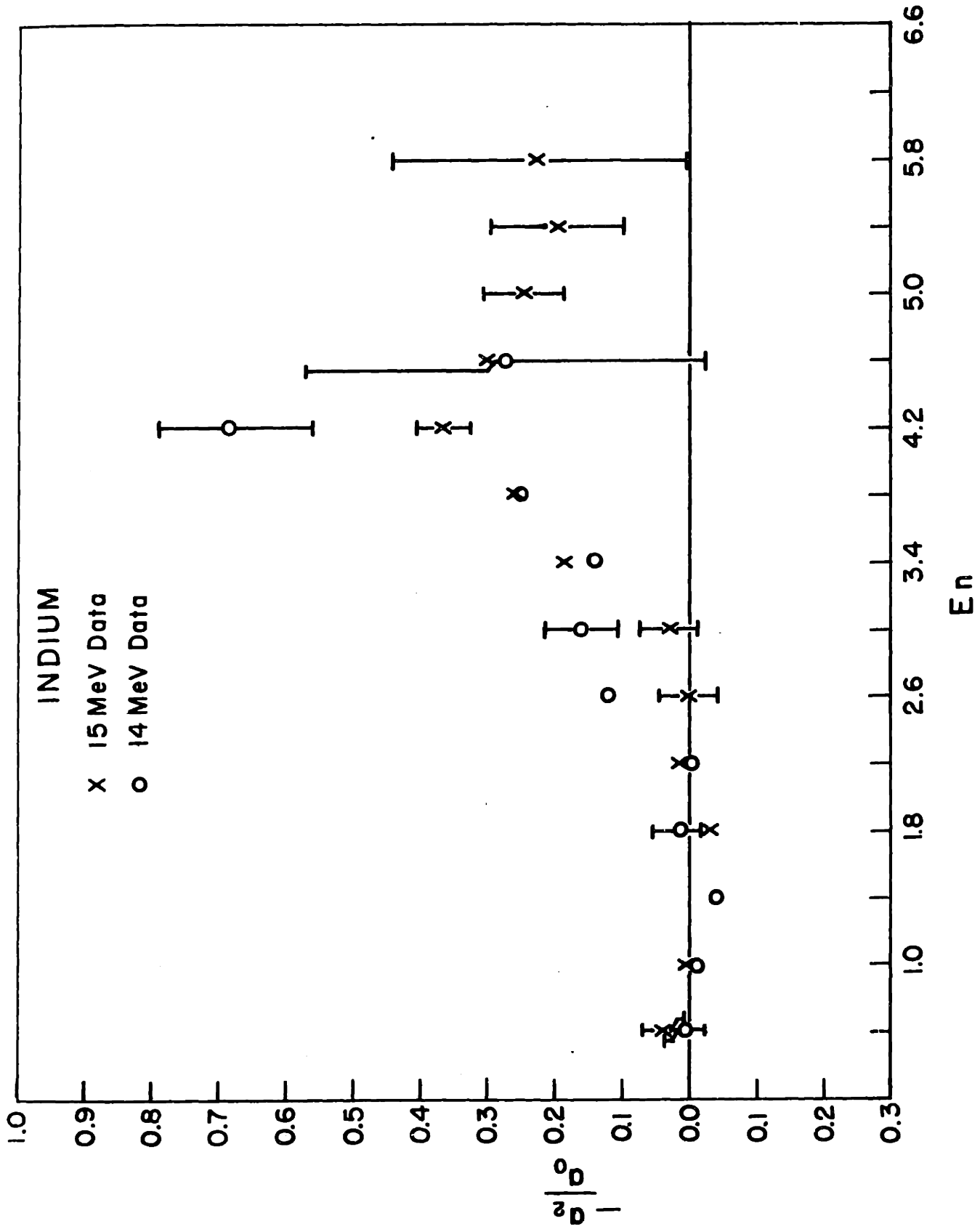


Fig. 102 Photoneutron Angular Distributions

resulted in a loss of the information about the number of counts lost due to coincidences between two counters.

## I. Level Density Parameter

For medium and heavy nuclei at excitations of a few MeV and higher, the nuclear level density is usually so high that it may be regarded as a continuous function of the excitation energy. Under these conditions the observed spectra of emitted particles are continuous, and the shapes of these spectra are closely related to the level density of the residual nucleus (43). The relative intensity,  $\frac{dN(E)}{dE_n}$ , of the emitted neutrons is given by

$$\frac{dN(E)}{dE_n} = \text{const } E_n \sigma_1(E_n, E^*) \omega(E^*) \quad (89)$$

for a fixed excitation energy  $E_0$ . The quantity  $\omega(E^*)$  is the density of states of the excited residual nucleus and  $\sigma_1(E_n, E^*)$  is the cross section for the inverse reaction.  $E^*$  is the excitation energy of the residual nucleus and is given by  $E^* = E_0 - E_n$ . The inverse cross section  $\sigma_1(E_n, E^*)$  is usually replaced by the cross section  $\sigma_C(E, E^*)$  for the formation of a compound nucleus by a neutron with energy  $E_n$  incident on the excited residual nucleus. Although  $\sigma_C(E, E^*)$  refers to an excited state of the nucleus, estimates of this quantity are generally taken from optical model cross sections  $\sigma_C(E_n)$ , which consider the target nucleus to be in its ground state. The values calculated by Perey and Buck (61) and by Auerbach and Moore (62) have been used in this thesis.

From Weisskopf's statistical treatment of nuclear level densities (43), a widely used approximation to the relative intensity distribution is obtained from a power series expansion of the nuclear entropy. The formula is

$$\frac{dN(E_n)}{dE_n} = \text{const } E_n \sigma_C(E_n) e^{-E_n/T} \quad (90)$$

which is similar to the Maxwell evaporation distribution. The quantity  $T$  is called the nuclear temperature. Detailed treatments of the nucleus as a Fermi gas of neutrons and protons (44, 81, 82) lead to expressions of the form

$$\omega_m(E^*) \propto (E^* + t)^{-m} e^{2\sqrt{a_m} E^*} \quad (91)$$



for the level density, where this equation is an approximation, valid for large  $E^*$ .

In a simple Fermi gas the density of states in the residual nucleus is given by Lang and LeCouteur (60) as

$$\omega(E^*) = \frac{\text{const}}{a^{1/4}(E^* + t)^{5/4}} e^{2\sqrt{aE^*}} \quad (92)$$

$$E^* = at^2 - t \quad (93)$$

where  $a$  = Fermi gas level density parameter

$t$  = thermodynamic temperature, defined as  $\frac{1}{t} = \frac{S}{E}$ , where  $S$  is the entropy of the system

The density of states in the residual nucleus with a given angular momentum  $J$  is given by the expression (Bethe (81))

$$\omega(E^*, J) = \frac{2J + 1}{\pi^{1/2}(2c\tau)^{3/2}} \exp[-(J + \frac{1}{2})^2 / 2c\tau] \omega(E^*) \quad (94)$$

The factor  $2c\tau$  is known as the 'spin cutoff' factor.  $c\hbar^2$  is the moment of inertia of the residual nucleus, and  $\tau$  is the nuclear temperature defined by

$$\frac{1}{\tau} = \frac{d \log \omega(E^*)}{dE^*} \quad (95)$$

$\hbar^2(J + \frac{1}{2})^2 / 2c\hbar^2$  is the average energy of rotation of the residual nucleus, and  $\tau$  is the average energy available to the residual nucleus. As can be seen from equations 90 and 95,  $\tau = T$ .  $\tau$  and  $t$  differ by a small constant for large  $E^*$  (83), therefore if  $t$  is substituted for  $\tau$  in the exponential of equation 94, and using

$$t = \frac{1}{a}(E^* + t)^{1/2} \quad (96)$$

equation 94 yields

$$\omega(E^*, J) = \text{const} \frac{(2J + 1)}{(E^* + t)^2} \exp[2\sqrt{aE^*}] \exp[-(J + \frac{1}{2})^2 / 2ct] \quad (97)$$

which is proportional to equation 91 with  $m = 2$  for large  $E^*$  and a fixed  $J$  value. Integration of  $\omega(E^*, J)$  over all  $J$  values leads to the total level density,

$$\omega'(E^*) = \frac{\omega(E^*)}{(2c\pi)^{1/2}} \quad (98)$$

Substitution of  $t$  for  $\tau$  as above, leads to

$$\omega'(E^*) = \frac{\text{const}}{(E^* + t)^{3/2}} e^{2\sqrt{aE^*}} \quad (99)$$

which is equation 91 with  $m = \frac{3}{2}$ .

It is therefore necessary to make an assumption about the experimental restrictions imposed on the spin,  $J$ , of the states excited in the residual nucleus before the level density coefficient,  $a_m$ , can be calculated from the data. These assumptions determine the appropriate value of  $m$  to be used in equation 91. According to Lang (83),  $m = \frac{5}{4}$  in equation 91 for a simple Fermi gas without spin;  $m = 2$  if states of only one spin  $J$  are observed; and  $m = \frac{3}{2}$  if states of all spins are observed. Since the photon excites at most three spin states, and the decay of the compound nucleus to the state of the residual favors small  $l$  values, only a few  $J$  values are involved in the  $(\gamma, n)$  reactions. Therefore  $m$  should be somewhat smaller than  $m = 2$ , with  $m = \frac{3}{2}$  as the lower limit. The data has been analyzed using both  $m = 2$  and  $m = \frac{3}{2}$ . The form  $\omega(E^*) \propto e^{-E_n/T}$  has also been used, primarily to compare this data with other experiments that use this last formalism. The three formulas for  $\omega(E^*)$  do not differ significantly over the small range of  $E^*$  available in the data (about 3 MeV). Therefore it was impossible to distinguish between the three formulas experimentally.

Hurwitz and Bethe (58) have suggested that the correlations of nuclear level densities with the odd-even character of the nucleus can be accounted for in terms of a pairing energy correction. The pairing energy may be regarded as a condensation energy that must be supplied to the nucleus before it can be considered a Fermi gas. For the purpose of these calculations, the excitation energy  $E^*$  was replaced by a fictitious excitation energy  $U$  based on the ground state of an odd nucleus where the pairing energy is taken to be zero. The relation between  $U$  and  $E^*$  is given by

$$U = E^* - \delta_p \quad (100)$$

where  $\delta_p$  is the pairing energy, or the energy required to provide two unpaired nucleons. The values of  $\delta_p$  used in this work were taken from Nemirovsky and Adamchuk (59). Each isotope, its binding energy, pairing energy and

maximum excitation energy,  $E_0$ , for the 14 MeV difference spectrum are listed in Table XXVIII. The maximum excitation energy is taken to be the energy of the peak of the photon difference spectrum. Notice that isotopes of widely different neutron binding energies have approximately the same excitation energy,  $E_0$ , due to the pairing energy. The excitation energy for a multi-isotopic target is calculated by summing the excitation energies for each isotope weighted by the isotopic abundances.

Combining equations 89, 91, and 100 yields

$$\frac{dN(E_n)}{dE_n} = \text{const} \frac{E_n \sigma_n C(E_n)}{(U+t)^m} e^{2\sqrt{a_m U}} \quad (101)$$

which is the form used to analyze the data, where  $t = \frac{1}{2a_m} + \sqrt{\frac{1}{4a_m^2} + \frac{E^*}{a_m}}$ .

$a_m$  was determined for each target with a least squares fit to the difference neutron spectra from 1.0 to about 3.0 MeV, in the manner described in Chapter IV, section D. The results are listed in Tables XXIX, XXX, and XXXI. The first column lists the target and the second lists the maximum excitation energy,  $E_0$ . The third column lists the temperature (from equation 90), the fourth lists the standard deviation for the temperature, the fifth lists  $a_{3/2}$ , the sixth tabulates the standard deviation of  $a_{3/2}$ , etc. The three tables list these quantities for each of the three methods of treating the data as explained in Chapter IV, section D. The values in Table XXIX were derived using the difference data without a correction for the direct component. Table XXX gives the values of  $T$ ,  $a_{3/2}$ , and  $a_2$  derived from the difference data minus the calculated direct energy spectrum,  $S(E_n)$ , by Method I. And finally Table XXXI tabulates these quantities for the isotropic portion of the difference data, that is, the difference data minus the direct spectrum derived from Method II.

The errors quoted in Tables XXIX; XXX and XXXI are derived from the fluctuations of the data in the least squares fit. There is another source of error, the variation in  $K$  in equation 53. As was stated in Chapter IV, section D,  $\Delta K$  is less than 6 per cent. The parameters listed in the tables were recalculated in a few cases, varying  $K$ . It was found that  $\Delta T \approx \frac{1}{2} \Delta K$  and  $\Delta a_m$

Table XXVIII

Pairing Energy and Maximum Excitation Energy for the Residual Nuclei

Parent Isotope	Isotopic Abundance	$E_{th}^*$	$\delta_p^{**}$	$E_{th} + \delta_p$	$E_o$
$^{209}_{83}\text{Bi}$	100.0	7.43	0	7.43	6.6
$^{208}_{82}\text{Pb}$	100.0	7.38	0.81	8.19	5.8
$^{207}_{82}\text{Pb}$	100.0	6.73	1.54	8.27	5.7
$^{206}_{82}\text{Pb}$	100.0	8.12	0.73	8.85	5.2
$^{205}_{81}\text{Tl}$	70.5	7.54	0	7.54	6.0***
$^{203}_{81}\text{Tl}$	29.5	7.89	0	7.89	
$^{204}_{80}\text{Hg}$	6.9	7.8	1.0	8.8	5.2
$^{202}_{80}\text{Hg}$	29.8	7.78	1.0	8.78	
$^{201}_{80}\text{Hg}$	13.4	6.24	1.85	8.1	
$^{200}_{80}\text{Hg}$	23.1	7.99	1.07	9.06	
$^{199}_{80}\text{Hg}$	16.8	6.69	1.95	8.64	
$^{198}_{80}\text{Hg}$	10.0	7.9	1.02	8.9	
$^{197}_{79}\text{Au}$	100.0	8.07	0	8.07	5.9
$^{186}_{74}\text{W}$	28.4	7.28	0.54	8.82	6.1
$^{184}_{74}\text{W}$	30.6	7.46	0.54	9.0	
$^{183}_{74}\text{W}$	14.6	6.19	1.25	7.44	
$^{182}_{74}\text{W}$	26.4	8.0	0.54	8.54	
$^{181}_{73}\text{Ta}$	100.0	7.65	0	7.65	6.4
$^{170}_{68}\text{Er}$	14.9	7.2	0.92	8.7	5.8
$^{168}_{68}\text{Er}$	27.1	7.78	0.92	8.7	
$^{167}_{68}\text{Er}$	24.6	6.54	1.68	8.22	
$^{166}_{68}\text{Er}$	33.4	8.55	0.93	8.7	
$^{165}_{67}\text{Ho}$	100.0	8.12	0	8.12	6.3
$^{154}_{62}\text{Sm}$	22.7	7.9	1.8	9.8	5.1
$^{152}_{62}\text{Sm}$	26.7	8.22	1.7	10.1	
$^{150}_{62}\text{Sm}$	7.4	8.0	1.54	9.54	
$^{149}_{62}\text{Sm}$	13.8	5.86	2.38	8.24	
$^{148}_{62}\text{Sm}$	11.2	8.13	1.3	9.43	
$^{147}_{62}\text{Sm}$	15.0	6.33	1.91	9.38	

\*Wapstra et al (70)

\*\*Nemirovsky and Adamchuk (59)

\*\*\* $E_{\gamma\text{max}} = 13.5$ .

Table XXVIII (Cont'd)

Pairing Energy and Maximum Excitation Energy for the Residual Nuclei

Parent Isotope	Isotopic Abundance	$E_{th}^*$	$\delta_p^{**}$	$E_{th} + \delta_p$	$E_o$
$^{141}_{59}\text{Pr}$	100.0	9.37	0	9.37	5.0
$^{139}_{57}\text{La}$	100.0	8.78	0	8.78	5.6
$^{127}_{53}\text{I}$	100.0	9.15	0	9.15	5.2
$^{124}_{50}\text{Sn}$	5.9	8.47	1.32	9.79	4.0
$^{122}_{50}\text{Sn}$	4.7	8.77	1.32	10.09	
$^{120}_{50}\text{Sn}$	32.9	9.1	1.32	10.56	
$^{119}_{50}\text{Sn}$	8.6	6.5	2.68	9.27	
$^{118}_{50}\text{Sn}$	24.0	9.25	1.5	10.75	
$^{117}_{50}\text{Sn}$	7.6	6.9	2.57	9.76	
$^{116}_{50}\text{Sn}$	14.3	9.6	1.55	10.94	
$^{115}_{49}\text{In}$	100.0	9.03	0	9.03	

\*Wapstra et al (70)

\*\*Nemirovsky and Adamchuk (59)

Table XXIX

## Level Density Parameters:Uncorrected for Direct Spectrum

Element	$E_0$	T	$\dagger \Delta T$	$a_{3/2}$	$\dagger \Delta a$	$a_2$	$\dagger \Delta a$
Bi	6.6	0.93	0.04	8.7	0.6	10.2	0.6
Bi	5.6	0.95	0.03	7.9	0.4	9.4	0.4
Pb <sup>208</sup>	5.8	1.31	0.03	5.0	0.2	6.3	0.3
Pb <sup>208</sup>	4.8	1.08	0.05	6.0	0.4	7.6	0.4
Pb <sup>207</sup>	5.7	1.24	0.05	5.1	0.3	6.6	0.3
Pb <sup>207</sup>	4.7	1.31	0.05	4.8	0.2	6.2	0.2
Pb <sup>206</sup>	5.2	1.19	0.04	5.5	0.2	6.9	0.2
Pb <sup>206</sup>	4.2	1.41	0.04	4.4	0.2	6.0	0.2
Tl	6.0	1.15	0.03	6.3	0.3	7.6	0.3
Hg	5.2	0.93	0.03	7.3	0.5	9.0	0.5
Hg	4.2	0.85	0.03	7.6	0.4	9.7	0.4
Au	5.9	0.76	0.03	11.0	1.0	12.8	1.1
Au	4.9	0.66	0.02	13.0	0.9	15.6	1.0
W	6.1	0.69	0.02	13.4	1.0	15.3	1.0
Ta	6.4	0.65	0.03	15.4	1.3	17.3	1.3
Ta	5.4	0.64	0.03	15.8	1.0	17.7	1.1
Er	5.8	0.71	0.02	12.7	0.3	14.6	0.3
Ho	6.3	0.83	0.03	10.4	0.6	12.0	0.6
Sm	5.1	0.83	0.02	9.0	0.2	10.8	0.3
Pr	5.0	0.77	0.02	10.2	0.3	12.0	0.5
La	5.6	0.90	0.03	8.5	0.6	10.1	0.6
I	5.2	0.82	0.05	9.2	1.0	11.0	1.0
Sn*	4.0	0.79	0.03	8.3	0.7	10.5	0.7
Sn**	4.0	0.69	0.01	10.5	0.5	10.7	0.5
In	5.4	0.69	0.02	12.3	1.0	14.2	1.0

\*Evaporation spectrum fit from 1.0 to 3.0 MeV.

\*\*Evaporation spectrum fit from 1.0 to 2.0 MeV.

Table XXX

Level Density Parameters: Direct Spectrum Derived from Method I

Element	$E_0$	T	$\pm\Delta T$	$a_{3/2}$	$\pm\Delta a$	$a_2$	$\pm\Delta a$
Bi	6.6	0.81	0.02	11.2	0.8	12.7	0.8
Bi	5.6	0.85	0.02	9.0	0.7	10.3	0.7
Pb <sup>208</sup>	5.8	1.20	0.04	5.2	0.3	6.3	0.4
Pb <sup>208</sup>	4.8	0.94	0.06	6.8	0.9	8.1	0.9
Pb <sup>207</sup>	5.7	0.97	0.06	7.4	0.9	8.7	1.0
Pb <sup>207</sup>	4.7	1.23	0.09	4.7	0.6	5.8	0.7
Pb <sup>206</sup>	5.2	1.14	0.06	5.4	0.4	6.7	0.5
Pb <sup>206</sup>	4.2	1.25	0.09	4.2	0.4	5.4	0.5
Tl	6.0	1.13	0.05	6.2	0.6	7.3	0.7
Hg	5.2	0.74	0.02	10.9	0.5	12.5	0.5
Hg	4.2	0.72	0.01	10.1	0.5	11.8	0.5
Au	5.9	0.66	0.03	15.2	2.0	17.0	2.1
Au	4.9	0.61	0.04	16.0	2.5	17.9	2.6
W	6.1	0.60	0.01	19.2	1.8	21.1	1.8
Ta	6.4	0.54	0.01	23.4	2.1	25.5	2.2
Ta	5.4	0.54	0.02	22.3	1.6	24.4	1.9
Er	5.8	0.62	0.03	17.3	1.8	19.2	1.9
Ho	6.3	0.60	0.04	19.9	3.7	21.9	4.0
Sm	5.1	0.73	0.02	12.0	0.5	13.7	0.5
Pr	5.0	0.66	0.05	14.1	2.3	15.8	2.4
La	5.6	0.77	0.03	10.7	0.6	12.2	0.6
I	5.2	0.68	0.01	13.0	0.8	14.7	0.8
Sn <sup>*</sup>	4.0	0.75	0.03	9.1	1.3	10.8	1.3
Sn <sup>**</sup>	4.0	0.66	0.01	12.6	1.2	14.1	1.0
In	5.4	0.67	0.02	14.0	1.9	15.8	2.0

\*Evaporation spectrum fit from 1.0 to 3.0 MeV.

\*\*Evaporation spectrum fit from 1.0 to 2.0 MeV.

Table XXXI

Level Density Parameters: Direct Spectrum Derived from Method II

Element	$E_0$	T	$\dagger\Delta T$	$a_{3/2}$	$\dagger\Delta a$	$a_2$	$\dagger\Delta a$
Bi	6.6	0.90	0.03	9.5	1.1	10.9	1.1
Bi	5.6	0.93	0.04	8.2	1.2	9.6	1.2
Pb <sup>208</sup>	5.8	1.26	0.04	5.1	0.3	6.2	0.4
Pb <sup>208</sup>	4.8	0.90	0.03	8.1	0.8	9.6	0.9
Pb <sup>207</sup>	5.7	1.18	0.09	5.0	1.0	6.3	1.1
Pb <sup>207</sup>	4.7	1.28	0.08	4.8	0.7	5.9	0.8
Pb <sup>206</sup>	5.2	0.92	0.07	8.1	1.5	9.6	1.6
Pb <sup>206</sup>	4.2	1.24	0.09	4.6	0.6	5.9	0.7
Tl	6.0	1.10	0.06	6.6	0.9	7.8	0.9
Hg	5.2	0.83	0.05	9.3	1.5	10.9	1.6
Hg	4.2	0.72	0.03	10.5	0.8	12.3	0.6
Au	5.9	0.56	0.02	20.7	1.7	22.8	1.8
Au	4.9	0.53	0.07	21.3	8.0	23.5	8.5
W	6.1	0.33	0.07	58.5	36.6	61.9	37.7
Ta	6.4	0.36	0.16	51.5	72.3	54.6	74.4
Ta	5.4	0.50	0.06	26.9	9.5	29.1	9.9
Er	5.8	0.26	0.10	88.1	105.3	92.2	107.7
Ho	6.3	0.64	0.07	17.6	5.2	19.5	5.5
Sm	5.1	0.80	0.08	10.3	2.9	11.9	3.1
Pr	5.0	0.77	0.06	11.1	2.3	12.7	2.5
La	5.6	0.76	0.02	11.7	0.8	13.3	0.8
I	5.2	0.75	0.08	11.7	3.7	13.4	4.0
Sn*	4.0	0.78	0.03	8.7	0.9	10.4	1.0
Sn**	4.0	0.77	0.07	9.6	2.5	11.3	2.6
In	5.4	0.78	0.07	11.0	3.0	12.6	3.2

\*Evaporation spectrum fit from 1.0 to 3.0 MeV.

\*\*Evaporation spectrum fit from 1.0 to 2.0 MeV.



$\approx \frac{1}{2}\Delta K$ . \* Therefore these uncertainties ( $< 3$  per cent) are small for  $a_m$  compared to the ones listed in Tables XXIX, XXX and XXXI, and may be comparable to the uncertainties in T.

When one attempts to compare this data with other experiments, several problems develop. First, most of the data available are found from  $(n, n')$  experiments (84, 85) or by counting resonances from thermal neutron capture experiments (86). In the first case, the residual nucleus is the target nucleus, and in the second case, the residual nucleus is the target nucleus plus one neutron. In  $(\gamma, n)$  experiments, the residual nucleus is the target nucleus minus one neutron. If one ignores the problem introduced by the different residual nuclei reached by the reactions (and  $\delta_p$  was introduced to eliminate this problem), this  $(\gamma, n)$  work can be compared with the results of the  $(n, n')$  experiments and the neutron capture experiments. Secondly, different experimenters use different approximations for the inverse capture cross section. Finally the forms used for the level of the residual nucleus vary considerably.

In the case of slow neutron resonance data, the average spacing between levels is used to determine the level density, and thus  $\sigma_C$  does not enter into the calculation. Erba et al (86) have used formula 91 with  $m = 2$  to calculate  $a_2$  from these average level spacings. His results are listed in Table XXXII along with the values of  $a_2$  for this experiment taken from Table XXX. The data were taken from Table XXX because the direct component was not removed from the neutron spectrum before calculating the level density parameters listed in Table XXIX, and the level densities listed in Table XXXI vary too widely in the rare earth region, where the angular distribution of the direct spectrum is small. In general the present values of  $a_2$  are lower than those listed by Erba near  $\text{Pb}^{207}$ , and comparable elsewhere.

The values of T and  $a_2$  measured in  $(n, n')$  experiments by Buccino et al (84) and D. B. Thomson (85) are listed in Table XXXIII. Data having an  $E_0$  close to the values used in this experiment were chosen whenever possible.

Buccino et al uses the  $\sigma_C$  calculated in ref 61, as was done in this thesis (ex-

\* Also:  $\Delta(-a_2/a_0) \approx \frac{1}{3}\Delta K$ ;  $\Delta f \approx \Delta K$ , where f is the direct fraction defined in the next section.

Table XXXII  
 Level Density Parameters: Comparison With  
 Thermal Neutron Capture Experiments

Element	$E_o$ (n, $\gamma$ )*	$a_2$	$E_o$ ( $\gamma$ , n)**	$a_2$
Bi			6.6	12.7
Bi	4.6	10.8	5.6	10.3
Pb <sup>208</sup>			5.8	6.3
Pb <sup>208</sup>	3.9	11.2	4.8	8.1
Pb <sup>207</sup>			5.7	8.7
Pb <sup>207</sup>			4.7	5.8
Pb <sup>206</sup>	6.7	10.5	5.2	6.7
Pb <sup>206</sup>			4.2	5.4
Tl	6.6	14.7	6.0	7.3
Hg	7.1	21.1	5.2	12.5
Hg			4.2	11.8
Au	6.5	19.1	5.9	17.0
Au			4.9	17.9
W	6.7	24.7	6.1	21.1
Ta	6.1	22.1	6.4	25.5
Ta			5.4	24.4
Er			5.8	19.2
Ho	6.4	20.2	6.3	21.9
Sm	8.0	21.8	5.1	13.7
Pr	5.8	16.6	5.0	15.8
La	5.0	15.6	5.6	12.2
I	6.7	17.9	5.2	14.7
Sn	8.0	18.5	4.0	14.1
In	6.6	18.2	5.4	15.8

\*Erba et al (86), Residual Nucleus A + 1

\*\*This experiment, Residual Nucleus A - 1

Table XXXIII

## Level Density Parameters: Comparison With (n, n') Experiments

Element	(n, n')*			(n, n')**			(γ, n)***		
	$E_0$	$a_2$	T	$E_0$	$a_2$	T	$E_0$	$a_2$	T
Bi	6.5	13.3	0.84	7.0	8.5	1.05	6.6	13.6	0.81
Bi	6.0	13.3	0.76	5.0	13.4	0.68	5.6	11.5	0.85
Pb <sup>208</sup>							5.8	7.7	1.20
Pb <sup>208</sup>							4.8	9.8	0.94
Pb <sup>207</sup>	6.0	11.7	0.71	7.0	9.9	0.92	5.7	10.3	0.97
Pb <sup>207</sup>	5.0	11.7	0.76				4.7	8.1	1.23
Pb <sup>206</sup>							5.2	8.4	1.14
Pb <sup>206</sup>							4.2	8.3	1.25
Tl	6.0	10.2	0.77	6.0	12.1	0.80	6.0	8.3	1.13
Hg	5.0	13.9	0.62				5.2	13.7	0.74
Hg	4.0	13.9	0.61				4.2	13.5	0.72
Au	6.0	16.6	0.62	7.0	21.9	0.60	5.9	18.0	0.66
Au	5.0	16.6	0.58	4.0	21.2	0.47	4.9	19.1	0.61
W	6.0	17.9	0.55	7.0	24.5	0.50	6.1	22.1	0.60
Ta	6.5	17.6	0.64	7.0	27.0	0.52	6.4	26.3	0.54
Ta	5.0	17.6	0.53				5.4	25.4	0.54
Er	6.0	13.0	0.64				5.8	20.2	0.62
Ho							6.3	22.8	0.60
Sm							5.1	15.0	0.73
Pr	5.0	15.8	0.69				5.0	17.1	0.66
La	6.0	12.3	0.71	5.0	13.6	0.69	5.6	13.4	0.77
I				4.0	23.6	0.41	5.2	15.9	0.68
Sn							4.0	14.5	0.66
In				5.0	21.7	0.48	5.4	16.9	0.67

\* Buccino et al (84)

\*\* Thomson (85)

\*\*\* This Experiment (adjusted).

cept for  $\text{Pb}^{208}$  and Bi, for which  $\sigma_C$  was taken from ref 62). Thomson used a constant for his values of  $\sigma_C$ . Thus differences in the results are to be expected. Both Buccino et al and Thomson analyzed their data using the level density formula (90). The values of T for the present data taken from Table XXX are listed in Table XXXIII and can be directly compared with the values of T obtained by Buccino et al and Thomson. In general the values of T from this experiment are larger than the results obtained by Buccino et al or Thomson for elements with masses near  $\text{Pb}^{207}$  and Tl, and are comparable elsewhere.

Since the nuclear temperatures are functions of the excitation energy of the residual nucleus, which is different for each set of data in Table XXXIII, it may be more meaningful to compare the level density parameters which should be independent of the excitation energy. Before comparing the values of  $a_2$  from this experiment with the values obtained by Buccino and Thomson, the three sets of data must be reduced to the same form. Specifically Buccino and Thomson have used  $\omega(U) \propto U^{-2} e^{2\sqrt{aU}}$  for the level density, while the form  $\omega(U) \propto (U+t)^{-2} e^{2\sqrt{aU}}$  was used for this thesis. Therefore the present values of  $a_2$  are smaller than the values given by Buccino et al and Thomson. The values of  $a_2$  found in this thesis can be adjusted to their formalism with the use of equation 89. Solving for  $a_2$ , one finds

$$a_2 = \frac{\bar{U}}{T^2} + \frac{4}{T} + \frac{4}{\bar{U}} \quad (102)$$

for  $\omega(U) \propto U^{-2} e^{2\sqrt{aU}}$ , and

$$a'_2 = \frac{\bar{U}}{T^2} \frac{4\bar{U}}{T(\bar{U} + T)} \frac{4\bar{U}}{(\bar{U} + T)^2} \quad (103)$$

for  $\omega(U) \propto (U + T)^{-2} e^{2\sqrt{aU}}$ , where t has been approximated by T. Then

$$a_2 = a'_2 + \Delta a \quad (104)$$

where

$$\Delta a = \left[ \frac{4}{T} + \frac{4}{\bar{U}} \left( \frac{2\bar{U} + T}{\bar{U} + T} \right) \right] \left[ \frac{T}{\bar{U} + T} \right] \text{ and } \Delta a \text{ is evaluated for } \bar{U} = E_0 - \delta_p - 2T.$$

(2T is the average energy of an emitted neutron.) The corrected values of  $a_2$ , calculated from equation 104 for this experiment are tabulated in

Table XXXIII along with the values of Buccino et al and Thomson. The adjusted values of  $a_2$  agree well with the values of Thomson, except for tin, where Thomson's values are larger. The adjusted values of  $a_2$  from this experiment are larger than the values found by Buccino et al in the region of the deformed nuclei.

When one tries to compare this experiment with other  $(\gamma, n)$  experiments (72, 73, 87, 88) where neutron energy spectra have been measured, one finds that the level density formulas used are generally of the form

$$\frac{dN}{dE_n} \propto e^{-E_n/T} \quad (105)$$

or

$$\frac{dN}{dE_n} \propto \exp[3.35(A - 40)^{1/2} U]^{1/2} \quad (106)$$

The values of  $T$  derived from the present experiment can be compared with other  $(\gamma, n)$  data, although  $T$  is dependent on the excitation energy. Most experimenters employ a bremsstrahlung spectrum, which results in an  $E_0$  of about  $E_{\max} - E_{\text{th}}$  where  $E_{\max}$  is the photon energy of the peak of the  $(\gamma, n)$  cross section. Therefore  $E_{\max} - E_{\text{th}}$  is nearly equal to the present maximum excitation energy,  $E_0(14 - E_{\text{th}})$ . Table XXXIV lists  $T$  from several experiments including this one. The values of  $T$  listed for the present data are taken from Table XXIX since other  $(\gamma, n)$  data are not generally corrected for the direct component. The values obtained vary widely, being generally lower than the present data.

The Livermore group (5, 6, 7) measured  $(\gamma, n)$  and  $(\gamma, 2n)$  cross sections using monochromatic photons from in-flight annihilation of positrons. They derive the level densities from the  $(\gamma, 2n)/[(\gamma, n) + (\gamma, 2n)]$  branching ratio (43). They use the form  $e^{2\sqrt{a}U}$  for the level density, and as a result their data can not be directly compared with the present data. However using equation 91 and solving for  $a_m$ ,

$$a_m = \frac{\bar{U}}{T^2} + \frac{2m}{T} + \frac{m^2}{U} \quad (107)$$

When  $m = 2$  and  $m = 0$  are substituted into equation 107, it yields

Table XXXIV

Nuclear Temperatures for Pb and Bi from ( $\gamma, n$ ) Experiments

Element	$E_{\gamma\max}$	T	$\sigma_C$	Reference
Pb	15	$1.31^{*\pm} 0.02$	Auerbach, Moore (62)	This Experiment
	70	$1.0 \pm 0.2$	1.0	Dixon (89)
	32.5	0.6	1.0	Breuer (90)
	23	1.35	$T_\ell (\ell = 0, \text{ from (43) })$	Toms (73)
	18.9	1.1	1.0	Zatsepina (71)
	16	$0.98 \pm 0.04$	1.0	Glazunov (14)
	Bi	15	$0.93 \pm 0.04$	Auerbach, Moore (62)
16		$0.84 \pm 0.04$	1.0	Glazunov (14)
14.1		$0.72^{**}$	1.0	Kuchnir (69)

\*Pb<sup>208</sup>

\*\*Monochromatic gammas.

Table XXXV

Nuclear Level Density Parameter from Livermore Data\*

Element	$a_0$	$\bar{U}$	$a_2$	$a_2$ (This Experiment)
Bi	10.2	6.1	11.7	13.6
Pb <sup>208</sup>	9.6	6.5	11.0	7.7
Pb <sup>207</sup>	13.5	8.2	14.9	10.3
Pb <sup>206</sup>	6.6	5.9	7.8	8.4
Au	17.1	7.0	18.8	18.0
Ta	15.7	7.0	17.3	26.3
Ho	22.0	7.0	23.9	22.8

\* Refs 5, 6, and 7.

$$a_2 = a_0 + 4 \left( \sqrt{\frac{a_0}{\bar{U}}} + \frac{1}{\bar{U}} \right) \quad (108)$$

where  $\bar{U}$  is given by  $E_0 - \delta_p - \bar{E}_n$ , and  $\bar{E}_n$  is the average neutron energy in the energy region used for determination of the nuclear temperature.  $\bar{E}_n = 2T$ , where the values of  $T$  found in this experiment have been used. Thus one can convert the  $a_0$  found in refs 5, 6 and 7 to  $a_2$ . These results are shown in Table XXXV, and the adjusted values of  $a_2$  from this experiment are also listed in the table. The Bi,  $Pb^{206}$ , Au, and Ho values for  $a_2$  agree reasonably well, but the Livermore data for  $Pb^{208}$  and  $Pb^{207}$  are larger than the present results, while their results for Ta are appreciably smaller. They used a value of 13.6 MeV for the  $(\gamma, 2n)$  threshold of Ta. The latest mass data compilation (70) lists 14.4 MeV. This may explain their low value of  $a_2$  for Ta.

The shell effects which are so evident in the data have been investigated by many authors. The level densities are estimated from the shell model levels in the treatment of Newton (91) and later Lang (83). They find

$$a_2 = K(\bar{j}_n + \bar{j}_z + 1)A^{3/2} \quad (109)$$

where  $A$  is the atomic mass,  $\bar{j}_n$  and  $\bar{j}_z$  are the effective values of the neutron and proton angular momentum taking some account of the deformation of non-magic nuclei and the overlapping of subshells. They used the sequence of  $\bar{j}$  values proposed by Klinkenburg (92). Newton found  $K = 0.06$ , and Lang found  $K = 0.075$ .

The adjusted values of  $a_2$  from Table XXXIII and some representative values of  $a_2$  from an  $(n, n')$  experiment (Buccino et al) are shown in Fig. 103. The curve was calculated from equation 109 for the isotopes reached by a  $(\gamma, n)$  reaction. As was explained in section H, the evaporation curve for tin did not fit the difference data well, probably due to  $S(E_n)$  being a poor approximation.  $a_2$  was recalculated at lower neutron energies and found to be 14.5 (see section H). This value,  $a_2 = 14.5$  for tin was plotted in Fig. 103. In this experiment the multi-isotopic elements in general are found to have lower values of  $a_2$  than nearby monoisotopic targets. This would appear to indicate that the attempts to average out the effects of differing thresholds was not totally successful.

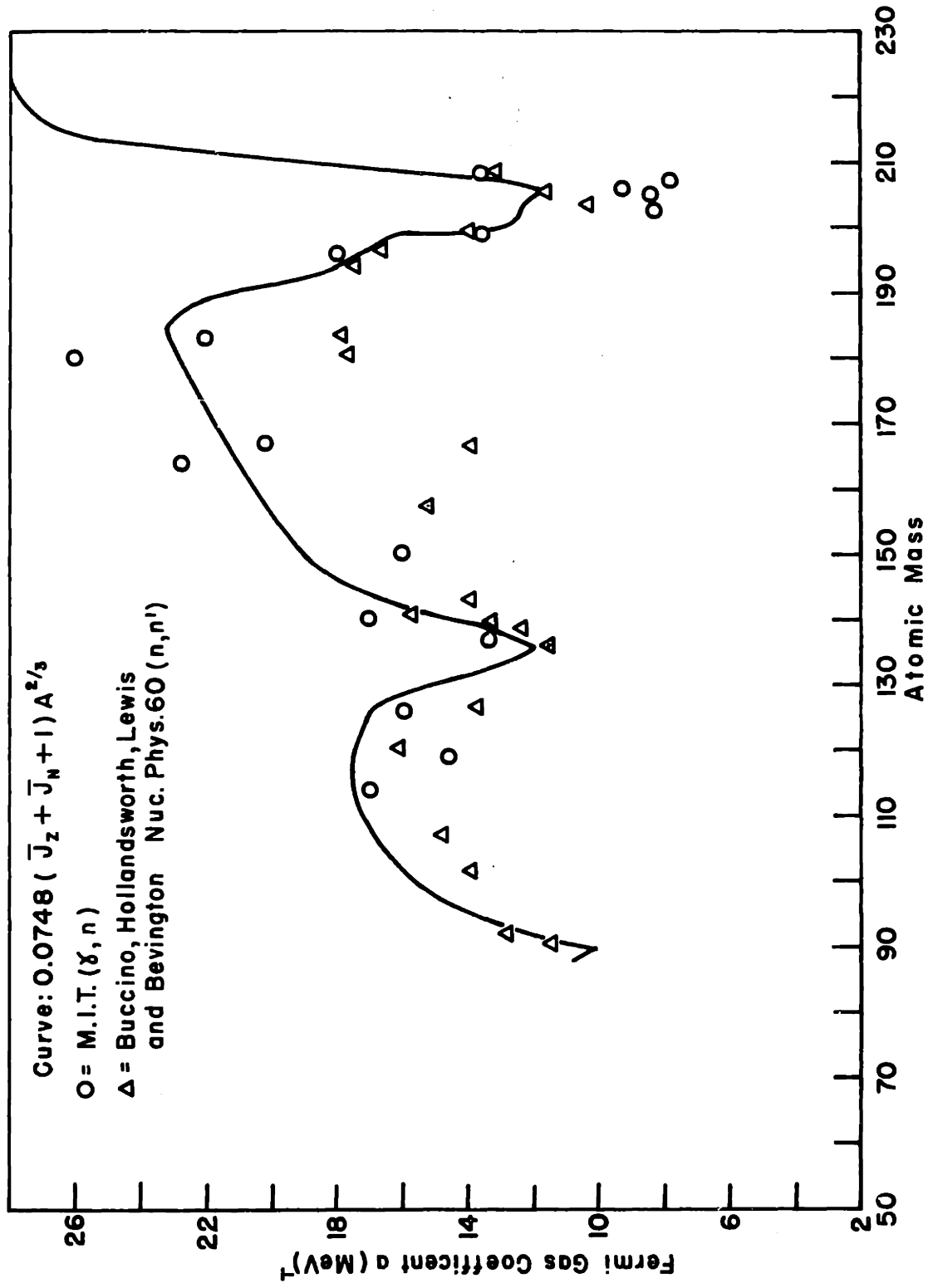


Fig. 103 Fermi Gas Level Density Coefficient vs Atomic Mass



The constant used for the curve in Fig. 103 ( $K = 0.0748$ ) was taken from Lang (83). Thomson found a value of  $K = 0.102$ . If the adjusted values of  $a_2$  are used (ie, those listed in Table XXXIII), a value of  $K = 0.067$  is obtained for the present data.

#### J Direct Fraction

The fraction of resonance direct neutrons,  $f$ , is defined by the equation

$$f = \frac{\sum_{3.0}^{E_{\max}} \frac{\Delta N(E)}{\Delta E} - c E_n \sigma_C \rho(E_o - E) \Delta E}{\sum_0^{E_{\max}} \frac{\Delta N(E)}{\Delta E} \Delta E} \quad (110)$$

where the factors in the equation have been previously defined. The lower value of the sum was chosen to be 3.0 MeV because the evaporation spectra dominated below this energy and the statistical errors on the direct spectrum become very large. Therefore the sum is cut off at 3.0 MeV and  $f$  represents a lower limit on the direct fraction. The contribution to  $f$  of directly emitted neutrons with energies less than 3.0 MeV is expected to be small. For example, this contribution is zero using the shape of the resonance direct spectrum  $S(E_n)$  calculated for the assumptions of the thesis for the distribution of discrete hole states in the residual nucleus (see section A of this Chapter). And it is estimated to be less than 10 per cent of  $f$  if  $S(E_n)$  was calculated assuming that the hole states are uniformly distributed in the residual nucleus (see section D).

The values of  $f$  from the two different methods of analyzing the data (see Chapter IV, section D), are listed in Table XXXVI. They are also shown in Fig. 104. The direct fraction is about 14 per cent and approximately constant with  $A$ , for the data calculated using the first method (ie, estimating the direct component theoretically). Using the second method (ie, estimating the direct fraction from the neutron angular distribution),  $f$  is about 13 per cent, and again approximately constant with  $A$ . However with Method II, there appears to be a pronounced peak in  $f$  at  $\text{Pb}^{208}$ . This peak is not so clearly

defined using the first method. The errors listed in the table include the statistical uncertainties and the uncertainty due to the errors in the level density parameters used to calculate  $\rho(E_0 - E)$  in equation 110. An additional uncertainty in  $f$  due to errors in the subtraction procedure used to find the difference spectrum is also included. As was mentioned in the previous section, this is about 6 per cent.

As can be seen from Table XXXVI, the direct fraction  $f$  depends on the maximum neutron energy  $E_{n \max}$ . In order to compare  $f$ 's from different elements, one would prefer that the neutron endpoints were constant with  $A$ . Therefore the data plotted in Fig. 104 is the direct fraction chosen so that the neutron endpoint is as near a constant as possible. That is, the 15 to 14 MeV difference data was chosen for isotopes with high  $(\gamma, n)$  thresholds, and the 14 to 13 MeV difference data was chosen for isotopes with low  $(\gamma, n)$  thresholds.

The direct fraction was calculated from equations 69 and 74 which are used to calculate the direct spectrum,  $S(E_n)$ . These equations reduce to

$$f = \sum_{\ell} \frac{\Gamma_{\alpha\ell} f_{\ell}}{\Gamma_a + \Gamma_{\alpha\ell}} \quad (111)$$

where  $\Gamma_{\alpha\ell} = \frac{T_{\ell} \hbar^2 K^2}{2MR}$  is the width for particle emission

$f_{\ell}$  = relative transition strength

$\Gamma_a = 2W$  is the width for particle absorption

$K^2 = k^2 + K_0^2$  is the wave number of the nucleon in the nucleus. The results are listed in Table XXXVII. The third column lists the values of  $f$  derived using the assumption of discrete hole states in the residual nucleus, which tends to underestimate  $S(E_n)$  at low neutron energy, while the fourth column lists the values of  $f$  derived using the assumption of a continuous spectrum of hole states in the residual nucleus which may overestimate  $S(E_n)$  at low neutron energies since the hole states may cluster at low excitation energy. In the cases where both  $f$ 's have been calculated, it can be seen that the second assumption yields smaller  $f$ 's. This is because the  $T_{\ell}$ 's decrease with decreasing neutron energies. The calculated values of  $f$  are  $\frac{1}{3}$  to  $\frac{1}{10}$  of the experimental values.

Table XXXVI

## Fraction of Direct Neutrons: Experimental Values

Element	(γ, n) threshold	E <sub>n max</sub>	Method I		Method II	
			f	±Δf	f	±Δf
Bi	7.4	8.0	0.21	0.015	0.17	0.02
Bi	"	7.0	0.13	0.01	0.12	0.01
Pb <sup>208</sup>	7.4	8.0	0.18	0.01	0.15	0.01
Pb <sup>208</sup>	"	7.0	0.15	0.01	0.21	0.015
Pb <sup>207</sup>	6.7	8.7	0.21	0.015	0.17	0.02
Pb <sup>207</sup>	"	7.7	0.09	0.01	0.12	0.01
Pb <sup>206</sup>	8.1	7.3	0.14	0.01	0.19	0.015
Pb <sup>206</sup>	"	6.3	0.08	0.01	0.13	0.01
Tl	7.6	7.8	0.10	0.01	0.11	0.01
Hg	7.7	7.7	0.18	0.015	0.14	0.015
Hg	"	6.9	0.13	0.01	0.11	0.01
Au	8.1	7.3	0.15	0.015	0.14	0.02
Au	"	6.3	0.11	0.01	0.08	0.015
W	7.5	7.9	0.13	0.01	0.13	0.04
Ta	7.7	7.7	0.14	0.015	0.15	0.045
Ta	"	6.7	0.10	0.01	0.08	0.025
Er	7.9	7.5	0.11	0.01	0.07	0.02
Ho	8.1	7.3	0.19	0.015	0.13	0.02
Sm	8.0	7.4	0.12	0.01	0.09	0.015
Pr	9.4	6.0	0.12	0.01	0.08	0.01
La	8.8	6.6	0.15	0.01	0.15	0.01
I	9.2	6.2	0.15	0.01	0.14	0.015
Sn	9.2	6.2	0.17	0.01	0.12	0.015
In	9.0	6.4	0.16	0.015	0.14	0.015

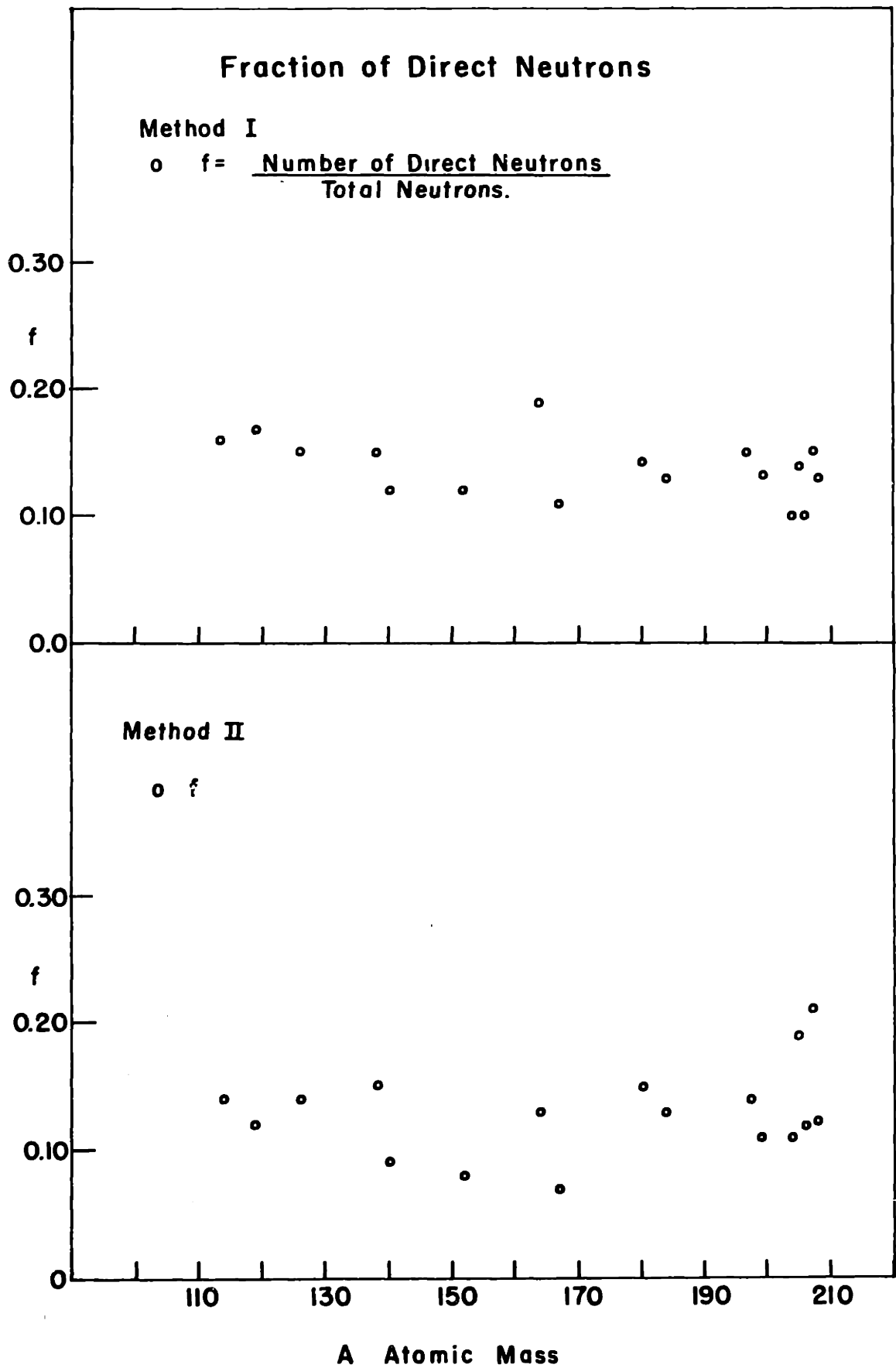


Fig.104

Table XXXVII

## Fraction of Direct Neutrons: Calculated Values

Element	$E_0$	Direct Fraction, f	
		Discrete hole states	Continuum of hole states
Bi	6.6	0.037	
Bi	5.6	0.028	
Pb <sup>208</sup>	5.8	0.037	
Pb <sup>208</sup>	4.8	0.027	
Pb <sup>207</sup>	5.7	0.037	
Pb <sup>207</sup>	4.7	0.026	
Pb <sup>206</sup>	5.2	0.039	
Pb <sup>206</sup>	4.2	0.030	
Tl	6.0	0.035	
Hg	5.2		0.028
Hg	4.2		0.019
Au	5.9	0.028	0.019
Au	4.9		0.014
W	6.1		0.039
Ta	6.4		0.034
Ta	5.4		0.024
Er	5.8		0.043
Ho	6.3		0.038
Sm	5.1		0.039
Pr	5.0	0.039	
La	5.6	0.044	
I	5.2		0.029
Sn	4.0	0.032	
In	5.4	0.028	

The validity of the calculated direct fraction,  $f$ , depends on the reliability of the three terms in equation 110,  $\Gamma_{\alpha\ell}$ ,  $f_{\ell}$ , and  $\Gamma_a$ . The estimate of the width for particle emission,  $\Gamma_{\alpha\ell}$ , depends on the number of single particle levels in the energy region of the excited nucleus. (43) Although the formula given is for a finite square well, a count of the number of experimental single particle levels in this energy region agrees quite well with the square well value. The  $T_j$ 's were calculated for a realistic potential, Saxon-Wood, with a spin orbit term (valid only for spherical nuclei, however). The width for particle absorption,  $\Gamma_a$ , was estimated by allowing the escaping neutron to interact with the residual nucleus, through the potential  $V = U + iW$ . Then the particle absorption width is given by  $2W$ .  $W$  was taken to be  $2.5 + 0.4 E_n$  MeV (63).<sup>\*</sup> Although other values of  $W$  have been used in the literature, ( $W = 2.1$ ,  $E_n = 0$ , Feshbach, Porter and Weisskopf (93), and  $W = 3.4$  MeV,  $E_n = 0$ , Seth et al (94), for example) these values fit a wide range of experimental data (Lane and Wandel (63)). Finally referring to Table XIII, one can see that the  $f_{\ell}$ 's for a square well (Wilkinson), which were the values used in the calculations listed in Table XXXVII, may differ by a factor of two from the values calculated for the more realistic Saxon-Wood potential, including particle-hole interactions, (Pal et al (65)). However the  $f_{\ell}$ 's for transitions with small  $\ell$  values, which are the ones that contribute the bulk of the direct fraction are greatly reduced by going to a more realistic potential, while the high  $\ell$  values, which contribute little, are changed only a small amount.

The large discrepancy between theory and experiment forces a re-examination of the simple model used for the calculations. It was assumed in section E of Chapter IV, that if a particle did not escape before interacting with the nucleus, it damped directly into the compound nucleus. This is probably an unrealistic assumption. One method in which a given particle-hole state could interact with the nucleus is to transfer all of its excitation energy directly to another particle-hole state through a two-body interaction. The resulting particle emission would be indistinguishable from "direct emission". In this manner the oscillator strength of particle-hole pairs that do not contribute

<sup>\*</sup>  $W$  was reduced by a factor of 1.85 for Bi and by 1.27 for  $Pb^{208}$  (see section E, Chapter IV).

bute to the direct emission, such as proton particle-hole pairs with large  $\ell$  values for the emitted neutrons ( $T_\ell < 10^{-3}$ ), could be transferred to neutron particle-hole pairs that contribute more strongly to the direct spectrum; that is, pairs with small  $\ell$  values ( $T_\ell \approx 0.3$ ) for the emitted neutrons.

The results of such a transfer of oscillator strength were estimated qualitatively by assuming that the strength for all of the proton transitions and the neutron transitions leading to directly emitted neutrons with  $\ell$ 's of 6 and 7 (for  $N = 126$ ) or 5\* and 6 (for  $N = 82$ ) were transferred to the remaining neutron transitions. These strengths were arbitrarily divided among the remaining neutron transitions in proportion to their original strengths. The results are listed in Table XXXVIII. Column one lists the ratio of the calculated direct spectrum, integrated from 3.0 MeV to the neutron endpoint, to the experimental value (Method I). The second column lists the fraction of the total neutron strength exhausted by the  $\ell = 6$  and  $\ell = 7$  (or  $\ell = 5$  and 6) transitions. If the nucleus does not have a closed neutron shell, transitions from the next lower shell are possible. These transitions do not contribute strongly to the direct spectrum since the residual states typically lie 5 to 10 MeV above the ground state. The strengths from these transitions have also been redistributed, as described above, and are included in the fraction listed in column two. The proton transitions account for 43 per cent of the total strength for both the  $N = 126$  and  $N = 82$  shells. These have also been redistributed in the manner described above. The third column lists the ratio of the calculated to experimental direct spectrum corrected for the redistributed strengths. It is equal to the first column divided by 100 per cent minus the neutron strength to be redistributed (column two) and then divided by 100 per cent minus the proton strength (43 per cent).

It is immediately evident that the direct fractions calculated using a continuous spectrum of residual states, Hg, Au, W, Ta, Er, Ho, Sm, and I, are still too low. According to Table XXXVII, the calculated direct fraction for Au is about 50 per cent smaller if a continuous spectrum of residual states  $T_{\ell=5} \geq 10^{-2}$ , hence redistributing all of the  $\ell = 5$  strength will tend to overestimate the direct fraction. This is seen in La, I, Sn and In, where the calculated value is larger than the average (see Table XXXVIII).

Table XXXVIII

Fraction of Direct Neutrons: Comparison of Theory and Experiment

Element	$E_0$	$\frac{\text{Theory}}{\text{Exper.}}$	High $l$ neutron strengths (per cent)	$\frac{\text{Theory}}{\text{Exper.}}$ corrected	Mult. by 1.45
Bi	6.6	0.095	63	0.87	
Bi	5.6	0.115	63	1.07	
Pb <sup>208</sup>	5.8	0.160	65	1.03	
Pb <sup>208</sup>	4.8	0.140	65	0.89	
Pb <sup>207</sup>	5.7	0.140	67	0.94	
Pb <sup>207</sup>	4.7	0.22	67	1.46	
Pb <sup>206</sup>	5.2	0.31	63	1.30	
Pb <sup>206</sup>	4.2	0.37	63	1.75	
Tl	6.0	0.35	63	1.43	
Hg	5.2	0.155	70	0.91	1.30
Hg	4.2	0.145	70	0.84	1.21
Au	5.9	0.125	74	0.84	1.21
Au	4.9	0.13	74	0.88	1.27
W	6.1	0.30	50	1.05	1.51
Ta	6.4	0.24	50	0.84	1.21
Ta	5.4	0.24	50	0.84	1.21
Er	5.8	0.39	32	1.00	1.45
Ho	6.3	0.26	32	0.53	0.76
Sm	5.1	0.33	40	0.77	1.11
Pr	5.0	0.24	64	1.17	
La	5.6	0.29	64	1.42	
I	5.2	0.195	67	1.04	1.50
Sn	4.0	0.19	75	1.32	
In	5.4	0.175	80	1.54	



is used, than if a discrete spectrum of residual states is used. Therefore the direct fractions calculated using the continuous spectrum were arbitrarily increased by a factor of 1.45 (which equalizes the two gold calculations). The results are listed in the last column of Table XXXVIII. Notice that now the values for Hg and Au are consistent with those for Tl and Pb<sup>206</sup>, and I is consistent with La and Sn. This consistency is the best justification for the factor 1.45. The average value of the ratio of theory to experiment is now 1.25, with a maximum deviation of only 40 per cent, from this average.

These results indicate that the simple model proposed by Wilkinson is inadequate. Instead one may have to take into account the particle-hole interactions, not only in calculating the resonance energy, but also in calculating the direct particle emission. Furthermore, the rough estimates made above indicate that most of the oscillator strengths residing in transitions with small escape widths must be transferred to the transitions with the larger escape widths. Unfortunately this also casts some doubts on the validity of the calculated shapes for  $S(E_n)$ . The transferred strengths have been arbitrarily distributed among the remaining neutron transitions in proportion to their original strengths. That is, the magnitude of  $S(E_n)$  has been increased but its shape has not been altered. Actually the coupling will be strongest between particle-hole states with the same number of radial nodes, and a minimal change in  $\ell$ -value. Thus the final distribution of strengths will not necessarily be the same as those given by Wilkinson. Therefore, the direct spectrum shapes,  $S(E_n)$ , may change. However the experimental data plotted in Figs. 17 to 20, 30 to 31, 38 to 40, 50 to 53, 66 to 71, 85, 86, 92, 96, and 100 show that  $S(E_n)$  cannot be altered too drastically. A detailed calculation for the case of Pb<sup>208</sup> is now being undertaken by L. Peterson of the MIT Theoretical Physics Group.

Measurements of  $f$  by other experimenters are difficult to compare with the data in this thesis, because they have generally used bremsstrahlung spectra, and have not separated the direct and evaporation components in a similar manner. Usually a neutron spectrum is measured, and evaporation

spectrum of the form  $\frac{dN}{dE_n} \propto E_n \exp[3.35(A - 40)^{1/2} U]^{1/2}$  is subtracted, and the result called the direct spectrum. Another method involves fitting the curve  $\frac{dN}{dE_n} \propto E_n e^{-E_n/T}$  to the data, determining a value of T by the fit at low neutron energies and subtracting this curve from the data. Both cases result in many resonance direct neutrons being included in the evaporation curve, as pointed out by Wilkinson (30). Also these results are taken for widely varying endpoints, which likewise invalidates comparison.

An example of such an experiment is the measurements of Zatsepina et al (71). They used a 19 MeV bremsstrahlung spectrum and nuclear emulsions, with Bi, Au and Ta as the targets. An evaporation spectrum of the form  $\frac{dN}{dE_n} \propto E_n \exp[3.35(A - 40)^{1/2} U]^{1/2}$  was normalized to the low energy data and subtracted. The experimental direct fractions were thus found to be

$$\text{Bi} = 14 \text{ per cent}$$

$$\text{Au} = 11 \text{ per cent}$$

$$\text{Ta} = 17 \text{ per cent}$$

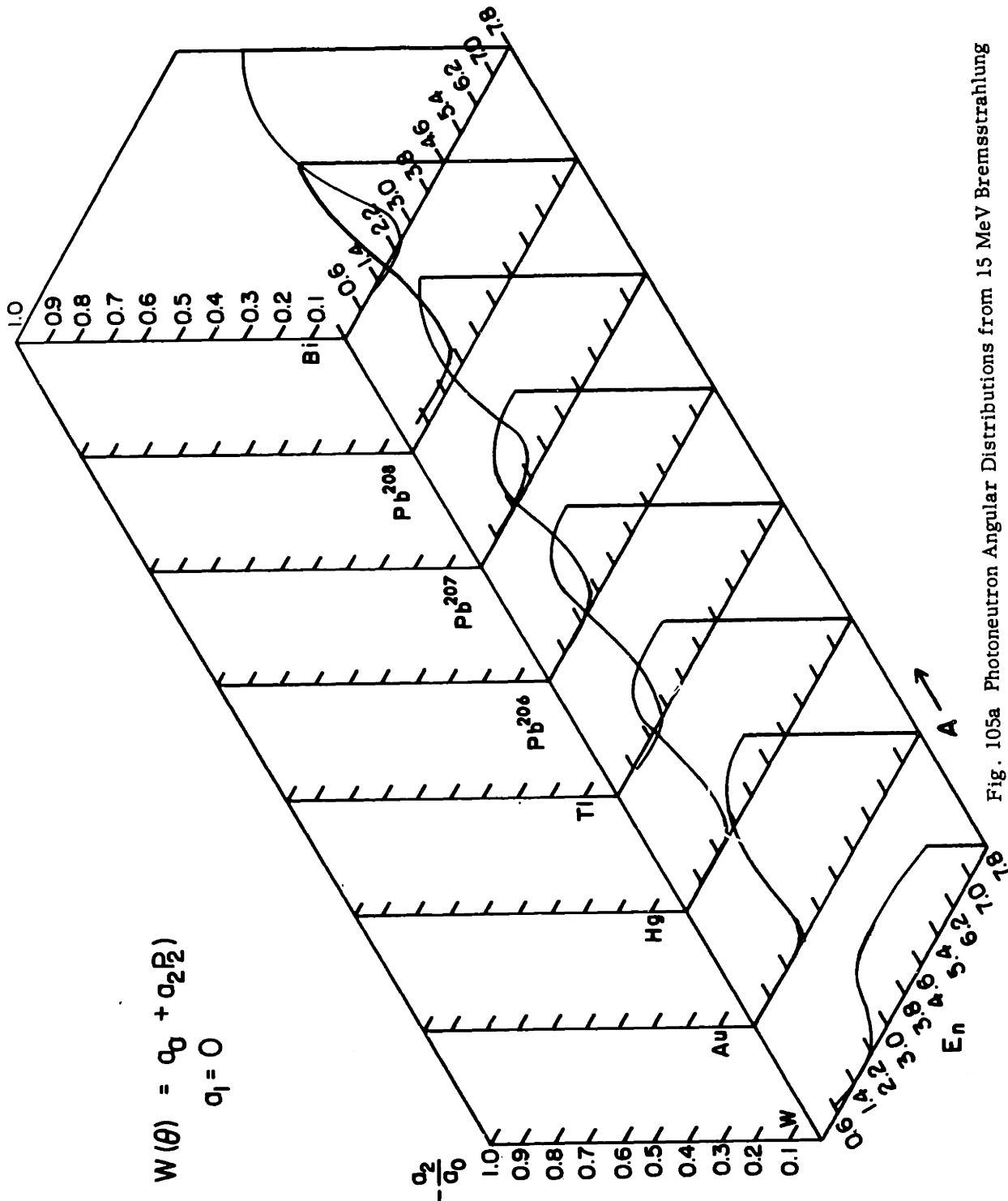
These results agree quite well with the present data. Zatsepina et al also calculated the direct fraction using Wilkinson's model. They found that the shapes agreed reasonably well, and that the theoretical values were 3 to 4 times smaller than the experimental values. However they used the transmission coefficients for a black nucleus listed by Blatt and Weisskopf (43). These transmission coefficients are larger than the values obtained for the more realistic Saxon-Wood potential used in this work. Thus their ratio of theory to experiment could reasonably be reduced, to obtain better agreement with the ratio of 0.1 found in this work.

Kuchnir et al (69) have measured the photoneutron energy spectra from bismuth using monochromatic gamma rays. This experiment is directly comparable to the present one, but unfortunately is still in the process of analysis at this writing. Preliminary results indicate the direct fraction from 14.0 MeV gammas would be comparable to the present data if the same  $S(E_n)$  were used in the analysis.

The angular distribution of the photoneutrons from a 15 MeV bremsstrahlung beam, for each of the 17 targets used, are shown in Figs. 105a and 105b. The curves are solid lines drawn by eye through the experimental points (not shown). Each curve is a plot of  $-a_2/a_0$  vs  $E_n$ , where the angular distribution is given by  $W(\Theta) = a_0 + a_2 P_2(\Theta)$ . The anisotropy at high neutron energies is a maximum for  $\text{Pb}^{208\text{o}}$  ( $-a_2/a_0 \approx 0.7$ ). It is 0.6 to 0.7 for bismuth through thallium, and decreases to 0.5 for mercury, and 0.4 for gold. In the region of the deformed nuclei, the maximum anisotropy at high neutron energies is much smaller, about 0.2 to 0.3. For La and Pr  $-a_2/a_0$  increases to 0.6, then decreases again to 0.3 to 0.4 for I, Sn and In. Notice the strong shell effects with a maximum anisotropy of 0.6 to 0.7 near the doubly magic  $\text{Pb}^{208}$ , and at the neutron closed shell at Pr and La. The nuclei between the closed shells have much smaller anisotropies, about 0.2 to 0.3.

As has been noted in previous sections of this chapter, the angular distribution depends strongly on the interference terms in equations 12 and 13 of Chapter I. However a qualitative explanation of the behavior of the anisotropy with increasing mass number can be obtained with the use of equation 11, Chapter I. \* Referring to the level diagram shown in Table XXII, it can be seen that in In and Sn the  $2d^{5/2}$ ,  $g^{7/2}$  and  $h^{11/2}$  subshells are filling. Considering only  $nl \rightarrow nl+1$  transitions,  $-a_2/a_0 = 0.31$  to 0.4 for these levels. The marked increase in anisotropy at  $N = 82$  is presumably due to the  $3s^{1/2} \rightarrow 3p^{3/2}$  and  $2d^{3/2} \rightarrow 2f^{5/2}$  transitions which have values of  $-a_2/a_0$  of 1.0 and 0.4 respectively. Above  $N = 82$ , the  $2f^{7/2}$ ,  $h^{9/2}$  and  $i^{13/2}$  subshells begin to fill.  $nl \rightarrow nl+1$  transitions from these levels yield  $-a_2/a_0 = 0.30$  to 0.36. For  $nl \rightarrow nl-1$  transitions,  $-a_2/a_0 = 0.14$  to 0.18. The former are suppressed by low transmission coefficients for high angular momentum neutrons, and the latter are suppressed by smaller relative transition strengths. Which transitions are dominant could be decided only by exact numerical calculations. However, the values listed do bracket the experimental values of 0.15 for W and 0.3 for Ho. At gold the  $3p^{3/2}$  subshell is filled, and the  $2f^{5/2}$  subshell is

\*This qualitative agreement was first pointed out by Baker and McNeil (95).



$$W(\theta) = a_0 + a_2 P_2(\cos \theta)$$

$$a_1 = 0$$

Fig. 105a Photon neutron Angular Distributions from 15 MeV Bremsstrahlung Spectra vs Atomic Mass

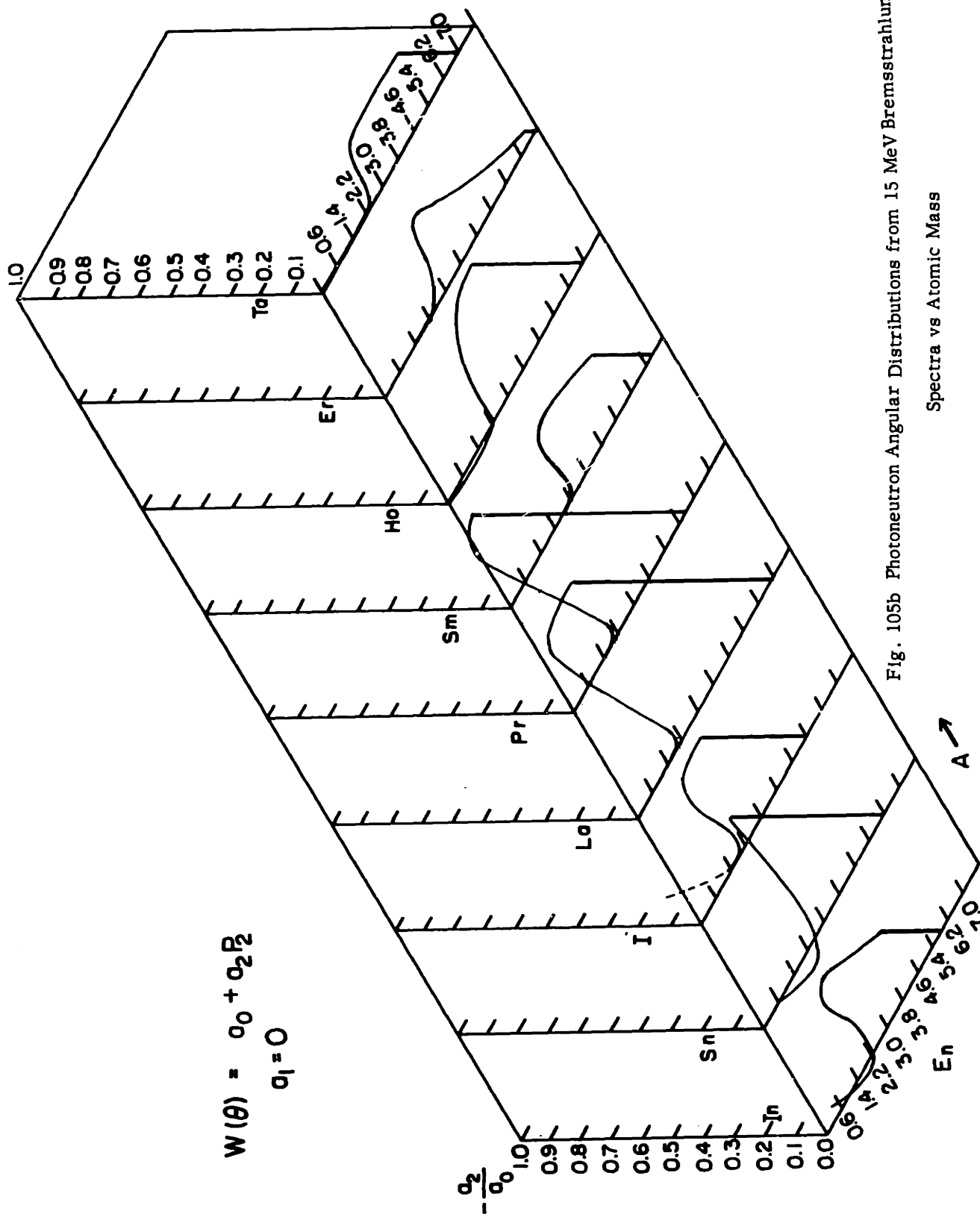


Fig. 105b Photon neutron Angular Distributions from 15 MeV Bremsstrahlung  
Spectra vs Atomic Mass

beginning to be filled in the mercury isotopes. These levels have a  $-a_2/a_0$  of 0.5 and 0.4 for  $n\ell \rightarrow n\ell+1$  transitions. Near the doubly magic  $\text{Pb}^{208}$ , the  $3p^{1/2}$  and  $2f^{5/2}$  subshells have been filled. However equation 11 predicts a maximum  $-a_2/a_0$  of 0.5 for the possible dipole transitions from the  $N = 126$  closed shell. The experimental data reaches a maximum  $-a_2/a_0$  of 0.7. This can be explained only by the interference terms given in equations 12 and 13. Heiss (46) has calculated  $-a_2/a_0$  vs  $E_n$  for Bi and La employing a Saxon-Wood potential, and including the interference terms. His results are listed in Tables XVI and XXIII. Good agreement with the present data is obtained.

The photoneutron spectra measured in this experiment have been separated into two components: the evaporation component and the resonance direct component as explained in Chapter IV section D. The angular distribution of the resonance direct component for all 17 targets is listed in Table XXXIX. These values were calculated by averaging the direct spectrum for each counter over the energy region where the direct spectrum dominates (about 4.0 MeV to the neutron endpoint). The direct spectrum angular distribution is given for both methods of determining the direct spectrum as described in Chapter IV. (The level density of the residual nucleus was assumed to be  $\omega(U) \propto (U+t)^{-3/2} e^{2\sqrt{aU}}$ .  $-a_2/a_0$  is not sensitive to the level density formula used.) The values of  $-a_2/a_0$  for the first method of determining the direct spectrum (calculating the shape of  $S(E_n)$ ) are plotted in Fig. 106. The graph shows  $-a_2/a_0$  vs  $A$ , the atomic mass. The other data shown in the figure are measurements of  $-a_2/a_0$  made with threshold detectors (25, 95, 89). The threshold detector results are generally smaller than the present results. This is probably due to the fact that the isotropic component has not been removed from the threshold detector data. Also the bremsstrahlung endpoints used are higher, which means that the high  $\ell$  transitions, which have lower values of  $-a_2/a_0$ , will have much larger transmission coefficients. While there has been a considerable amount of work carried out in this field, the results of different workers are not in agreement. This disagreement may be attributed largely to an ill-defined detector threshold, varia-

Table XXXIX

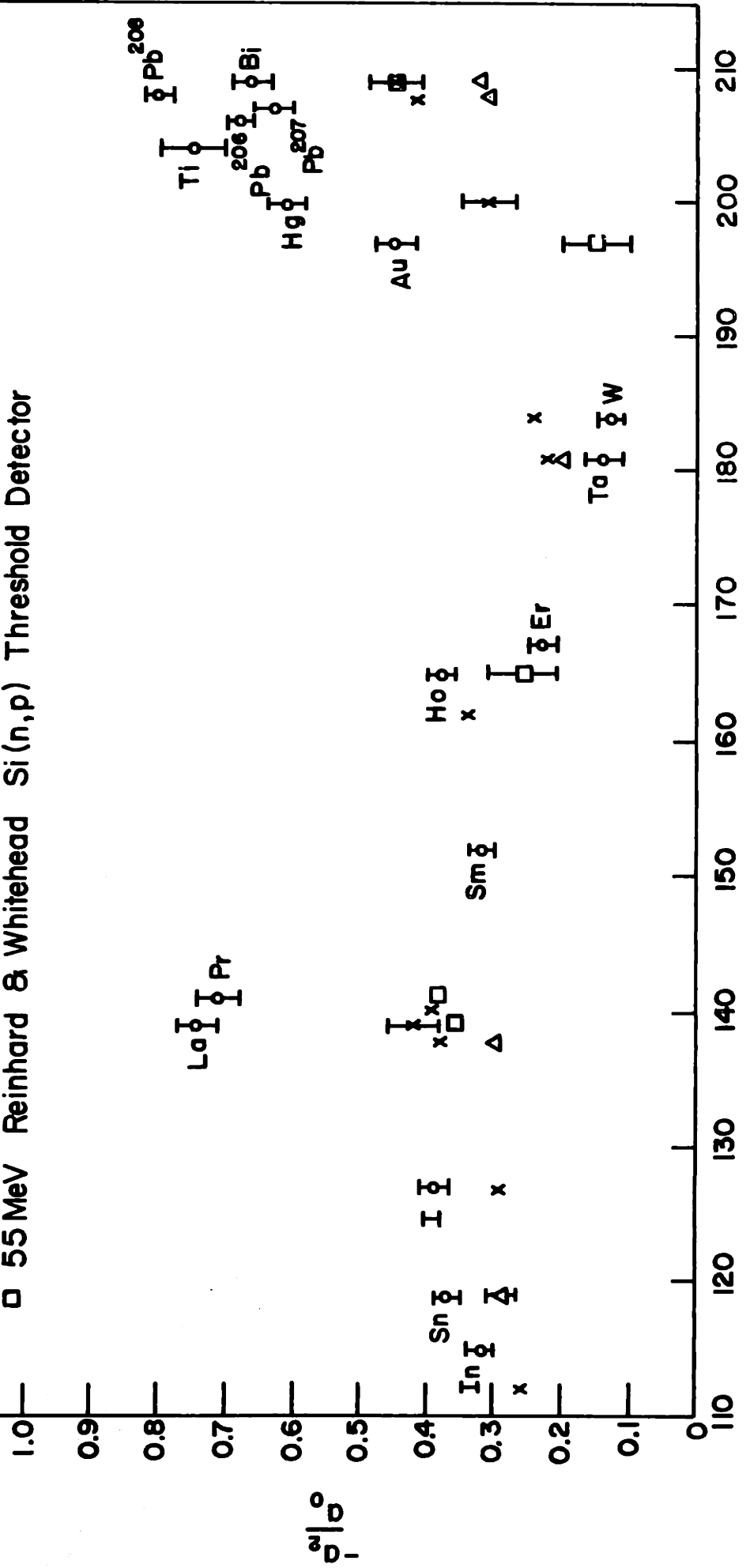
## Angular Distribution of Direct Component

Element	$E_0$	Method I		Method II	
		$-a_2/a_0$	$\Delta a_2/a_0$	$-a_2/a_0$	$\Delta a_2/a_0$
Bi	6.6	0.65	0.03	0.67	0.03
Bi	5.6	0.64	0.02	0.67	0.03
Pb <sup>208</sup>	5.8	0.73	0.02	0.74	0.03
Pb <sup>208</sup>	4.8	0.62	0.02	0.57	0.02
Pb <sup>207</sup>	5.7	0.61	0.03	0.63	0.05
Pb <sup>207</sup>	4.7	0.72	0.02	0.70	0.05
Pb <sup>206</sup>	5.2	0.64	0.02	0.59	0.02
Pb <sup>206</sup>	4.2	0.67	0.02	0.63	0.05
Tl	6.0	0.73	0.05	0.69	0.07
Hg	5.2	0.61	0.03	0.63	0.03
Hg	4.2	0.58	0.02	0.57	0.02
Au	5.9	0.45	0.03	0.44	0.03
Au	4.9	0.38	0.03	0.37	0.03
W	6.1	0.13	0.02	0.12	0.02
Ta	6.4	0.14	0.03	0.14	0.03
Ta	5.4	0.16	0.02	0.15	0.02
Er	5.8	0.22	0.02	0.22	0.02
Ho	6.3	0.38	0.02	0.38	0.02
Sm	5.1	0.32	0.02	0.33	0.03
Pr	5.0	0.66	0.03	0.72	0.06
La	5.6	0.69	0.03	0.67	0.02
I	5.2	0.39	0.02	0.41	0.03
Sn	4.0	0.39	0.02	0.39	0.02
In	5.4	0.32	0.02	0.35	0.03

# ANGULAR DISTRIBUTION OF FAST NEUTRONS

$$W(\theta) = a_0 (p_0 + a_1 p_1 + a_2 p_2)$$

- o 15 MeV MIT  $a_1 = 0$  "Direct" Component
- x 22 MeV Baker & McNeil Si(n,p) Threshold Detector
- Δ 34 MeV Allum, Quirk & Spicer Al(n,α) Threshold Detector
- 55 MeV Reinhard & Whitehead Si(n,p) Threshold Detector



A Atomic Mass

Fig. 106



tions in spectral sensitivity of the various detectors used, and variation in bremsstrahlung endpoint. Many of these results are listed in Table XL. For each entry, the method used in detection of the direct (fast) photoneutrons, the maximum photon energy of the bremsstrahlung spectrum, an estimate of the detector threshold, and the formula used to analyze the data are listed. The angular distributions have been recalculated, and are listed in terms of the formula  $W(\Theta) = a_0 + a_1 P_1(\cos \Theta) + a_2 P_2(\cos \Theta)$ .

#### L. Summary

The photoneutron energy spectra for 17 targets, Bi, Pb<sup>208</sup>, Pb<sup>207</sup>, Pb<sup>206</sup>, Tl, Hg, Au, W, Ta, Er, Ho, Sm, Pr, La, I, Sn, and In, were measured at 156°, 76°, and 24° to the photon beam using bremsstrahlung endpoints of 15, 14, and, in some cases, 13 MeV. Subtracting the 14 MeV (or 13 MeV) data (properly normalized) from the 15 MeV (or 14 MeV) data yielded neutron spectra generated by an equivalent photon spectrum peaked at 14 MeV (or 13.2 MeV) with a FWHM of 2 MeV.

The angular distributions of these spectra were assumed to have the form  $W(\Theta) = a_0 + a_1 P_1(\cos \Theta) + a_2 P_2(\cos \Theta)$ . The ratio of photoneutron spectra at 24° to those at 156°, which determines  $a_1$ , is listed in Table X for each target. (The data are from 15 MeV bremsstrahlung spectra, not photon difference spectra.) The data was summed from 1.0 to 3.0 MeV, and from 3.0 MeV to the neutron endpoint, because of the poor statistics. The ratio for the low energy bin was 0.93 to 1.05 with an average statistical error of 0.02, and 0.92 to 1.14 with an average statistical error of 0.08 for the high energy bin. The possible systematic uncertainties in this ratio were investigated and it was found that the ratio could be corrected to unity for the low energy bin by small changes in the counter thresholds (about 6 per cent), small changes in the calculated correction for counting losses due to coincidences (about 7 per cent) and larger changes in the background (about 20 per cent). In general the ratio in the high energy bin was  $1.0 \pm 0.08$  after the low energy bin had been corrected to unity. It was concluded that the unknown systematic errors in this ratio were larger than the statistical uncertainties.

Table XL

## Angular Distributions of Fast Photoneutrons

$$W(\Theta) = 1 + a_1 P_1 + a_2 P_2$$

Element	$E_0$	$-a_2$	$a_1$	formula	$E_n$ (min)	Detector	Reference
Bi	22	0.40±0.04	0.14±0.09	1	3.5	Al(n, p)	Price (96) 1954
	30	0.31±0.05	0.05±0.02	5	3.5	Al(n, p)	Ferrero (87) 1956
	30	0.38±0.05	0.12	5	5.5	Si(n, p)	"
	19	0.57	0.04±0.07	1	4	Emulsion	Zatsepina (72) 1957
	19	0.61±0.12	0.0±0.06	1	7	"	"
	22	0.35±0.1	0.06±0.06	3	3	Al(n, p)	Baker (95) 1961
	22	0.45±0.04	0.05±0.03	3	5.5	Si(n, p)	"
	55	0.37±0.05	0.18±0.04	3	5.5	Si(n, p)	Reinhardt(89) 1961
	55	0.45±0.09	0.11±0.15	4	5.5	"	"
	85	0.62±0.02	0.03±0.09	2	4.0	Emulsion	Anashkina (88) 1964
	22	0.36±0.05	0.10±0.04	5	3.0	Emulsion	Wataghin (97) 1961
	22	0.38±0.13	---	5	6.0	"	"
	31	0.32±0.05	0.0±0.08	1	4.0	Emulsion	Emma (74) 1960
	22	0.42±0.07	0.0±0.06	1	5.5	Si(n, p)	Tagliabue (98) 1961
	17.5	0.48±0.07	-0.01±0.03	3	4.5	Stilbene	Allum (99) 1964
	19	0.48±0.07		1	5.5	Emulsion	Zatsepina (71) 1963
	14	0.47±0.05		1	3.5	"	"
	34	0.33±0.02	0.20±0.03	3	6.0	Al(n, $\alpha$ )	Allum (25) 1964
	Pb	22	0.07		1		ZnS
65		0.40	0.0±0.03	1	5	ZnS	Johansson (101) 1955
70		0.05±0.05		1		ZnS	Dixon (89) 1955
17		0.17±0.06	0.0±0.02	1		ZnS	Asada(102) 1958
22		0.36±0.04	0.02±0.02	1	3	Al(n, p)	Price (96) 1954
23		0.13		1	4	Emulsion	Toms (73) 1957
22		0.51±0.07	-0.004±0.05	3	3	Al(n, p)	Baker (95) 1960
22		0.42±0.03	0.02±0.02	3	5.5	Si(n, p)	"
22		0.40±0.20	0.0±0.06	1	5.5	Si(n, p)	Tagliabue (98) 1961
34		0.30±0.02	0.22±0.03	3	6	Al(n, $\alpha$ )	Allum (25) 1964
17.5		0.30±0.04	0.03±0.03	3	4.5	Stilbene	Allum (99) 1964
Hg	22	0.31±0.04	0.04±0.03	3	5.5	Si(n, p)	Baker (95) 1961
Au	22	0.30±0.12		1	5.5	Si(n, p)	Tagliabue (98) 1961
	55	0.15±0.05	0.15±0.04	3	5.5	Si(n, p)	Reinhardt (103) 1962
W	22	0.24±0.04	-0.07±0.03	3	5.5	Si(n, p)	Baker (95) 1960

- formula: 1)  $A + B \sin^2 \Theta$   
 2)  $1 + a_1 P_1 \cos \Theta + a_2 P_2 \cos^2 \Theta$   
 3)  $1 + a_1 P_1 + a_2 P_2$   
 4)  $1 + a_1 P_1 + a_2 P_2 + a_3 P_3$   
 5)  $a + b \sin^2 \Theta + c \cos \Theta$

Table XL (Cont'd)

Element	$E_0$	$-a_2$	$a_1$	formula	$E_n$ (min)	Detector	Reference
Ta	22	$0.22 \pm 0.04$	$0.04 \pm 0.03$	3	5.5	Si(n, p)	Baker (95) 1961
	22	$0.19 \pm 0.14$	$0.14 \pm 0.14$	3	3.5	Al(n, p)	"
	34	$0.20 \pm 0.02$	$0.13 \pm 0.02$	2	6.0	Al(n, $\alpha$ )	Allum (25) 1964
	65	0.37	---		5	ZnS	Johansson (101) 1955
Ho	55	$0.26 \pm 0.05$	$0.14 \pm 0.04$	3	5.5	Si(n, p)	Reinhardt (103) 1962
Pr	22	$0.19 \pm 0.07$	---	1	5.5	Si(n, p)	Tagliabue (98) 1961
	55	$0.32 \pm 0.07$	$0.20 \pm 0.05$	3	5.5	Si(n, p)	Reinhardt (103) 1962
	55	$0.39 \pm 0.12$	$0.13 \pm 0.20$	4	5.5	"	"
La	22	$0.31 \pm 0.24$	---	1	5.5	Si(n, p)	Tagliabue (98) 1961
	22	$0.42 \pm 0.04$	$0.02 \pm 0.03$	3	5.5	Si(n, p)	Baker (95) 1961
	22	$0.43 \pm 0.10$	$0.05 \pm 0.07$	3	3.5	Al(n, p)	"
	55	$0.30 \pm 0.04$	$0.16 \pm 0.03$	3	5.5	Si(n, p)	Reinhardt (103) 1962
	55	$0.37 \pm 0.09$	$0.09 \pm 0.13$	4	5.5	"	"
I	22	$0.04 \pm 0.06$	---	1	5.5	Si(n, p)	Tagliabue (98) 1961
	22	$0.29 \pm 0.05$	$0.04 \pm 0.04$	3	5.5	Si(n, p)	Baker (95) 1961
Sn	70	$0.07 \pm 0.11$	---	1		ZnS	Dixon (89) 1955
	34	$0.34 \pm 0.02$	$0.14 \pm 0.01$	2	6.0	Al(n, $\alpha$ )	Allum (25) 1964
In	28	0.31	---	1	1.0	Emulsion	Anashkina (104) 1962

- formula: 1)  $A + B \sin^2 \Theta$   
 2)  $1 + a_1 \cos \Theta + a_2 \cos^2 \Theta$   
 3)  $1 + a_1 P_1 + a_2 P_2$   
 4)  $1 + a_1 P_1 + a_2 P_2 + a_3 P_3$   
 5)  $a + b \sin^2 \Theta + c \cos \Theta$

Therefore, relying on the dominance of the dipole interaction, and previous measurements of the fore-aft symmetry of low energy ( $\approx 10$  MeV) photoneutrons from medium and heavy targets,  $a_1$  was assumed to be zero and the angular distributions were taken to be of the form  $W(\Theta) = a_0 + a_2 P_2(\cos \Theta)$ . The angular distributions of the photoneutrons from 15, 14, and 13 MeV endpoint bremsstrahlung spectra are displayed graphically in sections A through H. The three sets of data coincide for each element, therefore the angular distribution of the photoneutron difference spectra are similar to that of the 15 MeV bremsstrahlung data.

The angular distribution of the photoneutrons is isotropic at low neutron energies. As the direct spectrum becomes equal in value to the evaporation component, the anisotropy is equal to one-half its maximum value. This continues up to the neutron endpoint in the case of Bi,  $Pb^{208}$ ,  $Pb^{207}$ , La, and Pr. In other elements the anisotropy reaches a maximum value, and then remains constant up to the neutron endpoint. (Some appear to decrease above this point, but the statistical accuracy of these particular runs -- Sm, In, and Er -- is not sufficient to determine the exact shape of the angular distribution curve up to the maximum neutron energy.) The maximum anisotropy shows marked shell effects. It is a maximum (about  $-a_2/a_0 \approx 0.7$ ) near the doubly closed shell at  $Pb^{208}$  and the closed neutron shell at Pr and La. It has minima (0.15 to 0.3) between these two closed shells in the region of deformed nuclei, and below the closed neutron shell of La and Pr. The qualitative behavior of the anisotropy can be explained by considering the subshells contributing to the direct emission. A more detailed estimate requires a knowledge of the phases of the various partial waves which can interfere with one another. In the two cases (Bi and La) where such a calculation has been performed, there is excellent agreement with the experiment.

The neutron difference spectra are characterized by an isotropic evaporation component which dominates at low neutron energies, and an anisotropic resonance direct component which dominates at high neutron energies. The transition from one component to the other is quite abrupt, typically taking place

in about 1 MeV. The photoneutron spectra were separated into these two components using two distinct methods. In the first method the shape of the resonance direct energy spectrum was calculated using a simplified model of the giant resonance described in Chapter IV, section E. In the second method, it was assumed that the evaporation component was isotropic and that the resonance direct component had an anisotropy, independent of neutron energy, given by the high energy limit of the angular distribution of the difference spectrum. Comparing the calculated direct spectra with the data, the first method yields the best results using discrete hole states in the residual nucleus, when these levels are known. This is the case for the isotopes near  $\text{Pb}^{208}$  which is doubly magic (such as  $\text{Bi}$ ,  $\text{Pb}^{207}$ ,  $\text{Pb}^{206}$  and  $\text{Tl}$ ), and near  $\text{La}$  and  $\text{Pr}$ , which are magic in neutrons. This method also yields good results using a continuous spectrum of hole states in the residual nucleus, when both the proton and neutron shells are partly filled. This is the case for  $\text{Hg}$ ,  $\text{Au}$  and  $\text{I}$ . The direct spectrum for deformed nuclei,  $\text{W}$ ,  $\text{Ta}$ ,  $\text{Er}$ ,  $\text{Ho}$ , and  $\text{Sm}$ , was calculated using the assumption of a continuous distribution of hole states. However this approximation fails to reproduce the observed effects of the double giant resonance caused by the nuclear deformation. In order to predict the resonance direct spectrum from deformed nuclei, the relative transition strengths calculated for a deformed well and a better approximation to the distribution of hole states in the residual nucleus are required. Neither method gives good results for tin and indium because the proton shell is magic, which invalidates the assumption of a continuous spectrum of hole states in the residual nuclei, while only a few of the discrete levels are known, and these are complicated configurations of single particle states. However calculations made using the few known levels indicate that if the configurations of many more levels were known, the assumption of discrete levels would probably work quite well.

The second method of calculating the direct spectrum yields results that generally agree with those obtained from the first method in the case of  $\text{Bi}$ ,  $\text{Pb}^{208}$ ,  $\text{Pb}^{207}$ ,  $\text{Tl}$ ,  $\text{Hg}$ ,  $\text{Au}$ ,  $\text{La}$ ,  $\text{Pr}$ ,  $\text{I}$ ,  $\text{Sn}$ , and  $\text{In}$ . The anisotropy in the deformed region is generally too small to allow this second method to be

applied successfully. The direct spectrum of  $\text{Pb}^{206}$  differs considerably for the two methods. The direct spectra derived for both methods are displayed graphically in sections A through H.

The fraction,  $f$ , of directly emitted neutrons was defined as the integral of the direct component from 3.0 MeV to the neutron endpoint divided by the integral of the total photoneutron spectrum. The integral of the direct spectrum was started at 3.0 MeV instead of zero MeV because of the great uncertainty in the value of the experimental direct spectrum in the region where the evaporation component is dominant. Therefore  $f$  is a lower limit on the fraction of directly emitted neutrons. The contribution to  $f$  of directly emitted neutrons with energies less than 3.0 MeV was estimated to be less than 10 per cent, using the theoretical direct spectrum,  $S(E_n)$ . The experimental values of  $f$ , listed in Table XXXVI, were about 14 per cent and approximately constant with  $A$ , the mass number. The theoretical estimates of  $f$ , given in Table XXXVII, were generally  $\frac{1}{3}$  to  $\frac{1}{10}$  of the experimental values. This indicates that the simple Wilkinson model of the giant resonance is not adequate to describe the directly emitted neutrons. The effect of particle-hole interaction was crudely estimated in section J. The results are given in Table XXXVIII. It was found that if all of the oscillator strength absorbed by the proton particle-hole pairs, and the oscillator strength absorbed by the neutron particle-hole pairs leading to the emission of neutrons with large  $\ell$  values ( $\ell = 6$  or 7 for elements near  $\text{Pb}^{208}$  and  $\ell = 5$  or 6 for elements near Pr) were transferred to the remaining neutron particle-hole states, the ratio of theory to experiment increased to  $1.25 \pm 0.5$ . Thus it seems that a calculation including particle-hole interactions may be adequate to explain the direct fraction. Such calculations have already correctly predicted the giant resonance energy (34, 35, 36, 37, and 65).

The evaporation component is found in the first method by subtracting the direct spectrum (normalized to the number of neutrons above 4.0 MeV) from the photoneutron difference spectrum. In the second method, the evaporation component is the isotropic portion of the photoneutron difference spectrum. The resulting experimental evaporation spectra were fit with the theoretical curves

$$\frac{dN}{dE_n} \frac{1}{E_n \sigma_C} = \text{const} \frac{e^{2\sqrt{a_m U}}}{(U+T)^m} \quad (112)$$

where  $m = \frac{3}{2}$  and 2, and

$$\frac{dN}{dE_n} \frac{1}{E_n \sigma_C} = \text{const} e^{-E_n/T} \quad (113)$$

using a least squares fit with  $a_m$  or  $T$  as the variable. The  $\sigma_C$ 's are approximated by optical model calculations of the ground state reaction cross section (61, 62). The experimental evaporation spectra and the theoretical curves fitted to the data are shown graphically in sections A through H.

After taking into account the possibility of neutrons from the  $(\gamma, 2n)$  process and the effect of the negative tail in the photon difference spectrum, all three formulas listed above were excellent fits to the data from 1.0 to 3 or 4 MeV. There are two exceptions to this statement: Ho and Sn. In the case of Sn, the direct spectrum was apparently badly underestimated below 4.0 MeV neutron energy. If the data is fit over 1.0 to 2.0 MeV, instead of 1.0 to 3.0 MeV as is usually the case, better agreement and a more reasonable value of the level density parameter is achieved. In the case of Ho, a drastic change in the shape of  $\sigma_C$  as a function of neutron energy would be required to achieve good agreement between the experimental evaporation spectrum and the theoretical curve. The values of  $\sigma_C$  for Ho increase sharply with decreasing neutron energy. If  $\sigma_C$  were a constant with neutron energy, or even decreased with decreasing neutron energy, a better agreement between theory and experiment would result. Since the optical model calculations were performed for a spherically symmetric well, it is not surprising that the results do not agree with experiment for a given deformed nucleus. The excellent agreement between theory and experiment for the rest of the data was due, to a large extent, to the energy variation of the  $\sigma_C$ 's from the optical model calculation. This is especially striking in the case of Bi and  $\text{Pb}^{208}$ , where the  $\sigma_C$  energy variation cancelled out a broad peak in the neutron energy spectra at 2.0 MeV.

The values of the level density parameters,  $a_2$  and  $a_{3/2}$ , and the nuclear temperature,  $T$ , are listed in Table XXIX, where the data is uncorrected for a direct component; in Table XXX, where the data is corrected for the direct component by Method I; and in Table XXXI, where the data is corrected for the direct component by Method II. The values of the level density coefficients obtained generally agreed with those obtained from  $(n, n')$  work, after corrections are made for the differences in level density formula used. The experimental values of  $a_2$  generally follow the predictions of Newton (91) and Lang (83), who find that  $a_2 = K(\bar{j}_z + \bar{j}_p + 1)A^{2/3}$ , based on shell model calculations.  $K = 0.067$  for the present data. This agreement is enhanced by the use of the pairing energy correction to the excitation energy which takes into account the binding energy difference between a paired and an unpaired nucleon. The multi-isotopic targets in general yield lower values of  $a_2$  than nearby monoisotopic targets. This would appear to indicate that the attempts to average out the effects of differing thresholds was not totally successful.

The sum of the resonance direct spectrum and the evaporation spectrum represents the theoretical fit to experimental photoneutron difference spectrum. Thus the data has been fit with the use of only two adjustable parameters,  $a_m$  (or  $T$ ), the level density parameter, and a normalizing constant for the direct spectrum. These two components were sufficient to explain the data in the case of nuclei near a closed neutron shell. In the case of elements with partially filled shells, the agreement between theory and experiment was poor at high energies where the directly emitted neutrons dominate, because of the difficulties encountered in calculating the direct spectrum. In some cases (specifically Au and I, where the residual nucleus is odd-odd) excellent agreement was obtained by approximating the distribution of hole states in the residual nucleus by a continuum. The results from tin suggest that if the position and configuration of the levels in the residual nucleus were known, the neutron spectrum shape could be predicted by the simple model used in the case of the closed shell nuclei, but not the magnitude.



This model breaks down in the case of the deformed nuclei which have structure in the giant resonance. This structure is the well-known splitting of the giant resonance into a double peak, one below 13 MeV and the other at 15 to 16 MeV. This gross structure was observable with the 2 MeV wide photon spectrum employed in this experiment. The monoisotopic deformed nuclei, Ta and Ho, exhibit a peak in their respective photoneutron spectra which apparently corresponds to the 12 MeV photon absorption peak in the giant resonance. The 16 MeV peak is at too high an energy to be seen in these experiments. Any fine structure that may exist in the giant resonance of closed shell nuclei could not be observed since the giant resonance has a width of less than 4.0 MeV near closed shell. If this type of experiment were performed using many closely spaced endpoints, about 0.5 MeV apart, such structure might be observable.

Appendix I  
Scattering Calculations

In order to perform the experiment to the desired statistical accuracy in a reasonable time, a considerable amount of ( $\gamma, n$ ) target material was used. The targets contained about 1 mole and were 1 to 2 cm thick. In the heavy elements this thickness corresponds to about  $\frac{1}{4}$  to  $\frac{1}{3}$  of a mean free path for 1 to 5 MeV neutrons. Therefore it is expected that neutron scattering in the target will have an appreciable effect on the measured angular distribution and energy spectra. The angular distribution will be particularly affected, since the targets were placed so that the neutron path length in the target material was not the same for the  $76^\circ$  counter as for the detectors at  $156^\circ$  and  $24^\circ$  (see Fig. 2). Neutron scattering in targets having cylindrical symmetry with respect to the three counters had very little effect on the angular distribution.

A Monte Carlo calculation would have required a prohibitive amount of computer time, therefore the following simplified procedure\* was used. The ( $\gamma, n$ ) target was divided into several (25 to 100) cells of equal volume and roughly cubical shape. Each cell was assigned a set of coordinates corresponding to its center, and a mass corresponding to its volume. The number of neutrons produced in cell  $i$  going in the direction  $\Theta_R$  is given by

$$\frac{dN_i(E_\gamma, \Theta_R)}{d\Omega} = n_P \sigma_P(E_\gamma, E_n, \Theta_R) e^{-\rho_0(E_\gamma)x_{oi}} e^{-\delta(x_i^2 + y_i^2)} \quad (113)$$

where  $n_P$  = number of atoms in mass  $m$

$\sigma_P(E_\gamma, E_n, \Theta_R)$  = differential ( $\gamma, n$ ) cross section. Since the ( $\gamma, n$ ) cross section as a function of  $E_\gamma$ ,  $E_n$  and  $\Theta_R$  is not known, the measured photoneutron spectra were used to estimate  $\sigma_P$ . These spectra include the effects of the photon spectra.

$e^{-\rho_0(E_\gamma)x_{oi}}$  = gamma ray attenuation in the target from the face of the target to cell  $i$ . The gamma attenuation coefficients are taken from the NBS tabulation (105).  $x_{oi}$  is the distance

\*Developed by Dr. Stanley Kowalski of this laboratory.

from the face of the target to the  $i^{\text{th}}$  cell along the z-direction.\*

$e^{-\delta(x_i^2 + y_i^2)}$  = a factor to take into account the forward peaking of the beam.  $\delta \approx 0.032 \text{ cm}^{-2}$  for this apparatus with an endpoint of 15 MeV.  $x_i$  and  $y_i$  are the coordinates of the  $i^{\text{th}}$  cell.

The neutron flux at the counter due to production alone is given by

$$\frac{dN(\Theta)}{d\Omega} = \sum_i \frac{dN_i(\Theta)}{d\Omega} e^{-\rho_n x_{fi}} \quad (114)$$

where  $\rho_n$  = the neutron attenuation coefficient in the target material  
 $x_{fi}$  = the distance from cell  $i$  to the face of the target nearest the detector

The neutron attenuation coefficient was calculated from the total cross section for neutron scattering tables from ref 53. However since the scattering calculation uses a limited number of points it does not treat the small angle scattering correctly. Therefore the total cross section was reduced by subtracting the forward scattering peak. The differential elastic cross section (106) at large angles was fitted with a fourth order polynomial in  $\cos \Theta$ , as follows:

$$\frac{d\sigma}{d\Omega} = \sum_{i=0}^4 a_i (\cos \Theta)^i \quad (115)$$

In general this did not account for the large peak at small angles. The integral of this small angle peak was subtracted from the total cross section.

This procedure assumes that the number of neutrons scattered out of the solid angle subtended by the counter at small angles is approximately equal to the number scattered into this solid angle. For example, if the small angle peak is approximated by

$$\frac{d\sigma}{d\Omega} = C, \quad 0 \leq \Theta \leq \Theta_{\text{max}} \quad (116a)$$

$$\frac{d\sigma}{d\Omega} = 0, \quad \Theta_{\text{max}} \leq \Theta \quad (116b)$$

then the scattering out along a path length  $R$  is given by

$$\text{Outscatt} = N_o (1 - e^{-\sigma_T R}) \approx N_o \sigma_T R \quad (117)$$

\*The z-axis is along the beam axis; as usual, x and y are perpendicular to it.

where  $N_0$  = the flux of neutrons per steradian per second towards the counter and  $\sigma_T$  = the integrated small angle cross section

$$\sigma_T = 2\pi C(1 - \cos \Theta_{\max}) \quad (118)$$

The amount scattered in is given by

$$\text{Inscatt} = \int N \frac{d\sigma(\Theta)}{d\Omega} d\Omega dr \quad (119)$$

In this equation  $N$  is the flux of neutrons across a small volume  $dV$  at distance  $r$  and angle  $\Theta$  from the neutron production point at the origin.  $d\Omega$  is the solid angle subtended by  $dV$ , and  $dr$  is its thickness.

$$d\Omega = \frac{dA}{r^2} = \frac{r^2 \sin \Theta d\Theta d\phi}{r^2} \quad (120)$$

$$N = N_0 e^{-\sigma_T r} = N_0 (1 - \sigma_T r) \approx N_0 \quad (121)$$

where the neutron flux is assumed to be isotropic. Then

$$\text{Inscatt} = N \frac{d\sigma(\Theta)}{d\Omega} \sin \Theta d\Theta d\phi dr \quad (122a)$$

$$= 2\pi NC \int_0^{\Theta_{\max}} \int_0^{R/\cos \Theta} \sin \Theta d\Theta dr \quad (122b)$$

$$= 2\pi NCR \ln \frac{1}{\cos \Theta_{\max}} \quad (122c)$$

Therefore

$$\frac{\text{Inscatt}}{\text{Outscatt}} = \frac{\ln \frac{1}{\cos \Theta_{\max}}}{1 - \cos \Theta_{\max}} \quad (123)$$

$$\ln x = \frac{x-1}{x} + \frac{1}{2} \left( \frac{x-1}{x} \right)^2 + \frac{1}{3} \left( \frac{x-1}{x} \right)^3 + \dots \quad (124)$$

$$1 - \cos \Theta_{\max} \approx \frac{\Theta_{\max}^2}{2!} - \frac{\Theta_{\max}^4}{4!} + \dots \quad (125)$$

$$\ln \frac{1}{\cos \Theta_{\max}} = \frac{1}{1 - \Theta_{\max}^2/2} \left[ \frac{\Theta_{\max}^2}{2} - \frac{\Theta_{\max}^4/8}{1 - \Theta_{\max}^2/2} + \dots \right] \approx \frac{\Theta_{\max}^2/2}{1 - \Theta_{\max}^2/2} \quad (126)$$

Therefore

$$\frac{\text{Inscatt}}{\text{Outscatt}} \approx \frac{1}{1 - \Theta_{\max}^2/2} \approx 1.03, \quad \Theta_{\max} = \frac{\pi}{12} \quad (127)$$

Thus if the forward peak is confined to small angles ( $10^\circ$  to  $20^\circ$ ) the amount of attenuation provided by it is negligible, and may be neglected. This is the case for the heavy elements.

Finally the scattering from the  $j^{\text{th}}$  cell is given by

$$\frac{dN_{ij}^S}{d\Omega} = \frac{dN_i(\Theta_P)}{d\Omega} \frac{e^{-\rho_n x_{ij}}}{x_{ij}^2} \sigma^S(\psi, E_n) n_s \quad (128)$$

where  $\frac{dN_i(\Theta_P)}{d\Omega}$  = the neutron flux in the direction  $\Theta_P$  of the  $j^{\text{th}}$  cell, produced in the  $i^{\text{th}}$  cell

$x_{ij}$  = the distance between the  $i^{\text{th}}$  and  $j^{\text{th}}$  cells

$\sigma^S(\psi, E_n)$  = the differential elastic scattering cross section

$n_s$  = the number of atoms in the  $j^{\text{th}}$  cell

The exponential gives the neutron attenuation from the  $i^{\text{th}}$  to the  $j^{\text{th}}$  cell, the factor  $x_{ij}^2$  gives the solid angle subtended by the  $j^{\text{th}}$  cell and  $\psi$  is the angle between the line from the  $i^{\text{th}}$  to  $j^{\text{th}}$  cell and the line from the  $j^{\text{th}}$  cell to the counter. The material from which the neutrons scatter may be the same or different from that which produces the neutrons. This takes into account targets made up of compounds ( $\text{Ho}_2\text{O}_3$  for example).

The scattered neutron flux is given by

$$\frac{dN^S}{d\Omega} = \sum_i \sum_{\substack{j \\ i \neq j}} \frac{dN_{ij}^S}{d\Omega} e^{-\rho_n x_{fl}} \quad (129)$$

where  $x_{fl}$  = the distance from the  $j^{\text{th}}$  cell to the face of the target nearest the detector

In addition an effort was made to estimate the inelastically-scattered neutrons. The neutron flux incident on the  $j^{\text{th}}$  cell was assumed to scatter inelastically with an energy distribution given by

$$\frac{dN_{\text{inel}}}{dE_n} \propto E_n e^{-E_n/T} \quad (130)$$

and with an isotropic angular distribution. The nuclear temperatures were taken from ref 84. The number of inelastically-scattered neutrons is given by

$$\frac{dN_{inel}(E_{no})}{d\Omega} = \sum_i \sum_{\substack{j \\ i \neq j}} \frac{dN_i(E_{no})}{d\Omega} n_s \frac{e^{-\rho_n(E_{no})x_{ij}}}{x_{ij}^2} \frac{\sigma_{inel}(E_{no})}{4\pi} \frac{E_{no}}{\sum_{E_n=0}^{E_{no}} \frac{E_n e^{-E_n/T}}{\int_0^{E_{no}} E_n e^{-E_n/T} dE_n}} e^{-\rho_n(E_n)x_{fl}} \quad (131)$$

where  $\sigma_{inel}(E_{no})$  = the total inelastic cross section from ref 107  
 when  $E_{no}$  = the energy of the produced neutron  
 and all other quantities have been defined above. The assumption is made that there is no recoil energy loss in the elastic scattering.

The next step in the calculation is to determine the total scattering (elastic and inelastic) within a given cell. To do this, a selected cell was divided into 125 subcells, and the scattering calculation was repeated with production and scattering taking place only within the selected cell. That is, this subdivided cell plays the role of the entire target in the above calculation. In addition, the gamma and neutron attenuation in the material outside the selected cell was included. The scattered neutrons were multiplied by the number of cells and added to the previous result. In general this second approximation accounted for about one-third of the total scattering.

The self scattering of each subcell could be calculated for a third step in the approximation. But, since each masspoint subtends a solid angle proportional to  $r_{ij}^2$  and contains a mass proportional to  $r_{ij}^3$ , the contribution from successively smaller subunits is expected to converge rapidly. The self scattering of the subcells was calculated in one case and found to be about 10 per cent of the total. Therefore the calculations were carried out to the second approximation only.

The results of these calculations are listed in Table XLI for Bi, Pb, Au, Hg, Ta, Er, Ho, La, I, In, and  $CD_2$ . The other targets were assumed to have similar scattering to one of these.\* A scattering calculation was not performed for the uranium target since this data was used only for comparing two counters, and its cylindrical symmetry resulted in approximately equal neutron scattering. The gamma ray attenuation effects in the target likewise cancelled out by the cylindrical symmetry of the hollow uranium cylinder. To see this, consider

\*The Pb scattering correction was used for Tl, Ta for W, Er for Sm, La for Pr, and In for Sn.

Table XLI  
Scattering Corrections

$E_n$	Bi cylinder		Bi disk		$Pb^{208}$	
	$S(76, E_n)$	$S(156, E_n)$	$S(76, E_n)$	$S(156, E_n)$	$S(76, E_n)$	$S(156, E_n)$
0.6	0.765	0.759	0.832	0.765	0.878	0.824
1.0	0.830	0.823	0.858	0.801	0.894	0.844
1.4	0.895	0.888	0.885	0.840	0.910	0.864
1.8	0.950	0.942	1.002	0.946	0.962	0.916
2.2	1.006	0.998	1.019	0.957	1.015	0.967
2.6	1.010	1.000	1.018	0.963	1.014	0.966
3.0	1.013	1.001	1.018	0.960	1.014	0.966
3.4	1.022	1.008	1.033	0.969	1.020	0.971
3.8	1.032	1.015	1.048	0.979	1.035	0.983
4.2	1.024	1.000	1.042	0.965	1.031	0.976
4.6	1.017	0.986	1.036	0.951	1.027	0.969
5.0	1.028	1.001	1.056	0.973	1.041	0.983
5.4	1.049	1.026	1.076	0.994	1.055	0.996
5.8	1.060	1.028	1.072	0.988	1.054	0.991
6.2	1.071	1.030	1.068	0.981	1.053	0.987
6.6	1.058	1.016	1.071	0.979	1.056	0.984
7.0	1.046	1.003	1.074	0.975	1.060	0.984
7.4	1.046	1.003	1.073	0.974	1.058	0.984
7.8	1.045	1.002	1.072	0.974	1.057	0.984

$E_n$	$Pb^{206}$		Au		Ta	
	$S(76, E_n)$	$S(156, E_n)$	$S(76, E_n)$	$S(156, E_n)$	$S(76, E_n)$	$S(156, E_n)$
0.6	0.834	0.784	0.901	0.869	0.765	0.688
1.0	0.860	0.813	0.914	0.886	0.902	0.824
1.4	0.887	0.843	0.928	0.903	1.039	0.966
1.8	0.947	0.902	0.966	0.937	1.036	0.963
2.2	1.006	0.960	1.005	0.973	1.032	0.961
2.6	1.008	0.962	1.005	0.975	1.047	0.972
3.0	1.010	0.963	1.005	0.978	1.062	0.983
3.4	1.022	0.973	1.016	0.979	1.078	1.009
3.8	1.033	0.981	1.026	0.981	1.095	1.035
4.2	1.028	0.974	1.028	0.998	1.090	1.026
4.6	1.026	0.969	1.031	1.017	1.084	1.016
5.0	1.041	0.983	1.034	1.008	1.071	1.001
5.4	1.055	0.996	1.037	1.000	1.058	0.987
5.8	1.054	0.991	1.034	0.994	1.047	0.974
6.2	1.053	0.987	1.032	0.989	1.036	0.960
6.6	1.056	0.984	1.033	0.990	1.021	0.945
7.0	1.060	0.984	1.034	0.992	1.016	0.940
7.4	1.058	0.984			1.018	0.942
7.8	1.057	0.984			1.019	0.943

Table XLI (cont'd)  
Scattering Corrections

$E_n$	Er		Ho		La	
	$S(76, E_n)$	$S(156, E_n)$	$S(76, E_n)$	$S(156, E_n)$	$S(76, E_n)$	$S(156, E_n)$
0.6	0.763	0.676	0.924	0.913	0.945	0.888
1.0	0.896	0.819	0.968	0.959	0.880	0.824
1.4	1.029	0.969	1.011	1.004	0.816	0.766
1.8	1.026	0.966	1.008	1.000	0.840	0.790
2.2	1.022	0.964	1.006	0.998	0.863	0.811
2.6	1.037	0.979	1.015	1.005	0.898	0.833
3.0	1.052	0.994	1.024	1.011	0.934	0.856
3.4	1.068	1.009	1.018	1.001	0.976	0.902
3.8	1.084	1.024	1.012	0.993	1.018	0.949
4.2	1.082	1.022	1.019	0.999	1.042	0.984
4.6	1.080	1.020	1.026	1.005	1.065	1.017
5.0	1.056	0.993	1.028	1.009	1.066	1.030
5.4	1.051	0.984	1.030	1.012	1.067	1.026
5.8	1.044	0.980	1.028	1.008	1.063	1.020
6.2	1.037	0.977	1.027	1.005	1.059	1.016
6.6	1.024	0.963	1.027	1.003	1.062	1.017
7.0	1.012	0.950	1.027	1.001	1.064	1.018
7.4	1.012	0.954				
7.8	1.013	0.959				

$E_n$	I		In	
	$S(76, E_n)$	$S(156, E_n)$	$S(76, E_n)$	$S(156, E_n)$
0.6	0.865	0.823	0.768	0.698
1.0	0.867	0.838	0.771	0.712
1.4	0.870	0.853	0.774	0.727
1.8	0.920	0.918	0.850	0.799
2.2	0.965	0.980	0.930	0.875
2.6	1.015	1.007	0.975	0.920
3.0	1.068	1.035	1.017	0.962
3.4	1.051	1.019	1.014	0.949
3.8	1.032	1.003	1.012	0.936
4.2	1.031	1.001	1.011	0.935
4.6	1.030	0.999	1.010	0.934
5.0	1.030	0.999	1.010	0.934
5.4	1.030	0.999	1.010	0.934
5.8	1.030	0.999	1.010	0.934
6.2	1.030	0.999	1.010	0.934
6.6	1.030	0.999	1.010	0.934
7.0	1.030	0.999	1.010	0.934
7.4	1.030	0.999	1.010	0.934
7.8	1.030	0.999	1.010	0.934



Fig. 107. The photon and neutron attenuation coefficients are approximately given by  $0.05 \text{ cm}^2/\text{g}$  for 6 to 15 MeV gammas, and  $0.02 \text{ cm}^2/\text{g}$  for 1 to 5 MeV neutrons. Therefore  $\sigma_{T\gamma} \approx 2.0 \sigma_{Tn}$ . In the figure,  $\Delta_1$  is the thickness of the shell and  $\Delta_2$  is the chord of the outer diameter drawn through the midpoint of the wall. Consider the gamma ray along the line labelled  $\gamma_1$ . On the side of the target near C1, the flux of neutrons to the counters at  $156^\circ$  and  $76^\circ$  are, on the average,

$$\text{Flux at } 156^\circ = A(1 - \Delta_1 \mu_T)(1 - \frac{1}{2} \Delta_1 \mu_T) \approx A(1 - \frac{3}{2} \Delta_1 \mu_T) \quad (132a)$$

$$\text{Flux at } 76^\circ = B(1 - \Delta_1 \mu_T)(1 - \frac{1}{2} \Delta_2 \mu_T) \approx B[1 - (\Delta_1 + \frac{1}{2} \Delta_2) \mu_T] \quad (132b)$$

where A and B are the products of the gamma flux and neutron production in the absence of attenuation and  $\mu_T$  is the linear attenuation coefficient for neutrons and one-half the linear attenuation coefficient for gamma rays.

On the other side of the target, at point 2, the average fluxes are given by

$$\text{Flux at } 156^\circ = A(1 - 3\Delta_1 \mu_T)(1 - \frac{3}{2} \Delta_1 \mu_T) \approx A(1 - \frac{9}{2} \Delta_1 \mu_T) \quad (133a)$$

$$\text{Flux at } 76^\circ = B(1 - 3\Delta_1 \mu_T)(1 - \frac{1}{2} \Delta_2 \mu_T) \approx B[1 - (3\Delta_1 - \frac{1}{2} \Delta_2) \mu_T] \quad (133b)$$

where the first bracket in the above expressions gives the gamma ray attenuation and the second bracket gives the neutron attenuation.

Therefore the neutron fluxes from points 1 and 2 are

$$\text{Flux at } 156^\circ = 2A(1 - 3\Delta_1 \mu_T) \quad (134a)$$

$$\text{Flux at } 76^\circ = 2B[1 - (2\Delta_1 - \frac{1}{2} \Delta_2) \mu_T] \quad (134b)$$

Now consider gamma rays entering along the lines labelled  $\gamma_2$ , and producing neutrons from the points labelled 3 and 4. Then the fluxes at point 3 are given by

$$\text{Flux at } 156^\circ = A(1 - \Delta_2 \mu_T)(1 - \frac{1}{2} \Delta_2 \mu_T) \approx A(1 - \frac{3}{2} \Delta_2 \mu_T) \quad (135a)$$

$$\text{Flux at } 76^\circ = B(1 - \Delta_2 \mu_T)(1 - \frac{1}{2} \Delta_1 \mu_T) \approx B[1 - (\Delta_2 - \frac{1}{2} \Delta_1) \mu_T] \quad (135b)$$

And at point 4 the fluxes are given by

$$\text{Flux at } 156^\circ = A(1 - \Delta_2 \mu_T)(1 - \frac{1}{2} \Delta_2 \mu_T) \approx A(1 - \frac{3}{2} \Delta_2 \mu_T) \quad (136a)$$

$$\text{Flux at } 76^\circ = B(1 - \Delta_2 \mu_T)(1 - \frac{3}{2} \Delta_1 \mu_T) \approx B[1 - (\Delta_2 - \frac{3}{2} \Delta_1) \mu_T] \quad (136b)$$

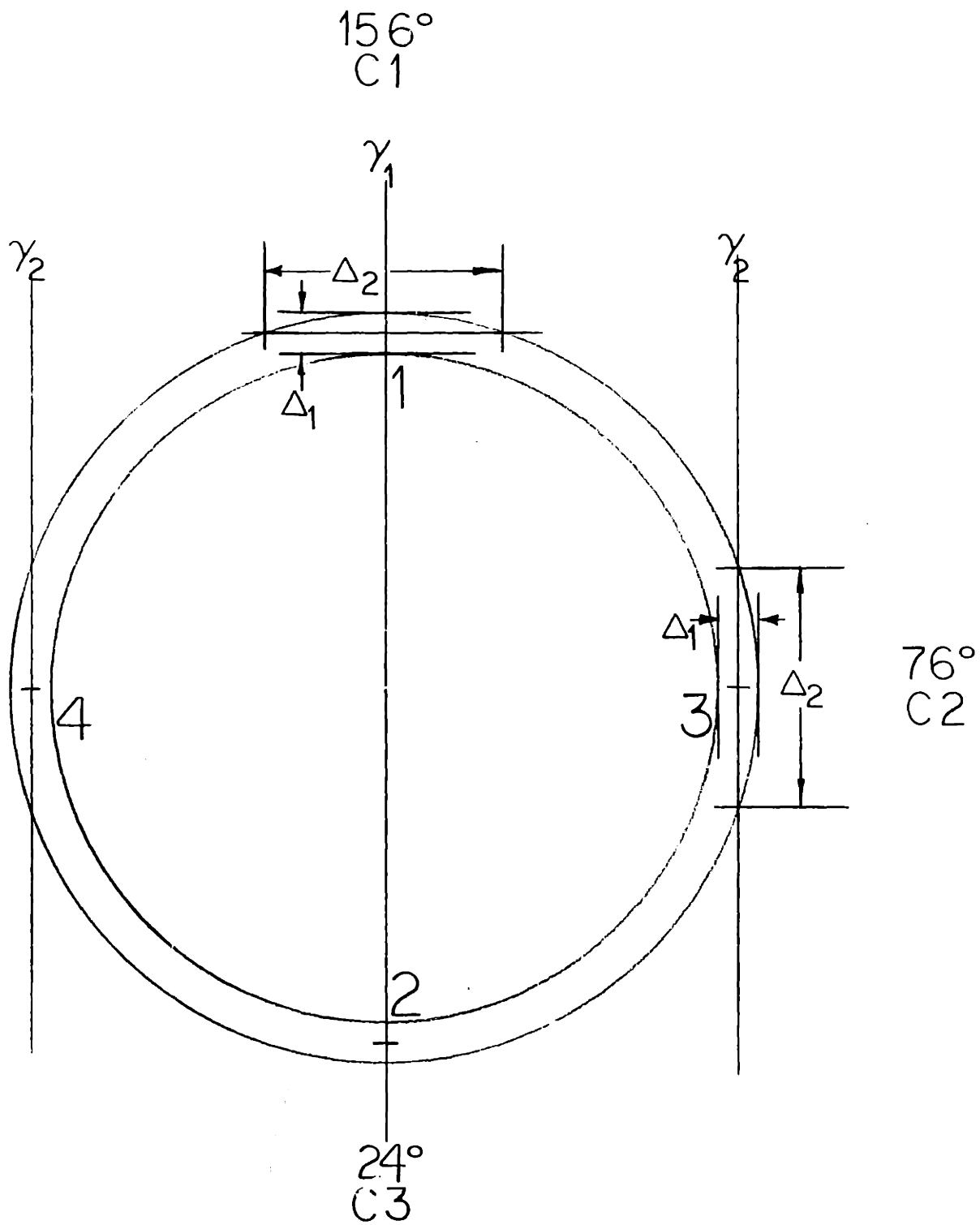


Fig. 107 Scattering in the Uranium Cylinder

The fluxes from points 3 and 4 are

$$\text{Flux at } 156^\circ = 2A\left(1 - \frac{3}{2}\Delta_2\mu_T\right) \quad (137a)$$

$$\text{Flux at } 76^\circ = 2B[1 - (\Delta_2 - \Delta_1)\mu_T] \quad (137b)$$

The total flux from points 1, 2, 3, and 4 is

$$\text{Flux at } 156^\circ = 2A\left[1 - (3\Delta_1 - \frac{3}{2}\Delta_2)\mu_T\right] \quad (138a)$$

$$\text{Flux at } 76^\circ = 2B\left[1 - (3\Delta_1 - \frac{3}{2}\Delta_2)\mu_T\right] \quad (138b)$$

Thus the gamma ray attenuation affects the angular distribution of photoneutrons from points 1, 2, 3, and 4 only in the second order of  $\Delta_1\mu_T$ . The other points in the shell can be paired off in a similar manner. Therefore one is justified in neglecting the effects of gamma ray attenuation on the uranium photoneutron angular distribution, due to the cylindrical symmetry of the target.

The calculation for deuterium was slightly different than the one explained in this appendix. In this case the energy loss in scattering was taken into account, and there was no inelastic scattering. (This is only approximately correct for the carbon in the  $\text{CD}_2$  sample.) Otherwise the calculation is the same as above. The results are listed in Table VI, Chapter III.

There is one additional neutron scattering correction. The rare earth targets were coated with a layer of plastic about  $\frac{1}{16}$ '' thick, to prevent oxidation. Also the  $\text{Ho}_2\text{O}_3$ , I and Au targets were powder or chips in plastic containers, whose walls were about  $\frac{1}{16}$ '' thick. Therefore a correction was made to the data to account for the attenuation in this material. The targets were grouped into two types: cylinders (Ho and I) whose energy spectra are affected, but not their angular distributions; and flat targets (Au, Er, Sm, La, and Pr) whose energy spectra and angular distributions are both affected. The attenuation through the appropriate thickness of material was estimated using the total neutron cross sections from ref 53. The results are listed in Table XLII as A and B. The  $156^\circ$  and  $24^\circ$  data is increased by factor A. The  $76^\circ$  data is increased by factor A for cylindrical targets and by the factor B for flat targets. Since a correction due to forward scattering in the plastic has not been made, the factors in Table XLII are probably overestimates. However, forward scattering is only appreciable in carbon, which makes up about one-third of the total cross section.

Table XLII  
 Scattering Correction Due to Plastic Coating on the Target

$E_n$	A	B
0.6	1.236	1.112
1.0	1.175	1.084
1.4	1.153	1.074
1.8	1.128	1.058
2.2	1.119	1.058
2.6	1.109	1.053
3.0	1.103	1.050
3.4	1.103	1.050
3.8	1.096	1.047
4.2	1.090	1.044
4.6	1.084	1.041
5.0	1.075	1.037
5.4	1.065	1.032
5.8	1.063	1.031
6.2	1.059	1.029
6.6	1.053	1.026
7.0	1.051	1.025
7.4	1.053	1.026
7.8	1.057	1.028
8.2	1.061	1.030
8.6	1.053	1.026
9.0	1.053	1.026

## Appendix II

### Electronics

The circuitry is presented in block form in Chapter II, Figs. 3, 4, and 5. Each block will be discussed in greater detail in this appendix.

#### A. Photomultiplier Circuitry and Tubes

The high voltage string and associated circuitry for the RCA 7046 photomultipliers are shown in Fig. 108. G2, the second focussing grid, is fixed at +900 V. The anode end of the string is held at about +3000 V. The high voltage supply is variable from +2000 V to +3500 V in steps of 70 V. It is regulated by a series string of 53 OG3 regulator tubes. (The voltage is varied by switching in additional OG3's.) The +900 V is obtained by tapping this string at the appropriate spot.

The first focussing grid, G1, is held at -105 V to bias the tube off, as is explained in Chapter II. A +200 V pulse is applied to the UHF connector, labelled "Gate" in the figure, to activate the tube. The photomultiplier pulses can be sampled at dynodes 11 and 14, and at the anode. The dynode 11 output is used to view large pulses, which would saturate at the anode.

The signal from the anode is limited to 10 ma by the biased diodes shown in the figures. A +15 V bias is applied to the resistor string in series with the Q6-100 diode. A 10 ma current flows through this diode, through the 75  $\Omega$  resistor and to ground. When an anode pulse is present, its current reaches 10 ma, the diode is shut off, and the current now flows from ground through the other diode, which had been biased off until this point.

The photomultiplier tubes were selected for low noise and high gain. To be acceptable a tube must have less than  $10^6$  noise-pulses/sec as large as a single photoelectron pulse. This would yield a counting rate of about  $10^{-2}$  counts/sec when the tube is used in triple coincidence with a 30 ns resolving time and  $10^{-4}$  duty ratio. A typical tube used had a noise level of  $2 \times 10^5$  to  $3 \times 10^5$  counts/sec.

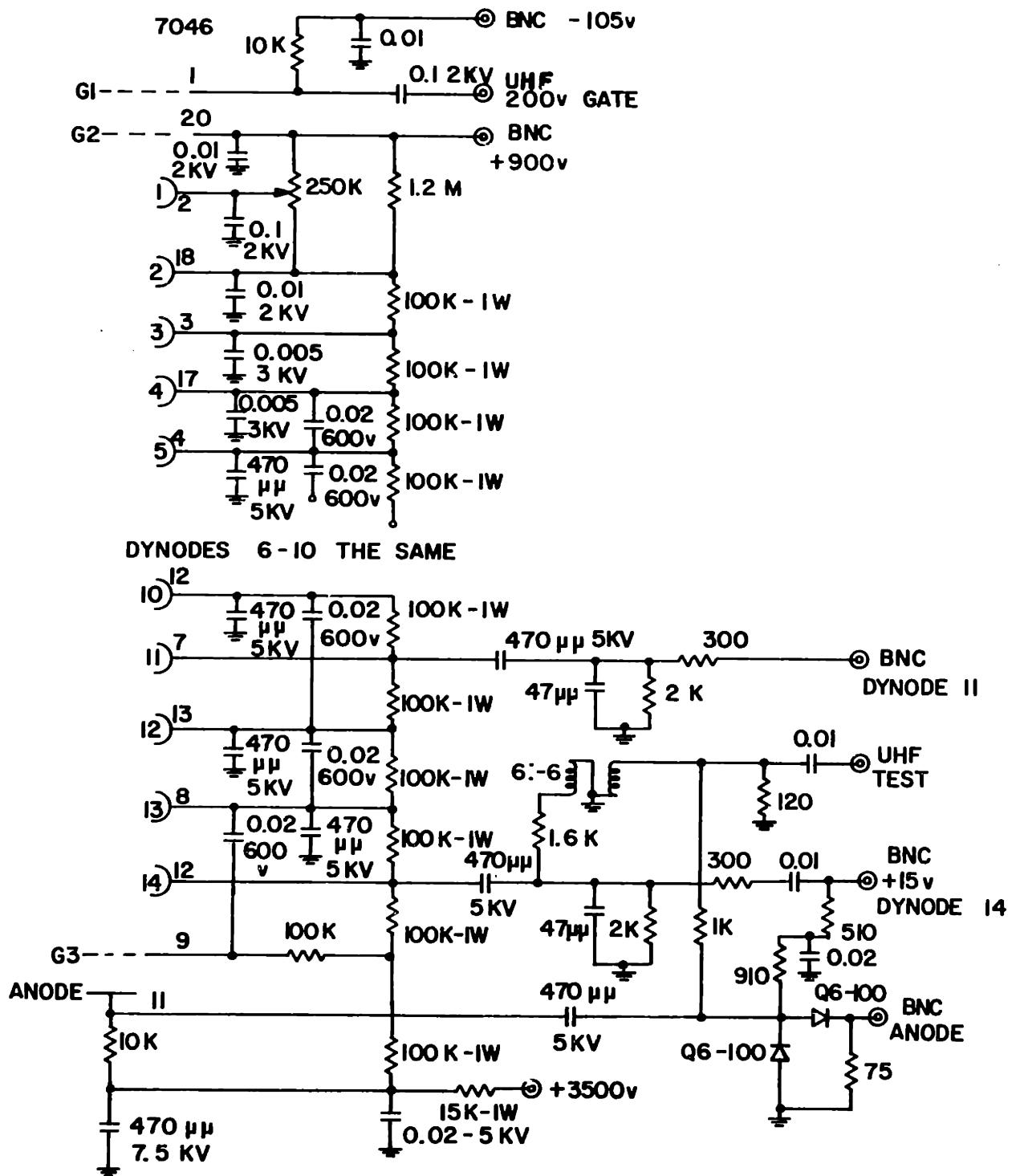


Fig. 108 7046 Voltage String and Anode Current Limiter

The tubes were adjusted for operation by the following procedure. A NaI crystal was placed on the tube face, and the photopeak from 0.51 MeV gamma rays from Na<sup>22</sup> was observed on dynode 11. The 250 K $\Omega$  potentiometer connected between G2 and dynode 2 was adjusted for maximum gain. The crystal was removed and a mask with a pinhole was substituted. The pulses from single photoelectrons caused by visible light were observed at the anode. The high voltage was adjusted until about 50 to 70 per cent of these pulses were greater than  $\frac{1}{2}$  ma into a 120  $\Omega$  cable. In this manner the tubes were set for equal gains at the desired level.

### B. Photomultiplier Gate Generator

The +200 V pulse used to switch on the photomultiplier is generated by the circuit shown in Fig. 109. Either of two inputs are amplified by the 2N1500 transistors and applied to the grid of the EFP60. This tube provides a large (about 350 V) positive pulse which is applied to the grids of a 2D21. The output is a 270 V pulse with a rise time of about 40 to 50 ns. This pulse is fed to a 400 ft RG-8 cable shorted at the opposite end. The reflected pulse quenches the 2D21 and determines the length of the output pulse (about 1.2  $\mu$ sec). The three grids of the three photomultipliers are connected in parallel to the RG-8 cable through three 400  $\Omega$  resistors, a few feet from the input end. The rise time of the pulse applied to the grid of the photomultiplier tubes is adjusted with these resistors to be about 90 ns.

### C. Tunnel Diode Pulse Shaper

The output from the photomultiplier anode is fed to the pulse shaper shown in Fig. 110. The input pulse passes through T1 which terminates the cable and provides a gain of two. The pulse changes the tunnel diode from its quiescent state of high current (about 9 ma), low voltage (about 0.2 V) to a low current (about 2 ma), high voltage state (about 0.8 V). This voltage level is amplified and applied to the base of T3. T3 is normally on, and is now cut off. The 10 ma it was carrying now appears on the output cables. The change in voltage across T3 causes T4 to conduct strongly, and a positive pulse is

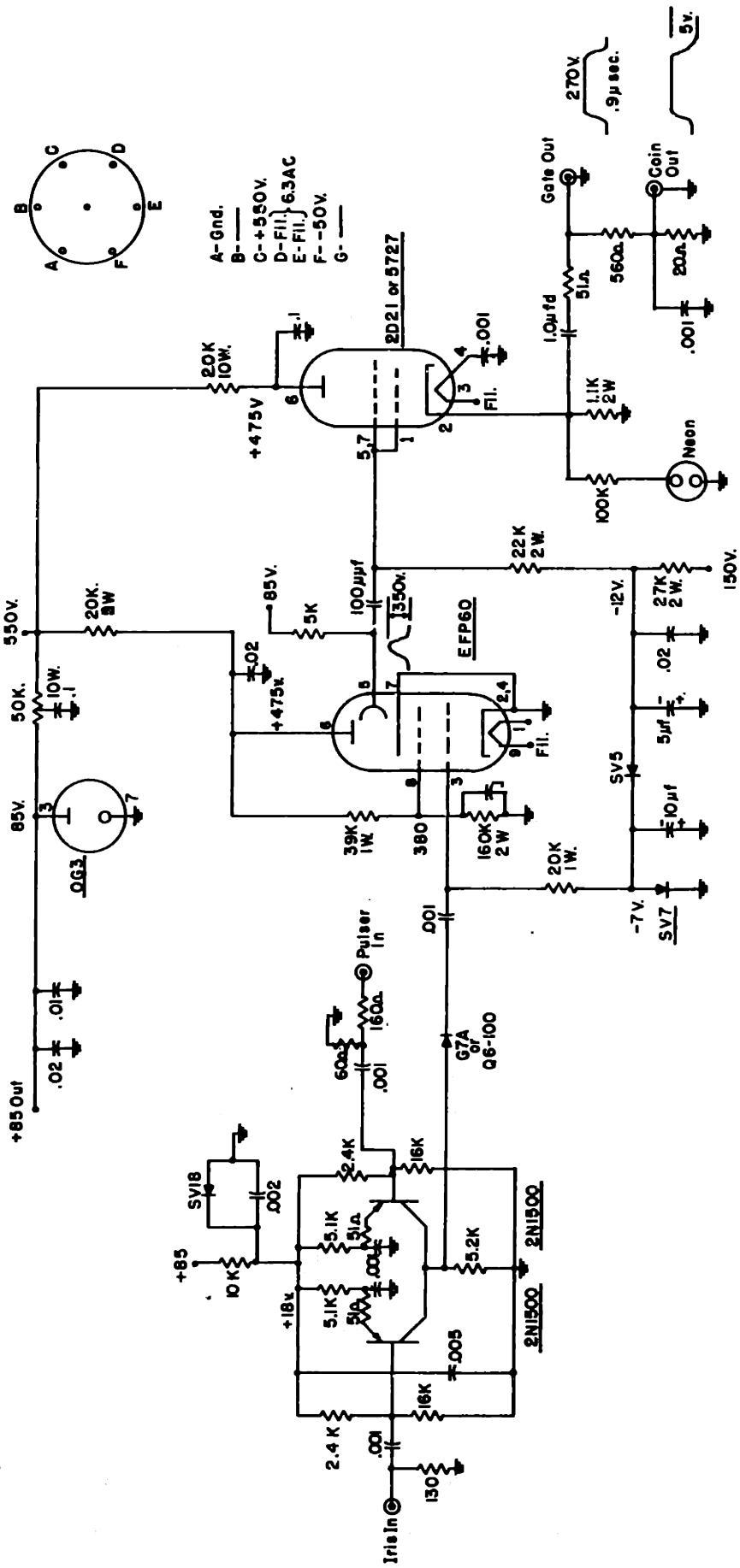


Fig. 109 Photomultiplier Gate Generator





propagated down a  $90 \Omega$  cable connected to 'BNC OUT' and 'BNC IN'. This pulse cuts off T2 and allows T3 to conduct again, thus stopping the output pulse. Thus the length of the output is determined by the cable delay time. The current needed to trigger the circuit is determined by the bias current which is set by the potentiometer R and which flows through the tunnel diode. The circuits proved to be reliable down to  $\frac{1}{4}$  ma input ( $\frac{1}{2}$  ma at the tunnel diode). It provides two negative outputs of 0.75 V on  $90 \Omega$  cable. The rise and fall time was measured to be less than 2 ns with a Tektronics sampling oscilloscope. If the input pulse is longer than twice the time determined by delay cable, a second output pulse is generated. Additional outputs continue until the input pulse is removed.

#### D. Triple Coincidence.

Fig. 111 shows one leg of three identical inputs to the triple coincidence circuit. The diodes are normally carrying a standing current,  $i$ , of 2 ma. The current through the  $3.0 \text{ K}\Omega$  resistor to ground is thus  $3i$  (6 ma). The input pulse is applied to the transistor which matches the cable impedance. This pulse results in 9 ma into R1, biasing the diode off. In order to maintain the standing current in the  $3.0 \text{ K}\Omega$  resistor, current flows through R2 and the other two R1's. Since  $R1 = R2$ , the current through R2 is about  $\frac{1}{3}i$ . If there are two simultaneous input pulses,  $\frac{1}{2}i$  is drawn through R2 and the remaining R1. In the case of three simultaneous input pulses, all of the standing current is switched through R2. Thus the output of the coincidence circuit is 1:3:9 for 1, 2, and 3 inputs respectively. The actual outputs are  $1:2\frac{1}{2}:6$ . These lower ratios are due to input impedances of the tunnel diode pulse shaper driven by the coincidence circuit. The TDPS is set to fire only on three pulses. The resolving time of the coincidence circuit is twice the width of the 15 ns input pulses. Because of the standard amplitudes on the input pulses, the coincidence circuit is quite reliable.

A nanosecond light pulse from a PEK-118 lamp was flashed into the counter to equalize the photomultipliers and cable delays occurring before the coincidence circuit.

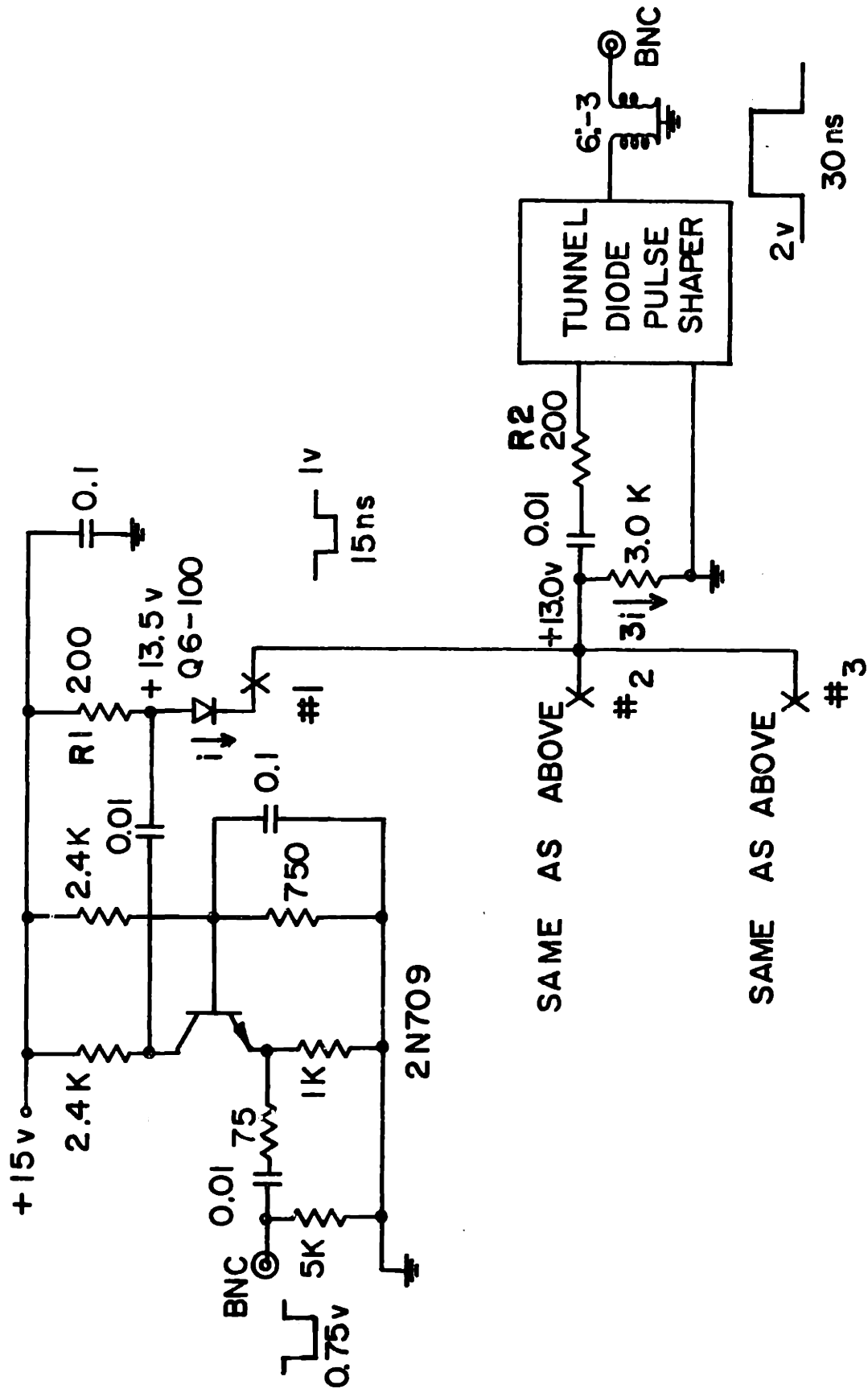


Fig. 11! Triple Coincidence Circuitry

The performance of the detector and the circuits up to this point was checked by placing a radioactive source ( $\text{Cs}^{137}$  with 0.6 MeV gammas) next to the counter and delaying one tube output with respect to the other two. In this manner the resolving time of the coincidence circuit was found to be about 30 ns. The rise time (10 per cent to 90 per cent) was about 6 ns.

#### E. Linear Gate

The linear gate, which is used both as the gate in the counter circuits and as the time T gates in the THC, is shown in Fig. 112. In the case of the detector gate, T1 is fed by three inputs in parallel from the tunnel diode pulse shaper. The input impedance of T is low ( $< 20 \Omega$ ) so that approximately  $\frac{2}{3}$  of the input current is useful, while the remaining  $\frac{1}{3}$  is split between the other two inputs. These pulses (about  $\frac{1}{6}$  of the input pulse) travel back to the pulse shaper and are inverted upon reflection. This mismatch has not caused any observable problems.

T1 is used to match the impedance of the input cables. T2 provides a gain of approximately two, and inverts the pulse. The output of T2 is applied to the emitters of T3 and T4, which comprise the actual gate. In the quiescent state the emitter of T4 is 0.2 V positive with respect to base and conducts, and T3 is 0.4 V negative with respect to its base and is cut off. Thus the input pulses are shunted into the dummy  $5.1 \Omega$  load. However if a positive gate pulse is applied to the base of T4, it is cut off and the standing current in the  $50 \text{ K}\Omega$  resistor is reduced. Thus the voltage on the emitter of T3 goes positive and it conducts, allowing input pulses to pass the gate. T3 and T4 can be either 2N769 or 2N976, which differ only in power rating. The specially wound 8:8 transformer provides an additional current gain of two, and T5 drives the output cable.

The positive gate pulse is +2 V and 30 ns wide. It is generated by the coincidence circuit. The input cables are about 15 ft long to place the leading edge of the first pulse within the 30 ns gate pulse (see block diagram Fig. 4). Since the three pulses are added, the output can vary from 2 V to 6 V over its

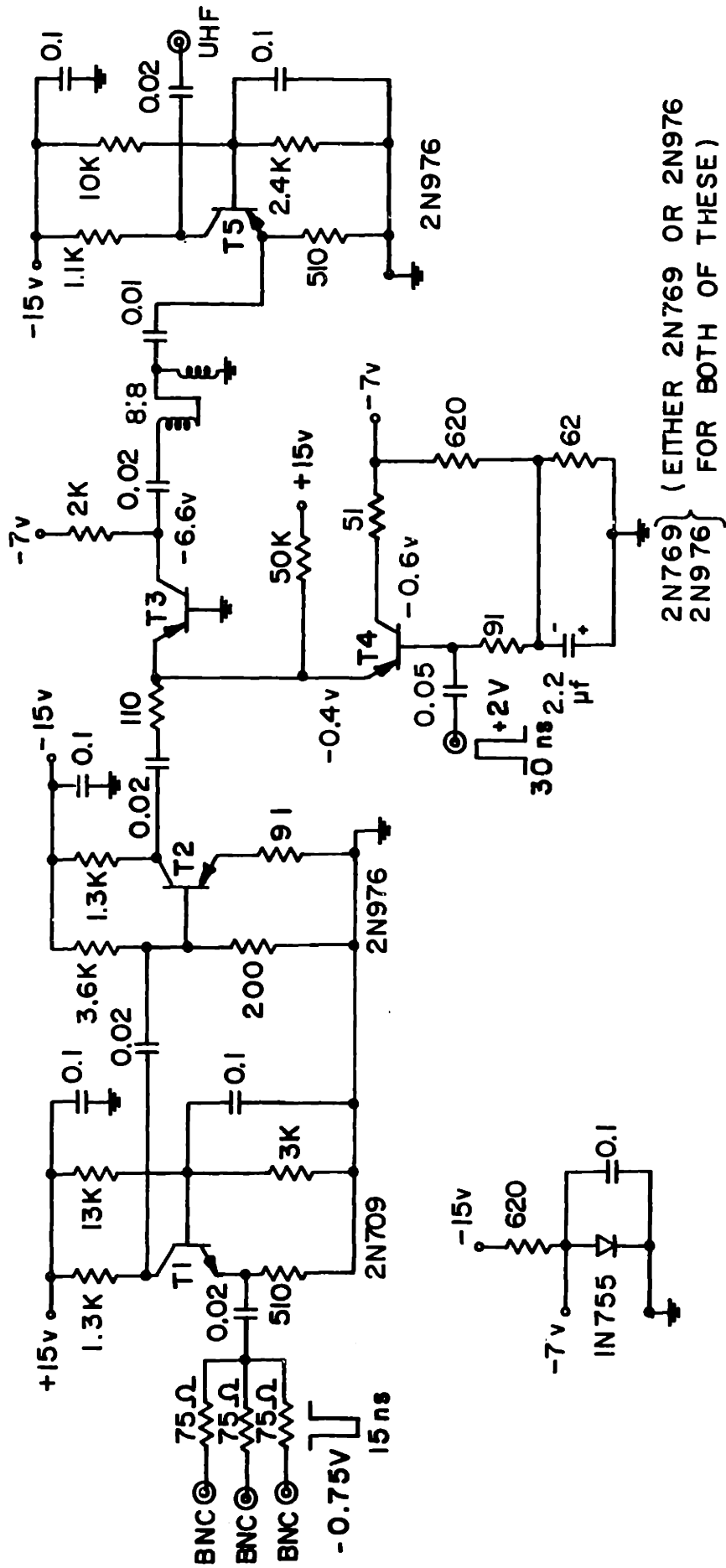


Fig. 112 Linear Gate

length depending on how many pulses are adding at a given instant. If a pulse is presented to the gate without a gate pulse, the feedthrough is less than 0.1 V. The time T gates are similar, but with only one input, terminated for 120  $\Omega$  cable.

#### F. Time-to-Height Converter (THC)

The circuit diagram for the THC is shown in Fig. 113. It would also be helpful to refer to the block diagram, Fig. 5.

The start pulse ( $T_0$ ) switches the tunnel diode to its high voltage state, and triggers a 2 $\mu$ sec univibrator, which is connected to "Trig Out". This univibrator provides a gate pulse for the three time T gates. When the tunnel diode changes state, the flip-flop consisting of transistors T1 and T2 is flipped and a pulse is applied to transistor T3 through the line A. In this manner T3 is biased on and a constant charging current is supplied to C, a 1500 pf silver-mica capacitor. C continues to charge as long as the tunnel diode remains in its second state.

When a time T pulse arrives at the THC it passes through one of the time T gates which are connected to the "STOP" inputs, T1, T2, and T3. This pulse restores the tunnel diode to its original state, the flip-flop reverts to its original state and T3 is cut off, stopping the charging current to C. A second output from the time T gates triggers one of three univibrators, any one of which in turn triggers another univibrator, "THC GATE TRIG". A 1.25  $\mu$ sec 5 V pulse is generated and applied, through "GATE INPUT" to the base of transistor T5, cutting it off. This allows transistor T4 to conduct, and the voltage signal on the capacitor C, after two stages of amplification, is allowed to pass through the gate formed by T4 and T5. This voltage level is amplified by the circuits labelled "Amplifier" in the figure, and is passed on to the analyzer. The amplifier has a large amount of negative feedback to insure linearity and stability. It is shielded from r-f pickup, but no effort was made to regulate the temperature. The long term stability of the time-of-flight spectrometer was less than 0.5 per cent, which sets an upper limit on the variation in gain of this amplifier. The output pulse is 1.25  $\mu$ sec long and 0 to 3 V in height, which is determined by the



time interval  $T_0$  to  $T$ . The voltage representing a given time interval could be varied, by changing the charging current. This was accomplished by a helipot, not shown in the diagram.

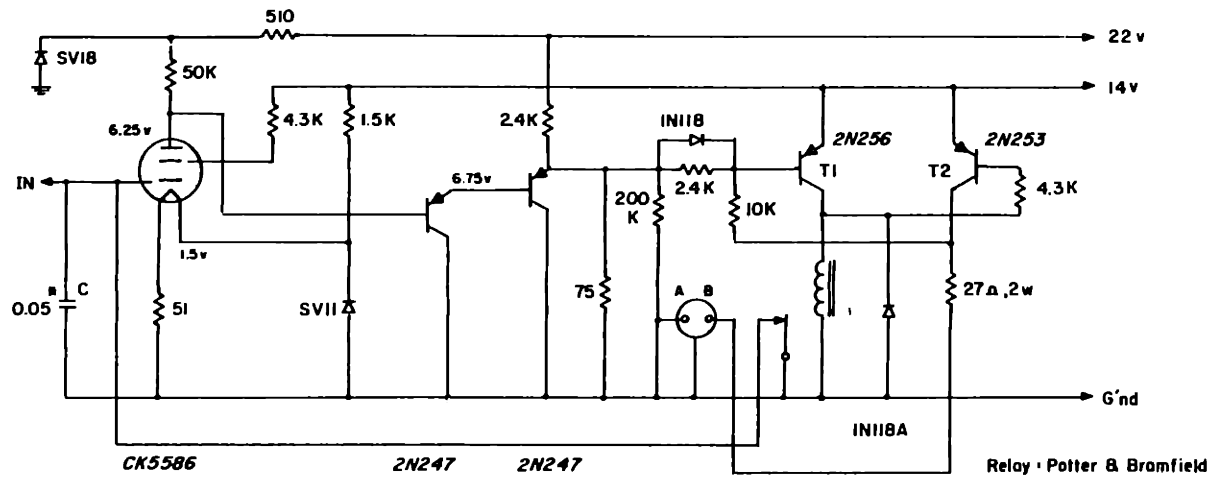
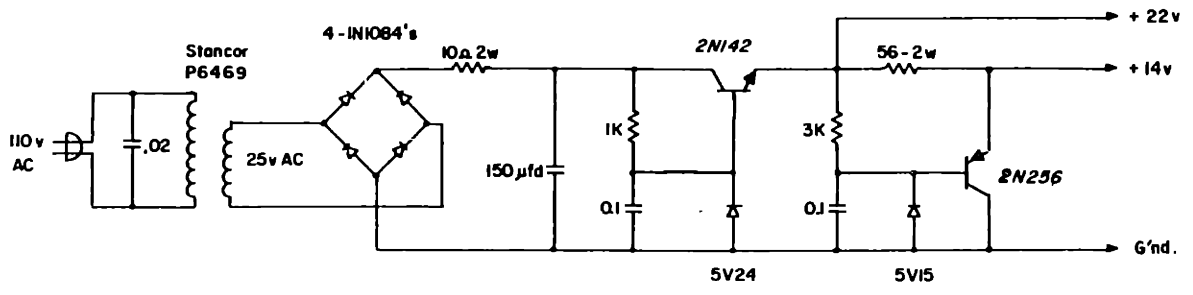
When the flip-flop formed by transistors T1 and T2 changed state, a pulse was sent through a delay cable connected to 'Restore Input'. After  $8 \mu\text{sec}$  delay, this pulse (or rather a pulse generated by it) is applied to the 'Restore Input' and discharges C. This enables the THC to run at a much higher repetition rate than if C were allowed to discharge through the resistors connected to it (about  $750 \mu\text{sec}$ ).

If a time  $T$  pulse is not applied to the THC after a  $T_0$  pulse (which is the more frequent case), the tunnel diode must be switched back to its original state by the THC. For this purpose, a pulse is sent through a 2 to  $3 \mu\text{sec}$  delay cable connected to 'DELAY IN'. It emerges at 'DELAY OUT' to flip the flip-flop and initiate the restore charging circuit. Such 'NO DUMP' cases result in 30 V outputs. However the analyzer is not gated on in such a case, since there was no time  $T$  pulse. In addition the analyzer gain is set such that these analogue pulses correspond to channels above the capacity of the analyzer.

#### G. Charge Integrator

The current integrator used to measure the beam intensity is shown in Fig. 114. The carbon block beam stopper is isolated from ground and connected to a  $0.05 \mu\text{fd}$  capacitor C. The voltage level accumulated on C is amplified by the electrometer tube CK5586 and applied to the base of T1 through two stages of DC amplification. The voltage on the base of T1 also causes a current to flow through the  $200 \text{K}\Omega$  resistor, and the cable attached to A. This current is registered on a microammeter in the Linac control room. When the voltage level at the base of T1 reaches a sufficient level T1 is cut off, and the relay is closed. This discharges capacitor C. At the same time T2 is switched on and draws a current through the cable attached to B. This current actuates a mechanical register located in the Linac control room. The act of discharging the capacitor C reduces the voltage on the base of T1, and T1 and T2 revert to their assigned state, ready for another cycle.





\* Dearborn SML -503-2M  
0.05 μfd, 2000 v

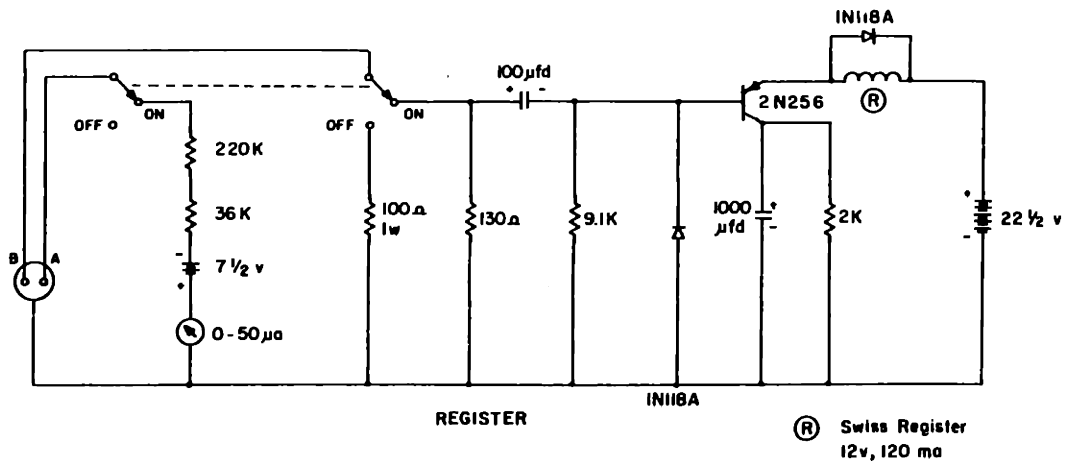


Fig. 114 Beam Integrator

### Appendix III

#### Uranium Reference Spectra

Uranium photoneutron spectra were convenient for use as a reference because they exhibit only a small anisotropy,  $\frac{A}{B} \geq 7$ , over the photon energy range of 5 to 15 MeV, and the cross section for neutron production is relatively high. However they are useful only if both the anisotropy and asymmetry about  $90^\circ$  are known. These quantities have been measured\* up to about 5 MeV neutron energy using a 14 MeV endpoint bremsstrahlung spectrum (52).

#### A. Asymmetry

The process of neutron production from photofission of even-A nuclei has been studied both theoretically and experimentally. Measurements by Baerg et al (108) agree with the theory of A. Bohr (109) in assigning the form  $A + B \sin^2 \Theta$  to the angular distribution of fission fragments emitted during photofission.\*\* Since the neutrons are emitted by the fragments during their de-excitation, the neutron angular distribution, as observed in the laboratory, has a form with no greater complexity than the  $A + B \sin^2 \Theta$  form of the fission fragment angular distribution. That is, by averaging over all angles of emission for the fission fragments, no new angular dependencies that were not present in the fragment distribution can arise in the neutron angular distribution. There is thus little possibility of asymmetry about  $90^\circ$ , produced by a  $\cos \Theta$  dependence, in the photofission neutron distribution. This is particularly likely in the case of  $\text{Th}^{232}$ , since this nucleus exhibits a sharply rising photofission cross section near threshold, and a large anisotropy of the fragments in that energy region. This suggests a single strongly predominant electric dipole transition, and reduces the likelihood of asymmetric fragment emission through the interference with other transitions. Measurement made by Sargent et al (114) indicate that the fraction of neutrons not emitted from fully accelera-

\*By Dr. D. B. McConnell in this laboratory.

\*\*A strong quadrupole part in the angular distribution of fission fragments from  $\text{U}^{238}$  was reported by Forkman and Johansson (110) and by Takekoshi (111). It has not been seen by Rabotnov et al (112) or by Albertson and Forkman (113).

ted fission fragments is  $0.07 \pm 0.09$  for bremsstrahlung endpoints of 6.75 and 7.75 MeV.

Therefore, Dr. McConnell measured the asymmetry of uranium photon-neutrons from a 14 MeV bremsstrahlung spectrum, which may or may not possess an asymmetric photon-neutron component, and compared it with the same measurement on  $\text{Th}^{232}$  using a 9.9 MeV bremsstrahlung beam, in which the symmetric neutrons emitted from the fission fragments predominate.

Therefore if

$$\left(\frac{d\sigma}{d\Omega}\right)_U = (A_U + B_U \sin^2 \Theta)(1 - C_U \cos \Theta) \quad (139a)$$

$$\left(\frac{d\sigma}{d\Omega}\right)_{\text{Th}} = (A_{\text{Th}} + B_{\text{Th}} \sin^2 \Theta) \quad (139b)$$

where the subscript U refers to uranium and the subscript Th refers to thorium, then the ratio of the counting rates at two angles  $\Theta_1$  and  $\Theta_2$  are given by

$$R_U = \frac{(A_U + B_U \sin^2 \Theta_1)(1 - C_U \cos \Theta_1)(g\eta)_1}{(A_U + B_U \sin^2 \Theta_2)(1 - C_U \cos \Theta_2)(g\eta)_2} \quad (140a)$$

$$R_{\text{Th}} = \frac{(A_{\text{Th}} + B_{\text{Th}} \sin^2 \Theta_1)(g\eta)_1}{(A_{\text{Th}} + B_{\text{Th}} \sin^2 \Theta_2)(g\eta)_2} \quad (140b)$$

where  $(g\eta)_i$  is the product of the absorber transmission,  $g(E_n)$ , and the detector efficiency,  $\eta(E_n)$ , for the counter at angle  $\Theta_i$ .

$\Theta_1$  and  $\Theta_2$  were chosen to be  $130.6^\circ$  and  $50.4^\circ$  respectively, so that

$$(A + B \sin^2 \Theta_1) \approx (A + B \sin^2 \Theta_2) \quad (141)$$

Hence

$$R_U = \frac{(1 - C_U \cos \Theta_1)(g\eta)_1}{(1 - C_U \cos \Theta_2)(g\eta)_2} \quad (142a)$$

$$R_{\text{Th}} = \frac{(g\eta)_1}{(g\eta)_2} \quad (142b)$$

and

$$\frac{R_U}{R_{\text{Th}}} = \frac{(1 - C_U \cos \Theta_1)}{(1 - C_U \cos \Theta_2)} \quad (143)$$

This ratio, as measured in ref 52 was  $1.0 \pm 0.02$  from the upper limit imposed by 2 per cent statistics at about 5 MeV in neutron energy down to about 1 MeV, the lower energy limit of the experiment. This corresponds to  $C_U = 0.0 \pm 0.016$ . It was assumed that at higher neutron energies the asymmetry was still negligible. (Since the higher neutron energies are predominantly fission neutrons, this is reasonable.  $E_{Th} = 5.3$  fission, 5.8 ( $\gamma, n$ ). )

## B. Anisotropy

A measurement of the anisotropy was made (52) by comparing uranium spectra obtained at  $\Theta_1 = 130.6^\circ$ ,  $\Theta_2 = 50.4^\circ$  and  $\Theta_1 = 167.3^\circ$ ,  $\Theta_2 = 87.1^\circ$  with the absorber, detector efficiency and physical location of the detectors unchanged. The angle was varied by changing the angle through which the beam was deflected by the analyzing magnet. Thus any difference between the ratios of the two counters is due to the anisotropy  $\frac{A}{B}$ . Defining

$$K = \frac{R(167^\circ, 87^\circ)}{R(130^\circ, 50^\circ)} \quad (144)$$

when both numerator and denominator are at the same neutron energy, the efficiencies and absorption factors cancel out in K leaving only the uranium anisotropy.

$$K = \frac{A/B + \sin^2 167^\circ}{A/B + \sin^2 87^\circ} \quad (145)$$

since the ratio for  $130.6^\circ$  and  $50.4^\circ$  is unity. Since  $A/B > 1$  experimentally,

$$K \approx \frac{A/B}{(1 + A/B)}, \quad \text{or} \quad \frac{A}{B} \approx \frac{K}{(1 - K)} \quad (146)$$

From the values of  $K(E_n)$  determined in ref 52,  $W(\Theta_1 = 156^\circ)/W(\Theta_2 = 76^\circ)$  was calculated for our present experiment (with  $C = 0.0$ ). This quantity is tabulated in Table III.

## C. Above 5 MeV

However McConnell determined K only up to 5 MeV. Beyond this, his counting rate was too low to accumulate the desired statistics. Similarly in the present experiment, the statistical accuracy of the uranium spectra becomes rapidly worse above 5 MeV.

However one should remember that the sole purpose of measuring the ratio of the uranium photoneutron spectra at  $156^\circ$  to that at  $76^\circ$  and of  $24^\circ$  to  $156^\circ$  was to measure the differences of the counter efficiencies ( $\eta$ ) and the neutron absorption in the flight paths ( $g$ ). The  $156^\circ$  and  $76^\circ$  counters were adjusted to have the same neutron thresholds, and therefore their efficiencies will be nearly identical above 5 MeV (see Appendix IV). The differences in absorption were calculated using the total neutron cross sections tabulated in ref 53. Using the angular distribution measured by McConnell and the neutron absorption calculated from ref 53, the data from the present experiment shows that the efficiencies of the counters at  $156^\circ$  and  $76^\circ$  are identical down to 1.5 MeV, within the uncertainty of the data. From the above remarks it is clear that the ratio  $g_1 \eta_1 \Delta\Omega_1 / g_2 \eta_2 \Delta\Omega_2$  was measured up to 5.2 MeV using the uranium ratios from the present work and the value of  $A/B$  measured by McConnell. Above that energy,  $g_i$  was calculated from ref 53, and  $\eta(156^\circ)$  and  $\Delta\Omega(156^\circ)$  were assumed equal to  $\eta(76^\circ)$  and  $\Delta\Omega(76^\circ)$  respectively.

For the case of the counter at  $24^\circ$ , the absorber differences are calculated above 5 MeV as in the case above. However the efficiency is substantially different from that at  $156^\circ$  because of the much higher threshold required by the large background encountered at  $24^\circ$ . The efficiency of the counter at  $24^\circ$  above 5 MeV was estimated from the equation

$$\frac{\eta(24^\circ)}{\eta(156^\circ)} = \frac{E_n - E_{th}(24^\circ)}{E_n - E_{th}(156^\circ)} \quad (147)$$

where  $E_{th}$  is the threshold of the counter at the angles given in parentheses. This formula was found to reproduce the  $24^\circ$  counter efficiency within statistics from 2 MeV to 5 MeV. Finally  $\Delta\Omega(24^\circ) = 0.6\Delta\Omega(76^\circ)$ .

Appendix IV  
 Detector Efficiency Calculation

The efficiency,  $\eta(E_0, E)$  is defined as the fraction of neutrons of energy  $E$  incident upon the full projector area of the detector scintillator, which is detected when the detector threshold is  $E_0$ . The detector threshold is a parameter that describes the minimum amount of light output from the scintillator required to operate the logic circuitry. For this discussion,  $E_0$  can be assumed to be the energy of the lowest energy neutron detected, and it is found by linearly extrapolating a photoneutron time spectrum to zero.  $E_0$  is taken to be 0.3 MeV. The following initial assumptions are made to calculate the detector efficiency: there are no photoelectron statistical effects--ie, the resolution of the photomultiplier is perfect and the neutrons do not lose energy in a collision with a carbon nucleus--and there is consequently no scintillation resulting from such a collision; and only collisions to second order are significant. The latter assumption enables one to write

$$\eta(E_0, E) \approx \eta_H(E_0, E) + \eta_{CH}(E_0, E) + \eta_{HH}(E_0, E) \quad (148)$$

where  $\eta_H(E_0, E)$  = the contribution to the efficiency arising from neutrons colliding first with a proton; this is expected to be the predominant effect.

$\eta_{CH}(E_0, E)$  = the contribution to the efficiency arising from neutrons which first collide with a carbon nucleus but then suffer a second collision with a proton

$\eta_{HH}(E_0, E)$  = the contribution to the efficiency arising from neutrons which are undetected following a first collision with a proton, but which yield a large enough additional scintillation in a second proton collision to be detected.

The volume of the scintillator is divided into 1000 cubes of equal volume. Each cell is assigned a set of coordinates corresponding to its center and an amount of material corresponding to its volume. Then  $\eta_H(E_0, E)$  can be written as

$$\eta_H(E_o, E) = \sum_i \left[ e^{-K_T(E)\ell_i} \right] \left[ 1 - e^{-K_T(E)a} \right] \frac{K_H(E)}{K_T(E)} \left[ \frac{E - E_o}{E} \right] \quad (149)$$

Where  $K_T(E)$  = the reciprocal of the total neutron scattering mean free path in p-terphenyl-activated toluene;  $K_H(E)$  and  $K_C(E)$  are similarly defined with respect to collisions with H or C alone;

$$K_T = K_H + K_C$$

$\ell_i$  = the distance from the face of the counter to the  $i^{\text{th}}$  cube

$a$  = the thickness of the  $i^{\text{th}}$  cube

In the above expression, the terms in brackets successively indicate, for the  $i^{\text{th}}$  cube, the fraction of neutrons incident, the fraction making a first collision, the fraction of the first collisions that is made with H, and the fraction detected. The last fraction derives from the assumption of an isotropic center of mass n-p interaction, and is just the fraction of collisions which transfer an energy greater than  $E_o$  to the proton.

To calculate  $\eta_{CH}(E_o, E)$ , the neutron is assumed to scatter off carbon in the  $i^{\text{th}}$  cell into one of 144 equal solid angles consisting of 12 equal azimuthal angles and 12 equal area zones. Then

$$\eta_{CH}(E_o, E) = \sum_i \left[ e^{-K_T(E)\ell_i} \right] \left[ 1 - e^{-K_T(E)a} \right] \frac{K_C(E)}{K_T(E)} \sum_j \left[ 1 - e^{-K_T(E)L_{ij}} \right] \frac{W_j K_H(E)}{K_T(E)} \left[ \frac{E - E_o}{E} \right] \quad (150)$$

where  $L_{ij}$  = the distance from the cell  $i$  to the wall of the detector in the direction of the  $j^{\text{th}}$  solid angle

$\frac{K_C(E)}{K_T(E)} W_j = \left( \frac{d\sigma_C}{d\Omega} \right) \frac{\Delta\Omega}{\sigma_C + \sigma_H} =$  the fraction of neutrons scattered off carbon into the  $j^{\text{th}}$  solid angle;  $\Delta\Omega = 4\pi/144$  steradians

$\left[ 1 - e^{-K_T(E)L_{ij}} \right] \frac{K_H(E)}{K_T(E)}$  represents the fraction of neutrons making a collision with hydrogen in the  $j^{\text{th}}$  case. The other terms are similar to those in the expression for  $\eta_H$ .

In calculating  $\eta_{HH}(E_o, E)$  the scintillations are assumed to add linearly, and the effect of time lag between collisions is neglected. With respect to the former assumption, Fowler and Roos (115) have found that the dependence of

light output with energy for a proton of energy below 0.7 MeV in an organic scintillator is proportional to a power of the proton energy between the first and second. The assumption of linear addition amounts to an overestimate of  $\eta_{HH}$  which is, however, partly compensated for by the present neglect of higher order collisions with H. In this calculation, one also notes that neutrons undetected after a first H collision all scatter into a forward cone between  $0^\circ$  and an upper limit  $\theta_m$ , determined by

$$\cos^2 \theta_m = \frac{E - E_0}{E} \quad (151)$$

$\eta_{HH}(E_0, E)$  can be written as

$$\eta_{HH}(E_0, E) = \sum_i \left\{ \left[ e^{-K_T(E)L_i} \right] \left[ 1 - e^{-K_T(E)a} \frac{K_H(E)E_0}{K_T(E)E} \right] \right\} \left\{ \left[ 1 - e^{-K_T(E)L_i} \frac{K_H(E)E - E_0}{K_T(E)E_0} \log \left[ \frac{E}{E - E_0} \right] \right] \right\} \quad (152)$$

where  $L_i$  is the distance from the  $i^{\text{th}}$  cell to the back face of the counter. The first curly bracket gives the fraction of neutrons undetected after a first H collision; the second curly bracket results from integrating over all pairs of energy losses suffered by neutrons in two H collisions which give a total energy loss greater than or equal to  $E_0$ . The results of this calculation are given in Table XLIII. Notice that  $\eta_{CH}$  and  $\eta_{HH}$  are significant. Contribution to the efficiency from higher order scatterings are therefore not negligible. Nevertheless, the theoretical efficiency is probably reasonably reliable with respect to shape above 3 MeV, since the hydrogen and carbon cross sections are smooth functions of neutron energy.



Table XLIII  
Counter Efficiency

$E_n$	$\eta_H$	$\eta_{CH}$	$\eta_{HH}$	$\eta$
0.5	0.273	0.059	0.123	0.455
1.0	0.452	0.106	0.078	0.636
1.5	0.504	0.125	0.053	0.682
2.0	0.521	0.127	0.039	0.687
2.5	0.515	0.127	0.028	0.670
2.9	0.415	0.137	0.015	0.567
3.1	0.556	0.109	0.025	0.690
3.5	0.432	0.132	0.013	0.577
4.0	0.442	0.125	0.011	0.578
4.5	0.456	0.137	0.011	0.604
5.0	0.473	0.109	0.010	0.592
5.5	0.465	0.098	0.009	0.572
6.0	0.451	0.093	0.007	0.551
6.5	0.441	0.092	0.006	0.539
7.0	0.433	0.082	0.006	0.521
7.5	0.364	0.113	0.004	0.481
8.0	0.350	0.118	0.003	0.471
8.5	0.400	0.059	0.004	0.463
9.0	0.377	0.085	0.003	0.465
9.5	0.361	0.085	0.003	0.449
10.0	0.348	0.084	0.002	0.434

## Bibliography

1. Corman, Jewell, John, Sherwood, and White, *Phys Lett* 10, 116 (1964)  
John, W., and Prosses, J. M., *Phys Rev* 127, 231 (1962)  
John and Martin, *Phys Rev* 124, 1596 (1961)
2. Yasumi, S., Yata, M., Takamotsu, K., Masaike, A., and Masuda, Y.,  
*J. Phys Soc Japan*, 15, 1913 (1960)
3. Penfold, A. S., Leiss, J. E., *Analysis of Photo Cross-sections* (University of Illinois, 1958)
4. Toms, M. E., *Bibliography of Photo- and Electronuclear Disintegrations*, July 1965 Bibliography No. 24, U. S. Naval Research Laboratory, Washington, D. C.
5. Fultz, Bramblett, Caldwell, and Kerr, *Phys Rev* 127 1273 (1962)
6. Bramblett, Caldwell, Auchampaugh, and Fultz, *Phys Rev* 129 2723 (1963)
7. Harvey, R. R., Caldwell, J. T., Bramblett, R. L., and Fultz, S. C., *Phys Rev* 136 126 (1964)
8. O'Connell, J. S., Tipler, P., and Axel, P., NP-9797 Technical Report No. 21, (Illinois Univ Urbana Phys Research Lab) jan 1961
9. Bertozzi, William, PhD Thesis (unpub) Physics MIT, 1958
10. Bertozzi, W., Paolini, F. R., and Sargent, C. P., *Phys Rev* 110 790 (1958)
11. Worthing, A. C., and Geffner, J., *Treatment of Experimental Data*, Chapter XI (Wiley and Sons, New York, 1943)
12. Firk, F. W. K., Reid, G. W., and Gallagher, J. F., *Nuc Insts* 3 309 (1958)
13. Yergin, P. F., Augustson, R. H., Kaushal, N. N., Medicus, H. A., Moyer, W. R., and Winhold, E. J., *Phys Rev Lett* 12 733 (1964)
14. Glazunov, Yu. Ya., Savin, M. V., Safina, I. N., Fomushkin, E. F., and Khoklov, Yu. A., *JETP* 46 1906 (1964)
15. Wilkinson, D. H., *Ann Rev of Nuc Sci* 9 1 (1959)
16. Levinger, J. S., *Nuclear Photo-disintegration*, (Oxford University Press, 1960)
17. Shevchenko, W., Yudin, N., (to be pub)
18. Fuller and Hayward, E., *Nuclear Reactions*, ed. by Endt, P. M., and Smith, P. B., North Holland Pub Co, Amsterdam (1962)
19. Jones, L. W., and Terwilliger, K. M., *Phys Rev* 91 699 (1957)
20. Kimura, M., Shoda, K., Matsuuro, N., Tohei, T., Sate, K., Kuroda, K., Kuriyama, K., and Akiba, T., *J. Phys Soc Japan*, 15 1128 (1960)
21. Fuller, E. G., and Hayward, E., *Phys Rev* 101 692 (1956)

22. Nathans, R. , and Halpern, J. , Phys Rev 93 437 (1954)
23. Lvinger, J. S. , and Bethe, H. A. , Phys Rev 28 115 (1950)
24. Shevchenko, V. C. , and Yruev, B. A. , Nuc Phys 37 495 (1962)
25. Allum, F. R. , Quirk, T. W. , and Spicer, B. M. , Nuc Phys 53 545 (1964)
26. Eichler, J. , and Weidenmuller, H. A. , Zeitschrift fur Physik, 152 291 (1958)
27. Goldhaber and Teller, Phys Rev 74 1046 (1948)
28. Steinwedel, H. , and Jensen, J. H. D. , Z. Naturforschung 59 413 (1950)
29. Danos, M. , Nuc Phys 5 23 (1958)
30. Wilkinson, D. H. , Physics 22 1039 (1956)
31. Kramer, Nature, Vol 113 (1924)
32. Cohen, B. L. , Fulmer, R. H. , McCarthy, A. L. , and Mukherjee, D. , Rev Mod Phys, 135 332 (1963)
33. Brown, G. E. , and Bolsteri, M. , Phys Rev Lett 3 472 (1959)
34. Vinh-Mau, N. , and Brown, G. E. , Nuc Phys 29 89 (1962)
35. Elliott, J. P. , and Flowers, B. W. , Proc Roy Soc A242 57 (1957)
36. Balashov, V. V. , Shevchenko, V. G. , and Yudin, N. P. , Nuc Phys 27 323 (1961)
37. Balashov, V. V. , Shevchenko, V. G. , and Yudin, N. D. , JETP 41 310 (1964)
38. Dushkov, I. I. , Ishkanov, B. S. , Kapitonov, I. M. , Yur'ev, B. A. and Shevchenko, V. G. , Phys Lett 10 310 (1964)
39. Wilkinson, D. H. , Phil Mag 3 567 (1958)
40. Nilsson, S. G. , Dan Mat Fys Medd, Vol 29, No. 16 (1955)
41. Nilsson, Sawicki, and Glendenning, Nuc Phys 33 239 (1962)
42. S. Hayakawa et al, Prog Theoret Phys 13 415 (1955)
43. Blatt, J. M. , and Weisskopf, V. F. , Theoretical Nuclear Physics (Wiley and Sons, New York, 1952)
44. Lang, and LeCouteur, Proc Phys Soc A67 585 (1954)
45. Courant, E. D. , Phys Rev 82 703 (1951)
46. Heiss, W. D. , Zeitschrift fur Physik, 129 Band 3 Heft (1964)
47. Fujii, S. , Prog Theoret Phys 21 511 (1959)
48. Quirk, T. W. , and Spicer, B. M. , Nuc Phys 51 345 (1964)
49. Ericson, T. , Phil Mag Supp, Vol 9 No. 36 p 425 (1960)
50. Bertozzi, W. , Demos, P. T. , Kowalski, S. , Paolini, F. R. , Sargent, C. P. , and Turchinets, W. , Nuc Inst and Meth 33 199 - 212 (1965)

51. Partovi, F. , Ann Phys 27 79 (1964)
52. McConnell, D. B. , PhD Thesis (unpub) Physics, MIT, Dec 1963
53. Hughes, D. J. , and Schwarz, R. B. , Neutron Cross Sections, BNL 325 2nd ed (1958)
54. Schiff, L. I. , Phys Rev 83 252 (1951)
55. Landau, J. Phys USSR 8 201 (1944)
56. Jackson, J. D. , Classical Electrodynamics (Wiley and Sons, New York 1963) Chapter 13
57. Rice, L. B. , Bolen, L. N. , and Whitehead, W. D. , Phys Rev 134 B537 (1964)
58. Hurwitz, H. , Jr. , and Bethe, H. A. , Phys Rev 81 898 (1951)
59. Nemirovsky, P. E. , and Adamchuk, Y. V. , Nuc Phys 39 562 (1962)
60. Lang, J. W. , and LeCouteur, K. J. , Nuc Phys 13 32 (1959)
61. Auerbach, E. H. , and Perey, F. G. T. , BNL 765 (1962)
62. Auerbach, E. H. , and Moore, S. O. , Phys Rev 135 B895 (1964)
63. Lane and Wandel, Phys Rev 98 1524 (1955)
64. Ross, Mark, and Lawson, Phys Rev 102 1613 (1956)
65. Pal, M. K. , Soper, J. M. , and Stamp, A. P. , to be published (private communication from J. M. Soper)
66. Nuclear Data Sheets, National Academy of Sciences, National Research Council (1965)
67. Erskine, J. R. , Phys Rev 135 B110 (1964)
68. Kim, Y. E. , and Rasmussen, J. O. , Phys Rev 135 B1 (1964)
69. Kuchnir, F. T. , Axel, D. , Criegee, L. , Drake, D. M. , Hanson, A. O. , and Sutton, D. C. , Univ of Illinois, Urbana, Illinois, private communication
70. Mattauch, J. H. E. , Thiele, W. , and Wapstra, A. H. , Nuc Phys 67 1 (1965)
71. Zatsepina, G. N. , Igonin, V. V. , Lazareva, L. E. , and Lepestkin, A. L. , Soviet Phys 17 1200 (1963)
72. Zatsepina, G. N. , Lazareva, L. E. , and Pospelov, A. N. , Soviet Phys 5 21 (1957)
73. Toms, M. E. , and Stephens, W. E. , Phys Rev 108 77 (1957)
74. Emma, V. , Milone, C. , Rubbino, A. , and Malvano, R. , Nuovo Cimento 17 365 (1960)
75. Guman, V. N. , Kharitanov, Yu. I. , Sliv, L. A. , and Sogomonova, G. A. , Nuc Phys 28 192 (1961)
76. Cohen et al, Nuc Phys 20 370 (1960)

77. Mukherjee, D. , and Cohen, B. L. , Phys Rev 127, 1284 (1962)
78. Mottleson, B. R. , and Nilsson, S. G. , Nuc Phys 13 281 (1959)
79. Montalbetti, R. , Katz, L. , and Goldemberg, J. , Phys Rev 91 654 (1953)
80. Sanders, J. B. , Nuc Phys 23 305 (1961)
81. Bethe, H. A. , Rev Mod Phys 9 69 (1937)
82. LeCouteur, K. J. , Nuclear Reactions Vol 1, ed. by Endt, P. M. , and Domeur (North Holland Pub Co, Amsterdam, 1959) Chapter VII
83. Lang, D. W. , Nuc Phys 26 434 (1961)
84. Buccino, S. G. , Hollandsworth, C. E. , Lewis, H. W. , and Bevington, P. R. , Nuc Phys 60 17 (1964)
85. Thomson, D. B. , Phys Rev 129 1649 (1963)
86. Erba, E. , Facchini, and Menichella, Nuovo Cimento 22 1237 (1961)
87. Ferrero, F. , Hanson, A. D. , Malvano, R. , and Tribuno, L. , Nuovo Cimento Seris X, 4 418 (1956)
88. Anashkina, E. S. , JETP 18 279 (1964)
89. Dixon, W. R. , Can J. Phys 133 785 (1955)
90. Breuer, H. , Z. Naturforsch 17a 584 (1962)
91. Newton, T. W. , Can J. Phys 34 804 (1956)
92. Klinkenberg, P. F. A. , Rev Mod Phys 24 63 (1952)
93. Feshbach, Porter, and Weisskopf, Phys Rev 96 448 (1954)
94. Seth, K. K. , Hughes, D. J. , Zimmerman, R. L. , and Garth, R. C. , Phys Rev 110 692 (1958)
95. Baker, R. G. , and McNeill, K. G. , Can J. Phys 39 1158 (1961)
96. Price, G. A. , Phys Rev 93, 1279 (1954)
97. Wataghin, A. , Costa, R. B. , Freire, A. M. , and Goldemberg, J. , Nuovo Cimento 19 864 (1961)
98. Tagliabue, F. , and Goldemberg, J. , Nuc Phys 23 144 (1961)
99. Allum, F. R. , Quirk, J. W. , and Spicer, B. M. , Aus J. Phys 17 420 (1964)
100. Geller, K. , Halpern, J. , and Yergin, D. F. , Phys Rev 95 659 (1954)
101. Johansson, S. A. E. , Phys Rev 97 434 (1955)
102. Asada, T. , Masuda, M. , Okumura, M. , and Okuma, J. , J. Phys Soc Japan 13 1 (1958)
103. Reinhardt, G. C. , and Whitehead, W. D. , Nuc Phys 30 201 (1962)
104. Anashkina, E. S. , JETP 43, 1197 (1962)

105. Grodstein, G. W. , ed. , NBS Circular 583 X-ray Attenuation Coefficients from 10 keV to 100 MeV
106. Goldberg, M. D. , May, V. M. , and Stehn, J. R. , Angular Distributions in Neutron Induced Reactions Vol I and II, BNL 400 2nd ed (1962)
107. Allen, R. C. , Carter, R. E. , and Taylor, H. L. , Fast Neutron Physics Part II, ed. by Marion, J. B. , and Fowler, J. L. , Chapter V H (Interscience Pub, New York, 1963)
108. Baerg, A. P. , Bartholomew, R. M. , Brown, F. , Katz, L. , and Kowalski, S. B. , Can J. Phys 37 1418 (1959)
109. Bohr, A. , International Conf of Peaceful Uses of Atomic Energy, Geneva 1955, UN, New York, Vol 2
110. Forkman, B. , and Johansson, S. A. E. , Nuc Phys 20 136 (1960)
111. Takekoshi, E. , J. Phys Soc Japan 15 2129 (1960)
112. Rabotnov et al, Congre International de Physique Nucleaire, 4e/C337 Vol II, Paris, p 1135 (1964)
113. Albertsson, E. , and Forkman, B. , Nuc Phys 70 209 (1965)
114. Sargent, C. P. , Bertozzi, W. , Demos, P. T. , Matthews, J. L. , and Turchinets, W. , Phys Rev 137 B85 (1965)
115. Fowler and Roos, Phys Rev 98 996 (1955)
116. Kuo Ch'i-ti, Ratner, B. S. , and Sergeev, B. V. , JETP 13, 60 (1961)

## Acknowledgement

The author gratefully acknowledges his indebtedness to the staff and students of the Linear Accelerator Group. Professor W. Bertozzi, Dr. C. P. Sargent, Dr. W. Turchinetz, Professor S. B. Kowalski, T. W. Phillips, F. A. Hanser and J. L. Matthews participated in the experimental work, and analysis and interpretation of the data. The author is also indebted to Professor E. Auerbach for supplying some theoretical parameters used in the data reduction.

The author is especially indebted to Professor W. Bertozzi, who spent a large amount of his limited time supervising and reading this thesis,

Above all, the author would like to thank his wife, Lynne, who spent many hours preparing the final text.

## Biographical Note

Gordon S. Mutchler was born in Iowa City, Iowa, on March 18, 1938. He received his diploma from Soldan Blewett High School in St. Louis, Missouri, in January 1956. Entering MIT in September 1956, he received the degree of Bachelor of Science in Physics in June 1960. He became a Fellow of the National Science Foundation, and attended MIT graduate school from September 1960 to 1965.

The article, "Magnetic Moments of  $Mn^{52}$  and  $Mn^{54m}$ ", by Rudolf W. Bauer, Martin Deutsch, Gordon S. Mutchler, and Donald G. Simons, was published in Physical Review, Vol 120 (p 946) in November 1960.